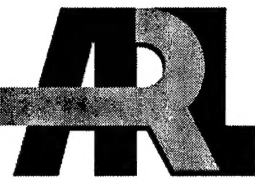


ARMY RESEARCH LABORATORY



Thermomechanical Behavior of Amorphous Polymers During High-Speed Crack Propagation

by Todd W. Bjerke

ARL-TR-2793

August 2002

Approved for public release; distribution is unlimited.

20021009 008

The findings in this report are not to be construed as an official Department of the Army position unless so designated by other authorized documents.

Citation of manufacturer's or trade names does not constitute an official endorsement or approval of the use thereof.

Destroy this report when it is no longer needed. Do not return it to the originator.

Army Research Laboratory
Aberdeen Proving Ground, MD 21005-5066

ARL-TR-2793

August 2002

Thermomechanical Behavior of Amorphous Polymers During High-Speed Crack Propagation

Todd W. Bjerke

Weapons and Materials Research Directorate, ARL

Approved for public release; distribution is unlimited.

Abstract

The dissipative processes that occur during opening and shear-dominated dynamic fracture of amorphous polymers were examined in a combined experimental, computational, and analytical investigation. Experiments were performed using two materials, nominally brittle polymethyl methacrylate and nominally ductile polycarbonate to quantify crack tip heating and identify dominant dissipative mechanisms. Shear-dominated dynamic fracture of polymethyl methacrylate was found to exhibit heating from craze formation and frictional sliding of the fracture surfaces aft of the propagating crack tip. Heating in polycarbonate during shear-dominated dynamic fracture was from two dissipative processes, the formation of an adiabatic shear band and plastic deformation surrounding the propagating crack. Plastic deformation heating was noted for opening mode fracture of polycarbonate. Finite-element simulations of dynamic crack growth in polycarbonate were performed to isolate the heating from thermoplasticity. The simulations indicated that although thermoplastic heating does occur, thermofracture heating may be significant. Heating from craze formation was observed during opening mode fracture of polymethyl methacrylate. A dissipative cohesive zone model was developed to predict heating from thermofracture mechanisms associated with polymer crazing. The model predictions were consistent with measurements of single craze heating during opening mode fracture of polymethyl methacrylate.

Acknowledgments

The work reported within this report was performed while on a long term training assignment at the University of Delaware. I would like to express my gratitude to Professor Lambros, now at the University of Illinois at Urbana-Champagne, for his technical guidance during the course of this research effort. I would also like to thank Professor Geubelle from the University of Illinois at Urbana-Champagne for the insightful discussions regarding this project. The assistance of Dr. Kubair, also from the University of Illinois, is sincerely appreciated. There are many people at the U.S. Army Research Laboratory I would like to thank for their helpfulness. In particular, Dr. McKnight, Dr. Hsieh, and Mr. Dehmer for sharing their insights of polymer mechanics with me, and Mr. Hubbard, Mr. Patton, Mr. Moy, Mr. Napadensky, and Mr. Gniazdowski for assisting me with equipment and testing needs.

INTENTIONALLY LEFT BLANK.

Contents

Acknowledgments	iii
List of Figures	ix
List of Tables	xix
1. Introduction	1
1.1 Background and Motivation.....	1
1.2 Literature Review	3
1.2.1 Mechanics of Propagating Cracks.....	3
1.2.1.1 Cohesive Failure Model	4
1.2.1.2 Shear-Dominated Dynamic Crack Growth.....	6
1.2.2 Thermomechanical Coupling	9
1.2.3 Crack Tip Temperature Measurements	12
1.3 Research Objectives.....	13
2. Experimental Techniques	14
2.1 Material Selection	14
2.2 Experimental Configuration and Impact Event.....	15
2.3 Gas Gun	19
2.4 Projectile Contact, Crack Initiation, and Crack-Speed Measurements	20
2.5 Dynamic Energy Release Rate Measurements.....	25
2.6 Thermal Measurements.....	31
2.6.1 Infrared Detector System and Operation.....	35
2.6.2 Alignment and Focusing Procedure.....	37
2.6.3 Analysis of Specimen Translation.....	39
2.6.4 Calibration	40
2.6.5 Sources of Potential Error.....	44

2.6.5.1 Detector Cross Talk.....	44
2.6.5.2 Depth of Field	44
2.6.5.3 Spherical Aberrations	44
2.6.5.4 Surface vs. Internal Heating	46
2.6.5.5 Temporal Resolution	46
2.6.5.6 Infrared Emission from Heated Surroundings....	47
2.6.5.7 Effect of Material Damage on Surface Emissivity	47
2.6.5.8 Adiabatic Conditions.....	47
3. Opening Mode Experiment	48
3.1 Introduction.....	48
3.2 Crack Tip Speed Measurements.....	51
3.3 Dynamic Energy Release Rate Measurements.....	54
3.4 Temperature Field Measurements	56
3.4.1 PC Experiments	58
3.4.2 PMMA Experiments.....	63
3.4.3 Discussion of Temperature Field Features	68
3.5 Thermal Dissipation of Mechanical Work	70
3.6 Fracture Surface Micrography	74
3.7 Additional Comments on Opening Mode Crack Tip Behavior...	77
4. Shear-Dominated Fracture Experiments	80
4.1 Introduction.....	80
4.2 Crack Tip Speed Measurements.....	82
4.3 Temperature Field Measurements	83
4.3.1 PC Experiment	84
4.3.2 PMMA Experiments.....	87
4.4 Thermal Dissipation of Mechanical Work	90
4.5 Model Friction Experiments	92
4.6 Fracture Surface Micrography	93

4.7 Additional Comments on Shear-Dominated Crack Tip Behavior	98
5. Effect of Plasticity in Thermomechanical Heating of Ductile Polymers During Opening-Mode Dynamic Fracture	100
5.1 Introduction.....	100
5.2 Finite-Element Model	101
5.3 Material Model.....	106
5.4 Simulation Results and Discussion.....	110
6. Dissipative Cohesive Zone Model	115
6.1 Introduction.....	115
6.2 Cohesive Zone Model	119
6.2.1 Thermal Dissipation in a Cohesive Zone	123
6.2.2 Cohesive Traction Laws and Stress Distributions	126
6.3 Comparison of Dissipative Cohesive Zone Model With Experiments.....	137
6.3.1 Single Craze Failure Mode	137
6.3.2 Distributed Damage Failure Mode	142
6.4 Further Analysis of Temperature Field Measurements.....	147
6.4.1 Flanking Thermal Signal Decay	148
6.4.2 Cohesive Zone Length.....	155
6.4.3 Effect of Temperature on μ and cp	156
7. Conclusions	156
7.1 Conclusions	156
7.2 Future Work	159
8. References	161
Appendix A. Closed Form Solution of Cohesive Zone Length	171

**Appendix B. Closed Form Solution of Cohesive Zone Opening
Rate**

173

Report Documentation Page

177

List of Figures

Figure 1. Three modes of crack loading.....	4
Figure 2. Schematic illustration of a cohesive zone idealization at the tip of a crack to model the inelastic material response. The applied cohesive stress, $\sigma(\delta)$, cancels the stress singularity at the crack tip.....	5
Figure 3. Crazing process at the tip of an advancing crack tip. Stresses ahead of the crack tip cause molecular chain alignment to occur. Further stretching of the material causes the aligned molecules to form large bundles called fibrils and the creation of small voids between fibrils. The location of molecular chain scission is the crack tip. Fibril recoil occurs as the crack faces separate.	7
Figure 4. Asymmetric loading geometries used to generate an adiabatic shear band and a shear-dominated crack tip. The left is the method introduced by Kalthoff and Winkler (1987). The right is the configuration used by Rosakis et al. (1999) and Ravi-Chandar et al. (2000).....	8
Figure 5. Low-rate tensile stress-strain curves for high molecular weight PMMA showing rate sensitivity of Young's modulus and ultimate strength. Two tests were performed for each strain rate. Brittle failure occurred during each test.....	16
Figure 6. Low-rate tensile stress-strain curves for PC showing strain-rate sensitivity of yield strength. Young's modulus was not rate sensitive. Two tests were performed for each strain rate.....	16
Figure 7. Opening mode dynamic fracture experiment configuration also showing infrared detector coverage and crack propagation gage. Crack propagates from right to left.....	18
Figure 8. Shear-dominated dynamic fracture experiment configuration also showing infrared detector coverage and painted wires for coarse crack speed measurement. Crack propagates from left to right.....	18
Figure 9. Photograph of gas gun, impact chamber, and infrared detector system.....	20
Figure 10. Projectile velocity measurement system using two infrared break-beams at the muzzle of the launch tube. Projectile interrupts infrared beam, causing infrared detectors to change response.....	21

Figure 11. Crack propagation gage constructed from thin lines of conducting silver paint. Top illustration shows gage configuration with the crack propagating from left to right, severing the painted lines sequentially. Bottom photograph is of a completed gage on a PC fracture specimen. Crack initiation gage is also shown.	23
Figure 12. Schematic of the crack propagation speed measurement circuit using painted silver lines on the polymer test specimen. The propagating crack sequentially severs the painted lines, changing the overall resistance of the circuit.	24
Figure 13. Strain gage coordinate system showing the gage orientation angle, α . Strain gage is fixed in space and the coordinate system origin is attached to the propagating crack tip that moves from left to right.	26
Figure 14. Coordinate system used in the constant crack tip speed analysis for determining the dynamic energy release rate from a strain gage. Coordinate system origin is at the crack tip and propagates with the crack.	28
Figure 15. Effect of the strain gage orientation on the location of peak strain as the crack propagates past the gage at 400 m/s in PMMA. Crack tip is located at $x = 0$. Acute angle results in the peak strain occurring 5 mm prior to crack passage, whereas the obtuse angle gives a peak strain when the crack is directly beneath the gage.	29
Figure 16. Sensitivity of strain gage response to crack tip speed for PMMA. Obtuse angle orientation is used.	30
Figure 17. Position and orientation of strain gages used to measure the dynamic energy release rate during opening mode dynamic fracture. Angle shown is for PMMA (119° was used for PC). Crack propagates from left to right.	32
Figure 18. Planck distribution for a black body emitter at several temperatures showing the shift in emitted radiation wavelength as the body is heated.	34
Figure 19. Spectral responsivity of several common photon detectors (Zehnder and Rosakis 1993).	34
Figure 20. Optical configuration used to measure the temperature field surrounding a propagating crack tip. Infrared detector array coverage is also shown.	36
Figure 21. Hot-wire jig used for alignment and focusing the infrared detector system. The 76- μm -diameter chromel-A wire serves as an infrared radiation source by passing current through it.	38

Figure 22. Finite-element mesh and boundary conditions used for numerical simulation of the projectile impacting the polymer specimen. Steel projectile moves from left to right.....	41
Figure 23. Finite-element results showing the horizontal displacement of a point 10 mm ahead of the initial notch tip due to projectile impact at various speeds.....	41
Figure 24. Typical calibration for one channel of the infrared detector system showing results for PMMA and PC.....	43
Figure 25. Typical calibration for one channel of the infrared detector system showing results for PMMA and PC using a grooved specimen. Groove was polished with 2000-grit sandpaper to achieve smooth finish.....	43
Figure 26. Infrared detector element cross talk observed using a 76- μ m heated wire. Cross talk of 7%-10% was recorded.....	45
Figure 27. Detector output measured as the detector array was translated in and out of focus to obtain an estimate of the infrared measurement system depth of focus.....	45
Figure 28. Temperature increase of several x locations below the surface of a semi-infinite PMMA solid with a suddenly applied surface temperature. Initial ambient temperature of solid was 293 K and suddenly applied constant surface temperature was 393 K.....	49
Figure 29. Typical crack propagation gage circuit output. The abrupt increases in voltage are generated by the painted wires being severed by the propagating crack.....	52
Figure 30. Crack tip position history obtained from the crack propagation gage timing data for PMMA. Two different experiments are shown, corresponding to different projectile-impact speeds.....	52
Figure 31. Crack tip propagation speed in PMMA for two experiments with different projectile-impact speeds. Propagation speed was determined from crack propagation gage timing data and the distance between the painted wires. Error bar shows typical measurement uncertainty for crack tip speed (estimated from Lambros and Rosakis [1995]).	53
Figure 32. Opening mode crack tip speeds for PC and PMMA as measured by the crack propagation gage for experiments with a projectile-impact speed of 40 m/s.	54
Figure 33. Measured strain from the strain gage circuits for a crack propagating at 0.55 c_R in PC. Distance between strain gages was 8 mm.	55

Figure 34. Measured strain from the strain gage circuits for a crack propagating at $0.55 c_R$ in PMMA. Separation between strain gages was 8 mm.....	55
Figure 35. Measured strain from the strain gage circuits for a crack propagating in PMMA. The crack accelerated to a terminal speed of ~ 450 m/s.....	56
Figure 36. Dynamic energy release rate for various crack tip speeds in PC and PMMA.....	57
Figure 37. Thermal detector output (after calibration) for opening mode fracture of PC with a crack tip speed of $0.55 c_R$	59
Figure 38. Thermal detector output from two detector elements for an opening mode crack propagating in PC at a terminal speed of $0.55 c_R$. Thermoelastic cooling is observed prior to dissipative crack tip heating.....	59
Figure 39. Thermal detector output (after calibration) for opening mode fracture of PC with a crack tip speed of $0.45 c_R$	61
Figure 40. Temperature contours for opening mode fracture of PC with a crack tip speed of $0.55 c_R$. The large lateral span on the heat-affected region suggests plastic deformation is a significant heating mechanism near the propagating crack tip.....	62
Figure 41. Temperature contours for opening mode fracture of PC with a crack tip speed of $0.45 c_R$. The lateral span on the heat-affected region is smaller than the higher speed crack tip experiment.....	62
Figure 42. Thermal detector output (after calibration) for opening mode fracture of PMMA with a crack tip speed of $0.55 c_R$	64
Figure 43. Thermal detector output (after calibration) of opening mode fracture of PMMA with the crack tip propagating between two detector elements.....	65
Figure 44. Thermal detector output (after calibration) for opening mode fracture of PMMA with a crack tip speed of $0.24 c_R$	65
Figure 45. Thermal detector output (after calibration) for opening mode fracture of low molecular weight PMMA with a crack tip speed of $0.24 c_R$	66
Figure 46. Thermal detector output (after calibration) for opening mode fracture of PMMA with the detector array rotated to the horizontal position. Crack tip may not have passed directly through the region monitored by the infrared detector system. Crack tip propagation speed is $0.57 c_R$	67

Figure 47. Temperature contours for opening mode fracture of PMMA with a crack tip speed of $0.55 c_R$. The contours are highly localized compared to those of PC, suggesting that plastic deformation does not contribute to the crack tip temperature increase.....	68
Figure 48. Rate of plastic work contours for opening mode fracture of PC with a crack tip speed of $0.55 c_R$. The heat source was assumed to be only ductile plastic deformation with a β of 0.5.	72
Figure 49. Rate of plastic work contours for opening mode fracture of PC with a crack tip speed of $0.45 c_R$. The heat source was assumed to be only ductile plastic deformation with a β of 0.5. The span of the contours are smaller than for the higher crack tip speed experiment, illustrating the influence of crack propagation speed.....	72
Figure 50. Rate of internal heat generation contours for opening mode fracture of PMMA with a crack tip speed of $0.55 c_R$. Internal heating was assumed to be the only source of crack tip heating.....	73
Figure 51. Photograph of PC fracture surface showing unique regions of smooth and rough surface texture.	75
Figure 52. SEM images of the smooth and rough regions of a PC fracture surface. The crack propagated from the bottom of the figure to the top.....	76
Figure 53. Photograph of a PMMA fracture surface showing the transition of surface roughness and eventual branching.....	77
Figure 54. SEM image of the smooth and rough regions of a high-speed crack growth PMMA fracture surface. The crack propagated from the bottom of the figure to the top. The rough region has a surface roughness of about 100–200 μm	78
Figure 55. Photograph of a low-speed crack growth PMMA fracture surface showing a glassy smooth surface corresponding to the passage of a single craze.	79
Figure 56. Opening mode maximum crack tip temperature as dependent on crack tip speed.	79
Figure 57. Empirical relationship between maximum crack tip temperature and dynamic energy release rate for opening mode fracture of PMMA.....	81
Figure 58. Typical output from the break-wire circuit used to determine the crack tip speed for shear-dominated dynamic fracture of PMMA. Output from the crack initiation and two crack-speed measurement circuits is shown.	83

Figure 59. Typical thermal detector output (after calibration) for shear-dominated fracture of PC with side grooves to suppress crack kinking. ΔT denotes temperature change from ambient, and $t = 0$ corresponds to time of impact.....	85
Figure 60. Temperature history of an adiabatic shear band and arrested crack in a PC specimen without side grooves. ΔT denotes temperature change from ambient, and $t = 0$ corresponds to time of impact.	86
Figure 61. Temperature contours around crack tip region for shear-dominated fracture of PC. Temperature increase from room temperature (K). Steady-state crack growth has been assumed.	87
Figure 62. (a) Thermal detector output (after calibration) for shear-dominated fracture of PMMA with side grooves to suppress crack kinking. ΔT denotes temperature change from ambient and $t = 0$ corresponds to time of impact. (b) Initial portion of thermal signal from shear-dominated fracture of PMMA with side grooves. Temperature field surrounding crack tip is shown. ΔT denotes temperature change from ambient and $t = 0$ corresponds to time of impact.. ..	88
Figure 63. Temperature contours at crack tip region for shear-dominated fracture of PMMA. Temperature increase from room temperature (K). Steady-state crack growth has been assumed.	89
Figure 64. Plastic work rate contours at crack tip region for shear-dominated fracture of PC. $\beta = 0.5$ and steady-state crack growth have been assumed.	90
Figure 65. Rate of internal heat generation contours at crack tip region for shear-dominated fracture of PMMA. Negligible plastic work rate and steady-state crack growth have been assumed.	91
Figure 66. Configuration for high-speed friction experiments. Infrared detector monitored the sliding interface between the top and middle PMMA pieces.....	94
Figure 67. Typical thermal detector output (after calibration) for high-speed friction experiments. ΔT denotes temperature change from ambient and $t = 0$ corresponds to time of impact.....	94
Figure 68. Photograph of fracture surface from shear-dominated dynamic fracture of PC with side grooves to suppress crack kinking. Fracture surface ripples are visible on the crack face.....	95
Figure 69. Photograph of fracture surface from shear-dominated dynamic fracture of PMMA with side grooves to suppress crack kinking. White-colored wear layer is visible on the crack face.....	96

Figure 70. SEM image of fracture surface from shear-dominated dynamic fracture experiment using PC with side grooves. The crack propagated from left to right leaving surface ripples covered with a molten coating.....	96
Figure 71. SEM image of fracture surface from shear-dominated dynamic fracture using PMMA with side grooves. Left-side image was taken in the interior of the panel. Right-side image is near location where infrared detector monitored. The crack propagated from left to right.....	97
Figure 72. SEM image of PMMA high-speed friction surface. The mating surface slid over the surface shown from left to right. Deposits are visible in the friction surface. The original surface condition prior to the experiment is shown on the right.....	98
Figure 73. Measured temperature field surrounding a crack tip propagating in PC at 550 m/s under mode I loading.....	102
Figure 74. Finite-element mesh used for the numerical simulations. Element size in the crack tip region is 80 μm . The plane-stress model has 77,600° of freedom.....	104
Figure 75. Dynamic crack initiation time measured during the opening-mode fracture experiments using PC for various projectile-impact speed.....	105
Figure 76. Crack tip position history measured during dynamic opening-mode crack growth in PC. Position history was used for timing the sequential release of nodes along the plane of symmetry to simulate crack tip propagation in the numerical simulation.....	105
Figure 77. Nominal stress-strain data for dynamic compression of PC reported by Li and Lambros (2001). Results from three different strain rates are shown.....	107
Figure 78. Approximation of the plastic part of the nominal stress-strain curve for PC at a strain rate of 1200 s^{-1} as used in the numerical simulation material model.....	108
Figure 79. Approximation of the plastic part of the nominal stress-strain curve for PC at a strain rate of 1700 s^{-1} as used in the numerical simulation material model.....	109
Figure 80. Approximation of the plastic part of the nominal stress-strain curve for PC at a strain rate of 2200 s^{-1} as used in the numerical simulation material model.....	109
Figure 81. Cauchy (true) stress as a function of plastic logarithmic strain for three different strain rates of dynamic compression for PC.	110

Figure 82. Temperature increase contours at the tip of a crack tip propagating in PC at a speed of 550 m/s predicted from the numerical simulation. Adiabatic heating was due solely to plastic work.....	111
Figure 83. Temperature contours surrounding a crack tip propagating in PC at 550 m/s under mode I loading.....	112
Figure 84. Temperature increase of a vertical array of finite elements located 3.2 mm from the initial notch tip for comparison to infrared detector measurements.....	113
Figure 85. The initiation, widening, and breakdown of a polymer craze during opening-mode fracture. Aligned molecular chains form thick fibrils that resist crack opening.....	116
Figure 86. Cohesive zone concept at the tip of a propagating crack. Crack face opening, δ , is resisted by a cohesive traction σ	118
Figure 87. Far field and near tip contours used for calculating energy flux into a crack tip with a cohesive zone of length L (Freund 1990).....	120
Figure 88. Heat source smaller than the infrared detector element passing over the region monitored by the detector. The element responds to the average radiation incident on the entire area monitored.....	125
Figure 89. Illustration of intrinsic and extrinsic cohesive traction laws (Kubair and Geubelle 2001).....	127
Figure 90. Form of constant and linear decay stress distributions used in the dissipative cohesive zone model.....	128
Figure 91. Temperature increase predictions made with the dissipative cohesive zone model using the constant stress and linear decay stress distributions. Baseline material properties for PMMA and a crack propagation speed of 300 m/s were used. Ambient temperature T_0 is 295 K.....	129
Figure 92. Calculated form of the constant stress and linear decay traction laws obtained from matching cohesive zone stress distributions.....	131
Figure 93. Temperature increase predictions using a linear decay $\sigma(\xi)$ relation from parametric study with E varied.....	132
Figure 94. Internal heating rate predictions using a linear decay $\sigma(\xi)$ relation from parametric study with E varied.....	133
Figure 95. Temperature increase predictions using a linear decay $\sigma(\xi)$ relation from parametric study with G varied.....	133
Figure 96. Internal heating rate predictions using a linear decay $\sigma(\xi)$ relation from parametric study with G varied.....	134

Figure 97. Temperature increase predictions using a linear decay $\sigma(\xi)$ relation from parametric study with σ_c varied.	134
Figure 98. Internal heating rate predictions using a linear decay $\sigma(\xi)$ relation from parametric study with σ_c varied.	135
Figure 99. Temperature increase predictions using a linear decay $\sigma(\xi)$ relation from parametric study with a varied.	135
Figure 100. Internal heating rate predictions using a linear decay $\sigma(\xi)$ relation from parametric study with a varied.	136
Figure 101. Leading portion of experimentally measured temperature signal from two different PMMA opening-mode fracture experiments with crack tip speeds of 300 m/s. Inset at top left shows a longer time span of the signals.	138
Figure 102. Rate of internal heating derived from dynamic opening-mode fracture of PMMA. The crack tip speeds were 300 m/s, and the experimental signals are from the peak detector.	139
Figure 103. Comparison of the temperature increase predicted by the dissipative cohesive zone model with experimental data for opening-mode fracture of PMMA with a crack speed 300 m/s. Constant stress and linear decay stress distributions were used in the model.	140
Figure 104. Form of the quad-high stress distribution compared to the constant stress and linear decay stress distribution.	141
Figure 105. Calculated shape of the quad-high traction law. The constant stress and linear decay traction laws are shown for comparison. The baseline parameters for 300 m/s crack growth in PMMA were used.	141
Figure 106. Temperature increase predicted by the dissipative cohesive zone model compared to experimental data for 300 m/s crack growth in PMMA.	142
Figure 107. Internal heating predicted by the dissipative cohesive zone model compared to experimental data for 300 m/s crack growth in PMMA.	143
Figure 108. Leading portion of experimentally measured temperature signal from three different PMMA opening mode fracture experiments with crack tip speeds of 300, 400, and 600 m/s. Inset at top left shows a longer time span of the signals. Peak detector only shown for 400 and 600 m/s experiments.	144
Figure 109. Rate of internal heating derived from dynamic opening mode fracture of PMMA. The crack tip speeds were 300, 400, and 600 m/s, and the experimental signals are from the peak detector.	144

Figure 110. Temperature increase predicted by the dissipative cohesive zone model compared to experimental data for 400 m/s crack growth in PMMA.....	145
Figure 111. Temperature increase predicted by the dissipative cohesive zone model compared to experimental data for 600 m/s crack growth in PMMA.....	145
Figure 112. Comparison of the internal heat rate predicted by using the quad-high stress distribution in the dissipative cohesive zone model with experimental data for low, mid, and high crack tip speed fracture of PMMA.....	146
Figure 113. Distribution of temperature among the vertically oriented infrared detector elements at the time of peak temperature.	148
Figure 114. Contours of temperature increase in PMMA for a propagating crack tip and trailing thermal wake. Crack tip propagation speed is ~300 m/s. The crack opening displacement is evident by the shape of the trailing wake region.	149
Figure 115. Depiction of craze thickening, splitting, and crack opening relative to the stationary infrared detector elements for a craze passing through the region monitored by an element. Bottom of figure is representative data for the configuration illustrated.	150
Figure 116. Depiction of craze thickening, splitting, and crack opening relative to the stationary infrared detector elements for a craze passing between two detector elements. Bottom of figure is representative data for the configuration illustrated.....	152
Figure 117. Depiction of crack opening relative to the stationary infrared detector elements for a craze passing below the detector element array. Bottom of figure is representative data for the configuration illustrated.	153
Figure 118. Crack face opening speed for fracture of PMMA with a crack tip speed of 300 m/s. Experimental data derived from temperature measurements are compared to analytical expression from Freund (1990).	154
Figure 119. Variation of density with absolute material temperature for PMMA (Domininghaus 1988).	157
Figure 120. Variation of specific heat with material absolute temperature for PMMA (Domininghaus 1988).	157

List of Tables

Table 1. Rate effects on elastic moduli of PMMA and PC.....	17
Table 2. Polymer properties.....	17
Table 3. Uniaxial high strain-rate yield stresses and fraction of plastic work converted to heat (β) from Li and Lambros (2001).	107
Table 4. Parameter values used for the parametric study.....	131

INTENTIONALLY LEFT BLANK.

1. Introduction

1.1 Background and Motivation

Polymeric materials are finding increased use in applications that subject the materials to intense, transient loadings. Examples of this include combat aircraft canopies that must withstand bird impacts and transparent face shields used by explosive ordnance disposal teams that cannot be perforated by small fragments. The design and evaluation of these devices is typically done through experimentation and numerical modeling because of the complexities of the transient loading and failure processes. The cost of performing extensive, detailed experiments on complex systems is becoming prohibitive, leading to an increased reliance on numerical simulations. Because of this, the modeling of localized failure in materials subject to extreme loading conditions has received increased attention during the past few years. In particular, emphasis has been placed on developing suitable crack- and shear-band initiation, growth, and arrest models for finite-element implementation. Key to achieving this is a thorough understanding of the failure event itself. This task is further complicated for failure events that are highly transient because of the small time scales involved.

As an elastic-plastic material undergoes plastic deformation, a portion of the work done on this material is stored internally, and the remainder is dissipated, usually in the form of heat. If the deformation event is rapid compared to the time required for conduction to take place, significant temperature increases may result, thus affecting material response. As such, the coupling between the deformation mechanics and thermal heating for high-loading rate events must be accounted for in any modeling. This is especially true for materials of low-thermal diffusivity such as polymers because the heat generated during localized deformation does not have time to conduct to surrounding regions. In addition, polymers are more susceptible to thermal effects than metals or ceramics in the sense that they exhibit larger stiffness and strength variations over smaller temperature changes. Thus, not only must a constitutive and failure model account for rate effects, but it must also account for the effects of temperature changes on material properties from thermomechanical heating.

During fracture, a process zone exists ahead of the propagating crack tip, in which the physical mechanisms associated with failure occur. If the material is brittle, the formation of new surfaces occurs within the process zone. The energy required for surface creation is twice (because two surfaces are created during fracture) the material's surface energy, γ , which is a material property. Surprisingly, studies have shown that crack tip heating does occur in what are

often thought of as brittle polymers during dynamic fracture (Döll 1976; Fuller et al. 1975), implying that additional energy beyond that needed for the creation of new surfaces is required to fracture such brittle materials. Sun and Hsu (1996) noted that the energy for opening mode fracture of a brittle material can in some cases be several orders of magnitude larger than 2γ . The excess energy is used in the process zone for microstructure breakdown and molecular bond scission and is eventually dissipated as heat. Because crack tip speeds during dynamic fracture are a significant fraction of the material dilatational wave speed, the generated heat does not have time to conduct to surrounding regions. This condition results in a temperature increase inside the process zone of the material. For a brittle polymeric material (i.e., one of low thermal diffusivity), a high crack tip temperature can lead to thermal softening that blunts the advancing crack tip and effectively "toughens" the material. For a ductile material, plastic deformation surrounds the crack tip process zone, contributing to the overall temperature increase. Thus, the temperature field surrounding a propagating crack is related to the dissipation of mechanical work that went into deformation and failure of the material. Measurement of this field at sufficient resolution can provide useful insight into the physical mechanisms within the process zone. Additionally, a detailed description of mechanical work dissipation will enable a crack tip failure law, or cohesive law, to be developed.

Additional motivation for measuring the temperature field around a propagating crack is found in the shear-dominated fracture experiments of Ravi-Chandar et al. (2000) and Rosakis et al. (1999). These experiments, discussed in detail in the next section and in section 4, used high-speed photography to examine the stress field surrounding a propagating shear crack in brittle polymers. The resulting fracture surfaces from the Ravi-Chandar et al. (2000) experiments showed distinct evidence of polymer melting: thin strands of material were drawn along the crack surface. The stress fields recorded by Rosakis et al. (1999) showed evidence of frictional crack surface contact aft of the advancing crack tip. It is not clear from these studies if the melted strands on the fracture surface were from frictional sliding or from the fracture process itself, much less what the dissipation mechanisms are for this mode of fracture. Temperature measurements during shear-dominated dynamic fracture will provide additional details and insight into these processes.

In the present work, the temperature field surrounding high-speed cracks in two amorphous polymers were studied. Polymethyl methacrylate (PMMA), a nominally brittle material commonly known as acrylic, and polydian carbonate, a nominally ductile material known as polycarbonate (PC), were used in the study. Two different modes of dynamic fracture were examined, opening and shear-dominated. Measurements of crack tip speed, dynamic fracture toughness, and temperature surrounding the propagating crack were made to establish the dissipative nature of the process zones for each material and mode of fracture.

Microscopy analyses of the resulting fracture surfaces provided additional physical insight into the dissipation mechanics involved. The contribution of heating from plastic deformation to the overall temperature field for the ductile polymer was quantified in a combined experimental-numerical effort. The body of experimental data (insights gained during the study) and measurements of the dynamic energy release rate during fracture led to the development of a dissipative cohesive material model applicable to opening mode fracture of PMMA. In the next section, a literature review is presented to introduce many of the concepts and to survey past studies of crack tip heating.

1.2 Literature Review

1.2.1 Mechanics of Propagating Cracks

Asymptotic Fields

The two-dimensional (2-D) asymptotic stress field surrounding a crack tip propagating dynamically with constant speed is given as (Freund 1990)

$$\sigma_{ij} \sim \frac{K_I^d}{\sqrt{2\pi r}} \Sigma'_{ij}(\theta, \dot{a}) + \frac{K_{II}^d}{\sqrt{2\pi r}} \Sigma''_{ij}(\theta, \dot{a}) + \frac{K_{III}^d}{\sqrt{2\pi r}} \Sigma'''_{ij}(\theta, \dot{a}), \quad (1)$$

for $r \rightarrow 0$, where (r, θ) are polar coordinates in the plane of deformation centered at the crack tip, K_I^d , K_{II}^d , and K_{III}^d are scalar multipliers called the dynamic stress intensity factors corresponding to mode I, mode II, and mode III loading respectively, \dot{a} is the crack tip speed, and $\Sigma_{ij}(\theta, \dot{a})$ are known angular functions for each mode of fracture. The three modes of loading that can be applied to a 2-D crack are shown in Figure 1. In this study, mode I and predominantly mode II fractures are examined. A significant aspect of equation (1) is the stress singularity that develops near the crack tip. In real material systems, stress singularities do not exist, the material near the crack tip deforms and fails, eliminating the stress singularity.

It is often more convenient to work with energy quantities instead of stress or deformation. The dynamic energy release rate, G , is defined as the rate of mechanical energy that flows into the advancing crack tip per unit crack advance. Freund (1990) derived an expression for plane stress relating the dynamic energy release rate to the dynamic stress intensity factors for linear elastodynamic crack growth as

$$G = \frac{A_I(\dot{a})}{E} (K_I^d)^2 + \frac{A_{II}(\dot{a})}{E} (K_{II}^d)^2 + \frac{A_{III}(\dot{a})}{2\mu} (K_{III}^d)^2, \quad (2)$$

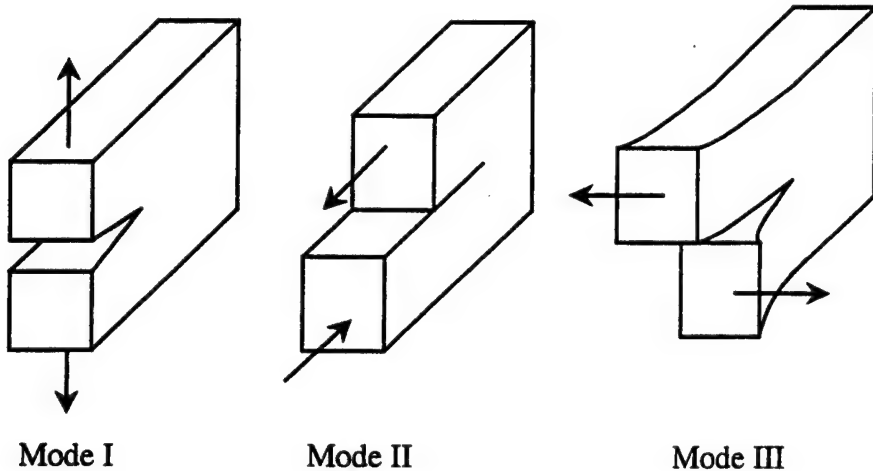


Figure 1. Three modes of crack loading.

where μ is the shear modulus, E is Young's modulus, and A_I , A_{II} , and A_{III} are universal functions that do not depend on loading or body geometry. Expressions for the universal functions can be found in Freund (1990). The energy release rate is essentially the amount of energy that must be supplied to the crack tip for it to propagate at a given speed and includes the energy needed to create free surfaces as well as that needed to alter the material at the macro-scale (e.g., plasticity) and microscale levels (e.g., molecular chain realignment).

Döll (1976) and Sharon et al. (1996) found G to increase nonlinearly with crack tip speed for mode I experiments using PMMA. These studies showed G to asymptote toward infinity when the crack tip speed approached 60% of the material's Rayleigh wave speed, c_R . Zehnder and Rosakis (1990) have shown the limiting crack tip speed in 4340 steel to also be approximately 0.6 c_R . When an attempt is made to drive the crack faster, the single crack will branch, or bifurcate symmetrically, into two cracks because of a change in the maximum elastodynamic hoop stress direction (Yoffe 1951), thereby splitting the available energy between two crack tips. Sharon et al. (1996) observed short microcracks, which they termed failed branching, that increased in occurrence as G was increased. It was reasoned that this accounted for the nonlinear relationship between G and crack tip speed.

1.2.1.1 Cohesive Failure Model

The notion of a cohesive zone at the tip of a crack was first introduced by Barenblatt (1959) and Dugdale (1960) to analytically eliminate the stress singularity at the tip of a crack under mode I loading. Freund (1990) extended the cohesive zone idea to the dynamic crack growth case. A cohesive zone is introduced as a line of length L that extends from the crack tip to model inelastic

material behavior ahead of the crack tip (as shown in Figure 2). Cohesive stresses act along the cohesive line to resist crack opening. The stress field outside this region has a stress intensity factor $K_{I,appl}$. Within this region, the opening of the crack is resisted by a cohesive stress denoted $\sigma(\delta)$, where δ is the opening displacement within the cohesive zone. The cohesive traction leads to a negative stress intensity factor $K_{I,coh}$ at the crack tip. The total stress intensity factor is the sum of the applied and cohesive stress intensity factors. The stress singularity is eliminated by selecting a cohesive zone length, L , such that the combined stress intensity factor is zero at the crack tip. The expression relating the cohesive stress to the cohesive zone length for plane stress conditions is given by Freund (1990) as

$$\int_0^{\delta_c} \sigma(\delta) d\delta = \frac{2A_I(\dot{a})}{\pi E} \left[\int_0^L \frac{\sigma[\delta(l)]}{\sqrt{l}} dl \right]^2, \quad (3)$$

where δ_c is the maximum opening displacement in the cohesive zone (see Figure 2). Furthermore, the cohesive stress is related to the dynamic energy release rate as

$$G = \int_0^{\delta_c} \sigma(\delta) d\delta. \quad (4)$$

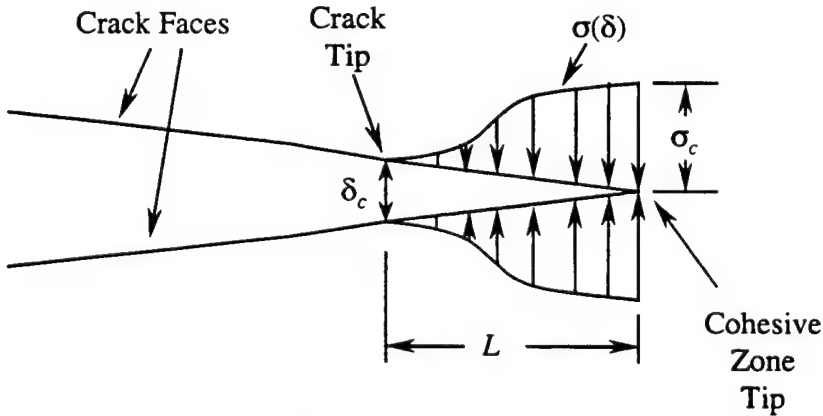


Figure 2. Schematic illustration of a cohesive zone idealization at the tip of a crack to model the inelastic material response. The applied cohesive stress, $\sigma(\delta)$, cancels the stress singularity at the crack tip.

The cohesive zone notion is ideal for the present study because the cohesive zone is by design the only region where mechanically dissipative processes occur. Thus, if the temperature field can be measured along with G , the necessary ingredients are in hand to assemble a meaningful cohesive model based on the actual dissipation from a dynamic fracture event. This is in contrast to earlier cohesive models (Tvergaard and Hutchinson 1992; Needleman 1992; Xu and

Needleman 1994; Tvergaard and Hutchinson 1996; Camacho and Ortiz 1996) where the traction-separation relation $\sigma(\delta)$ was based on theoretical arguments or postmortem fracture surface observations and not on experimental measurements taken during the decohesion process.

The cohesive zone concept is also attractive for this study because the phenomenon of crazing that causes brittle fracture in amorphous polymers conceptually resembles a cohesive zone. Amorphous polymers consist of long molecular chains randomly oriented and entangled. Their mechanical response is governed by two types of bonds at the microscopic level: covalent bonds between the atoms themselves and van der Waals forces between molecule segments. The viscoelastic behavior of polymers is a direct result of the forces between the entangled molecular chains. As an amorphous polymer cools from the liquid state, it remains viscous until it reaches the glass transition temperature, T_g , at which time the relative motion of the molecules becomes restricted. Amorphous polymers do not have a defined melt temperature. Unlike crystalline materials, there is not a threshold temperature that separates fluid and solids states. When heated beyond T_g , the material becomes less viscous until it eventually reaches a fluidlike state.

Polymer crazing is the disentanglement and alignment of molecular chains into large fibrils, or groups of chains, as a result of high-tensile loading. Voids form between the fibrils due to the relatively weaker van der Waals forces. Kambour (1964, 1965, 1966a, 1966b) observed the formation of crazes at the tip of statically grown cracks in glassy polymers using optical methods. Subsequent studies have concluded that brittle fracture in polymers is the result of craze formation followed by fibril breakdown (molecular chain scission) and fibril stub recoil (Beahan et al. 1973; Murray and Hull 1970; Kramer 1983; Kramer 1984; Yang et al. 1986; Henkee and Kramer 1984; Donald and Kramer 1982; Berger 1990). Figure 3 depicts the craze formation process ahead of a propagating crack tip.

When a polymer well below the glass transition temperature is subjected to an imposed strain, a competition between classic shear yielding and craze formation occurs. A large hydrostatic tensile component in the stress tensor is conducive to crazing, while shear yielding is favored by a large deviatoric stress component (Anderson 1995). Ravi-Chandar (1995) found the competition between plasticity and craze formation to be load-rate sensitive, with craze formation favored at high load rates.

1.2.1.2 Shear-Dominated Dynamic Crack Growth

There recently have been numerous studies on the mechanics of shear-dominated dynamic fracture of materials. Typically, mode II loading will cause a crack to immediately kink at an angle of approximately 70° relative to the

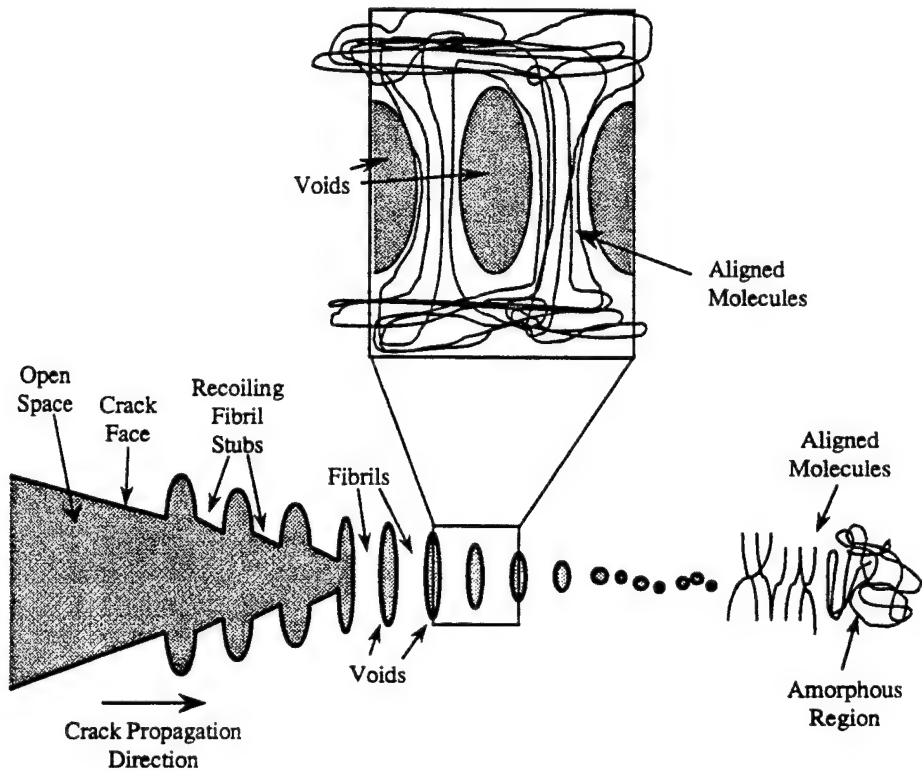


Figure 3. Crazing process at the tip of an advancing crack tip. Stresses ahead of the crack tip cause molecular chain alignment to occur. Further stretching of the material causes the aligned molecules to form large bundles called fibrils and the creation of small voids between fibrils. The location of molecular chain scission is the crack tip. Fibril recoil occurs as the crack faces separate.

original crack direction. In doing so, the crack propagates under locally mode I conditions. This is due to the fracture toughness for mode I being lower than mode II. The fracture mechanisms associated with mode I dynamic crack growth have lower energy requirements than do those associated with mode II. Broberg (1987) found the mode I toughness of PMMA to be 2.5 times lower than the mode II toughness. The kink angle of approximately 70° was found by Erdogan and Sih (1963) to be the result of the maximum hoop stress direction for shear-loading conditions.

There are generally three ways to suppress crack kinking during shear-dominated crack loading. The first method is to apply sufficient in-plane compressive tractions to eliminate the possibility of opening mode cracking. This was demonstrated by Broberg (1987) who successfully grew mode II cracks in PMMA. The second method is to exploit a failure mode transition that occurs in ductile materials subjected to dynamic shear loading. This was demonstrated by Kalthoff and Winkler (1987) for steel and Ravi-Chandar (1995) for

PC. These studies used the asymmetric impact-loading geometry introduced by Kalthoff and Winkler (1987) and shown in Figure 4, to generate a dynamic shear crack. For ductile materials, a failure mode transition from mode I crack kinking to highly localized adiabatic shearing, i.e., adiabatic shear band formation (as defined in Duffy [1984]), was found to occur when the impact speed of the projectile exceeded a threshold value. This transition did not occur in brittle materials, crack kinking occurred regardless of projectile impact speed.

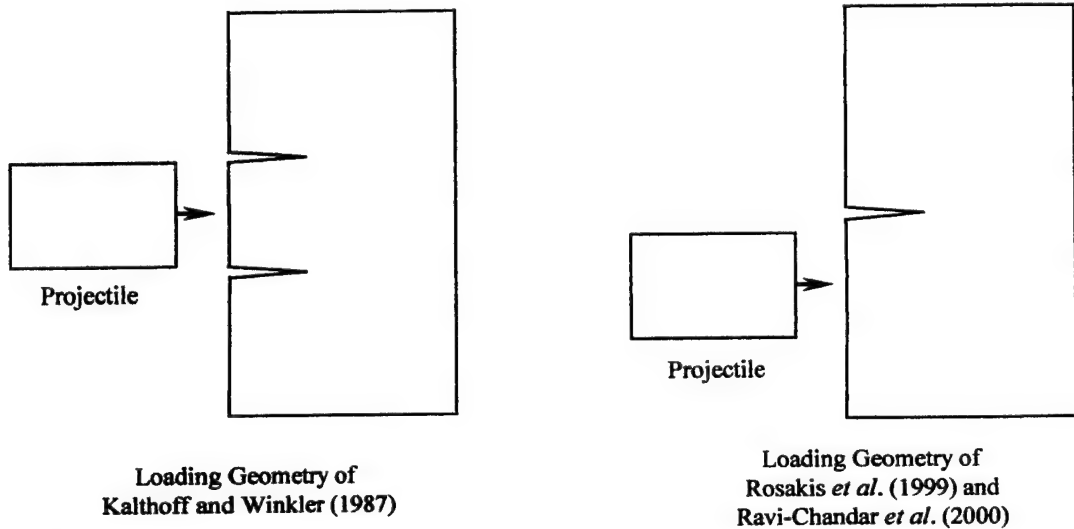


Figure 4. Asymmetric loading geometries used to generate an adiabatic shear band and a shear-dominated crack tip. The left is the method introduced by Kalthoff and Winkler (1987). The right is the configuration used by Rosakis *et al.* (1999) and Ravi-Chandar *et al.* (2000).

The third method for suppressing crack kinking is to introduce a path of weakened material, effectively reducing the mode II fracture toughness. This approach has been used successfully by Rosakis *et al.* (1999) and Ravi-Chandar *et al.* (2000), and is the method used in this study. A geometric weakening was implemented by Ravi-Chandar *et al.* (2000). Grooves were machined along the sides of edge-cracked panels of PMMA, providing a preferred crack propagation path. Rosakis *et al.* (1999) on the other hand were able to generate shear-dominated fracture of weakly bonded Homalite 100 panels. Transient shear-dominated loading was achieved using a slight modification of the Kalthoff and Winkler (1987) asymmetric loading configuration, also shown in Figure 4. High-speed photoelasticity was used by Ravi-Chandar *et al.* (2000) to measure the shear stresses in panels of PMMA. Rosakis *et al.* (1999) used the method of coherent gradient sensing (Rosakis 1993) to record the maximum in-plane principal stresses surrounding the propagating shear crack in the Homalite 100 panels. In both cases, intersonic crack tip speeds, i.e., lying between the shear and dilatational wave speeds, were observed. This aspect of shear crack

propagation will be discussed further in section 4. The fracture surfaces from the PMMA experiments of Ravi-Chandar et al. (2000) showed signs of polymer melting. Thin strands of material were deposited on the fracture surface oriented along the crack propagation direction. The stress field images of Rosakis et al. (1999) showed evidence of crack face contact slightly aft of the crack tip. It was speculated that this was frictional sliding of the crack faces, but it occurred over a small portion of the crack face. As will be seen in section 4, the crack face contact results in significant heating and is likely a result of frictional sliding.

1.2.2 Thermomechanical Coupling

During dynamic fracture, energy flows into the region surrounding the propagating crack tip. This energy originates from the applied external loading and is used for two things, plastic deformation and fracture. Part of the energy that goes into plastic deformation is stored internally and the remainder is dissipated as heat, referred to as thermoplastic heating. The portion that is stored internally remains in the material microstructure and represents a change in internal energy. From a modeling perspective, it will be convenient to consider energy and work rates. The fraction of plastic work rate that goes to dissipative heating is denoted as β . The value of β has been the source of many investigations that are reviewed later in this section. Generally, β is about 0.9 for metals and 0.5 for polymers.

Of the energy that is used for fracture, some is used to create new surfaces. This energy requirement is due to the increased stored energy of a free surface and is a material property, denoted as γ . Because two surfaces are created during fracture, 2γ is needed for fracture. The remaining energy used for fracture manifests itself in the form of internal heating. This quantity, denoted as \dot{q} , is termed the thermofracture heating. If the deformation is sufficiently transient such that thermal convection and radiation to the surrounding environment and thermal conduction within the body does not have time to occur, a local increase in temperature will result. The focus of this study is to examine the thermoplastic and thermofracture events, with a particular emphasis on the thermofracture event.

For a material exhibiting plasticity, the relationship between heat generation and mechanical fields during time-dependent deformation and fracture can be incorporated into the heat energy equation as

$$kT_{,u} - \alpha(3\lambda + 2\mu)T_0\dot{\varepsilon}_{kk}^e + \beta\sigma_{ij}\dot{\varepsilon}_{ij}^p + \dot{q} = \rho c_p \dot{T}, \quad (5)$$

where k is the thermal conductivity, T is the absolute temperature, T_0 is the initial temperature, α is the coefficient of thermal expansion, c_p is the specific heat, λ and μ are the Lamé elastic constants, ρ is the density, σ_{ij} are the stress components, ε_{ij}^e and ε_{ij}^p are the elastic and plastic strain components,

respectively, β is the fraction of plastic work rate that is converted to heat, and \dot{q} is the rate of internal heat generation. The dot denotes differentiation with time. The first term on the left hand side is due to parabolic heat conduction, the second term is the reversible thermoelastic effect, and the third term represents the rate of plastic work converted to heat. The rate of internal heat generation term, \dot{q} , encompasses all dissipative processes present during fracture that generate heat, excluding gross plastic deformation. Sun and Hsu (1996) provide an analytic expression, of the form $(G - 2\gamma)\dot{a}\delta(x - x_0)\delta(y - y_0)$, for \dot{q} , under the conditions of stable crack growth, where G is the Irwin strain energy release rate, and γ is the work to create a single fracture surface, δ is the Dirac-delta function, x and y are coordinates, and the zero subscript denotes the current crack tip coordinates. Physically, the term $(G - 2\gamma)$ represents energy that has flowed through the crack tip region (G) but is in excess of that needed for crack surface formation (2γ). This excess energy would be dissipated as heat. The analytic expression for \dot{q} , given above by Sun and Hsu (1996), conceptually makes sense; however, it is incorrect. The expression has units of J/m s , whereas the governing equation for which it was derived requires it to have the units of $\text{J/m}^3 \text{s}$.

The heat energy equation given by equation (5) was derived using a linear thermoelastic stress-strain relation given as

$$\sigma_{ij} = \lambda\delta_{ij}\varepsilon_{kk} + 2\mu\varepsilon_{ij} - (3\lambda + 2\mu)\delta_{ij}\alpha(T - T_0), \quad (6)$$

where T_0 is the initial temperature. This elastic constitutive relation is fully coupled in the sense that an imposed stress or strain will alter the temperature, and an imposed temperature will produce a stress and/or strain. The heat energy equation given by equation (5) is not fully coupled, however, because the dissipative term associated with plastic deformation is not fully coupled. To make equation (5) fully coupled would require a coupled thermoplastic constitutive relation. Additionally, the material properties would need their temperature dependence, if any, also included.

For a viscoelastic material that does not exhibit plastic deformation, equation (5) can be rewritten as (Boley and Weiner 1997):

$$kT_{,ii} - \alpha(3\lambda + 2\mu)T_0\dot{\varepsilon}_{kk} + s'_{ij}d'_{ij} + \dot{q} = \rho c_p \dot{T}, \quad (7)$$

where s_{ij} is the deviatoric stress tensor, d_{ij} is the viscous strain tensor, and superscript l is a summation index. However, in this study polymers well below the glass transition temperature are investigated at very high load rates. Thus, equation (5) is sufficient for the investigation of thermomechanical effects, because the viscous dissipation strain, d_{ij} , would be small.

If the duration of the fracture event is sufficiently short, the thermal conduction term in equation (5) becomes negligible (i.e., nearly adiabatic conditions prevail).

Furthermore, the thermoelastic term is usually small compared to the thermoplastic term (shown in section 3 for our case) and can also be neglected. This reduces equation (5) to

$$\beta \sigma_{ij} \dot{\epsilon}_{ij}^p + \dot{q} = \rho c_p \dot{T} . \quad (8)$$

Equation (8) provides the coupling between temperature rise in a material and dissipative processes that generate heat during highly transient deformation. The thermal dissipation terms in equation (8) can be quantified by measuring the temperature rise of material in the vicinity of a propagating crack tip. Thus, if a material is known to exhibit negligible plastic deformation at room temperature and quasi-static loading rates ($\sim 10^{-3}$ – 10^{-2} s $^{-1}$), referred to herein as a nominally brittle material, temperature measurements of the propagating crack tip region will lead to quantifying \dot{q} . Conversely, if a material is known to exhibit significant plastic deformation at room temperature (referred to as a nominally ductile material), temperature measurements will lead to the total thermal dissipation, which includes the plastic work rate and the additional dissipation mechanisms. Quantifying and understanding these two terms during dynamic fracture of amorphous polymers is the primary focus of this study.

The question of what fraction of plastic work is converted into heat (i.e., β in equations [8]) has been under investigation for many years. A large volume of research on this topic has concentrated on metals. Most studies conclude that the fraction of plastic work rate converted to heat for metals is about 0.9. The dependence of β on strain rate remains controversial. Farren and Taylor (1925) and Taylor and Quinney (1934) found β to be ~ 0.85 for steel and copper using thermocouples and calorimetry techniques. Mason et al. (1994) and Hodowany et al. (2000) found β to vary from 0.6 to 0.9 for steel, aluminum, and titanium alloys and to be dependent on strain and strain rate. Kapoor and Nemat-Nasser (1998) reported all of the mechanical work to be converted to heat (i.e., $\beta = 1.0$) for steel, aluminum, titanium, and tantalum alloys.

In contrast, limited work has been done on the determination of β for polymers. During the investigation of cold drawing processes of PC, Adams and Farris (1998) performed a series of tests at low strain rates (from 0.18 to 1.8 min $^{-1}$) and studied the energy conversion between mechanical work, heat, and internal energy using deformation calorimetry. They found 50%–80% of the mechanical work was dissipated into the environment as heat while the rest was stored as internal energy in the material. Rittel (1999) conducted a study of heat generation during high-rate deformation of PC. He found β to vary from 0.4 to 1.0, depending on strain rate. More recently, Li and Lambros (2001) found β for PC to range from 0.5 to 0.6 during high-rate compression. For PMMA, β is not defined because it is nominally brittle at room temperature and high loading rates.

1.2.3 Crack Tip Temperature Measurements

Early estimates of opening mode crack tip temperatures in the nominally brittle amorphous polymer PMMA were deduced by Fuller et al. (1975) using a single unfocused infrared detector along with a thermocouple and liquid crystal films. The actual temperature measurements made by Fuller et al. (1975) were peripheral to the crack tip and did not constitute a temperature field measurement. A transient heat conduction analysis was used to deduce the crack tip temperature. This analysis required an estimate of the dissipation region responsible for heat generation, which Fuller et al. (1975) assumed to extend below the fracture surface by no more than 3 μm . With this assumption, Fuller et al. (1975) reported a temperature rise above room temperature of ~ 500 K for cracks propagating within a velocity range of 200–650 m/s. However, as will be seen later, the region responsible for heat generation actually extends ~ 100 μm below the fracture surface for PMMA used in the present study. The larger dissipation region will significantly lower the estimated crack tip temperature using the technique of Fuller et al. (1975). In sharp contrast, Döll (1976) measured a temperature increase of ~ 0.85 K at a single location using an embedded thermocouple a short distance away from the opening mode crack tip path in PMMA. It should be noted that the peak temperature recorded by Döll was 1.7 s after crack initiation, indicating that thermal conduction had occurred. Rittel (1998) also used a single embedded thermocouple in PMMA and recorded a peak temperature increase of ~ 50 K during dynamic opening mode fracture. Thus, the limited thermal data for opening mode fracture of polymers suggests that a temperature increase does occur, but that its magnitude is considerably lower than the temperature increase observed in metals. In addition, it should be pointed out that the studies of Fuller et al. (1975), Döll (1976), and Rittel (1998) provide measurements at only one point on the sample.

To date, there have not been any published results of the temperature fields during either opening or shear-dominated crack growth in polymers. However, studies have been made to measure the temperature of adiabatic shear bands. Using the loading geometry introduced by Kalthoff and Winkler (1987), Zhou et al. (1996a) and Mason et al. (1994) studied the temperature rise surrounding adiabatic shear bands in C-300 maraging steel and 4340 steel. The adiabatic shear band that developed in the metal during their experiments was followed by a dynamically propagating opening crack. A similar experiment was performed by Rittel (2000) to measure the temperature surrounding a dynamically propagating adiabatic shear band in PC. Using a single embedded thermocouple, he reported a temperature increase of 75 K when the adiabatic shear band propagated directly through the thermocouple. However,

this study focused on the shear band and did not examine the fracture process itself. Thus, little is known regarding the dissipative processes present during the shear fracture of ductile and brittle polymers.

1.3 Research Objectives

The present study improves upon the previous temperature measurements by directly measuring the temperature field surrounding the propagating crack tip in amorphous polymers. This has been done for ductile metals using infrared detector arrays (Zehnder and Rosakis 1991; Kallivayalil and Zehnder 1994; Mason and Rosakis 1992; Zehnder et al. 2000). This study will use a one-dimensional (1-D) infrared detector array to measure the temperature field for not only ductile, but also brittle polymeric materials.

The overall goal of this research is to provide a better understanding of the dissipative processes that occur during high-speed opening and shear-dominated fracture of amorphous polymers. The specific objectives of the current study are as follows:

- Quantify in high resolution the temperature field surrounding a dynamically propagating crack tip in a nominally brittle and nominally ductile amorphous polymer.
- Identify the portion of heating due to plastic deformation in the overall crack tip temperature field for the ductile polymer.
- Provide insight into the process zone for shear-dominated fracture of amorphous polymers.
- Develop a dissipative, cohesive-based failure model for predicting heat generation in a brittle polymer.

These objectives will be achieved through comprehensive experimentation, finite-element analysis, fracture surface microscopy, and analytical modeling. Although aspects of materials science and micromechanics are used to provide a deeper understanding of the process zone physics, an attempt is made here to cast the modeling and analyses in a continuum mechanics framework.

This study presents significant contributions to the area of dynamic fracture. Crack tip temperature fields are measured in polymeric materials for the first time. More significantly, the temperature field of a shear crack was obtained for the first time in any material. For mode I cracks, the crack tip speed, temperature field, and fracture energy are measured simultaneously for the very first time, offering the ability to directly correlate the crack tip temperature field with crack tip energy and kinematics. Finally, an appropriate form for a dissipative crack tip cohesive law is obtained and compares well with the thermal measurements made for low-speed opening mode fracture in a brittle polymer.

2. Experimental Techniques

2.1 Material Selection

The polymer materials used for this study were PMMA and extruded PC. PMMA exhibits negligible plastic deformation and is prone to craze formation when loaded beyond its elastic limit at room temperature (Kambour 1964). Polycarbonate is a relatively ductile material that exhibits significant plastic deformation under large loads (Adams and Farris 1998). The PMMA used for most of the study was obtained from the Polycast Technology Corporation under the trade name PolyCast. A second smaller supply of PMMA was obtained from CYRO Industries under the trade name Acrylite FF. The two sources of PMMA provided material with significantly different molecular weights, 1,400,000 and 140,000, respectively. In the subsequent text, the 1,400,000 molecular weight PMMA will be referred to as high molecular weight, and the 140,000 PMMA will be referred to as low molecular weight. The PC material was Hyzod from Sheffield Plastics. All materials were purchased as flat panels with a nominal thickness of 8.5 mm.

Both materials are transparent to radiation in the visible and near infrared spectrum, but are opaque to radiation in the mid- and far-infrared spectrum (Incropera and DeWitt 1980). The transmissivity of each material is about 90% for radiation in the 0.4–3 μm wavelength range and quickly drops to 0% outside this wavelength band. As will be seen later in this section, heating of the material will cause radiation emission in the 6–12 μm range. This is well outside the radiation transmissivity wavelength band for these materials. This means that the radiation that is measured originates from the surface of the specimen and not the interior. An experiment is described in section 2.6.4 that verifies this.

The technique used to make the PolyCast PMMA is a casting technique that renders the molecular chains completely unoriented. Acrylite FF PMMA is made in such a way that a slight amount of chain orientation does occur and the molecular weight is significantly reduced. The extrusion process used in forming PC results in considerable orientation of molecular chains. The fracture experiments were performed such that the crack propagated along the molecular chain orientation direction for Acrylite FF PMMA and perpendicular to the extrusion-oriented molecular chains for PC. The temperature increase above room temperature necessary to reach the glass transition temperature of PC is 125 K (Domininghaus 1988). The corresponding temperature increase for PMMA is 90 K (Domininghaus 1988).

The analyses used throughout this study require known values for the mechanical and thermal properties of PMMA and PC. The needed properties were obtained either from the literature or were determined as part of this study. Young's modulus, E , was directly measured from a series of standard tension tests performed in accordance with the American Society for Testing and Materials (ASTM) D638 standard. Tensile test specimens were prepared from the PC and PolyCast PMMA material. The PC specimen was made such that the molecular chain orientation relative to the tensile traction direction would be the same as for the dynamic fracture experiments, i.e., perpendicular to applied load. Quasi-static and low-rate tests were performed on a conventional load frame instrumented with a load cell to measure force and a clip-on displacement gage to determine specimen strain. The strain rates were either $4.5 \times 10^{-4} \text{ s}^{-1}$ or 0.1 s^{-1} . The resulting stress-strain curves from these tests are shown in Figures 5 and 6 for PMMA and PC, respectively. Young's modulus, determined in the manner specified in ASTM D638, is listed in Table 1. The modulus for PMMA was found to be rate dependent, with the material behaving stiffer at higher loading rates. The PC modulus was independent of loading rate for the rates tested. These results are consistent with those of Theocaris and Andrianopoulos (1982) and Li and Lambros (2001), who examined the elastic constants of PMMA and PC at intermediate and high loading rates. Theocaris and Andrianopoulos (1982) observed the high-rate elastic modulus for PMMA to increase 90% for a strain-rate increase from quasi-static to 60 s^{-1} . The modulus for PC was found to increase 6% for a similar increase in rate. Li and Lambros (2001) reported a similar increase in the modulus for PMMA as the strain rate increased from quasi-static to 5000 s^{-1} . Given that high strain rates accompany dynamic crack growth, the high-rate Young's moduli for PMMA and PC are also included in Table 1 and were the moduli used throughout the study. Additional mechanical and thermal properties obtained from the literature, including the dilatational, shear, and Rayleigh wave speeds (c_d , c_s , and c_R , respectively) are listed in Table 2. It should be noted that Theocaris and Andrianopoulos (1982) found Poisson's ratio, ν , for both materials to be independent of load rate.

2.2 Experimental Configuration and Impact Event

Opening and shear-dominated dynamic fracture experiments were performed at room temperature on PMMA and PC. Single edge notched panels with a nominal height of 292 mm, length of 127 mm, and thickness of 8.5 mm were impacted by a steel projectile having the shape of a right circular cylinder with a length of 75 mm and a diameter of 38 mm. A starter notch (25 mm long and 1-mm wide) was cut into one edge of each panel with a band saw. A razor blade was used to create a sharp end to the otherwise blunt notch. The polymer specimen was placed on two cantilevered glass microscope slides to provide a

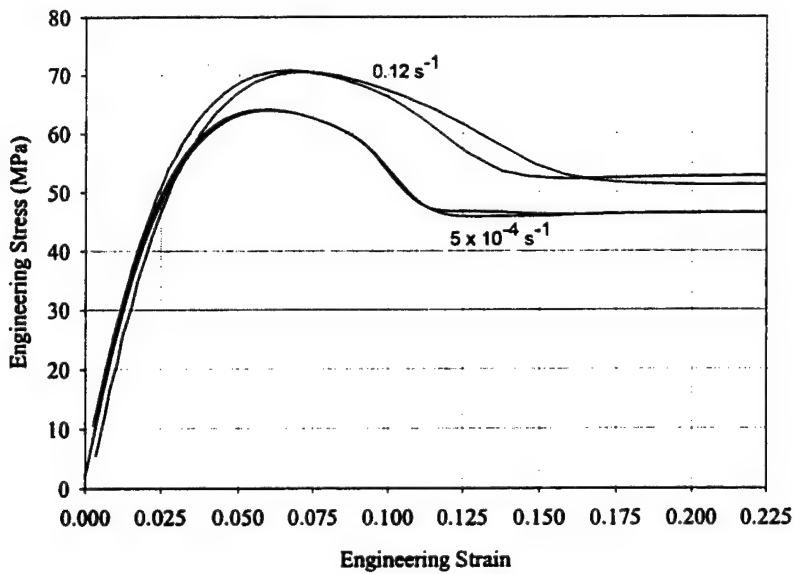


Figure 5. Low-rate tensile stress-strain curves for high molecular weight PMMA showing rate sensitivity of Young's modulus and ultimate strength. Two tests were performed for each strain rate. Brittle failure occurred during each test.

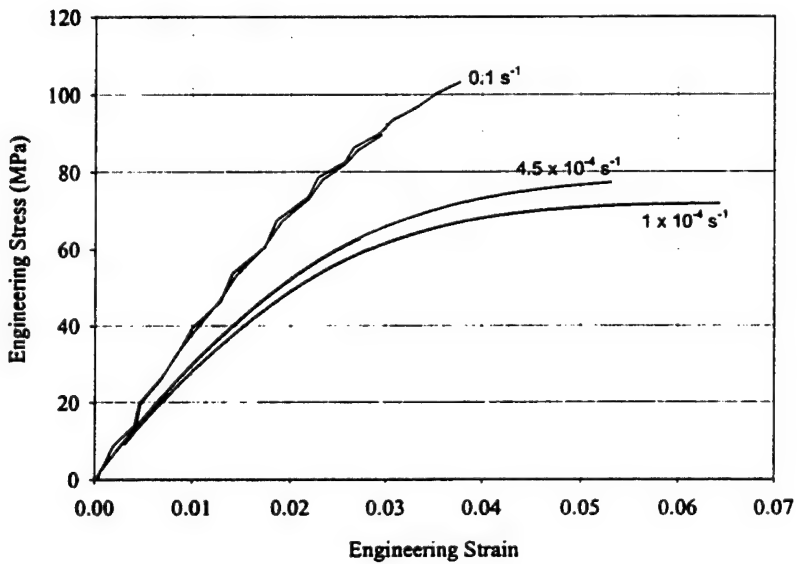


Figure 6. Low-rate tensile stress-strain curves for PC showing strain-rate sensitivity of yield strength. Young's modulus was not rate sensitive. Two tests were performed for each strain rate.

Table 1. Rate effects on elastic moduli of PMMA and PC.

	E (GPa)		
	$\dot{\epsilon} = 4.5 \times 10^{-4} \text{ s}^{-1}$	$\dot{\epsilon} = 0.1 \text{ s}^{-1}$	$\dot{\epsilon} = 60 \text{ s}^{-1}$
PMMA	2.9	4.0	5.5
PC	2.3	2.3	2.5

Table 2. Polymer properties.

	ρ (kg/m ³)	ν	k (W/m·K)	c_p (J/kg·K)	c_d^a (m/s)	c_s^a (m/s)	c_R^a (m/s)
PMMA	1190 ^b	0.36 ^b	0.19 ^b	1470 ^b	2330 ^c	1330 ^c	1243 ^c
PC	1200 ^b	0.31 ^b	0.21 ^b	1170 ^b	1750 ^d	1075 ^d	1000 ^d

^a Dynamic plane stress values.

^b Domininghaus (1988).

^c Singh et al. (1997).

^d Ravi-Chandar et al. (2000).

break-away support that approximates traction-free boundary conditions. This was done for two important reasons: First, it greatly simplifies the boundary conditions for finite-element modeling performed later. Second, it was found that placing the specimen directly on a steel stand provided a path for energy to flow out of the specimen, reducing the energy available to the propagating crack tip. High crack speeds and crack branching, discussed in section 3, occurred only when the specimen was isolated from the steel stand with the break-away supports. The impact event occurred inside an impact chamber to contain debris. Opening mode dynamic fracture was achieved by impacting the panel in a symmetric manner as shown in Figure 7. The edge opposite the starter notch was impacted.

Shear-dominated fracture was achieved by asymmetric impact with the panel edge containing the starter notch, as shown in Figure 8. The experimental configuration was adopted from Ravi-Chandar et al. (2000). Grooves were milled along each side of the specimen to provide a preferential crack propagation path and to suppress crack kinking and branching. The grooves each had a width of 3.2 mm, a depth of 2.5 mm, and the bottom surface of each groove was polished smooth with 2000 grit sand paper. Approximately 60% of the specimen thickness was removed along the grooves, consistent with the amount Ravi-Chandar et al. (2000) found necessary to ensure that a shear-dominated crack would propagate. It is worth noting that Ravi-Chandar et al. also observed that an opening crack at an angle to the initial starter notch propagated simultaneously into the upper half of the specimen. Details of the Ravi-Chandar et al. (2000) experiments are provided in section 4.

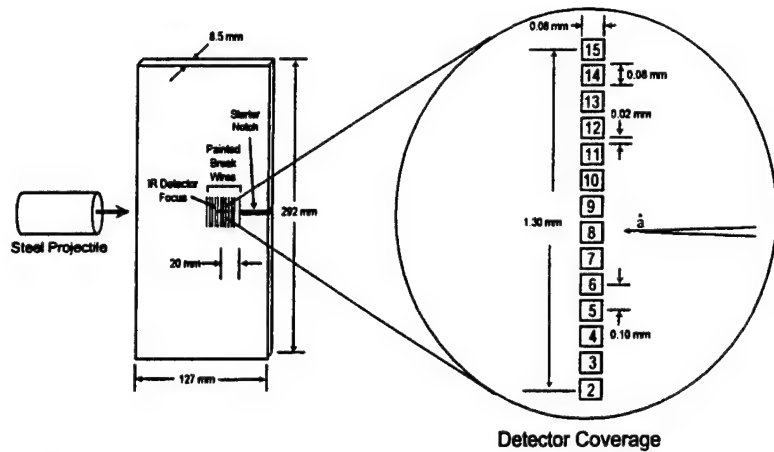


Figure 7. Opening mode dynamic fracture experiment configuration also showing infrared detector coverage and crack propagation gage. Crack propagates from right to left.

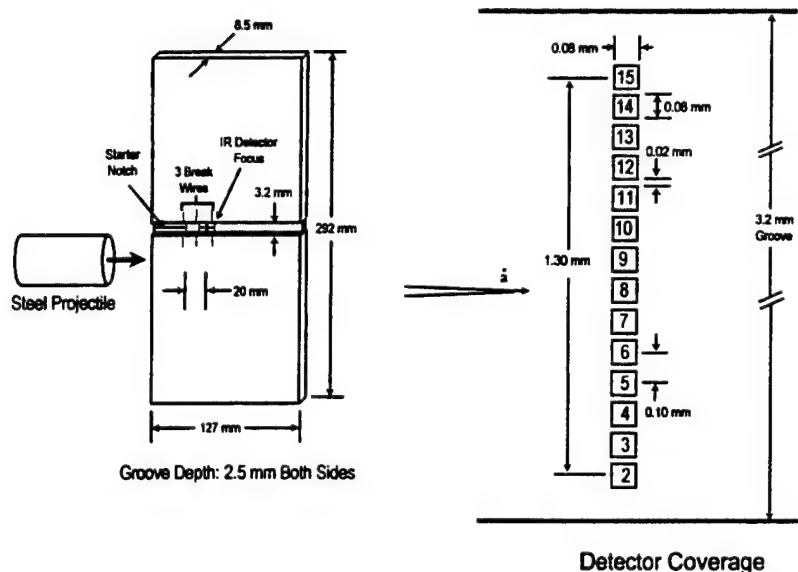


Figure 8. Shear-dominated dynamic fracture experiment configuration also showing infrared detector coverage and painted wires for coarse crack speed measurement. Crack propagates from left to right.

The projectile speed was low enough to prevent deformation of the projectile during impact (i.e., it served as a rigid body to generate a stress pulse at the projectile-panel interface). An alignment procedure was followed prior to each experiment to ensure that a planar impact occurred between the flat front face of the projectile and the edge of the polymer panel. The asymmetric impact that occurs during the shear-dominated experiments causes a compressive stress pulse to propagate from the projectile-panel contact region. Because the loading is asymmetric relative to the starter notch, a shear-dominated stress field develops at the notch tip after the passage of the stress wave that leads to crack initiation and propagation. During the opening mode experiments, the stress pulse resulting from symmetric impact travels to the opposite end of the panel and reflects as a tensile pulse. As the reflected wave passes the starter notch, the presence of traction free surfaces belonging to the notch induce an opening mode (mode I) stress field at the notch tip, where eventually an opening, or mode I, dynamic fracture event commences. Explicit finite-element simulations of the initial impact and subsequent propagation of waves into a notched panel of PMMA to confirm the explanation of events leading to crack initiation were performed using the ABAQUS finite-element code (Hibbit et al. 1998). Details of the finite-element simulations are provided in section 2.6.2. These calculations, combined with crack initiation times obtained from initial experiments, indicated that significant material motion in the horizontal direction would occur prior to the crack tip reaching the desired region of interest. This issue is of considerable consequence for infrared detector alignment and is discussed further in section 2.6.2.

2.3 Gas Gun

The projectile was accelerated with a compressed gas gun to a speed ranging between 8 and 40 m/s. The gun, shown in Figure 9, has a 50-mm inside diameter and a 2.1-m-long launch tube. The breech of the gun is a high-pressure reservoir with a piston assembly inside. The interior diameter of the breech is 180 mm. The piston consists of two disks connected with a threaded rod. The rear disk has a diameter of 178 mm, which allows it to freely move and air to pass by. The front disk has a diameter of 60 mm. Prior to each experiment, the piston was moved to the forward position to seal the breech from the launch tube. High-pressure air was then pumped into the breech chamber. A valve on the rear of the breech was opened, allowing the high-pressure air to vent to ambient. The resulting pressure differential inside the breech caused the piston assembly to move towards the rear of the breech, breaking the seal to the launch tube. The remaining high-pressure air then moved into the launch tube, accelerating the projectile to the desired speed. A typical breech pressure needed to obtain a projectile speed of 40 m/s was 350 MPa. The 75-mm-long, 38-mm-diameter projectile was made from maraging C350 steel. A PC jacket was

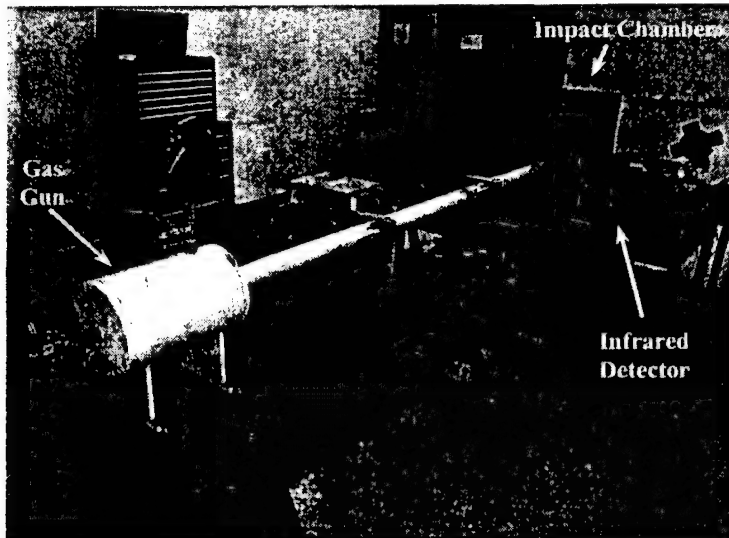


Figure 9. Photograph of gas gun, impact chamber, and infrared detector system.

placed around the steel projectile to match the bullet diameter with the launch tube diameter. The jacket had a length of 50 mm and was placed such that the rear of the jacket was flush with the rear of the steel projectile. This ensured the jacket did not come in contact with the PMMA or PC test specimen.

The energy available for high-speed crack growth comes from the kinetic energy of the impacting steel projectile. In order to quantify the conditions that led to crack growth and to model the impact and crack growth event numerically, projectile speed must be measured. Projectile speed at the gun muzzle was measured with the interruption of two infrared beams in the travel path of the projectile, illustrated in Figure 10. Two sets of holes were drilled through the launch tube wall at the muzzle end to accept two commercially available IR emitter and detector pairs. The two infrared emitters, separated 50 mm along the projectile travel direction, were constantly emitting infrared energy with a wavelength of 940 nm. The detectors were located on the opposite side of the launch tube wall and registered the infrared energy. As the projectile traveled past this region of the gun tube, it interrupted the first infrared beam, which began an external time interval counter. Interruption of the second beam stopped the counter. The projectile speed was determined by dividing the distance between break beams by the time required for the projectile to traverse this distance.

2.4 Projectile Contact, Crack Initiation, and Crack-Speed Measurements

Projectile contact with the test specimen was determined with a voltage completion circuit. Two bare-ended wires were attached to the test specimen at

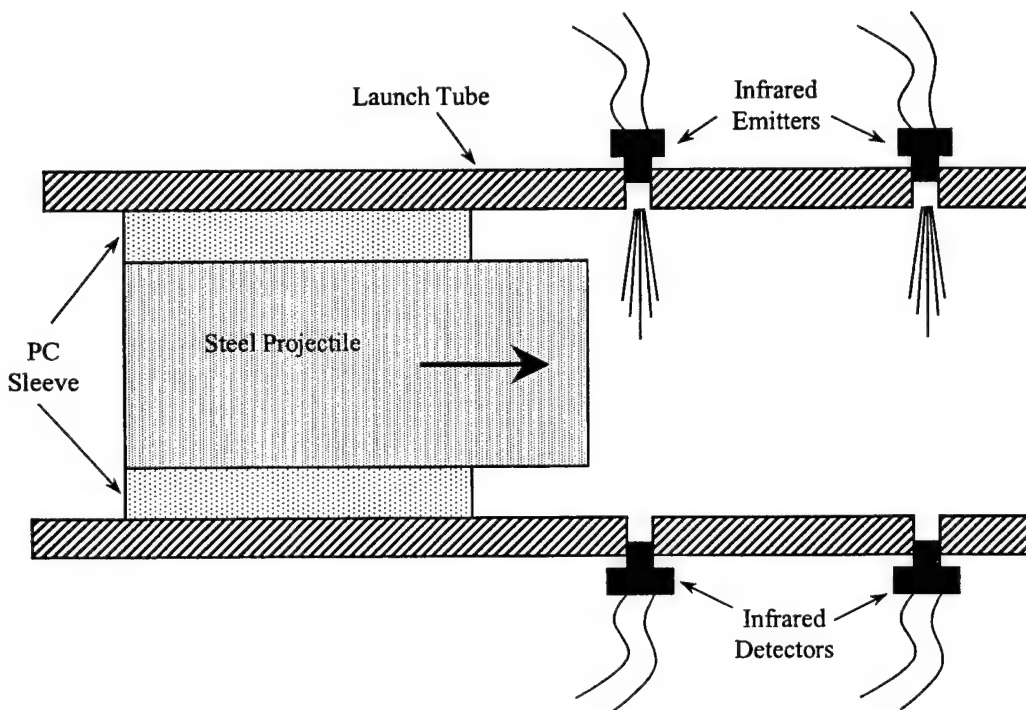


Figure 10. Projectile velocity measurement system using two infrared break-beams at the muzzle of the launch tube. Projectile interrupts infrared beam, causing infrared detectors to change response.

the location of projectile contact. The bare ends were separated by several millimeters, preventing electrical continuity. The opposite ends of the wires were connected to a $10\text{ k}\Omega$ resistor in series with a 9 V battery. Upon impacting the test specimen, the steel face of the projectile made contact with the two bare wire ends and completed the electrical circuit. A 500 MHz digital storage oscilloscope (Tektronix TDS 540B) recorded the time of circuit completion by monitoring the voltage across the resistor. This technique served as a very reliable method for determining the time of initial projectile contact with the test specimen and served as the trigger source for all of the transient recorders used for each experiment.

Crack initiation time was measured with a break wire painted on the specimen to complete a voltage interruption circuit. A fine line of conducting silver paint (SPI Corp. product no. 5001) was hand painted on the test specimen at the initial crack tip location such that it would be severed when the crack initiated (i.e., the paint line was perpendicular to the crack propagation direction). Wires were attached to the paint line and connected to a $10\text{ k}\Omega$ resistor in series with a 9 V battery. Initiation of crack propagation severed the painted line, opening the electrical circuit. The time of crack initiation was determined by monitoring the voltage across the resistor with a digital storage oscilloscope.

There are two techniques that can be used to directly measure the speed of a propagating crack tip, high-speed photography, and electrical resistance grids. High-speed photographic techniques require an intense light source to illuminate the crack tip region in either a front-lit or back-lit configuration, and a multi-frame camera with an extremely fast shutter and framing times. Because crack tip speeds can be on the order of 10^3 m/s, framing times of less than one microsecond and shutter speeds a fraction of this are necessary to obtain precise crack-speed measurements. A variation of this technique is to use an open shutter camera with a pulsing light source (usually a laser) that serves as the shutter. Crack-speed measurements can be made simultaneously with photoelasticity or other full-field imaging techniques provided the crack tip is clearly discernable on the sequence of full-field images. The experiments of Ravi-Chandar et al. (2000) used high-speed photoelasticity to measure crack tip speed during shear-dominated dynamic crack growth. Rosakis (1993) and Rosakis et al. (1999) used the high-speed photographic technique of coherent gradient sensing to simultaneously measure crack tip speed and full-field in-plane principal stresses.

The electrical resistance grid technique uses a number of electrical wires laid across the path of the crack. As the crack propagates, it severs the wires sequentially and provides an electrical signal which can then be used to determine the crack position and speed with time. This technique was used by Dulaney and Brace (1960), Cotterell (1965), Anthony et al. (1970), and Paxson and Lucas (1973) with great success. A drawback to this technique is that the resolution of the grid dictates the resolution of the speed measurement, and it is difficult to create very fine grids. This can be improved by using an electrically conductive film instead of discrete wires (Stalder et al. 1983; Fineberg et al. 1991). This approach offers the continuous measurement of crack tip position. However, it does require depositing a conductive film over a portion of the test specimen, which can be quite challenging.

Crack propagation speed was measured in this study with the electrical resistance grid technique. The crack propagation speed measurements made by Ravi-Chandar et al. (2000) in PMMA and PC using high-speed photography were used to design a conductive grid of suitable spatial coverage and resolution. Details of this gage, including the circuitry, gage size, and fabrication, are provided below.

A series of break wires painted on the side of the test specimen, as shown in Figure 11, was used to complete a voltage interruption circuit. Two designs were used, one having 11 painted lines, and the other having 21 lines. Each line, or wire, was 0.3 mm thick, and the spacing between the middle of adjacent lines was either 1.5 or 3 mm. The 21-line gage is shown in Figure 11. The painted

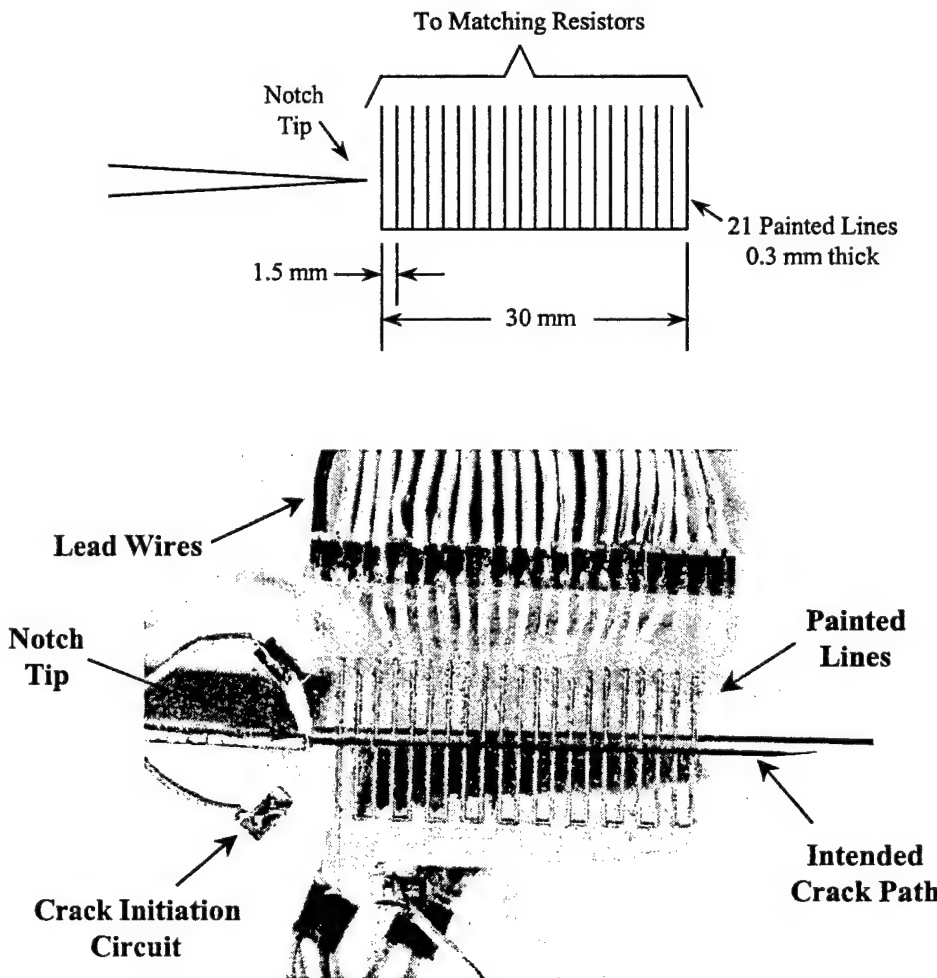


Figure 11. Crack propagation gage constructed from thin lines of conducting silver paint. Top illustration shows gage configuration with the crack propagating from left to right, severing the painted lines sequentially. Bottom photograph is of a completed gage on a PC fracture specimen. Crack initiation gage is also shown.

lines were connected as a single parallel resistor circuit and then included in the circuit shown in Figure 12. The measured voltage output, E_0 , for this circuit is given by the following relation:

$$E_0 = \left[\frac{\frac{1}{\sum_{l=1}^p \frac{1}{R_l}}}{\left(\sum_{l=1}^p \frac{1}{R_l} \right) + R_s} \right] E_i, \quad (9)$$

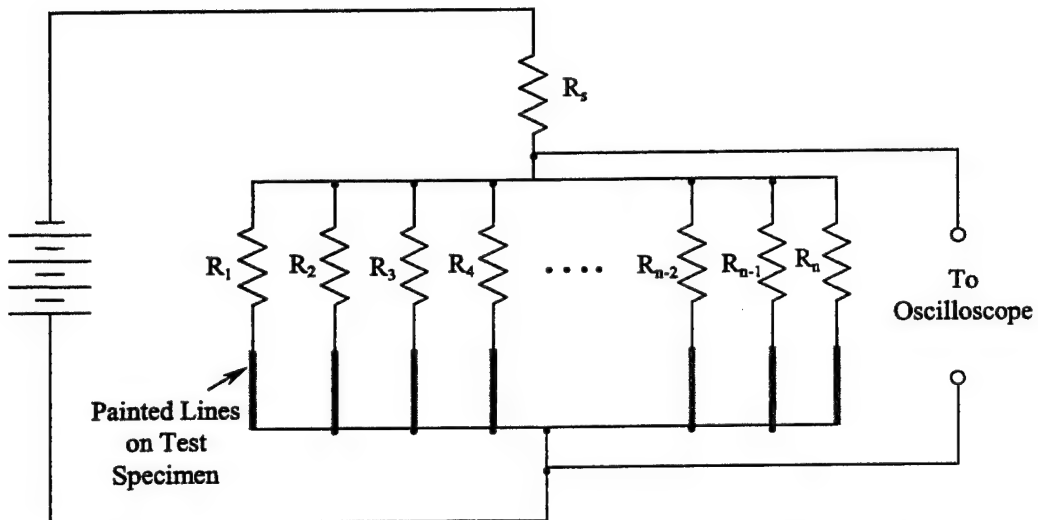


Figure 12. Schematic of the crack propagation speed measurement circuit using painted silver lines on the polymer test specimen. The propagating crack sequentially severs the painted lines, changing the overall resistance of the circuit.

where E_0 is the voltage of the power supply (9 V), R_i are the resistances of the painted line paths remaining intact, p is the number of intact lines, and R_s is a series resistor. As the crack propagates, it severs each of the painted lines one at a time, changing the overall resistance of the parallel resistor portion of the circuit. This, in turn, causes an abrupt change in the monitored voltage, E_0 . The time between abrupt changes in E_0 , along with the known spacing between painted lines, enables the crack propagation speed to be determined.

An accurate crack speed requires the lines to be placed on the test specimen with precision. This was accomplished with a custom made template. A 0.2-mm-thick piece of spring steel was made into a template for painting the silver lines by cutting the desired line pattern in the steel with a numerically controlled electro-discharge machining technique. Eleven lines were cut, each line having a width of 0.3 mm and a centerline-to-centerline spacing between lines of 3.0 mm. A second template with 21 lines having a line-to-line spacing of 1.5 mm was used to double the resolution of the crack-speed measurements. The first line was placed 3 mm from the initial notch tip for both templates. To keep the template from shifting and the paint from wicking between the template and test specimen during paint application, a spray adhesive was applied to the template prior to placing it on the specimen. Ends of the painted lines were either grouped together to form a single conductor or connected to a resistor, as shown in Figure 12. The resistance for each line was selected such that the same abrupt change in E_0 occurred as each painted line was sequentially severed. A photograph of a completed 21-line gage on a PC test specimen is shown in Figure 11.

The groove that was present on the test specimen used for the shear-dominated fracture experiments prevented a template from being used to paint the conductive lines. For these experiments, only three wires were hand painted and used in circuits identical to the one used for determining crack initiation time (see Figure 8). This enabled a coarse estimate of the crack tip speed to be made. The Ravi-Chandar et al. (2000) data, obtained under crack growth conditions similar to this study, were used to verify the coarse speed measurements for the shear crack.

2.5 Dynamic Energy Release Rate Measurements

The total energy that flows into the crack tip region during dynamic fracture is the dynamic energy release rate, G , discussed in section 1. This energy represents to total energy available for fracture and is partitioned between plastic work and fracture energy. An accurate determination of G is critical for the cohesive zone modeling that is performed in section 6. The dynamic energy release rate has been measured for various crack tip speeds in PMMA by Döll (1976) and Sharon et al. (1996). These studies used a single-edge-notched plate specimen under quasi-static loading. If the initial notch tip is blunt, significant energy is stored in the material prior to crack initiation. This stored energy then flows into the crack tip region, driving it to high-speed. Analytic expressions for G are available for the configuration used by Döll (1976) and Sharon et al. (1996), and require accurate measurement of the crack tip speed. Unfortunately, the results reported by Döll (1976) and Sharon et al. (1996) are not consistent. The energy values reported by Sharon et al. (1996) are higher than those of Döll (1976) for the same crack tip speed, often by a factor of 2 or more. For this reason, independent measurements of G were made during this study. Furthermore, these measurements were made simultaneously with the temperature field measurements, something that had never been done before. The simultaneous measurement left no doubt of the energy responsible for a given temperature field.

The dynamic energy release rate, G , was determined for a selected number of mode I experiments using a strain gage technique. The approach used in this study is identical to that published by Khanna and Shukla (1995), which was built upon the pioneering work of Sanford and Dally (1987) and Sanford et al. (1990) and is summarized next for completeness.

A series solution for the stresses near the tip of a crack propagating at constant speed was derived by Irwin (1980). Chona (1987) added to this expression the higher order terms needed to account for the influence of finite boundaries. For a linear elastic, isotropic material, the strain, $\varepsilon_{xx'}$, sensed by a strain gage oriented at an angle α as shown in Figure 13 is (using the notation of Khanna and Shukla [1995]),

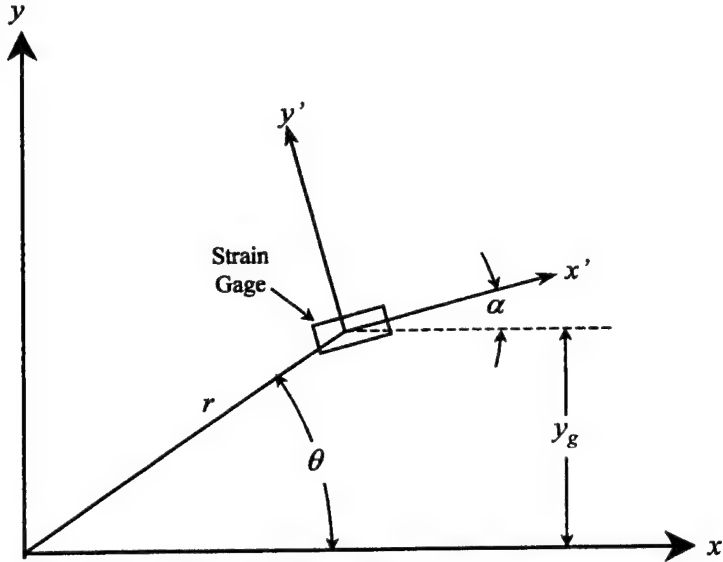


Figure 13. Strain gage coordinate system showing the gage orientation angle, α . Strain gage is fixed in space and the coordinate system origin is attached to the propagating crack tip that moves from left to right.

$$\begin{aligned}
 2\mu\varepsilon_{x'x'} = & \left[\kappa(\lambda_1^2 - \lambda_2^2)\{\operatorname{Re}\Gamma_1(z_1) + \operatorname{Re}\Psi_1(z_1)\} + (1 + \lambda_1^2)\{\operatorname{Re}\Gamma_1(z_1) + \operatorname{Re}\Psi_1(z_1)\}\cos 2\alpha \right. \\
 & - \frac{4\lambda_1\lambda_2}{(1 + \lambda_2^2)}\operatorname{Re}\Gamma_2(z_2)\cos 2\alpha - (1 + \lambda_2^2)\operatorname{Re}\Psi_2(z_2)\cos 2\alpha \\
 & + 2\lambda_1\{-\operatorname{Im}\Gamma_1(z_1) + \operatorname{Im}\Gamma_2(z_2) - \operatorname{Im}\Psi_1(z_1)\}\sin 2\alpha \\
 & \left. + \frac{(1 + \lambda_2^2)^2}{4\lambda_1\lambda_2}\operatorname{Im}\Psi_2(z_2)\sin 2\alpha \right], \tag{10}
 \end{aligned}$$

where

$$\beta_1 = \frac{1 + \lambda_2^2}{4\lambda_1\lambda_2 - (1 + \lambda_2^2)^2}, \quad \kappa = \frac{1 - \nu}{1 + \nu},$$

and μ and ν are the shear modulus and Poisson's ratio, respectively. The velocity-dependent functions, λ_1 and λ_2 , are defined as

$$\lambda_1^2 = 1 - \left(\frac{\dot{a}}{c_d} \right)^2, \tag{11a}$$

$$\lambda_2^2 = 1 - \left(\frac{\dot{a}}{c_s} \right)^2, \tag{11b}$$

where \dot{a} is the crack propagation speed and c_d and c_s are the longitudinal and shear wave speeds respectively. The complex valued functions Γ_1 , Γ_2 , Ψ_1 , and Ψ_2 , are defined in a series form as

$$\Gamma_k(z_k) = \sum_{n=0}^{\infty} C_n z_k^{n-1/2}; \quad k = 1, 2 \text{ (no sum)}, \quad (12a)$$

$$\Psi_k(z_k) = \sum_{m=0}^{\infty} D_m z_k^m; \quad k = 1, 2 \text{ (no sum)}, \quad (12b)$$

where the velocity transformed variables z_k are defined in Figure 14 as

$$z_k = x + i\lambda_k y = r_k e^{i\theta}; \quad k = 1, 2, \quad (13)$$

and C_n and D_m are constant coefficients depending on applied loading and geometry. The stress intensity factor is given in terms of the first coefficient of the Γ_k series (equation 12a) by

$$K_I^d = C_0 \sqrt{2\pi}. \quad (14)$$

A three-parameter representation of the strain field is obtained by setting $n = 1$ and $m = 0$ in equation (12a) and (12b), yielding

$$\begin{aligned} 2\mu\varepsilon_{xx} &= C_0 \beta_1 \left[\frac{1}{\sqrt{\rho_1}} \left\{ \kappa(\lambda_1^2 - \lambda_2^2) \cos \frac{\phi_1}{2} + (1 + \lambda_1^2) \cos 2\alpha \cos \frac{\phi_1}{2} + 2\lambda_1 \sin 2\alpha \sin \frac{\phi_1}{2} \right\} \right. \\ &\quad \left. - \frac{1}{\sqrt{\rho_2}} \left\{ \frac{4\lambda_1\lambda_2}{(1 + \lambda_2^2)} \cos 2\alpha \cos \frac{\phi_2}{2} + 2\lambda_1 \sin 2\alpha \sin \frac{\phi_2}{2} \right\} \right] \\ &\quad - C_1 \beta_1 \left[\frac{1}{\sqrt{\rho_1}} \left\{ \kappa(\lambda_1^2 - \lambda_2^2) \cos \frac{\phi_1}{2} + (1 + \lambda_1^2) \cos 2\alpha \cos \frac{\phi_1}{2} - 2\lambda_1 \sin 2\alpha \sin \frac{\phi_1}{2} \right\} \right. \\ &\quad \left. - \frac{1}{\sqrt{\rho_2}} \left\{ \frac{4\lambda_1\lambda_2}{(1 + \lambda_2^2)} \cos 2\alpha \cos \frac{\phi_2}{2} - 2\lambda_1 \sin 2\alpha \sin \frac{\phi_2}{2} \right\} \right] \\ &\quad + D_0 \beta_1 [(\lambda_1^2 - \lambda_2^2)(\kappa + \cos 2\alpha)]. \end{aligned} \quad (15)$$

The coefficient of the D_0 term in equation (15) can be set to zero if

$$\cos 2\alpha = -\kappa. \quad (16)$$

Note that the solution of equation (16) for the gage orientation angle α yields two values, an acute and an obtuse angle. When the obtuse angle is used, the peak in the strain profile occurs when the crack is directly below the strain gage. At this instant, $\theta = \phi_1 = \phi_2 = \pi/2$ (see Figure 14).

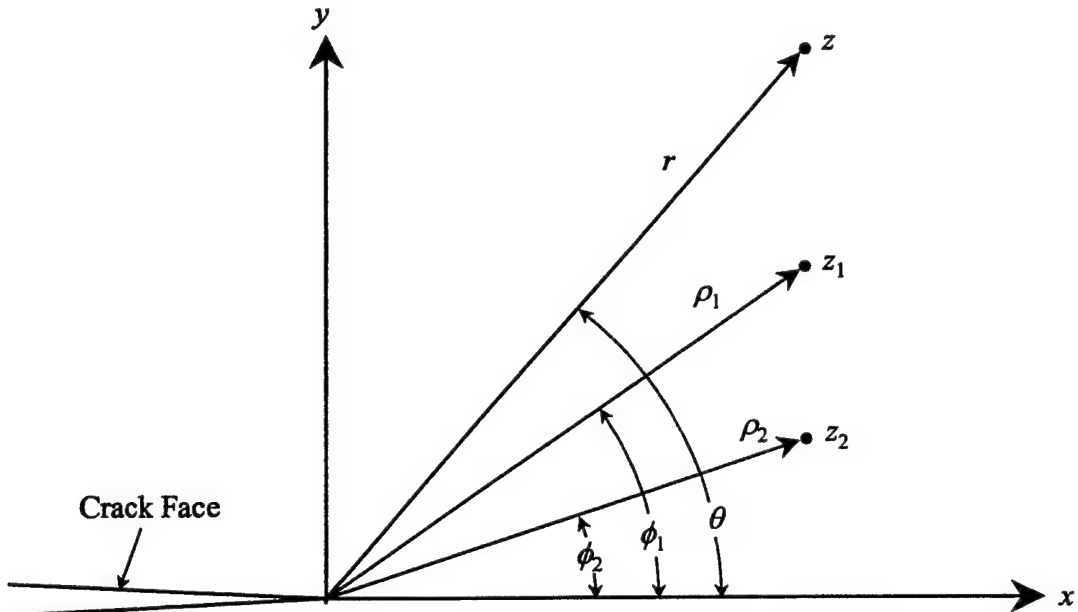


Figure 14. Coordinate system used in the constant crack tip speed analysis for determining the dynamic energy release rate from a strain gage. Coordinate system origin is at the crack tip and propagates with the crack.

The first term of equation (15) gives an accurate representation of the strain field around the crack tip provided the strain gage is located within the singularity-dominated region. This eliminates the influence of the second term. By placing the strain gage sufficiently close to the crack tip at an obtuse angle α and using equation (14), equation (15) gives an expression for the dynamic stress intensity factor, K_I^d :

$$K_I^d = \frac{1}{\beta_1} 4\mu(\varepsilon_{xx'})_p \sqrt{\pi y_g} \left[\frac{1}{\lambda_1} \left\{ \kappa(\lambda_1^2 - \lambda_2^2) + (1 + \lambda_1^2) \cos 2\alpha + 2\lambda_1 \sin 2\alpha \right\} - \frac{1}{\sqrt{\lambda_2}} \left\{ \frac{4\lambda_1\lambda_2}{1 + \lambda_2^2} \cos 2\alpha + 2\lambda_1 \sin 2\alpha \right\} \right]^{-1}, \quad (17)$$

where $(\varepsilon_{xx'})_p$ is the peak strain obtained during the experiment and y_g is the perpendicular distance from the crack path to the strain gage centroid.

As mentioned earlier, there are two angles that satisfy equation (16), an acute and an obtuse angle. The advantage of using the obtuse angle is that the crack is directly under the strain gage at peak strain, which aids in coordinating the crack tip position with the crack propagation gage and the thermal

measurements. The location of the peak strain for the two angles is shown in Figure 15, where the first term of equation (15) is plotted as a function of distance along the crack plane ($x = 0$ corresponds to the crack tip position). For illustrative purposes, a crack propagating at 400 m/s in PMMA was used, along with an assumed K_I^d value of 2.2 MPa·m^{1/2}. The corresponding obtuse and acute angles are 121° and 59°, respectively. The peak strain for the acute angle occurs about 5 mm ahead of the crack tip and is 30% lower in magnitude. The sensitivity of the obtuse angle solution of equation (15) to the crack tip speed is shown in Figure 16. The strain variation with position is shown for crack tip speeds ranging from 200 to 800 m/s. PMMA material properties were used. Sensitivity is seen to improve for the higher crack speeds, although there is some difference in peak strains for lower crack speeds. Figure 16 indicates that the strain gage technique does provide sufficient sensitivity to crack tip speed.

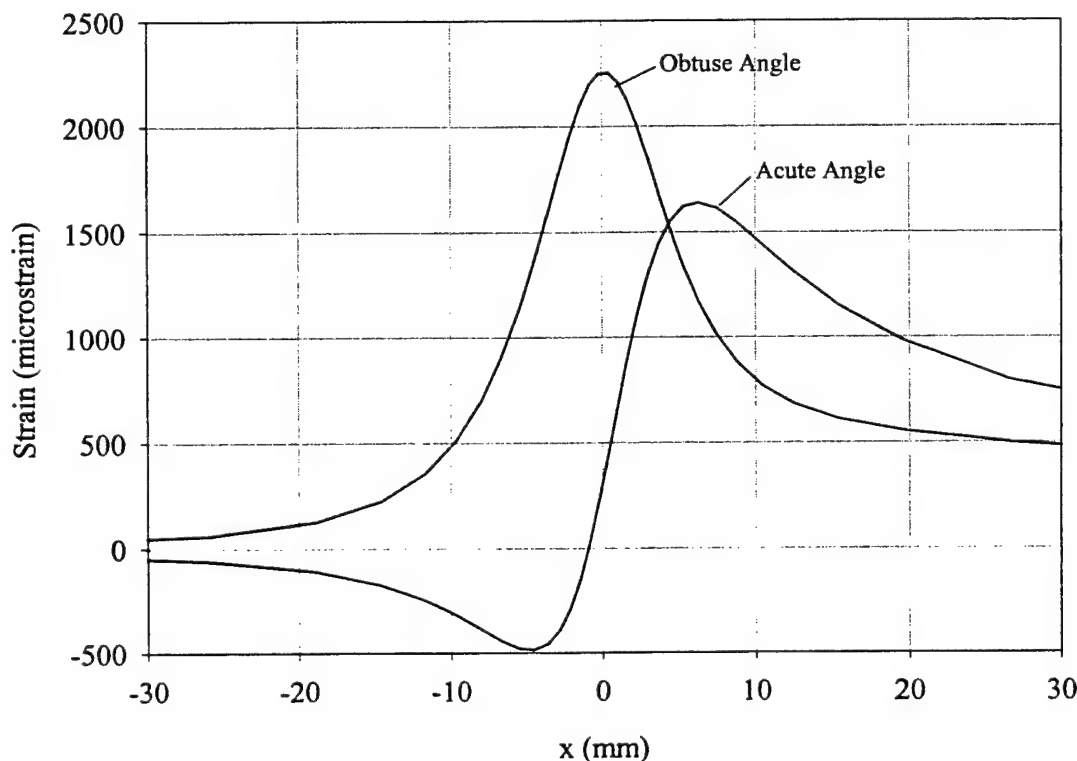


Figure 15. Effect of the strain gage orientation on the location of peak strain as the crack propagates past the gage at 400 m/s in PMMA. Crack tip is located at $x = 0$. Acute angle results in the peak strain occurring 5 mm prior to crack passage, whereas the obtuse angle gives a peak strain when the crack is directly beneath the gage.

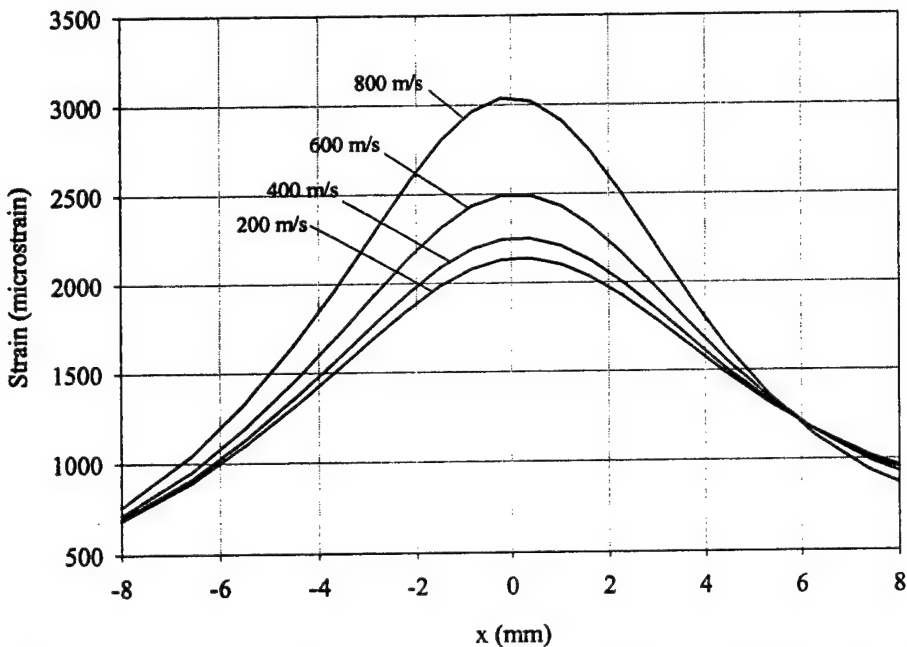


Figure 16. Sensitivity of strain gage response to crack tip speed for PMMA. Obtuse angle orientation is used.

The conversion of K_I^d to the dynamic energy release rate G for plane stress is given by Freund (1990) as

$$G = \frac{A_I(\dot{a})}{E} (K_I^d)^2, \quad (18)$$

where E is Young's modulus (dynamic value for polymers) and A_I is the mode I universal function

$$A_I = \frac{\dot{a}^2 \lambda_1}{(1-\nu)c_s^2 D}, \quad (19)$$

where $D = 4\lambda_1\lambda_2 - (1 + \lambda_2^2)^2$ and λ_1 and λ_2 are defined by equations (11a) and (11b), and c_s is the material shear wave speed. Implicit in the above derivation is that the material is isotropic and linear elastic, that the strain gage is located within the singularity-dominated zone, and that steady-state plane stress conditions exist.

Strain measurements were made with a conventional foil grid strain gage (Measurements Group Inc. No. CEA-13-125UN-350) configured as a quarter-Wheatstone bridge. The strain gage had an active grid length and width of 3.18 mm and 2.54 mm, respectively, and a gage factor, F , of 2.11. The bridge completion circuit and associated signal conditioning amplifiers were Pacific Instruments Model 3210 and had a bandwidth of 150 kHz. The signal from the

amplifier was recorded with a Tektronix TDS 540B 500 MHz digital storage oscilloscope. The bridge excitation voltage was 4 V. The voltage signal from the signal conditioning amplifier was converted to strain using the standard quarter-bridge equation (Measurements Group Inc. 1982)

$$\hat{\varepsilon} = \frac{4 \frac{E_0}{E}}{F(1000 - 2 \frac{E_0}{E})} \times 10^6, \quad (20)$$

where E_0 is the output voltage in mV *after* compensating for the amplifier gain, E is the bridge excitation voltage in mV, F is the gage factor, and $\hat{\varepsilon}$ is the indicated strain, given in microstrain. The output from a quarter Wheatstone bridge circuit becomes nonlinear for large changes in the strain gage resistance, i.e., large strains. The indicated strain given by equation (20) can be corrected for this nonlinearity by the following relation (Measurements Group Inc. 1982) to give true strain, ε .

$$\varepsilon = \frac{2\hat{\varepsilon} \times 10^{-6}}{2 - F\hat{\varepsilon} \times 10^{-6}} \times 10^6. \quad (21)$$

Two strain gages were attached to the polymer test specimens as shown in Figure 17. The obtuse angle α used for PMMA and PC was 121° and 119° , respectively. The gages were placed with their centroid at 7 mm above the crack propagation path. Because the actual crack path varied somewhat, this distance was measured for each gage after the test, and this measured distance is what was used for y_g in equation (17). The gages were located 7 mm and 15 mm aft of the initial notch tip, as shown in Figure 17. The adhesive used to bond the strain gages to the polymer test specimen was Measurements Group Inc. M-Bond 200. The gages were placed on the side opposite the crack propagation gage.

After each test, the recorded voltage signal was converted to strain using equations (20) and (21). The maximum value for each gage was then used in equations (17) and (18) to give the dynamic energy release rate, G . Typical measurements for G and corresponding crack tip speed are presented in section 3.

2.6 Thermal Measurements

In addition to the measurements of crack tip speed and dynamic energy release rate, simultaneous temperature field measurements were also made. There are numerous experimental techniques, and transducers are available for measuring the temperature of a body. These techniques fall into four general categories: (1) thermistors, or technology based on materials whose electrical impedance changes with temperature, (2) thermocouples, (3) methods that rely on direct

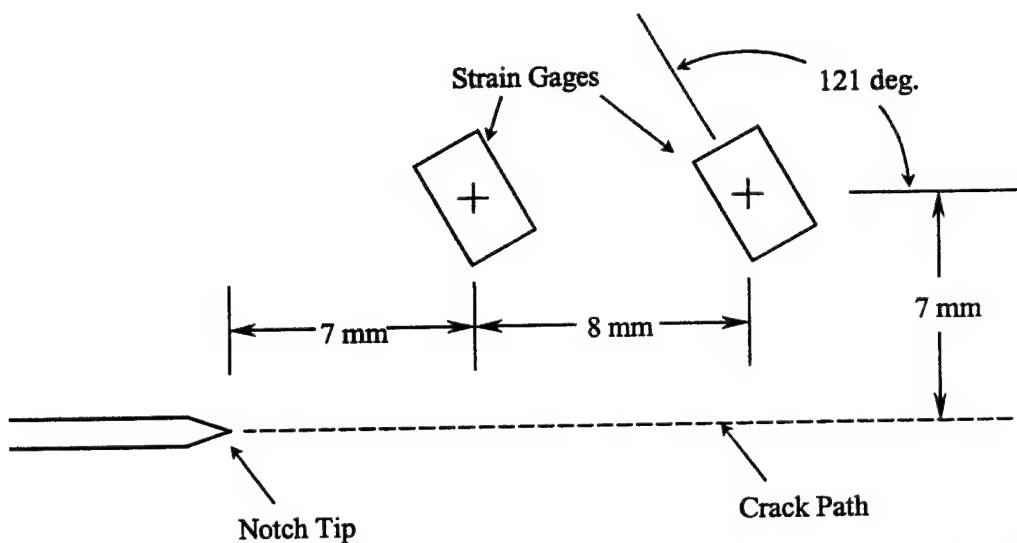


Figure 17. Position and orientation of strain gages used to measure the dynamic energy release rate during opening mode dynamic fracture. Angle shown is for PMMA (119° was used for PC). Crack propagates from left to right.

heat transfer, such as thermally sensitive films, and (4) photon detectors, which are semi-conductor devices that produce voltage or current flow when excited by photons having energy at particular wavelength bands. Each method has a characteristic response time and spatial resolution. Thermistors are relatively slow devices, relying on thermal conduction to heat a resistor. They are useful for discrete point measurements of temperature within an existing temperature field and must be affixed to the material of interest. Thermocouples are devices that consist of two dissimilar metallic conductors joined at their ends. When the metal conductors are exposed to a heat flux, they heat to different temperatures (because of differing thermal properties) and an electromotive force proportional to the temperature difference is induced. If the junction of the two conductors is very small, response times on the order of microseconds can be achieved. Like thermistors, they measure the temperature of a discrete point and must be attached to the test specimen. Rittel (1998, 1999, 2000) and Döll (1976) used miniature thermocouples to make discrete point measurements of the temperature increase in polymers during dynamic deformation. Thermally, sensitive films are applied directly to the test specimen and change colors in response to the temperature of the underlying surface. Calibration and interpretation of the colors is subjective. They were used by Fuller et al. (1975) to measure the temperature increase of a propagating crack in PMMA. The newest generation of commercially available photon detectors are highly sensitive to radiation in a number of wavelength bands, measure temperatures remotely, and have response times less than 0.5 ms. Additionally, the detectors can be configured in 1-D and 2-D arrays for measuring temperature

fields. The disadvantage of this technique is their high costs. Proton detectors have been used to measure the temperature field of cracks propagating in ductile metals (Zehnder and Rosakis 1991; Mason and Rosakis 1992).

For the measurement of the temperature field surrounding a rapidly propagating crack tip, a high resolution, fast response method is needed. Additionally, a method that does not influence the dynamic fracture event, such as drilling holes or attaching mass to the surface, is desired. Detectors that respond to photons are ideally suited for crack tip temperature measurements because they can be made very small (less than 100 μm) and have a response time of less than 0.5 ms. The photon detector method was used in this study for temperature field measurements.

Electromagnetic radiation is emitted from any body that has a temperature greater than absolute zero. The particular wavelength of energy emitted by a body is related to its absolute temperature. For a black body emitter, the relation between spectral emissive power, E_λ , wavelength, λ , and absolute temperature, T , is given by the Planck distribution (Planck 1959),

$$E_\lambda = \frac{C_1}{\lambda^5 \left(e^{\frac{C_2}{\lambda T}} - 1 \right)}, \quad (22)$$

where the first and second radiation constants, C_1 and C_2 , respectively, are $3.742 \times 10^8 \text{ W}\cdot\mu\text{m}^4/\text{m}^2$ and $1.439 \times 10^4 \mu\text{m}\cdot\text{K}$. Equation (22) is plotted in Figure 18 for several selected temperatures. Figure 18 shows that the spectral region in which the radiation is concentrated depends on temperature. Hotter objects emit energy of a shorter wavelength. Additionally, the peak in spectral emissive power is higher for hotter objects. In the context of crack tip temperatures, Figure 18 indicates that lower crack tip temperatures result in the emission of longer wavelength radiation at lower power levels. Zehnder and Rosakis (1993) have compiled the spectral responsivity of several common photon detectors. This comparison, illustrated in Figure 19, shows that a detector made from one material, such as InAs, can be very sensitive at a particular wavelength band, but may be completely unresponsive to radiation at a different wavelength band. The maximum temperature in the crack tip field anticipated for this study is on the order of 300 K. Using Figure 18, this temperature gives peak spectral emissive power at $\sim 10\text{-}\mu\text{m}$ wavelength. The ideal detector for this wavelength indicated by Figure 19 is HgCdTe. For this reason, a custom-built HgCdTe detector was procured for the study of polymer heating during high-rate deformation and fracture.

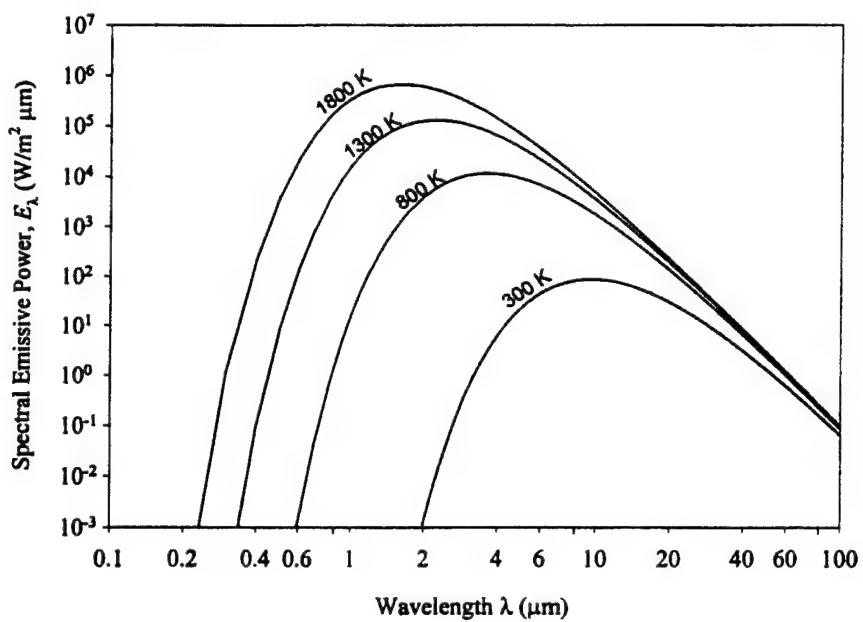


Figure 18. Planck distribution for a black body emitter at several temperatures showing the shift in emitted radiation wavelength as the body is heated.

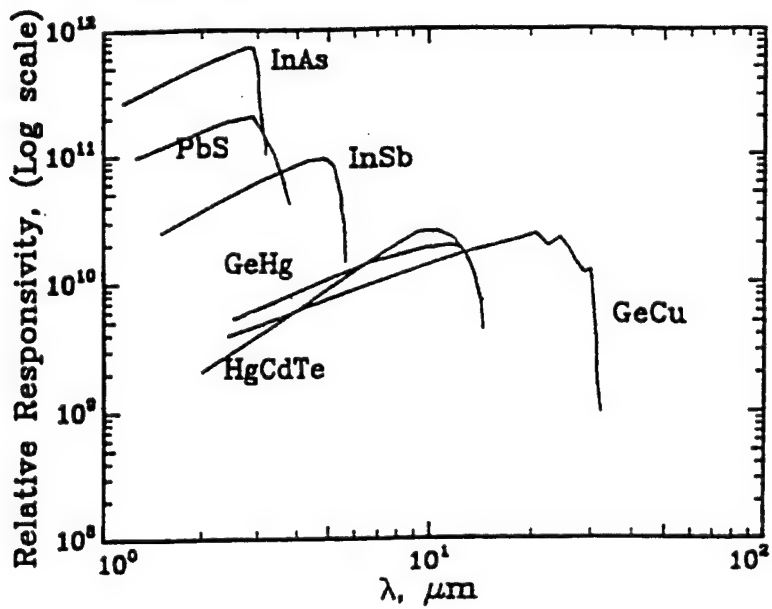


Figure 19. Spectral responsivity of several common photon detectors (Zehnder and Rosakis 1993).

2.6.1 Infrared Detector System and Operation

The temperature field surrounding the propagating crack tip and the trailing thermal wake was measured in real time with a high-speed infrared detector and focusing optics. The detector was manufactured by the Fermionics Corporation and consists of 16-square HgCdTe (mercury cadmium telluride) photovoltaic elements of size 80 μm , arranged in a linear array with a spacing between elements of 20 μm . The detector elements are sensitive to radiation in the mid-infrared spectrum, 6-12 μm wavelength, corresponding to black-body temperatures ranging from 300 to 400 K (Incropera and deWitt 1981). The linear array is cooled to 77 K with liquid nitrogen to increase the signal-to-noise ratio of the detector system. The detector was connected to a 16 channel, 10 MHz preamplifier that was also custom made by Fermionics Corporation, and the system output was recorded with digital storage oscilloscopes having a bandwidth of 500 MHz (Tektronix TDS 540B). The response time of the detector and preamplifier was less than 0.25 μs , which provided sufficient temporal resolution to capture the expected transient thermal event.

The radiation emitted from the specimen surface was focused on the detector elements by what is essentially a short focal length Newtonian telescope similar to the optical configuration used by Hodowany et al. (2000) and is depicted in Figure 20. A spherical mirror served as the focusing element and a square flat mirror was used to fold the optical axis. The spherical mirror has a diameter and focal length of 150 mm. The height and width of the flat mirror was 30 mm. The surfaces of the spherical and flat mirrors were gold plated to minimize reflective losses. The optical configuration allows the magnification to be varied by adjusting the distances of the detector and polymer test specimen to the spherical mirror according to the mirror equation (O'Shea 1985):

$$\frac{1}{t_1} - \frac{1}{t_0} = \frac{1}{f}, \quad (23)$$

where $-t_0$ is the distance from the detector element to the spherical mirror, t_1 is the distance from the polymer test specimen to the spherical mirror, and f is the focal length of the mirror. The magnification, M , is given as (O'Shea 1985)

$$M = \frac{t_1}{t_0}. \quad (24)$$

Note that the magnification is negative because t_0 is always negative (an artifact of the sign convention used in the optics community), indicating that the image is inverted by the optical system. Hence, a magnification of -1, which was the primary configuration used for most of this study, is achieved when the absolute distances t_0 and t_1 are both 300 mm. This magnification gave a detector spatial resolution of 80 μm .

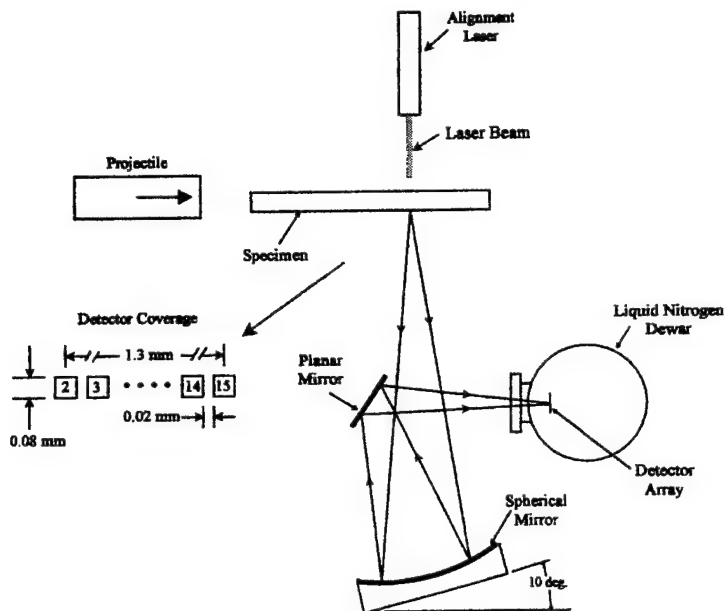


Figure 20. Optical configuration used to measure the temperature field surrounding a propagating crack tip. Infrared detector array coverage is also shown.

The spherical mirror was rotated about 10° off of the optical axis it forms with the polymer specimen, as shown in Figure 20, which introduced a small amount of optical distortion. This was necessary because of the need to place the flat mirror in front of the spherical mirror in order to fold the optic axis of the reflected infrared radiation. If the spherical mirror was not rotated, the flat mirror would have to be placed directly in front of it, blocking *all* of the incoming energy (for the case of $M = -1$). By rotating the spherical mirror a small amount, the reflected beam is cast slightly off to the side, which eliminates the need to place the flat mirror directly in the incident energy path. The amount of distortion was qualitatively identified by placing a clear piece of plastic with a grid printed on it at the polymer specimen location and examining the projected image at the IR detector with a white screen. An incandescent light bulb was used as the illuminating light source behind the clear plastic. In this way, the rotation of the spherical mirror and the placement of the flat mirror could be adjusted to give good optical throughput while minimizing the optical distortion. Although this was done using white light rather than radiation in the infrared wavelength, the mirror position minimizing distortion is identical. This is due to the fact mirrors were used to focus the system, which reflect radiation in the same direction regardless of wavelength.

The linear array was placed so that it was perpendicular to the crack propagation direction, as shown in Figures 6 and 7. Up to 14 of the 16 detector elements were used in the array during any given test. The resulting area observed by the detector array for the opening mode and shear-dominated experiments is shown

in the insets of Figures 6 and 7, respectively. For most experiments, a location \sim 15–20 mm from the initial notch tip was monitored by the detector. If strain gages were present, this location was adjusted to coincide with one of the gage locations.

The region monitored by the detector elements for the shear-dominated experiments was on the grooved surface and was always contained within the width of the groove because surface emissivity greatly depends on surface roughness. Variations of surface emissivity were minimized by polishing the grooves with 2000-grit sandpaper to achieve a smooth surface. This was also done for the calibration specimens discussed in section 2.6.3.

Some of the experiments discussed in sections 3 and 4 resulted in temperature increases that were less than 20 K above ambient. The infrared detector output for these low temperature events had a considerable level of noise. A digital filtering scheme was used to improve the signal to noise ratio of the thermal signals. The infrared detector output that was digitized and stored with a digital storage oscilloscope was transferred to a computer. The signals were then processed with the software package, TableCurve 2D, where they were smoothed in the time domain using a 4-point polynomial interpolation routine resident in the software (Jandel Scientific 1994). The smoothing algorithm performs five passes through the data. One pass of the algorithm consists of moving across the data and, at each time point, performing a polynomial interpolation using the two points lower in time and two points greater in time. The y-value (detector voltage output) from the interpolation replaces the original y. The algorithm was designed for low levels of smoothing. It is nearly impossible to oversmooth the data using this approach. To ensure this, all smoothing was performed interactively to verify features of the original thermal signals were not lost.

2.6.2 Alignment and Focusing Procedure

Precise alignment and focus of the infrared detector system are critical to achieving high-resolution measurements of the crack tip temperature field. During the initial equipment set up process, the axis of the gun launch tube was placed level and perpendicular to a leveled sighting laser used subsequently to aid in alignment and focusing tasks. The intersection of the 1-mm-diameter laser beam with the launch tube centerline is the location where the infrared detector system was focused. The initial coarse alignment was achieved by placing a clear piece of plastic with markings on it at the intended focus point and shining an incandescent light through it towards the infrared detector system. The projected image at the infrared detector was visually monitored while the mirrors were adjusted on an optical breadboard to obtain the correct magnification, maximize brightness, and minimize optical distortion due to spherical mirror rotation. Once the mirror locations were fixed, the infrared

detector unit was placed on a translation stage that permitted precise movement in three orthogonal directions, and this assembly was then placed on the breadboard at the appropriate location. With the optical components in their proper place, a final alignment was performed using a hot-wire technique that is discussed next.

A hot-wire jig was made by taking a polymer test specimen and drilling two holes in it, as shown in Figure 21. A 76- μm -diameter Chromel-A wire was placed across each of the holes and held tightly by wrapping it around screws located at the periphery of the holes. The wire was oriented horizontally across one hole and vertically across the other. To hold the hot-wire jig in place, a fixture was attached to the inside of the impact chamber and served as a guide for the jig (and polymer test specimens) to lean against. The fixture made contact with the jig side at three points, one near the top and two at the bottom, and was made from PC. This fixture ensured that when the hot-wire jig was removed after the focusing process was completed, the test specimens were placed at exactly the same position and remained in focus. A scissors jack with cantilevered glass microscope slides was placed underneath the jig to allow vertical positioning. With the jig in place inside the impact chamber, the horizontal wire was placed so that it intersected the center of the alignment laser beam. The wire was then heated by passing ~ 0.4 A of current through it, which caused emission of infrared radiation from the wire.

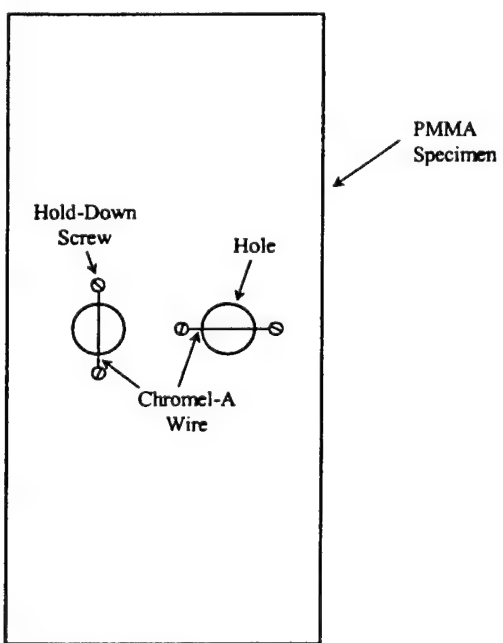


Figure 21. Hot-wire jig used for alignment and focusing the infrared detector system. The 76- μm -diameter chromel-A wire serves as an infrared radiation source by passing current through it.

The infrared detector preamplifier does not respond to a constant or slowly varying signal, so a rotating chopper wheel was placed in the optical path between the hot wire and the detector to modulate the infrared signal at ~ 50 Hz. Modulation of the infrared signal in this manner is standard practice with infrared detection instrumentation. The detector output was then monitored with digital storage oscilloscopes automatically measuring the amplitude of the resulting square wave signal. Because the detector array is vertical and the hot wire is horizontal and smaller than a single detector element (wire diameter is 76 μm and the detector element is 80 μm), proper focus is achieved when only one detector element responds with a square wave signal. The translation stage underneath the detector is adjusted to obtain this condition. Once focused, the detector array was adjusted vertically so the hot wire was imaged onto the element in the middle of the array. The vertical hot wire is then placed so that it intersects the alignment laser beam, and the process is repeated. However, with the detector array and hot wire both being vertical, alignment is achieved when all detector channels register a square wave signal. The hot-wire alignment and focusing procedure was performed prior to each experiment.

Once the infrared detector system was focused and aligned, the instrumented polymer test specimen was placed in the impact chamber against the alignment fixture. The detector aim point on the specimen was marked prior to this with an ink marker on the side opposite that monitored by the infrared detector system. The specimen was moved vertically by the scissors jack and slid horizontally across the glass microscope slides until the marked observation point was in the center of the laser beam. This process, although laborious, ensured proper alignment and focus for each experiment.

2.6.3 Analysis of Specimen Translation

The detector aim point marked on the specimen was not the desired observation point because of the significant particle motion that occurs prior to the crack reaching this region. Impact-induced stress waves create a particle motion field that results in significant displacements of regions ahead of the notch tip. Finite-element simulations of the mode I specimen configurations discussed in section 2.2 were used to quantify this motion.

Explicit linear elastic plane stress simulations of the impact event were performed with the finite-element code ABAQUS. Detailed descriptions of the finite-element code and modeling procedure are presented in section 5. Both the polymer specimen and the steel projectile were included in the simulation. The finite-element mesh used to discretize the polymer specimen and steel projectile consisted of 2-D plane stress quadrilateral elements with a size of 5 mm each. The notch tip in the fracture specimen was modeled as a wedge with

straight faces, having an opening of 2 mm at the specimen edge and coming to a point at the notch tip 25 mm from the specimen edge. Figure 22 shows the finite-element mesh used. Because the configuration is symmetric, only the top half of along the plane of symmetry were imposed to prevent node motion perpendicular to the axis of symmetry. The polymer material was modeled as linear elastic, using the material properties listed in Tables 1 and 2. The steel projectile was also modeled as linear elastic with a modulus of 200 GPa, density of 7850 kg/m³, and Poisson's ratio of 0.3. The interface between the projectile and polymer specimen was a frictionless contact zone that permitted the exchange of energy and momentum. The remaining boundaries of the projectile and specimen were traction free. Because the simulation was explicit, additional boundary conditions were not required (i.e., the specimen was held in place by its the polymer specimen and steel projectile were modeled. Boundary conditions own inertia). The projectile speed was varied from 8 to 40 m/s. The goal of the simulation was to identify the horizontal translation of material located 10 mm in front of the initial notch tip. The translation occurs from momentum transfer from the projectile through wave propagation. In this spirit, the crack was not permitted to propagate and the stresses at the notch tip were permitted to grow unbounded. A convergence study was not performed because the mesh used was fine enough for the wave speeds obtained in the simulation to be identical to those of the material listed in Table 2.

The results are shown in Figure 23, which plots the motion of material 10 mm ahead of the initial notch tip as a function of time for impact velocities ranging from 8 to 40 m/s. Given that typical crack initiation times for PMMA are on the order of 100 μ s, Figure 23 indicates that motion ranging from 1 to 4 mm can occur. The aim point marked on the test specimen was compensated to account for this motion. This adjustment increased the likelihood that the temperature measurement location would coincide with the strain gage location discussed in section 2.5, and helped reconcile timing data from the crack propagation gage and the infrared detector signals to identify the true crack tip location.

2.6.4 Calibration

The output of the infrared detector system is in the form of voltage. As such, a calibration between output voltage and specimen temperature is needed. Zehnder and Rosakis (1993) discuss a calibration method based on the detector spectral response and the test specimen surface emissivity. Unfortunately, these quantities are difficult to quantify. Therefore, an empirical calibration was performed to provide the necessary relation between detector output and specimen temperature.

Specimens with a thickness identical to those used in the fracture experiments were used to calibrate the infrared detector system. This included using

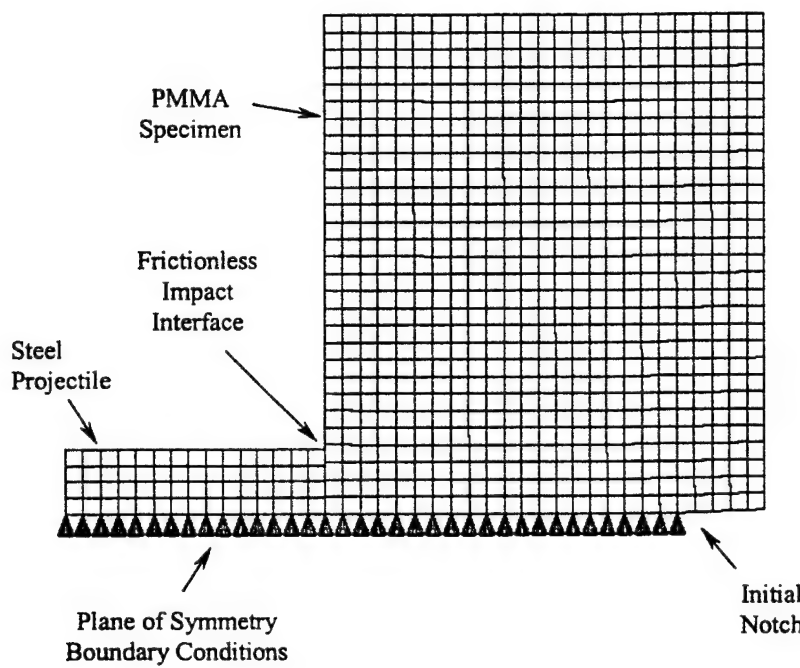


Figure 22. Finite-element mesh and boundary conditions used for numerical simulation of the projectile impacting the polymer specimen. Steel projectile moves from left to right.

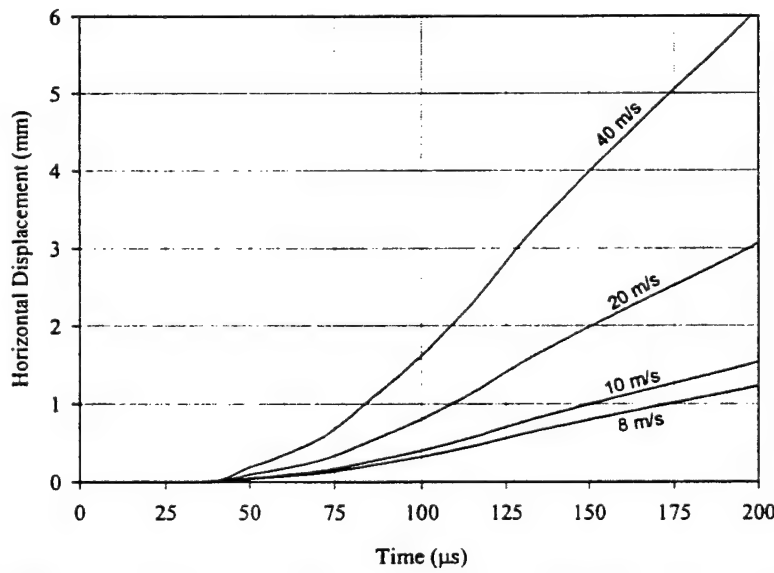


Figure 23. Finite-element results showing the horizontal displacement of a point 10 mm ahead of the initial notch tip due to projectile impact at various speeds.

specimens with a polished groove to provide a suitable calibration for the shear-dominated experiments. The grooves on these specimens were polished with 2000-grit sandpaper to achieve a nearly mirror-smooth appearance. This was necessary to minimize the variation in surface emissivity, which the infrared detector is sensitive to. Calibration consisted of placing either an oven-heated or ice bath-cooled polymer specimen in the impact chamber at the object plane of the detector optics and recording the infrared detector system output for each detector channel as the specimen returned to room temperature. The calibration specimen was held in place with a PMMA fixture attached to the muzzle end of the gun. The detector was aligned and focused on this fixture using the hot wire method discussed in section 2.6.2. Because the detector preamplifier does not respond to a constant or slowly varying signal, a rotating chopper wheel was placed in the optical path between the calibration specimen and the detector to modulate the infrared signal. The actual temperature of the specimen during the calibration process was measured with a K-type (Chromel-Alumel junction) thermocouple embedded in the specimen. Prior to calibration, the thermocouple was placed in a small hole drilled in the calibration specimen and then potted with a material of similar thermal diffusivity (PMMA monomer with the appropriate catalyst/hardening agent, Weld-On 10 adhesive from San Diego Plastics). The thermocouple was within 1 mm from the surface that the detector system monitored. Multiple calibrations were performed for each specimen and optical configuration was performed to ensure repeatability.

From the calibration data, a correlation between detector output and specimen surface temperature was obtained for each detector channel, each optical configuration, and each material used throughout the study. A hyperbolic curve of the form

$$y(x) = \frac{ax}{b+x} + cx, \quad (25)$$

where $y(x)$ is the temperature increase, x is the detector output, and a , b , and c are fitting parameters, was fitted to the data for each channel using the curve fitting routines in the SigmaPlot software package (SPSS Inc. 2000). This provided an analytic expression for converting the detector output to temperature increase. Typical calibration curves for both PC and PMMA, for one channel of the detector system are shown in Figures 24 and 25, with and without grooves, respectively. Note that the temperature increase denoted in Figures 24 and 25 (and all subsequent figures depicting temperature) corresponds to a temperature increase above ambient room temperature, not absolute temperature. The calibration for the grooved specimens was found to be slightly different from the non-grooved specimens (attributable to the different surface emissivity), but was highly repeatable.

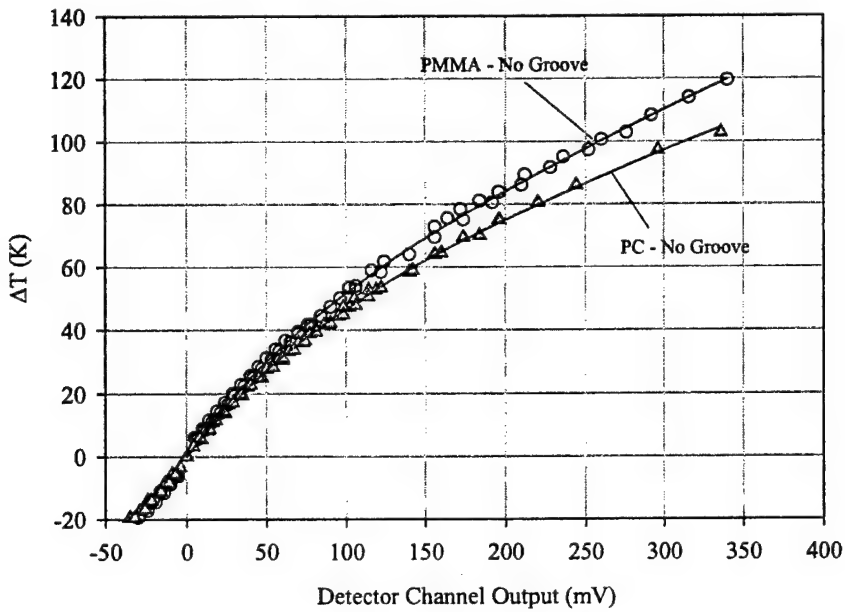


Figure 24. Typical calibration for one channel of the infrared detector system showing results for PMMA and PC.

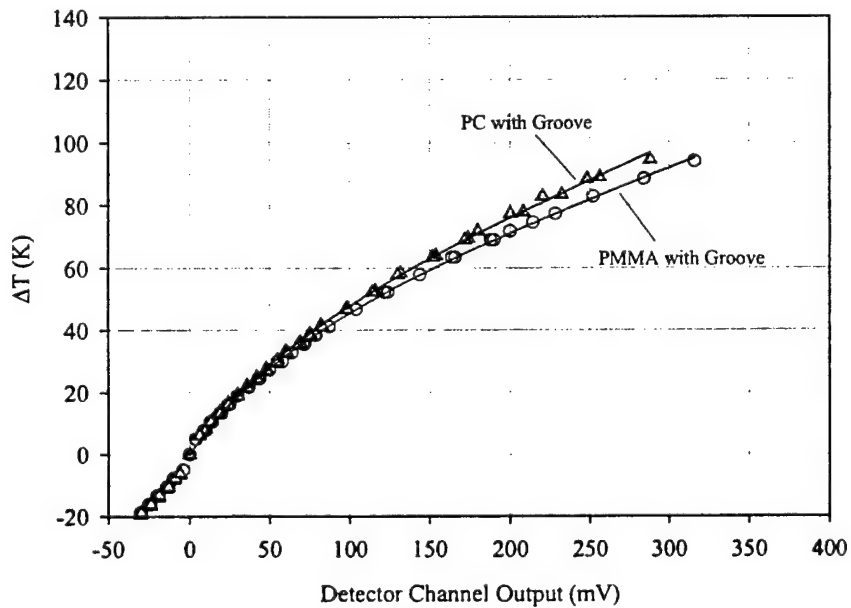


Figure 25. Typical calibration for one channel of the infrared detector system showing results for PMMA and PC using a grooved specimen. Groove was polished with 2000-grit sandpaper to achieve smooth finish.

2.6.5 Sources of Potential Error

There are a number of potential error sources associated with the use of a focused infrared detector system for measuring the temperature field surrounding a propagating crack tip. These sources include a phenomenon known as detector cross talk, limitations of the optical depth of field, detector resolution, radiation transmissivity, and calibration issues. Each of these sources is explored in this section. Additionally, the notion of adiabatic heating near the crack tip is confirmed with an analysis presented at the end of this section, thus providing the necessary foundation for proper interpretation of the thermal measurements in the sections that follow.

2.6.5.1 Detector Cross Talk

The infrared detector used in this study has individual semiconductor elements spaced only 20 μm apart. If radiation falling upon one detector element results in neighboring elements responding because of their close proximity, a phenomenon known as cross talk has occurred. Reasons for this include electromagnetic field effects, focusing errors, and optical aberrations. Significant detector cross talk effectively reduces the system spatial resolution by smearing a well-defined signal over numerous detectors. The detector-element cross talk was determined by placing a heated wire with a diameter less than the detector-element size at the test specimen location and recording the voltage output for each channel of the detector system after it was carefully focused. Figure 26 shows the output for the detector array focused on a 76- μm wire. Detector cross talk was found to be ~75%-10%.

2.6.5.2 Depth of Field

The depth of focus of the optical system was also determined using a small diameter-heated wire. With the hot wire at the test specimen location, the detector was moved along the optic axis using a translation stage to bring it in and out of focus. The output of the detector array was recorded as the translation occurred. Figure 27 shows how the image of the wire began to spread to other detector elements as the system became unfocused. The results indicated that the optical configuration had approximately a 1-mm depth of field. A consequence of this small depth of field is that the specimen positioning fixture discussed in section 2.6.2 was required for accurate placement of each test specimen.

2.6.5.3 Spherical Aberrations

Spherical aberrations occur when a large diameter-focusing element, such as the spherical mirror used in this study, is used in a short focal-length optical system. The aberration is due to light from the outer and inner regions of the mirror

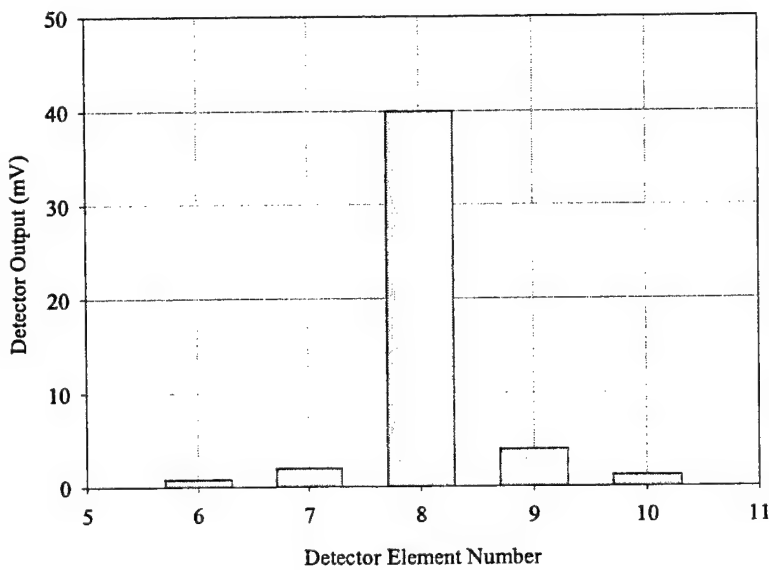


Figure 26. Infrared detector element cross talk observed using a 76- μm heated wire. Cross talk of 7%-10% was recorded.

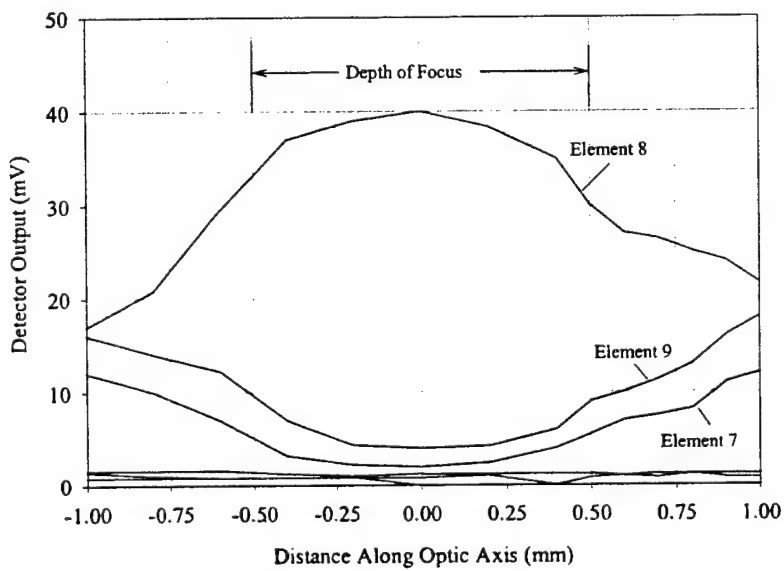


Figure 27. Detector output measured as the detector array was translated in and out of focus to obtain an estimate of the infrared measurement system depth of focus.

being focused at different locations. A qualitative estimate of the degree of spherical aberration present in the optical configuration was made by covering the outer regions of the spherical mirror during the detector cross talk assessment. No difference in the level of detector cross talk was noted when various apertures were placed on front of the mirror. Hence, the optical configuration was free of significant spherical aberration.

2.6.5.4 Surface vs. Internal Heating

It was asserted in section 2.1 that both materials are not transparent to radiation in the mid- to far infrared spectrum. This was verified by placing a 3-mm-thick piece of each material in the optical of a hot wire (and chopping wheel) and the focused detector. The detector response indicated that thin sheets of PC and PMMA completely blocked the transmission of infrared energy from the hot wire to the detector array, thus confirming the assertion. As a result of this, only surface temperature measurements can be made with the infrared detector system. Near the surface, a state of plane stress exists. In the interior of the polymer specimen near the crack front, the stress state changes to approximately plane strain (Krishnaswamy et al. 1991). An implication of this is that the temperature at the crack tip will likely not be uniform through the specimen thickness. As such, the temperature measurements made in this study are likely to be different from those made with an embedded thermocouple, such as the kind used in Rittel (1998). In addition, local temperatures will be underestimated using this measurement technique if the heat source of interest is less than the detector element size, because each detector records the average temperature of an $80\text{-}\mu\text{m} \times 80\text{-}\mu\text{m}$ area. If the crack tip process zone has a lateral span less than $80\text{ }\mu\text{m}$, the true temperature can be determined only if the size of the zone is known. This is discussed further in section 6.

2.6.5.5 Temporal Resolution

Errors in the temporal resolution of the detector array will occur if the time for the thermal source to propagate a distance equal to a detector-element width is less than the detector response time. Such a situation will lead to the detector increasing the time duration of the actual thermal signal. The time for an abrupt thermal pulse propagating at 600 m/s (the approximate limiting crack speed in PMMA and PC) to travel an element distance of $80\text{ }\mu\text{m}$ is $0.13\text{ }\mu\text{s}$, which is slightly less than the system response time of $0.25\text{ }\mu\text{s}$. Thus, if the thermal signals encountered during the experiments were abrupt (i.e., a step-shaped pulse), a correction would be required to resolve the true rise time. However, as will be seen later, the thermal signals from the experiments had rise times an order of magnitude greater than the infrared detector system response time. This suggests the temporal resolution is limited only by the detector amplifier response time.

2.6.5.6 Infrared Emission from Heated Surroundings

Kapoor and Nemat-Nasser (1998) investigated the fraction of plastic work converted to heat for several metals. Their experimental approach used a focused infrared detector to directly measure the surface temperature of the deforming specimen, and a Hopkinson bar technique to indirectly determine specimen temperature. The two methods gave differing temperatures. The infrared detector calibration procedure, similar to the one used in this study, was offered as a possible error source that led to the temperature discrepancy. It was suggested that the hot calibration specimen might produce excessive heating of the surrounding air during the relatively slow calibration procedure, leading to additional infrared energy being emitted. To investigate this possible error source for the infrared detector configuration used in the present study, air heated to 175 K above room temperature was suddenly permitted to flow past the focus point of the optical configuration. Virtually no change in signal from ambient was recorded by the detector system (compared to actual temperatures recorded in the fracture experiments). Hence, the infrared contribution from heated air during the calibration is negligible, at least for the optical configuration used in the present study.

2.6.5.7 Effect of Material Damage on Surface Emissivity

The surface emissivity of the craze material in the crack tip process zone may be considerably different from that of the calibration sample, leading to errors in converting the detector output to temperature. This was investigated by focusing the detector system on a heated piece of PMMA containing an arrested crack. The detector was translated vertically while maintaining focus to determine if detector output changed when the elements moved from the original PMMA surface to the process zone. Although no difference in detector output was observed, this test was not conclusive because of potential differences in the process zone of a stationary, arrested crack, and an active, growing crack. This remains a potential error source.

2.6.5.8 Adiabatic Conditions

Interpretation of the recorded infrared detector signals is based on an assumption that the failure event is nearly adiabatic. The condition of adiabatic heating presumes that the time intervals of interest in the experiments are sufficiently small to neglect thermal conduction and the loss of heat to convection and radiation. An upper bound of the heat loss due to convection and radiation effects can be made from the rate of calibration specimen cooling. For a calibration specimen with an initial temperature 80 K above room temperature (typical temperature increases measured during the fracture experiments) the maximum cooling rate was approximately 1 K/s. Given that the time intervals of interest in this study were on the order of 100 μ s, cooling

due to radiation and convection would result in a temperature decrease of 0.001 K. Thus, although radiation losses do occur (in fact that is what is detected by the highly sensitive infrared detector system), the losses are negligible from an engineering perspective.

As will be seen in the following sections, the measured temperature field surrounding a propagating crack tip is highly localized. This leads to the potential for heat conduction to occur during the time interval of interest, invalidating the adiabatic heating assumption. The heat conduction solution for a semi-infinite solid initially at ambient temperature whose entire surface is suddenly heated to a constant temperature was used. The solution for this situation is given by Poulikakos (1994) as

$$T(x,t) = (T_i - T_0) \operatorname{erf} \left(\frac{x}{\sqrt{4\eta t}} \right) + T_0, \quad (26)$$

where $T(x,t)$ is the dependent temperature sought, T_0 is the constant temperature suddenly applied to the entire free surface at time $t = 0$, T_i is the initial ambient temperature, x is the distance in the solid from the free surface, η is the thermal diffusivity defined as $k/\rho c_p$, and erf is the error function. This relation is plotted in Figure 28 for several different locations below a PMMA crack surface suddenly heated to a temperature 100 K above ambient room temperature. As a specific example, consider a location 0.1 mm below the fracture surface in PMMA. For a surface with a sudden temperature increase 100 K above ambient, the time required to raise the temperature 1 K at the location 0.1 mm below the surface is 6.72 ms for PMMA and 4.88 ms for PC. These times are far in excess of the time intervals of interest in these experiments. This analysis indicates that adiabatic heating is a reasonable assumption.

3. Opening Mode Experiment

3.1 Introduction

As mentioned in section 1, a competition between classic shear yielding and craze formation occurs when a polymer well below the glass transition temperature is subjected to an imposed strain. During opening mode fracture of brittle materials, the failure mechanism was noted by Kambour (1964) to be from craze formation and breakdown. As the fracture event becomes increasingly dynamic, Kambour et al. (1978) found that craze formation becomes the failure mechanism for both brittle and ductile materials, although plasticity is still

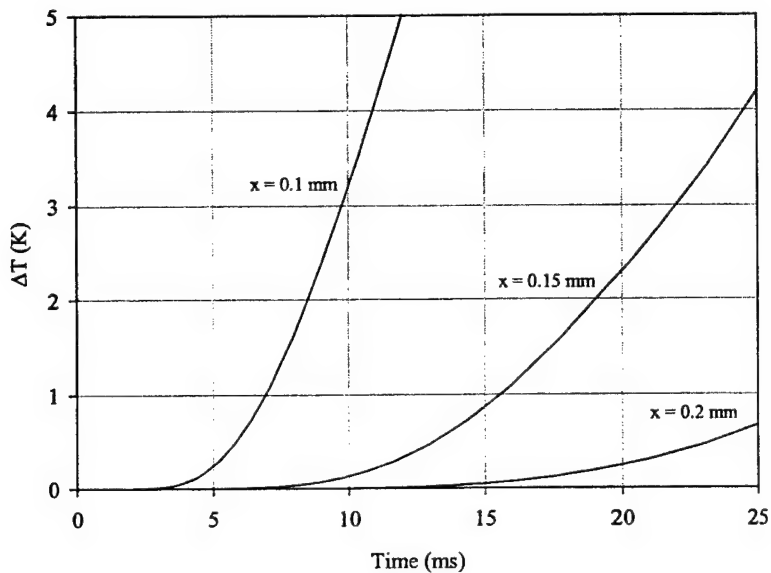


Figure 28. Temperature increase of several x locations below the surface of a semi-infinite PMMA solid with a suddenly applied surface temperature. Initial ambient temperature of solid was 293 K and suddenly applied constant surface temperature was 393 K.

present at the crack tip region. Increasing the energy available for crack growth (the energy release rate, G) causes the crack tip speed to increase until a limiting speed of about 60% c_R is reached. Attempts to drive the crack faster cause it to split into two advancing cracks (Yoffe 1951), effectively decreasing the energy flowing into each crack. Döll (1976) and Sharon et al. (1996) found G to increase nonlinearly with crack tip speed for mode I experiments using PMMA. These studies showed G to asymptote towards infinity when the crack tip speed approached 60% c_R .

The fracture surface of brittle polymers was observed by Döll (1989) to roughen as the crack tip speed increases. The roughness has been attributed to an evolution of the crack tip structure from a single craze front to multiple, layered craze fronts propagating simultaneously. Sharon et al. (1996) measured the increase in surface area for PMMA resulting from high-speed crack growth. They found the surface area to increase sixfold and concluded the increased energy required for fast crack growth is used solely for the creation of new surfaces. Sun and Hsu (1996) noted the energy needed for fracture in brittle materials is several orders of magnitude greater than the surface energy, γ , suggesting that the increased surface energy requirements alone do not account for the energy increases needed for high-speed crack growth.

Studies have shown that crack tip heating does occur in brittle materials during dynamic fracture (Döll 1976; Fuller et al. 1975), implying that additional energy beyond that needed for the creation of new surfaces is required to fracture a brittle material, as noted by Sun and Hsu (1996). The excess energy is used in the process zone for microstructure breakdown and molecular bond scission, leading to the generation of heat. Because crack tip speeds during dynamic fracture are a significant fraction of the material dilatational wave speed, the generated heat does not have time to conduct to surrounding regions. This condition results in a temperature increase inside the process zone of the polymer. For a ductile material, plastic deformation surrounds the crack tip process zone, contributing to the overall temperature increase. Thus, the temperature field surrounding a propagating crack is related to the dissipation of mechanical work that went into deformation and failure of the material. Measurement of the crack-driving energy and crack tip kinematics, along with the resulting temperature field at sufficient resolution can provide useful insight into the physical mechanisms within the process zone.

The study of opening mode fracture in PC and PMMA involved examining the crack tip propagation behavior, the flow of energy into the propagating crack tip, measurement of the thermal field surrounding the crack tip, and subsequent examination of the fracture surfaces. This combined approach led to an understanding of the crack tip process zone that would be useful for subsequent modeling efforts.

The experiments are conceptually simple; however, in practice, there were numerous challenges. Measurement of the temperature field surrounding a propagating crack tip with a focused infrared detector array can be a difficult task because of the limited array size. For the configuration used in this study, the detector will miss the passage of the crack if the propagation path differs from the intended path by as little as 1 mm. To minimize path deviation, shallow grooves could be machined along the side of the test specimen to provide a preferential path. Unfortunately, this would alter the stress field and possibly the process zone. The approach used in this study was to perform a large number of experiments using polymer specimens free of any geometric or material alterations along the intended crack path. With a large enough group of experiments, the crack tip temperature field would be captured by the detector array for a sufficient number of experiments to draw scientifically sound conclusions. This resulted in well over 100 opening mode experiments being performed during the course of the study.

This section discusses the results of these experiments by way of presenting data from a few selected tests that are representative of the entire collection of successful experiments. The section is organized by the type of measurement or phenomenon being observed. The results for both PMMA and PC are included in each section to better aid in comparing the relative behavior of the brittle and

ductile materials. Unless otherwise noted, the results presented for PMMA are for high molecular weight PMMA. The results presented for low molecular weight PMMA will be clearly indicated as such.

3.2 Crack Tip Speed Measurements

The energy that drives a crack to high-speed comes from the kinetic energy of the impacting projectile, as discussed in section 2. However, a one-to-one correspondence of crack tip speed with impact velocity does not exist. Because it is desired to quantify the conditions responsible for the crack tip temperature fields presented later in this section, measurements of the crack tip propagation history were made. The crack propagation gage discussed in section 2 was used to determine the crack tip location during propagation. Recall the principle of operation is the severing of consecutive electrically conductive wires painted on the test specimen as the crack propagates. The electrical circuit for the gage was discussed in section 2.4. The circuit output was recorded on a digital storage oscilloscope. A typical output record from the gage is shown in Figure 29. The severing of a wire corresponds to an abrupt increase in circuit voltage. The sequence of wire break times was used to locate the crack tip position within the region monitored by the propagation gage. This was possible because the location of the wires on the test specimen was known *a priori*. The position history of a crack propagating in PMMA is shown in Figure 30. Two examples are presented in Figure 30, one corresponding to a projectile impact speed of 40 m/s, and the other corresponding to an impact speed of 8 m/s. As mentioned earlier, a higher impact speed generally results in a higher crack tip speed. This is evident in Figure 30 by the different slopes of the two experiments shown. The crack tip speed was determined by numerically differentiating the crack tip position vs. time data shown in Figure 30. A central differencing scheme was used. The crack tip speed determined in this manner from the data in Figure 30 is shown in Figure 31. Both cracks accelerate to a nearly steady-state propagation speed, dependent upon the projectile-impact speed. Although numerical differentiation of data signals can amplify the data scatter, the resolution of the propagation grids used in this study kept the data scatter to an acceptable level. The error bar shown in Figure 31 has a magnitude typical of crack tip speed measurement uncertainty in dynamic fracture mechanics (Lambros and Rosakis 1995).

Typical crack tip speed history obtained from break-wire signals for numerous opening mode fracture experiments on both polymers are shown in Figure 32. The data set in Figure 32 corresponds to experiments with projectile impact speeds of \sim 35–40 m/s for PMMA and 25–40 m/s for PC. The uncertainty in crack tip speed is approximately \pm 50 m/s (from Figure 31). In PMMA the crack tip accelerates to a terminal speed of \sim 680 m/s, or 0.55 c_r . Terminal speed is achieved after the crack tip has traveled 10–15 mm. Post-mortem

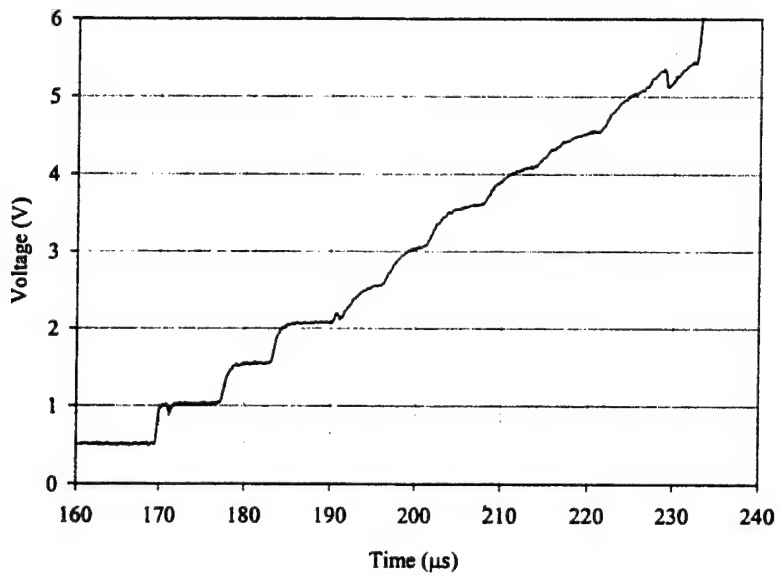


Figure 29. Typical crack propagation gage circuit output. The abrupt increases in voltage are generated by the painted wires being severed by the propagating crack.

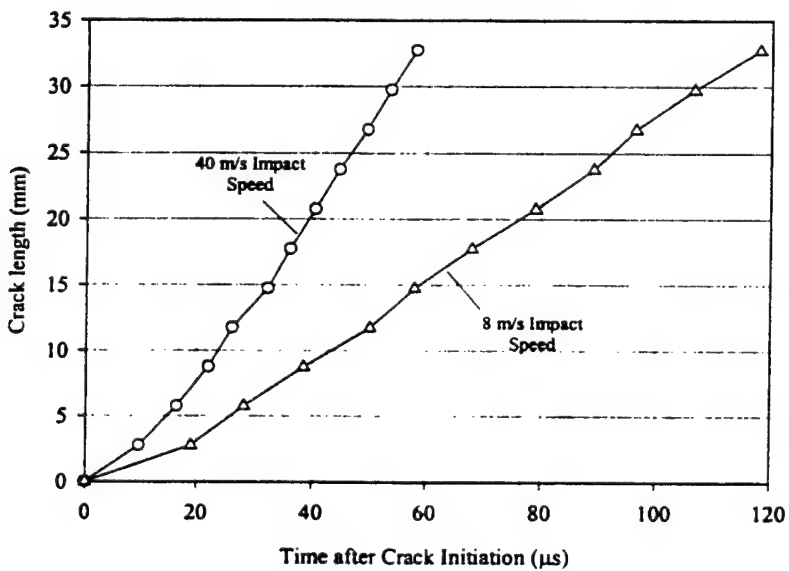


Figure 30. Crack tip position history obtained from the crack propagation gage timing data for PMMA. Two different experiments are shown, corresponding to different projectile-impact speeds.

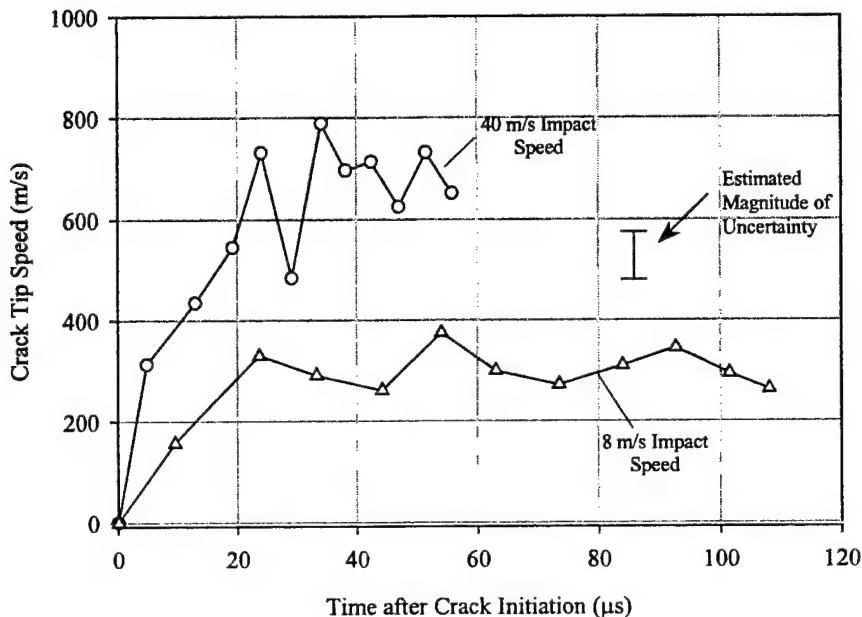


Figure 31. Crack tip propagation speed in PMMA for two experiments with different projectile-impact speeds. Propagation speed was determined from crack propagation gage timing data and the distance between the painted wires. Error bar shows typical measurement uncertainty for crack tip speed (estimated from Lambros and Rosakis [1995]).

examination of the PMMA specimens indicated that crack branching occurred 20–25 mm from the starter notch tip. This correlates to the region where the terminal crack tip speed was sustained and is consistent with theoretical crack tip speeds required to produce branching (Broberg 1960). For the case of PC, the terminal crack tip speed is ~ 550 m/s ($0.55 c_r$). Crack branching also occurred in PC after terminal speed was achieved.

Impact speeds less than 35 m/s for PMMA and 25 m/s for PC, but above 10 m/s, resulted in terminal speeds identical to the high impact speed experiments. However, the distance the crack propagates prior to reaching terminal speed increases. As the impact speed is lowered to values of ~ 10 m/s in PMMA, the crack no longer accelerates to a speed of $0.55 c_r$. Instead, a lower terminal speed of ~ 300 m/s ($0.24 c_r$) is achieved (as shown in Figure 31) and the crack does not branch.

Measurements of the crack tip speed in low molecular weight PMMA were not made because the test specimens used during the low molecular weight PMMA experiments were not instrumented. However, differences in crack branching were observed. The crack in low molecular weight PMMA was observed to branch much earlier than the high molecular weight PMMA, whereas branching occurred 20–25 mm from the notch tip for the high molecular weight

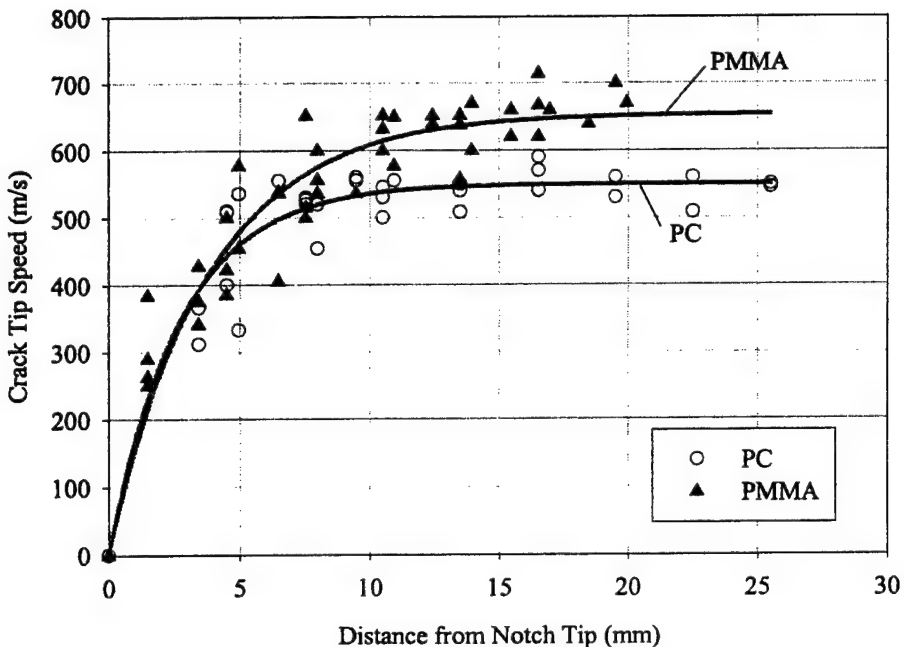


Figure 32. Opening mode crack tip speeds for PC and PMMA as measured by the crack propagation gage for experiments with a projectile-impact speed of 40 m/s.

experiments, it occurred at ~ 10 mm from the notch in the low molecular weight tests. It is not known if branching in the low molecular weight material occurs at a lower speed or if the crack tip accelerated to the same terminal speed as the high molecular weight material, but over a shorter distance.

3.3 Dynamic Energy Release Rate Measurements

The dynamic energy release rate was measured using the strain gage technique discussed in section 2. The output voltage from the strain-gage signal conditioning amplifier was converted to strain using equations (20) and (21). Typical signals recorded from the strain gage system (after converting voltage to strain) for PC and PMMA with crack speeds near the terminal speed are shown in Figures 33 and 34, respectively. The two strain gages were located 7 mm and 15 mm from the initial notch tip (see Figure 17). The peak strains for the two gages were not identical for either material, indicating the crack speed was not the same at the two strain-gage locations. The timing data from the crack propagation gage indicated the crack tip was still accelerating at the first gage location, but had achieved steady-state speed before reaching the second gage location. The condition of steady-state crack propagation (i.e., no crack branching) in PMMA was verified for the low impact speed case using three strain gages located 7, 15, and 25 mm from the notch tip. The strain signals for this case (projectile impact speed of 8 m/s) are shown in Figure 35.

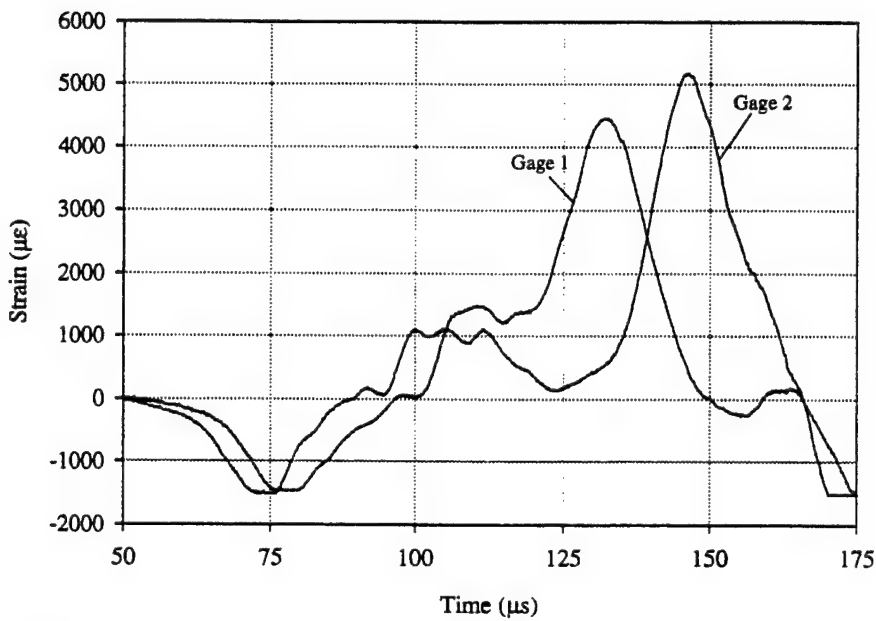


Figure 33. Measured strain from the strain gage circuits for a crack propagating at $0.55 c_R$ in PC. Distance between strain gages was 8 mm.

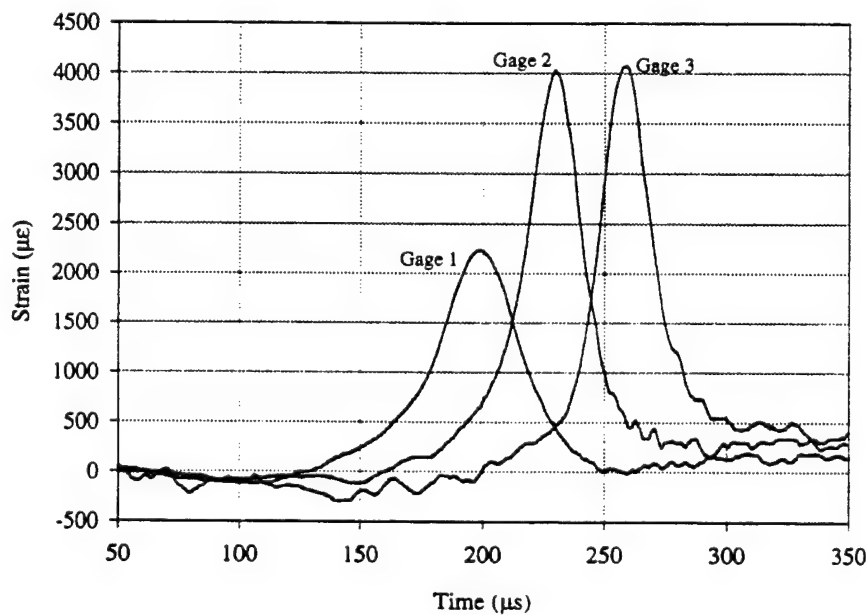


Figure 34. Measured strain from the strain gage circuits for a crack propagating at $0.55 c_R$ in PMMA. Separation between strain gages was 8 mm.

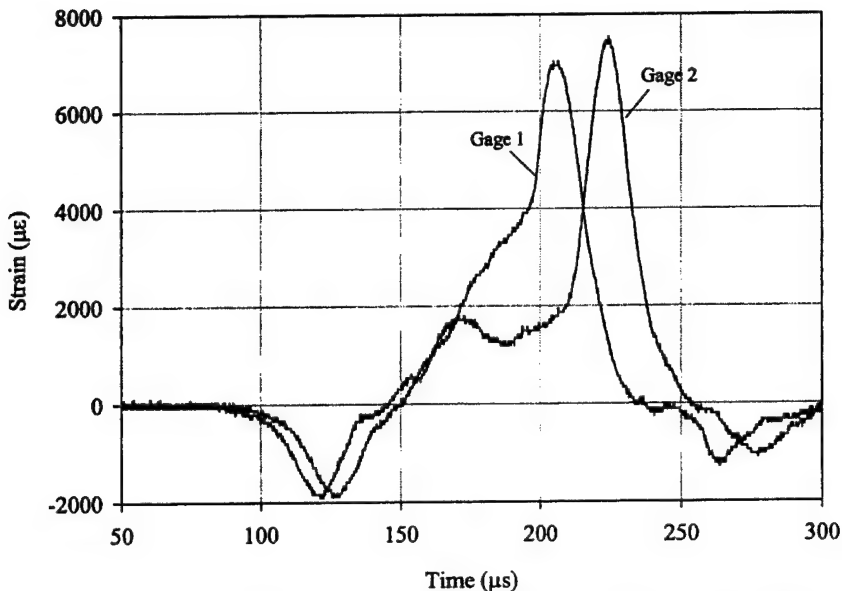


Figure 35. Measured strain from the strain gage circuits for a crack propagating in PMMA. The crack accelerated to a terminal speed of ~ 450 m/s.

The projectile impact speed was 8 m/s. The gages located 15 and 25 mm from the notch tip have the same peak strain, indicating steady-state crack propagation. Timing data from the crack propagation gage was consistent with the time of peak strain for the mode I experiments.

Calculation of the dynamic energy release rate, G , requires not only peak strain values, but also crack tip speed, \dot{a} , and the perpendicular distance between the strain-gage centroid and crack propagation path, y_g . The crack tip speed was obtained from the crack propagation gage as seen in Figures 31 and 32. The distance between the strain gage and crack path, y_g , was measured after each experiment for each gage. These values were then used in equations (17) and (18) to give G . The calculated values of G are shown as a function of crack tip speed for PC and PMMA in Figure 36. Note that measurements of G for PC were limited to the terminal crack speed. The values reported here are consistent with those reported for PMMA by Döll (1976).

3.4 Temperature Field Measurements

Previous measurements of opening mode crack tip temperature in PMMA were made by Fuller et al. (1975), Döll (1976), and Rittel (1998). As discussed in section 1, Fuller et al. (1975) used a thermocouple and heat sensitive film to determine the total heat evolved at points along the crack path in one series of experiments and an unfocused infrared detector to measure the radiation

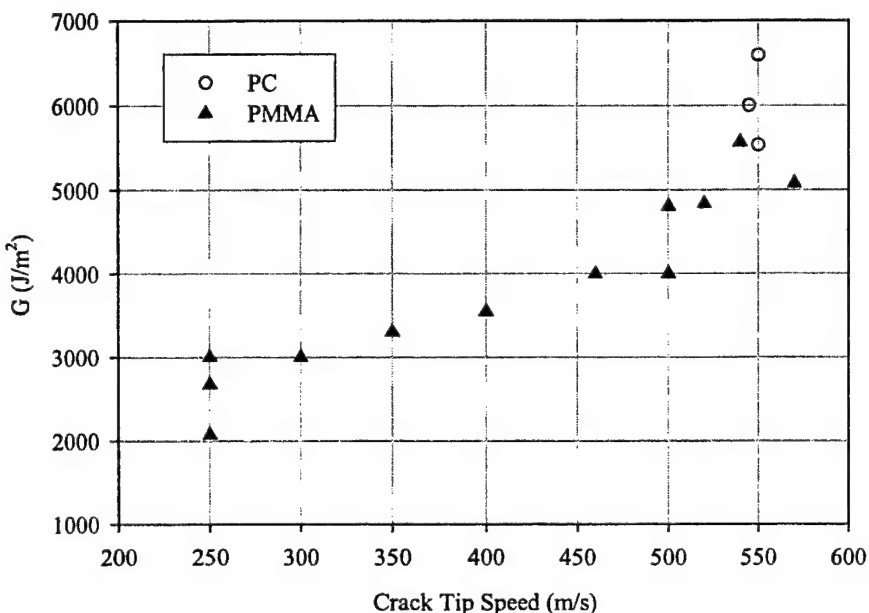


Figure 36. Dynamic energy release rate for various crack tip speeds in PC and PMMA.

emitted from the entire heat affected zone at the crack tip during a different set of experiments. The results from both sets of experiments were combined to deduce a maximum crack tip temperature increase of 500 K. Using thermocouples embedded a short distance from the crack path in PMMA, Döll (1976) measured a temperature increase of ~ 0.85 K at a single location. However significant heat conduction had occurred by the time the peak temperature was recorded. Rittel (1998), also using an embedded thermocouple in PMMA, recorded a peak temperature increase of ~ 50 K during dynamic opening mode fracture.

The previous approaches to measuring the temperature of a crack tip propagating in a polymeric material were limited to discrete point measurements or collection of the entire heat flux from a large region. Furthermore, the techniques were invasive in the sense that a thermocouple was embedded in the material that the crack was to propagate through, possibly affecting the propagation mechanics. This study improves upon the previous temperature measurements by directly measuring the temperature field surrounding the propagating crack tip in amorphous polymers using a noninvasive approach. This has been done for ductile metals using infrared detector arrays (Zehnder and Rosakis 1991; Kallivayalil and Zehnder 1994; Mason and Rosakis 1992; Zehnder et al. 2000). This study will use a 1-D infrared detector array to measure the temperature field for not only ductile, but also brittle polymeric materials.

The infrared detector used for this study was discussed in section 2. All of the temperature field measurements were made with the detector optics configured for a magnification of -1 (negative implying inverted image). The infrared detector system monitored a location on the polymer panel within the region covered by the crack propagation gage (when used), but prior to the location where branching occurred. Recall from section 3.2 that the crack tip accelerated to a terminal speed over a short distance. This distance was influenced by the impact velocity. As such, temperature measurements made at crack tip speeds less than terminal could be made by reducing the impact speed and moving the detector focus point closer to the initial notch tip. This approach, although not precise and requiring significant trial and error, did permit the temperature fields of slower crack tips to be measured. The temperature measurements of cracks propagating in PC are presented first in this section, followed by the measurements made using PMMA specimens. This section concludes with a discussion of the general features found in the temperature signals and comparison of the measurements made in this study with those of others in the literature.

3.4.1 PC Experiments

Figure 37 shows the infrared detector signals (after calibration and data smoothing, described in section 2) for a crack propagating in PC at approximately its terminal speed. The quantity ΔT shown in Figure 37 on the vertical axis represents temperature increase over ambient. The projectile-impact speed was 25 m/s. No increase in temperature is observed before the time window shown in Figure 37, indicating that stress wave propagation in the polymer specimen does not cause dissipative heating. Detector 11 recorded the highest temperature increase for this particular experiment. The maximum temperature increase over ambient was 105 K. The subsequent detector elements flanking detector 11 registered decreasing peak temperatures. Each of the temperature curves in Figure 37 show an increase in temperature followed by a slower, monotonic decrease. There is a small amount of thermoelastic cooling that precedes crack tip heating. This was detected by the infrared measurement system. Figure 38 presents the infrared detector output for only elements 10 and 11 from Figure 37. With the traces from the additional detector elements removed, the thermoelastic cooling ahead of the crack tip is clearly visible. The amount of cooling was ~5 K below ambient. Thermoelastic cooling was observed on nearly all mode I experiments for both PC and PMMA. A theoretical estimate of thermoelastic cooling is given in section 3.4.3.

The crack propagation gage and strain gages provide data relative to a frame of reference attached to the polymer specimen. The infrared detector is fixed in space and monitors the passage of the crack tip as the crack and polymer

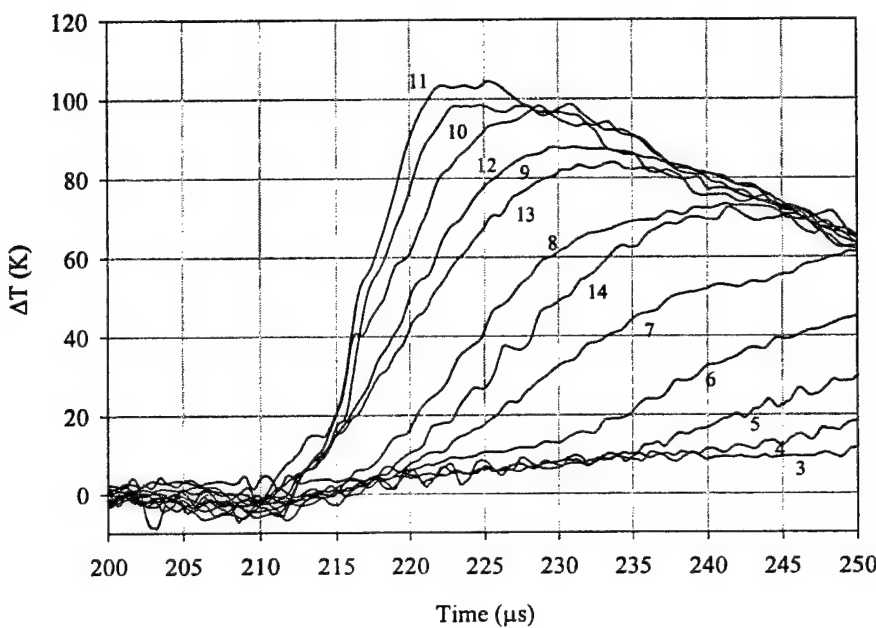


Figure 37. Thermal detector output (after calibration) for opening mode fracture of PC with a crack tip speed of $0.55 c_R$.

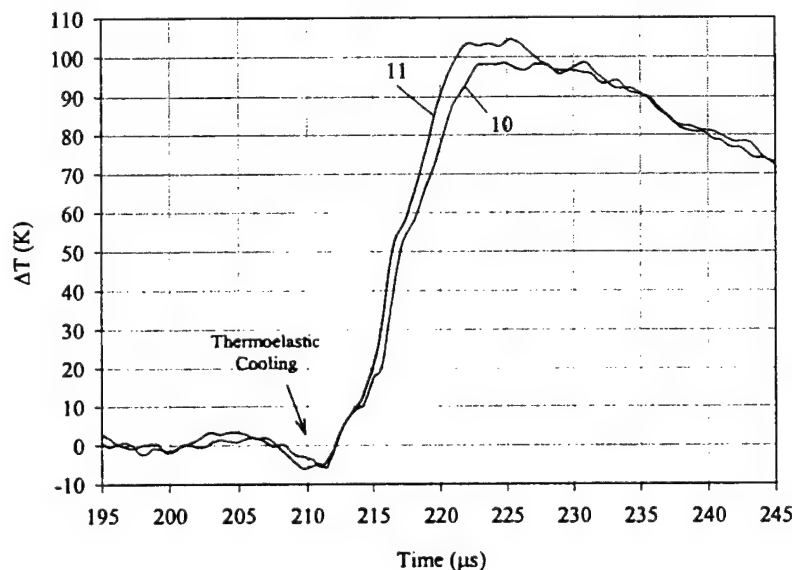


Figure 38. Thermal detector output from two detector elements for an opening mode crack propagating in PC at a terminal speed of $0.55 c_R$. Thermoelastic cooling is observed prior to dissipative crack tip heating.

specimen translates before it. The impact-induced specimen translation was discussed in section 2, along with finite-element simulations to quantify this specimen translate before it. The impact-induced specimen translation was motion. The translation data in Figure 23 was used to reconcile the timing of events measured with the crack propagation gage, strain gages, and the infrared detector. The disturbance that severed the painted lines of the propagation gage is located at $\sim 213 \mu\text{s}$ on the temperature plots shown in Figures 37 and 38. It does not correspond to the peak temperature. Although the location of the strain gages seldom coincided with the location that the infrared detector monitored at the time of material heating (due to variations in crack initiation time), the times of peak strain did correlate with the crack propagation gage. It must be kept in mind that some of the temperature signal rise time may be artificial. This possibility is discussed in detail in section 6.

The temperature profile for a crack propagating in PC at 450 m/s ($0.45 c_R$) was obtained by decreasing the projectile-impact speed to 25 m/s and moving the detector so that it monitored a region 5 mm from the initial notch tip. The results from this experiment are shown in Figure 39. For this lower speed case, the maximum crack tip temperature increase was 57 K and was measured by detectors 7 and 8. In this case, the crack propagated virtually in the middle of the gap between detectors 7 and 8. Flanking elements 6 and 9 also have similar signals, as do elements 5 and 10. The crack propagation gage registered the presence of a disturbance at $196 \mu\text{s}$ in Figure 39, well ahead of the peak temperature. Attempts to capture the temperature field for a crack propagating slower than 450 m/s were unsuccessful because impact speeds less than 25 m/s were unable to initiate a crack in the ductile PC.

The approximate temperature beyond which the molecular chains of an amorphous polymer begin to move (albeit in a highly viscous manner) is the glass transition temperature, T_g . For PC, the temperature increase above room temperature necessary to reach T_g is 125 K. The temperature increase measured at the tip of a mode I crack propagating at a speed of $0.55 c_R$ was 105 K, just below T_g .

There is a noticeable difference in the rise time of the temperatures presented in Figures 37 and 39. Because the crack tips were propagating at different speeds for these two figures, a direct comparison of rise time is inappropriate. A valid comparison can be made after the time scales in Figure 37 and 39 have been converted to length, which is discussed next.

The physical size of the regions where crack tip plasticity and internal heat generation occur is crucial to developing an understanding of the process zone for high-speed crack propagation. The size of these regions can be determined through the temperature measurements given their dissipative nature. Determination of physical size entails a measurement of the length along the

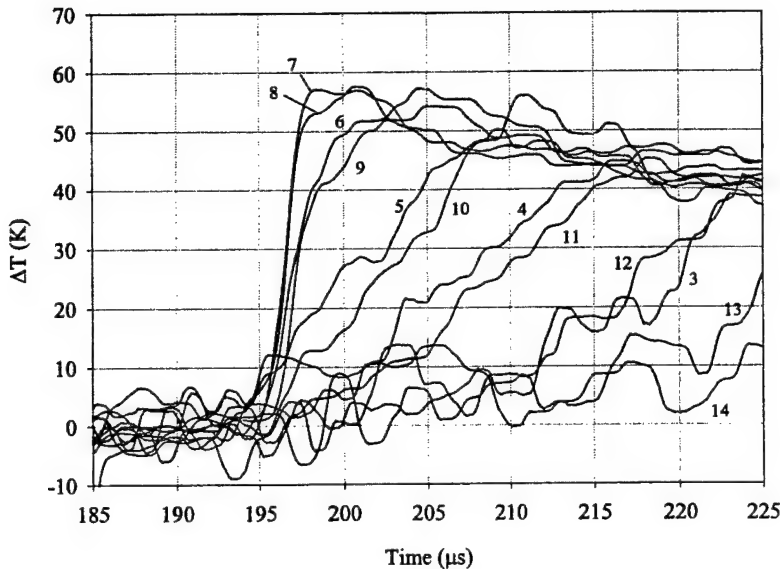


Figure 39. Thermal detector output (after calibration) for opening mode fracture of PC with a crack tip speed of $0.45 c_R$.

propagation direction as well as a dimension transverse to crack tip motion. The infrared detector monitors the temperature field surrounding a propagating crack tip with a series of closely spaced detectors oriented transversely to the crack propagation direction. The spacing of the detector elements in the array provides the transverse dimension of the thermal field. The lengthwise dimension can be obtained by a time-length transformation exploiting a steady-state crack growth assumption. For a constant crack tip speed, \dot{a} , the transformation of time to length is given by

$$\xi = \dot{a}t, \quad (27)$$

where ξ is length and t is time. This transformation was applied to the PC temperature data shown in Figures 37 and 39 to convert the time scales to length. Contours of the temperature field were then constructed knowing the vertical spacing of the detector elements in the array. The temperature contours for the high- and low-speed PC experiments are shown Figures 40 and 41, respectively. A violation of the steady crack growth assumption used in equation (27) would affect only the length of the contours in the propagation direction; the vertical dimensions would not be affected. The peak temperature is indicated by the left side of a horizontal dashed line included in the figures. It should be kept in mind when looking at the contour figures that the vertical distance between adjacent detector element centers is 0.10 mm, and only the region near the crack tip is shown. The ductile nature of PC is evident by the large region of temperature increase surrounding the crack tip in Figures 40 and 41, suggesting that plastic deformation is a significant thermal dissipation mechanism. The

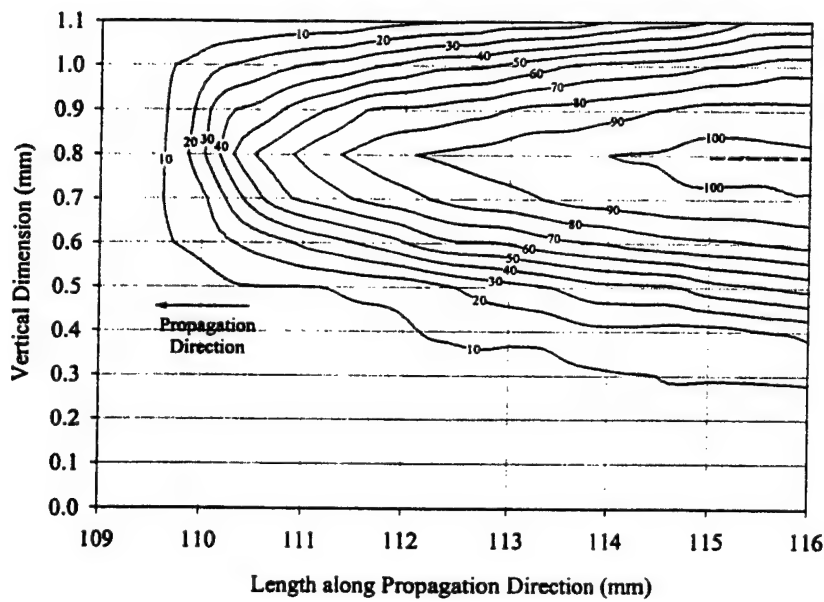


Figure 40. Temperature contours for opening mode fracture of PC with a crack tip speed of $0.55 c_R$. The large lateral span on the heat-affected region suggests plastic deformation is a significant heating mechanism near the propagating crack tip.

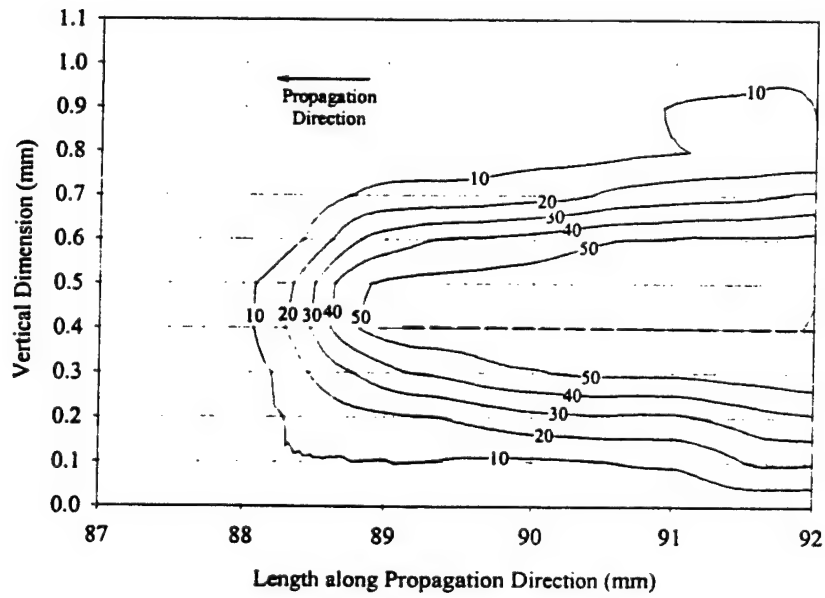


Figure 41. Temperature contours for opening mode fracture of PC with a crack tip speed of $0.45 c_R$. The lateral span on the heat-affected region is smaller than the higher speed crack tip experiment.

lateral span of the heat-affected zone in the high-speed case is ~ 1 mm, whereas the width for the lower speed case is about 0.65 mm. The length of the zone is shorter for the lower speed case as well. These two experiments indicate that the thermally dissipative zone at the tip of a crack propagating in PC increases in size as the crack speed increases. This will be discussed further in section 3.5.

An estimate of the plastic deformation zone can be made using the asymptotic nature of the crack tip stress and the measured energy release rate. Anderson (1995) presents an analytic expression for the size of the crack tip plastic region for an elastic-plastic material under plane stress quasi-static mode I loading as

$$r_p = \frac{1}{\pi} \left(\frac{K_I}{\sigma_y} \right)^2, \quad (28)$$

where r_p is the radius of the plastic zone, K_I is the quasi-static mode I stress intensity factor, and σ_y is the yield strength of the elastic-plastic material. An estimate of the plastic zone size will be made by replacing the quasi-static stress intensity factor with a dynamic value. The relationship between the dynamic energy release rate and the dynamic stress intensity factor was given by equations (18) and (19). The dynamic energy release rate measured for a crack propagating in PC with a speed of 550 m/s was 6600 J/m². Using the material properties for PC in Tables 2.1 and 2.2 and a yield stress of 70 MPa (see Figure 6), the radius of the plastic zone is estimated by equation (28) as 0.7 mm, giving a total lateral span of 1.4 mm. The predicted lateral span compares to a heat-affected zone shown in Figure 40 of about 1 mm. Given that equation (28) is an engineering approximation, the two measures of plastic-zone size are in reasonable agreement.

3.4.2 PMMA Experiments

Figure 42 shows the temperature variation obtained from a crack propagating at $\sim 0.55 c_R$ in high MW PMMA. As was the case for PC, dissipative heating due to stress wave propagation was not observed. The maximum temperature increase recorded here was 66 K. Despite the fact that PMMA is brittle at room temperature, the temperature curves have the same general characteristics as those observed for PC. In this case the crack tip passed near detector element 11. Note, however, that the detector elements immediately flanking element 11 (i.e. elements 10 and 12) respond slower and reach a lower peak temperature than the corresponding ones in PC (i.e., elements 10 and 12 in Figure 37). This suggests a more localized thermal signal in the case of PMMA. Spatial resolution of the detector array becomes an issue for localized thermal sources, such as that found

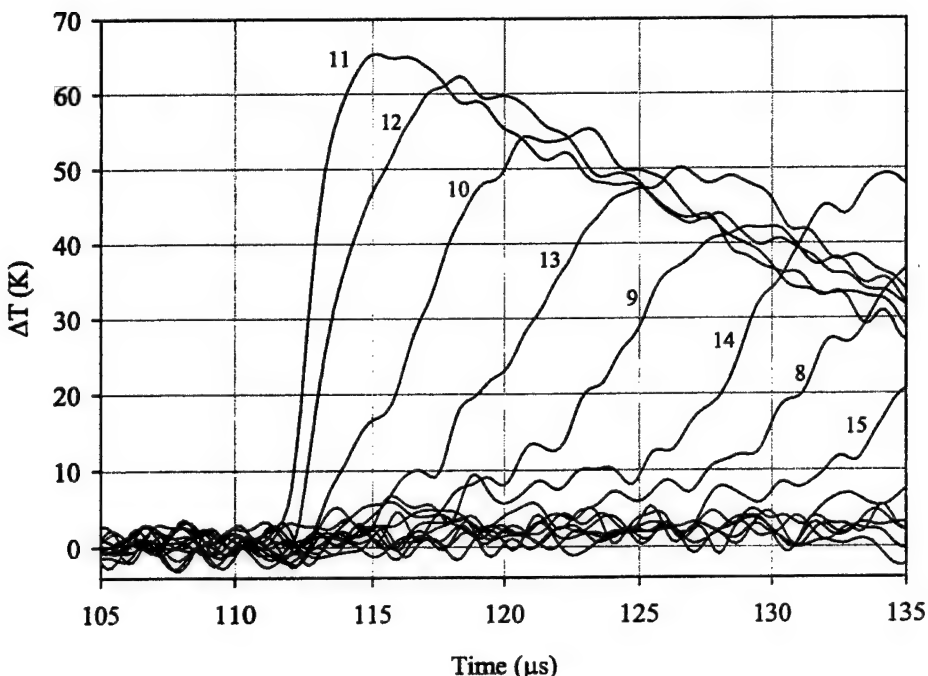


Figure 42. Thermal detector output (after calibration) for opening mode fracture of PMMA with a crack tip speed of $0.55 c_R$.

for PMMA. If the source is small enough, it could pass between two adjacent detector elements and only its thermal wake would be sensed. This is illustrated in Figure 43, which shows the temperatures recorded for an experiment similar to the one shown in Figure 43, except this time, the thermal source propagated between two detector elements instead of directly across an element.

As opposed to PC, it was possible to dynamically propagate cracks in PMMA at a relatively slow speed. A projectile impact speed of 8 m/s was sufficient to cause a constant crack growth speed of 250–300 m/s (0.20–0.24 c_R). The temperature curves for a PMMA experiment with a crack propagating 250 m/s are shown in Figure 44. A maximum temperature increase of 23 K was registered by detector element 9. Flanking detector elements did not begin to register any temperature increase until after the peak temperature on element 9 was obtained. This indicates that the thermal source responsible for the temperature increase had a lateral span (dimension along the detector array direction) approximately the same as a single detector element or less. This will be shown more precisely later when looking at the temperature contours surrounding the crack tip. The flanking elements detected the passage of the crack faces as the crack opened. Using the present loading system, it was not possible to dynamically propagate cracks in PMMA slower than 250 m/s.

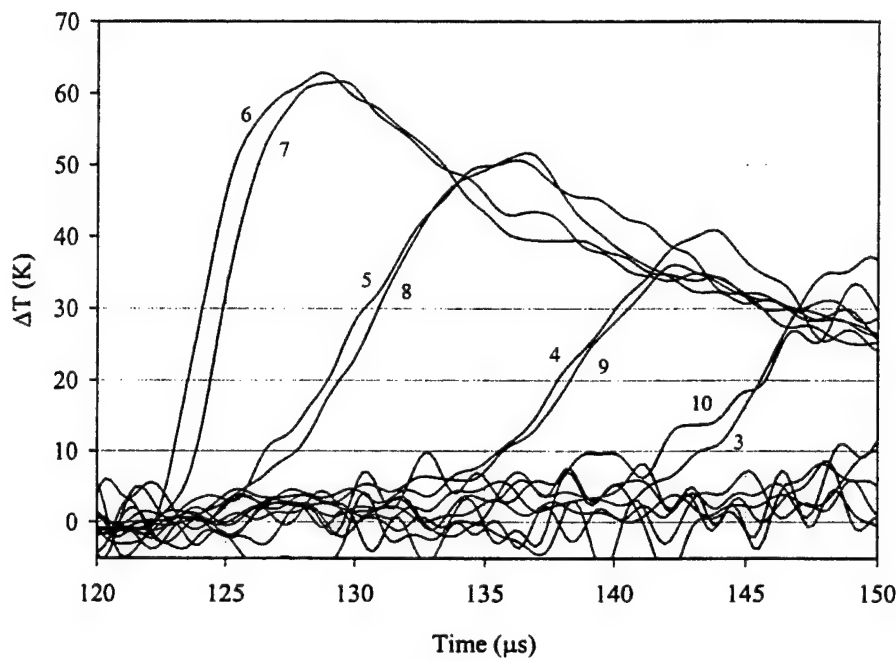


Figure 43. Thermal detector output (after calibration) of opening mode fracture of PMMA with the crack tip propagating between two detector elements.

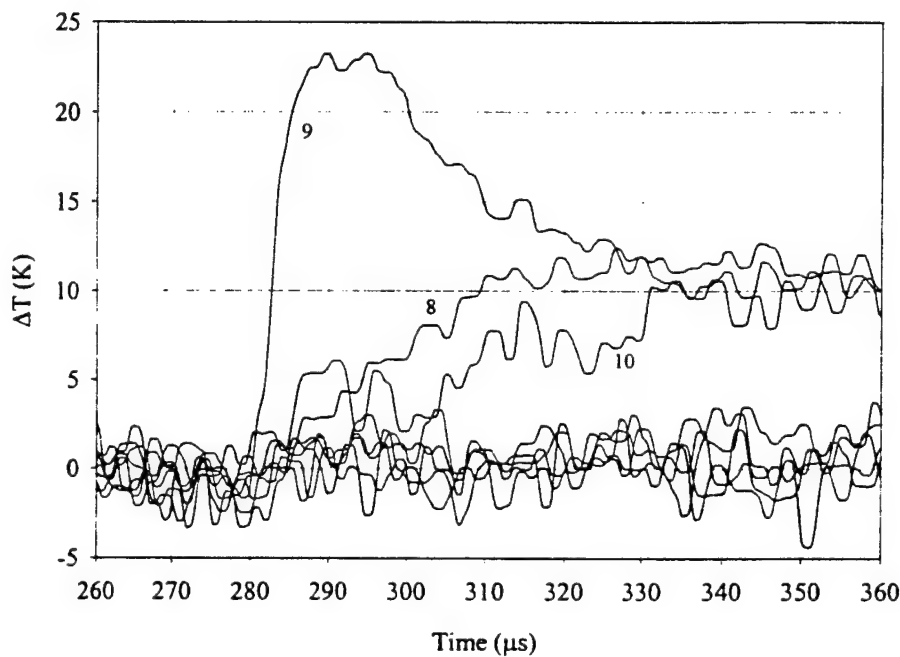


Figure 44. Thermal detector output (after calibration) for opening mode fracture of PMMA with a crack tip speed of $0.24 c_R$.

The thermal signal for a crack propagating at low speed in low molecular weight PMMA is shown in Figure 45. Although the speed was not measured directly, it was estimated to be ~ 300 m/s by observation of the resulting fracture surface (discussed in section 3.6). The maximum temperature increase measured for this material was only 8 K, and only one detector element sensed the passage of the crack tip. With such a low-temperature increase, the signal-to-noise ratio of the detector output is very low. For this reason, only the detector that responded to the crack passage is shown in Figure 45. Note that the signal shown is also quite noisy. The recorded temperature for the low molecular weight PMMA was only 35% that of the high molecular weight PMMA under similar crack growth conditions. This limited data set suggests that the magnitude of the temperature field surrounding a propagating crack is dependent on molecular weight and is consistent with the trend Döll (1976) found to exist between energy release rate, G , and molecular weight.

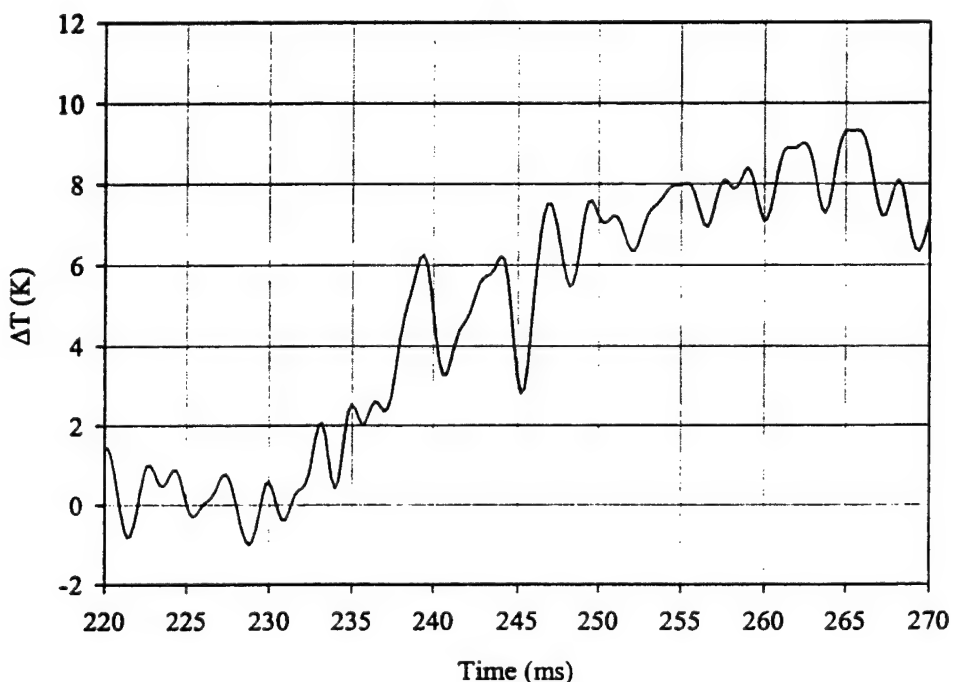


Figure 45. Thermal detector output (after calibration) for opening mode fracture of low molecular weight PMMA with a crack tip speed of $0.24 c_R$.

A final series of experiments using PMMA was performed with the detector array rotated to a horizontal position. This was done to monitor the thermal source at various locations along the propagation direction instead of perpendicular to it, and as such, it provided a measure of crack tip speed. These experiments required many repetitions because the crack path deviation had to be within $80 \mu\text{m}$ for the array to register its passage. The results from an

experiment for which the projectile-impact speed was 25 m/s are presented in Figure 46. The temperature from detector elements 2 and 15 are shown. Both elements detected a thermal source with a temperature increase of ~ 10 K, followed by a plateau and late time rise. Although the latter features of the signals are not well understood, the initial portion corresponds to crack tip passage. It is not known if the crack tip passed directly over the detector array or if it traversed slightly above or below. However, the measured temperature is lower than what had been recorded for experiments of similar impact speed, but with the detector array in the vertical position, suggesting that the crack tip was not directly over the array. Timing of the initial portion of temperature increase for each element indicated a crack tip speed of 400 m/s. The important aspect of Figure 46 is the qualitative agreement between the two signals, confirming the thermal source in PMMA does not fluctuate significantly.

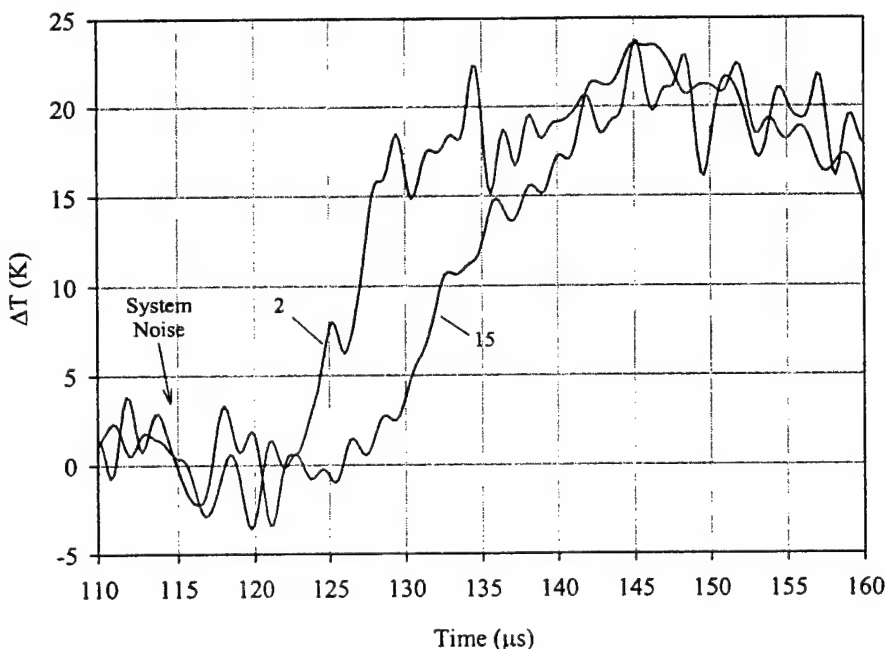


Figure 46. Thermal detector output (after calibration) for opening mode fracture of PMMA with the detector array rotated to the horizontal position. Crack tip may not have passed directly through the region monitored by the infrared detector system. Crack tip propagation speed is 0.57 c_r .

A temperature contour plot was generated for the PMMA high crack tip speed experiment shown in Figure 42 using the same procedure and assumptions used for generating the PC contour plots. The temperature contour for PMMA, shown in Figure 47, has a lateral span at peak temperature of ~ 0.3 mm (compared to 0.65 mm and 1 mm for PC). The region of temperature increase is more localized and will be shown in section 3.6 to correlate with crazing along

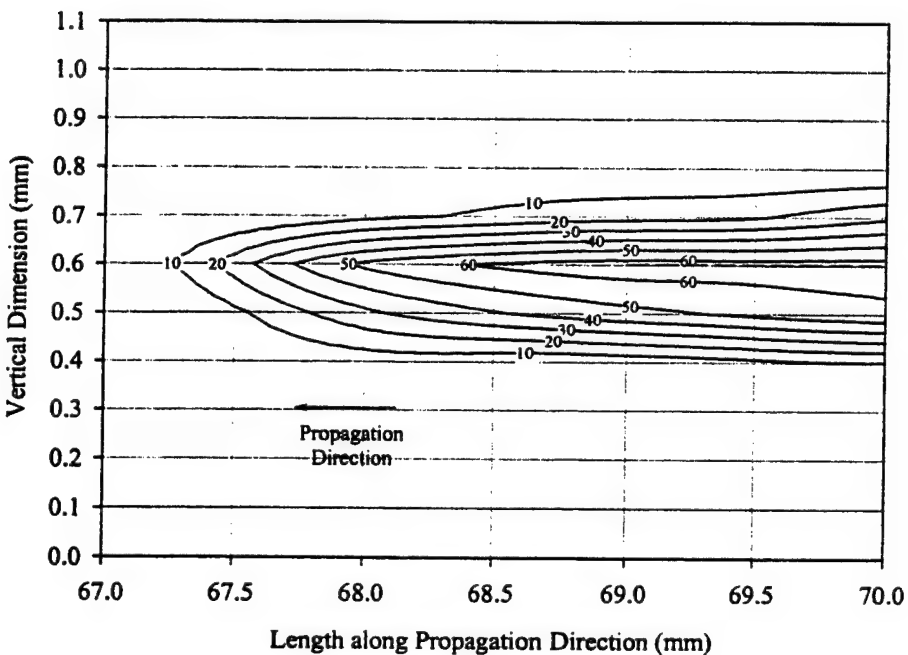


Figure 47. Temperature contours for opening mode fracture of PMMA with a crack tip speed of $0.55 c_R$. The contours are highly localized compared to those of PC, suggesting that plastic deformation does not contribute to the crack tip temperature increase.

multiple layers. A temperature contour plot could not be generated for the low-speed PMMA experiment because only one detector responded at the time of crack tip passage. Given this, the detected heat source may be smaller than the detector height (i.e., 0.08 mm), which will cause the temperature measurement system to underestimate the true temperature. This is because the detector element, being of finite size, averages the radiation incident over its entire area. This will be addressed in detail in section 6.

3.4.3 Discussion of Temperature Field Features

The temperature curves for both materials show a rise in temperature followed by a slower decrease. As suggested by Mason and Rosakis (1992), a likely reason for the decrease in temperature is crack opening. If the crack is assumed not to open and adiabatic conditions exist (due to the short times involved), the temperature curves would be expected to increase to a peak value and remain constant in the trailing thermal wake (as will be seen later in the shear-dominated fracture experiments where there is no crack face opening this is precisely what happens [see Figures 62a and 62b]). This would continue until sufficient time elapses for thermal conduction to occur. If, on the other hand, crack opening occurs, the temperature recorded would decrease as the detector

began to view the air gap between separated fracture surfaces. The detector element sequence for temperature decrease is consistent with this possible cause. The effect of crack face motion on the temperature measurements will be pursued in section 6.

There is an additional early time feature present on nearly all of the temperature curves. Immediately prior to the initial increase in temperature, a small amount of cooling was recorded. This was shown in Figure 38 for PC. The amount of cooling in PC was about 5 K. For PMMA, the decrease in temperature was less than 2 K and was barely discernable from signal noise. This is the thermoelastic cooling effect discussed in detail by Rittel (1998). It results from the large tensile triaxial stress state developed near the crack tip prior to initiation. The magnitude of the cooling observed in this study, however, is much smaller than the 60-K cooling discussed by Rittel (1998).

An estimate of the thermoelastic cooling can be made using the heat energy equation given by equation (5) in section 1. Considering only the elastic components and assuming adiabatic conditions, the heat energy equation simplifies to

$$\rho c_p \dot{T} = -\alpha(3\lambda + 2\mu)T_0 \dot{\varepsilon}_{kk}^e, \quad (29)$$

where the parameters were defined in section 1. The Lamé elastic constants λ and μ are related to material properties through the relations

$$\lambda = \frac{\nu E}{(1+\nu)(1-2\nu)}, \quad (30)$$

$$\mu = \frac{E}{2(1+\nu)}. \quad (31)$$

Integrating equation (29) and solving for the temperature increase, ΔT , yields

$$\Delta T = \frac{-\alpha(3\lambda + 2\mu)T_0 \varepsilon_{kk}^e}{\rho c_p}, \quad (32)$$

where the initial state of the fracture specimen was assumed strain free. Material strain is related to stress through the isotropic form of Hooke's law:

$$\varepsilon_{ij} = \frac{1+\nu}{E} \sigma_{ij} - \frac{\nu}{E} \delta_{ij} \sigma_{kk}, \quad (33)$$

where δ_{ij} is the Kronecker Δ function. The maximum amount of thermoelastic cooling will occur near the boundary between elastic and inelastic material behavior ahead of the propagating crack tip. Assuming plane stress conditions, the stress state at the location of maximum elastic stress will be $\sigma_{11} = \sigma_{22} = \sigma_c$, where σ_c is a critical stress, and the other stress components equal to zero. The

critical stress for PC is the yield stress, observed in the uniaxial stress-strain curve of Figure 6 to be ~ 70 MPa. For PMMA, the critical stress is the stress beyond which inelastic behavior occurs. This is discussed in detail in section 6, where a value of 120 MPa is used. These critical stresses were used in equations (32) and (33) to give an estimate of the amount of thermoelastic cooling for each material. Using a coefficient of thermal expansion of 65×10^{-6} K $^{-1}$ for PC and 70×10^{-6} K $^{-1}$ for PMMA (Domininghaus 1988) along with the material properties listed in Tables 1 and 2, the amount of thermoelastic cooling given by equation (33) was 1.8 K for PC and 2.6 K for PMMA. These estimates are near the values observed on the infrared detector signals and are considerably less in magnitude than the 60 K cooling reported by Rittel (1998).

The measured maximum temperature increase surrounding the opening mode crack tip in PMMA differs from that reported by Fuller et al. (1975), who cite a temperature increase at the crack tip of 500 K. The crack tip temperature was deduced by Fuller et al. (1975) using a single unfocused infrared detector along with a thermocouple and liquid crystal films. The actual temperature measurements were peripheral to the crack tip and did not constitute a temperature field measurement. A transient heat conduction analysis was used to deduce the crack tip temperature. This analysis required an estimate of the dissipation region responsible for heat generation, which Fuller et al. (1975) assumed to extend below the fracture surface by no more than 3 μm . With this assumption, Fuller et al. (1975) reported a temperature rise above room temperature of ~ 500 K for cracks propagating within a velocity range of 200–650 m/s. Results from the fracture surface micrography examination presented in section 3.6 indicate that the region responsible for heat generation during high-speed fracture in PMMA consists of multi-layered crazes that form a “craze band.” These features extend below the surface 100–200 μm for cracks that were near the terminal speed. This larger heat affected zone would significantly lower the estimated crack tip temperature if using the method of Fuller et al. (1975). The dependence of the technique used by Fuller et al. (1975) on the estimated craze width accounts for the discrepancy of their results with the more direct measurements performed in this study.

3.5 Thermal Dissipation of Mechanical Work

The heat energy equation given by equation (5) for an adiabatic event with negligible thermoelastic cooling reduces to the form

$$\beta\sigma_{ij}\dot{\epsilon}_{ij}^p + \dot{q} = \rho c_p \dot{T}, \quad (34)$$

with the parameters having been defined in section 1.2.2. The two quantities on the left hand side of equation (34) represent the heat generation due to plastic work ($\beta\sigma_{ij}\dot{\epsilon}_{ij}^p$) and the internal heat generation from a dissipative crack tip process zone (\dot{q}). As presented in Zehnder and Rosakis (1993), these quantities

can be extracted from the recorded infrared detector signals by numerically differentiating the temperature data and multiplying by the polymer specific heat and density (given in Table 2). This was done for four of the experiments presented in section 3.4, specifically the two PC experiments shown in Figures 37 and 39 and the high and low crack speed PMMA experiments shown in Figures 42 and 44. Numerical differentiation was performed on the temperature data using the following algorithm:

$$\dot{T}(t) \approx \frac{T(t_{i+1}) - T(t_i)}{t_{i+1} - t_i}, \quad (35)$$

where $T(t_{i+1})$ and $T(t_i)$ are the temperatures corresponding to the times t_{i+1} and t_i , and i signifies the sequential ordering of temperature with time. Differentiation using equation (35) was a trivial matter because the data was collected with a digital storage oscilloscope and stored as a sequence of time-temperature pairs.

The large lateral span of the temperature contours for PC, shown in Figures 40 and 41, is indicative of significant plastic deformation. As such, the plastic work rate was assumed to be the only dissipation term for PC. A value of 0.5 was assumed for β (Li and Lambros 2001). Contours of plastic work rate for the high and low crack speed PC experiments are presented in Figures 48 and 49. Increasing the crack propagation speed from 450 to 550 m/s results in the plastic work rate zone increasing in size. The peak work rate was 94×10^{12} J/m³s for the low-speed case and 106×10^{12} J/m³s for the high-speed experiment. The lateral span increased from 0.3 mm to ~ 0.42 mm as the crack speed increased from 450 to 550 m/s. The length of the plastic work rate region increases as well.

The highly localized temperature signals recorded for PMMA suggest that plastic deformation is not a dominant dissipative mechanism associated with fracture of PMMA. For a purely brittle material, all of the fracture energy is used to create new surfaces. Under these conditions, $G = 2\gamma$, there is no excess energy available to dissipate as heat. Yet, opening mode dynamic fracture of brittle PMMA did result in crack tip heating. This suggests that the internal heating term \dot{q} , is of appreciable magnitude in equation (34). Given this, internal heating was assumed to be the sole contributor to thermal heating for PMMA when calculating the dissipation terms in equation (34). A contour plot of the rate of internal heating for the PMMA high crack speed experiment is shown in Figure 50. The maximum rate of heat generation is 75×10^{12} J/m³s, and the width of the zone is ~ 100 μ m. The low crack speed PMMA experiment resulted in only one detector element sensing the passage of the crack tip. Although the rate of internal heat generation could be determined, a contour plot could not be constructed. Moreover, the fact that only one detector responded implies that the size of the thermally active region is at most 80 μ m, (i.e., one detector element

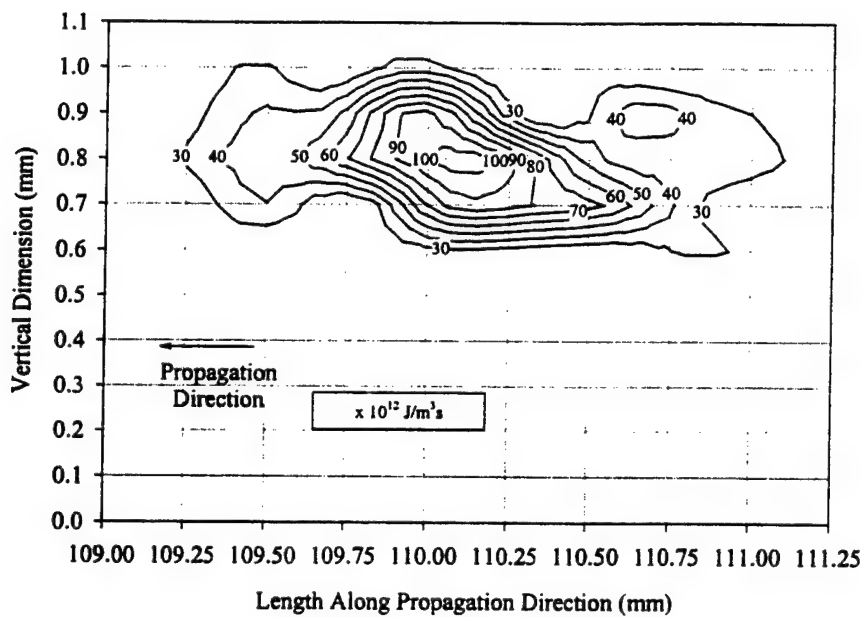


Figure 48. Rate of plastic work contours for opening mode fracture of PC with a crack tip speed of $0.55 c_R$. The heat source was assumed to be only ductile plastic deformation with a β of 0.5.

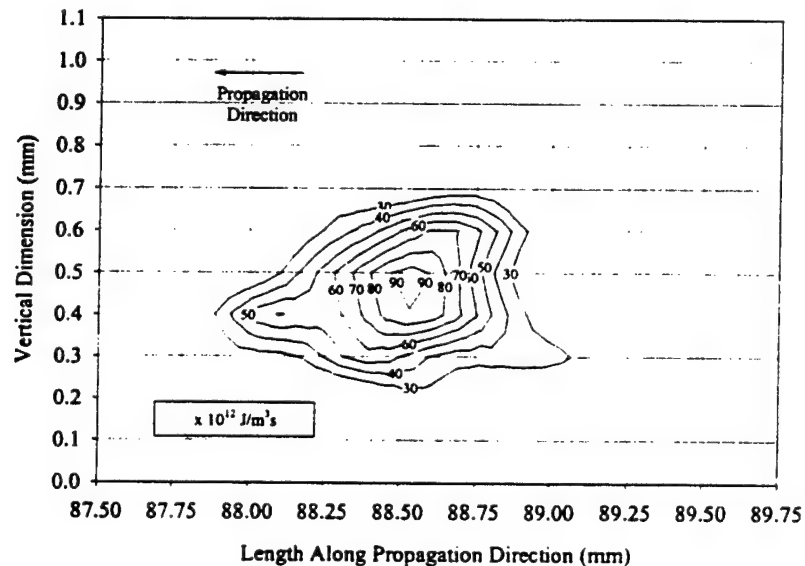


Figure 49. Rate of plastic work contours for opening mode fracture of PC with a crack tip speed of $0.45 c_R$. The heat source was assumed to be only ductile plastic deformation with a β of 0.5. The span of the contours are smaller than for the higher crack tip speed experiment, illustrating the influence of crack propagation speed.

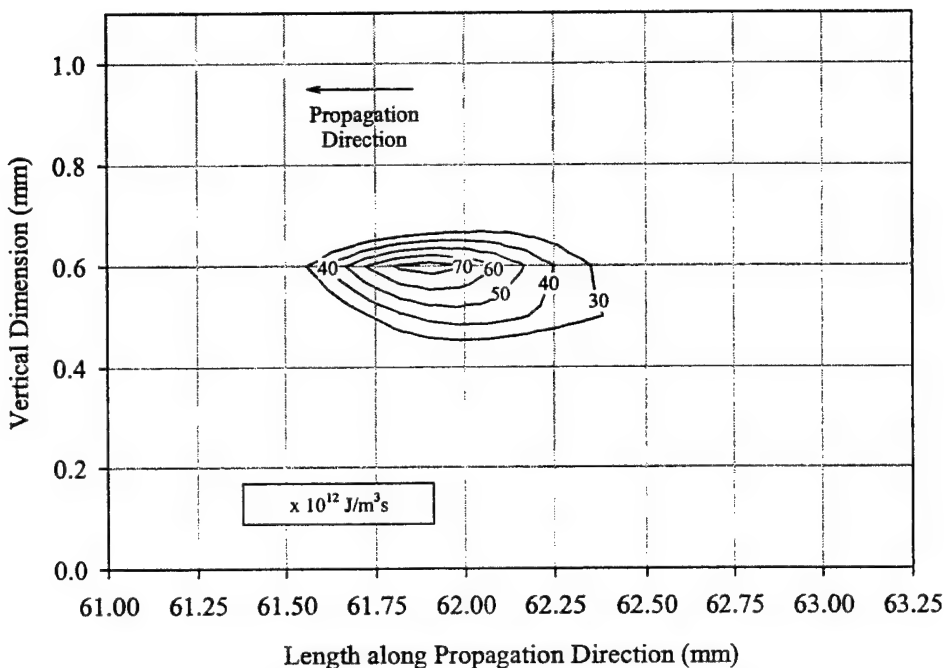


Figure 50. Rate of internal heat generation contours for opening mode fracture of PMMA with a crack tip speed of $0.55 c_R$. Internal heating was assumed to be the only source of crack tip heating.

height). The maximum rate of heat generation for this case was $11 \times 10^{12} \text{ J/m}^3\text{s}$. A 60% reduction in crack tip speed reduced the magnitude of the internal heat source by $\sim 85\%$. However, a word of caution is due here. The high-speed PMMA case resulted in a heat-affected region larger than one detector element (as shown in the temperature contour plot in Figure 47). The heat source responsible for the temperature field will be shown in the next section to be from multilayered crazing. The low-speed PMMA experiment showed a temperature field that was more localized. Only one detector element responded. This situation must be treated with caution. The heat source may be smaller than the detector area, which will cause the temperature measurement system to underestimate the true temperature. This is because the detector element, being of finite size, averages the radiation incident over the entire detector area. This will be addressed in detail in section 6. The calculated rate of internal heating ($11 \times 10^{12} \text{ J/m}^3\text{s}$) may also be incorrect because the temperature may be underestimated. If the thermal source is smaller than the detector element size, the internal heating rate will be higher than calculated here.

Comparing the general features of the heat source contours of PC and PMMA reveals a fundamental difference in their structure. The PC contours have significant lateral span, whereas the PMMA contours are much more localized.

This is further evidence that the crack tip process zone for PMMA does not have significant plastic deformation associated with it, whereas the opposite is true for PC. The next section will present the findings from a detailed examination of the resulting fracture surfaces for both materials and will add yet additional evidence of the mechanisms associated with the crack tip process zones.

3.6 Fracture Surface Micrography

The fracture surfaces resulting from high-speed crack growth in both polymers were glassy smooth in appearance near the starter notch tip and became increasingly rough farther from the notch as crack tip speed increased, consistent with the observations of Döll (1989) for accelerating cracks. A photograph of typical fracture surfaces for high-speed crack growth in PC is shown in Figure 51. The PC fracture surface clearly shows the rough region to be confined to the middle of the specimen thickness where a state of plane strain existed during fracture. The region near the surface monitored by the infrared detector remained smooth. Kambour (1964) associated the glassy smooth region with the formation of a single polymer craze. Scanning electron microscope images (SEM) of the smooth and rough regions of the PC fracture surface are shown in Figure 52. The smooth surface shown in the bottom image of Figure 52 is essentially flat and featureless, confirming that it was formed by a single craze. Because this is the region viewed by the infrared detector system, the large heat-affected region for PC is likely from high-rate plastic deformation only. An image of the rough region is shown on the top of Figure 52. This portion of the fracture surface shows multiple layers of material to have partially separated by layered crazing and then deformed by what appears to be gross-plastic deformation. Given the limited depth of focus of the infrared detector optics, it is unlikely that the detector observed this event. The images do suggest that the detector sensed the plastic deformation occurring ahead of the crack tip and the crazing process along a single plane.

The evolution of fracture surface roughness for the high-crack growth speed PMMA specimen, shown in the photograph of Figure 53 was quite different than was observed for PC. The transition from smooth to rough occurred somewhat uniformly through the specimen thickness i.e., the rough region was not confined to the middle of the thickness as it was for PC. SEM images of the smooth and rough fracture surface regions for PMMA are shown in Figure 54. As was the case for the smooth PC fracture surface, the smooth region for PMMA is featureless and is consistent with the formation of a single craze. When capturing the thermal signals for the high-crack speed case, the detector monitored a location on the specimen where the fracture surface was rough. Using an optical microscope, the PMMA fracture surface roughness near the region of infrared observation was measured to be ~ 0.10 mm. This roughness

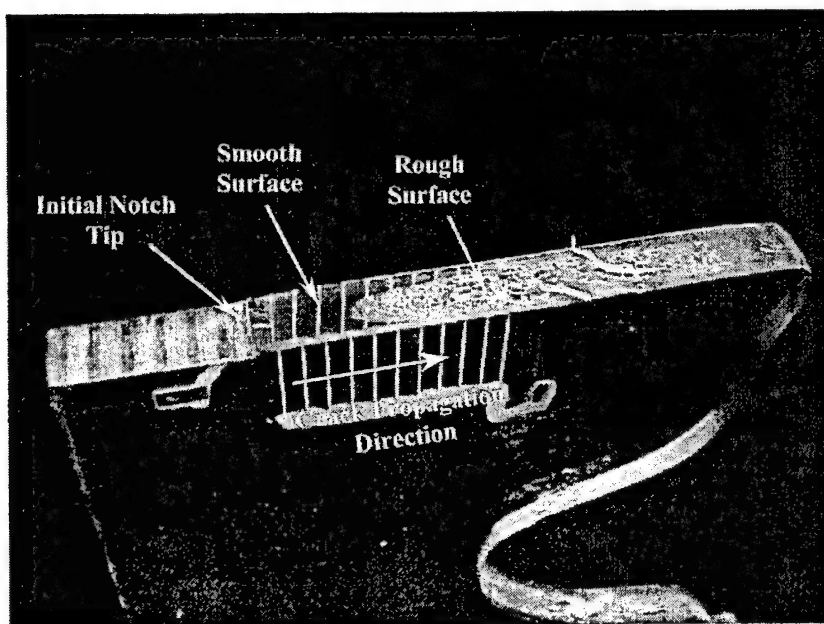


Figure 51. Photograph of PC fracture surface showing unique regions of smooth and rough surface texture.

was due to the development of multiple craze fronts below the exposed surface. Sharon et al. (1996) reported an increasing degree of microcracking in their high crack speed PMMA experiments, which is consistent with this observation. The SEM picture of this region, shown on the top of Figure 54, was taken at 45° to the fracture surface and shows these multiple craze fronts and the surface roughness that their interaction has produced. The inset for the rough region image shows the surface of one of the resulting multiple craze layers. The partially removed layers do not show signs of plastic deformation as was observed for PC. The pair of mating PMMA fracture surfaces thus indicate that the dynamic fracture process zone responsible for multiple crazing has a width of about $100\text{--}200\text{ }\mu\text{m}$. Because PMMA exhibits little ductility at room temperature, it would be expected that any thermomechanical heating in this case would be limited only to this $100\text{--}200\text{ }\mu\text{m}$ "craze band." The temperature and internal heating contours shown in Figures 47 and 50 are consistent with this explanation.

In addition, the experiments that produced low-crack tip speeds (250 m/s) yielded fracture surfaces that were completely smooth, the crack tip never entered the speed regime that causes surface roughness. Figure 55 shows a photograph of this glassy smooth surface that corresponds to the passage of one single craze. Recall that in these experiments only one detector responded. Given this, it is possible that in these experiments, the craze lateral width was

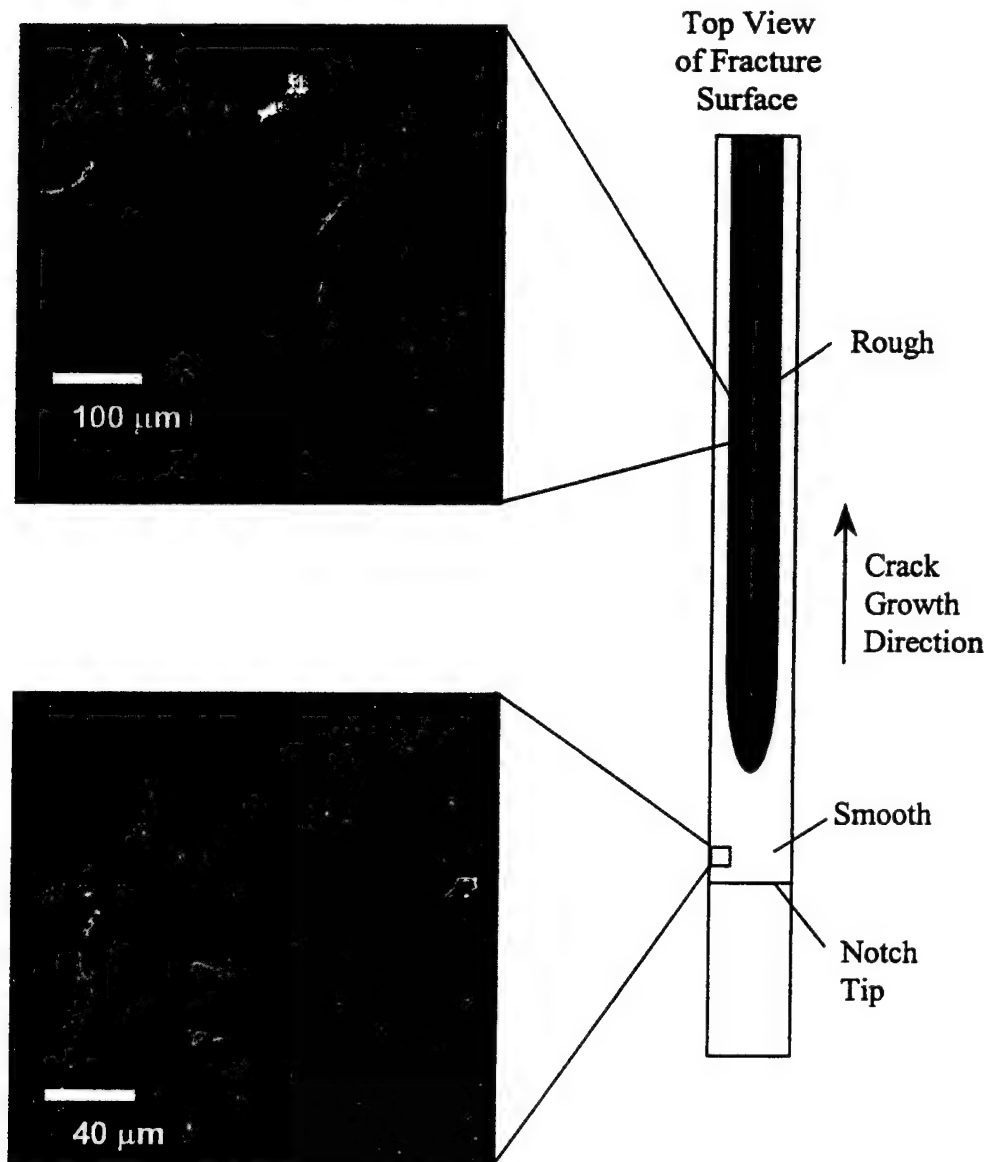


Figure 52. SEM images of the smooth and rough regions of a PC fracture surface. The crack propagated from the bottom of the figure to the top.

less than 80 μm , the size of a single detector element. If this was in fact the case, the temperature reported for the slow-speed PMMA experiment is an underestimate because the detector element output is proportional to the radiation falling upon its total area. The true temperature could be calculated only if the lateral width of the craze was known. This is discussed further in section 6.

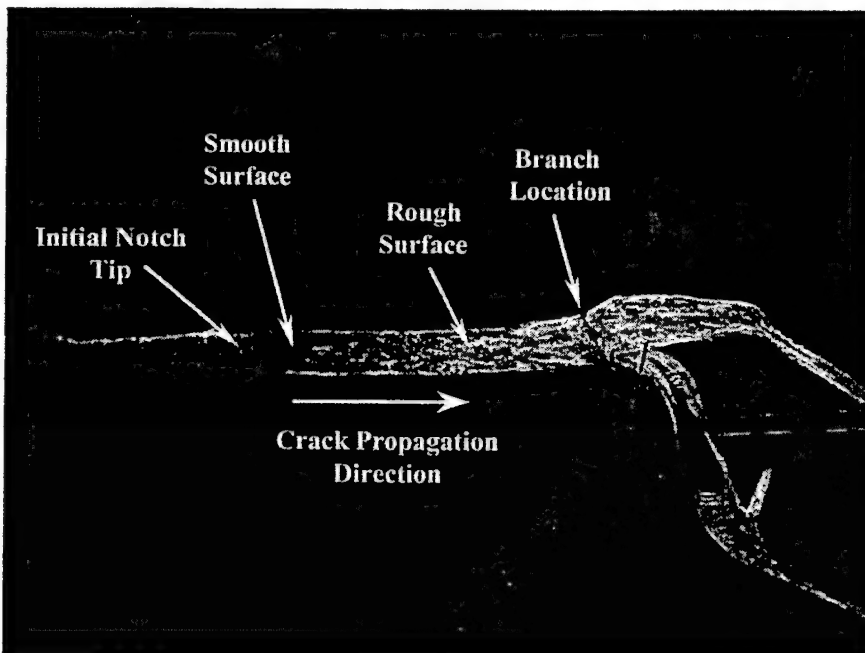


Figure 53. Photograph of a PMMA fracture surface showing the transition of surface roughness and eventual branching.

The fracture surfaces for the low molecular weight PMMA were qualitatively the same for all crack speeds as discussed above, except the onset of microcracking and crack-branching occurred earlier. The observations described above enabled an estimate of crack tip speed to be made based on the appearance of the fracture surface for polymer specimens that were not instrumented with a crack propagation gage.

3.7 Additional Comments on Opening Mode Crack Tip Behavior

To complete the discussion of opening mode fracture behavior of PC and PMMA, the dependence of crack tip temperature on the dynamic energy release rate is obtained, followed by a brief summary of the crack tip process zone mechanisms. The dependence of the maximum recorded temperature change on crack tip propagation speed is shown in Figure 56 for both PC and PMMA. The maximum crack tip temperature increase that was recorded is plotted as a function of the crack tip speed, \dot{a} , normalized by c_s for each material. The data indicate a trend of increasing crack tip temperature with increasing speed. A similar result was observed in metals by Mason and Rosakis (1992) and is consistent with the trend of increasing energy flux into the crack tip process zone with increasing crack speed in PMMA reported by Sharon et al. (1996). However, Sharon et al. (1996) noted that near the terminal crack tip speed, increasing the energy flux into the crack tip did not result in a commensurate increase in crack tip speed. Instead, they found that energy was dissipated in the

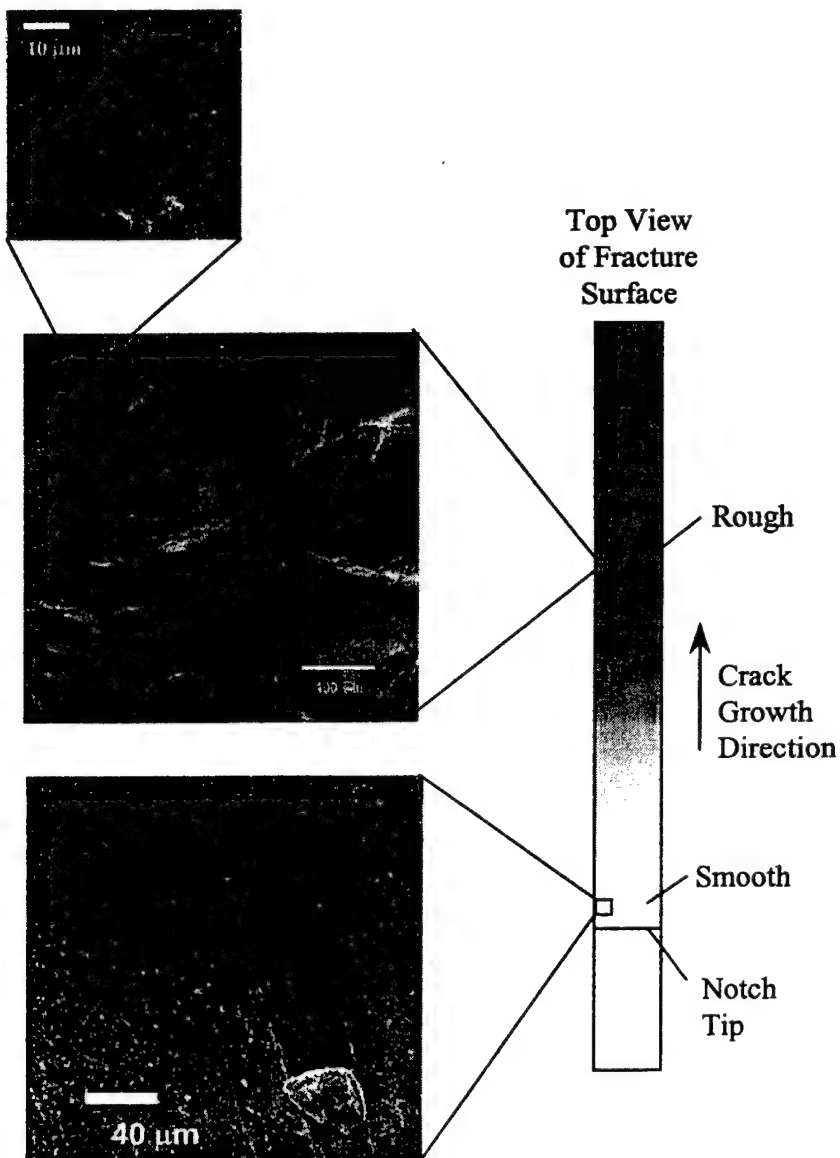


Figure 54. SEM image of the smooth and rough regions of a high-speed crack growth PMMA fracture surface. The crack propagated from the bottom of the figure to the top. The rough region has a surface roughness of about 100–200 μm .

form of new surface creation (microcracking in the case of PMMA), thereby limiting the maximum achievable crack tip speed. As discussed in section 3.1, Sharon et al. (1996) measured a sixfold increase in surface area from the microcracking. For a perfectly brittle material, all of the fracture energy is used to create new surfaces. However, Sun and Hsu (1996) noted that the energy needed for fracture in some nominally brittle materials is several orders of magnitude greater than the surface energy. Despite the increase in surface

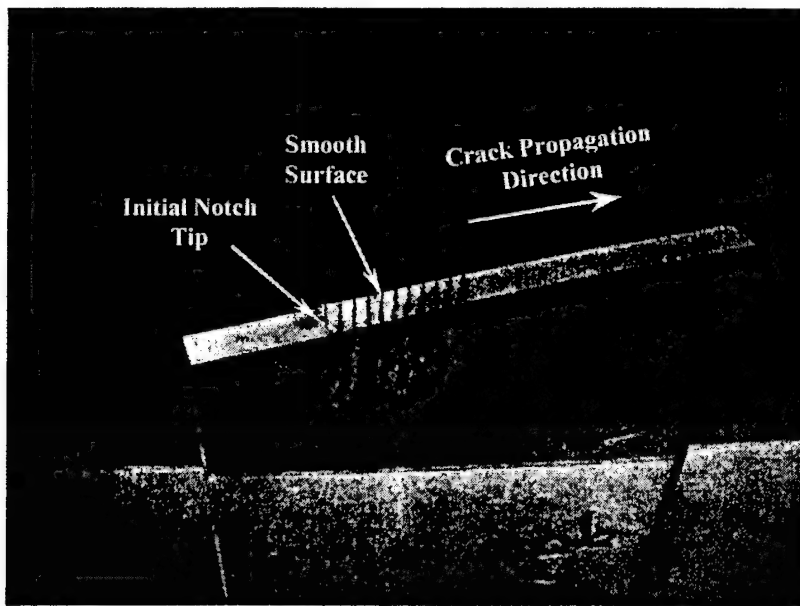


Figure 55. Photograph of a low-speed crack growth PMMA fracture surface showing a glassy smooth surface corresponding to the passage of a single craze.

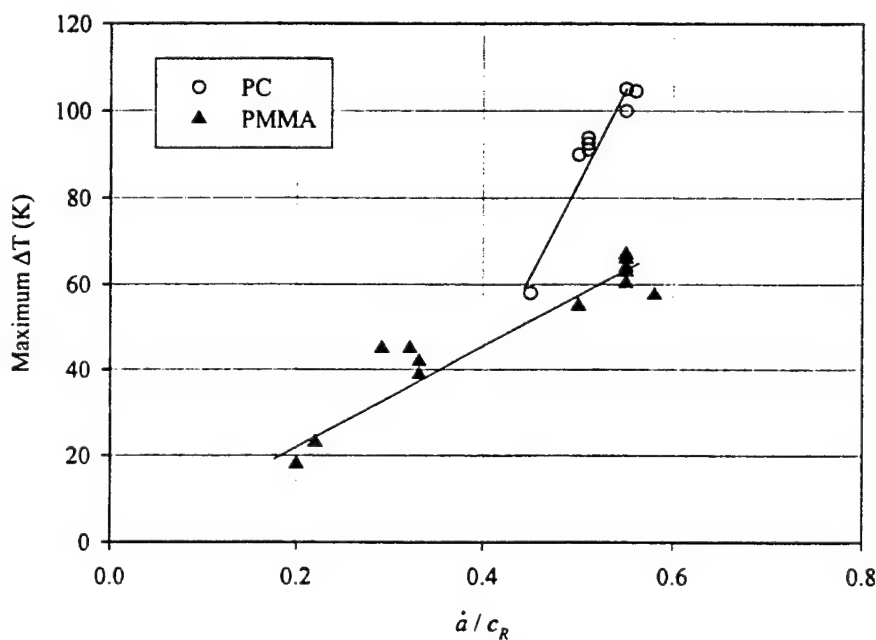


Figure 56. Opening mode maximum crack tip temperature as dependent on crack tip speed.

energy requirements due to microcracking, there is still a significant excess of fracture energy. The opening mode temperature data indicate that the increase in energy flux to the crack tip goes into more than just creating new surfaces, as stipulated by Sharon et al. (1996), but is also dissipated as heat. This is illustrated in Figure 57 which shows the relation between the maximum temperature increase with a dynamic energy release rate for PMMA. This curve was generated by combining polynomial curves that were fitted to the data presented in Figures 36 and 56. No line is shown for PC because of the limited dynamic energy release rate data available (see Figure 36). The rate of temperature increase for PMMA becomes less as G is increased. It is speculated that this occurs because some of the available energy is diverted into creating an increasing number of microbranches and also because the temperature is approaching the material glass transition temperature. The trend observed in Figure 57 establishes a link between the dissipation of heat in a craze-dominant crack tip process zone and the amount of energy flowing into the process zone.

The process zone at the tip of a propagating crack in PC appears to contain a single craze preceded by gross-plastic deformation. The middle of the specimen thickness shows evidence of multiple craze layers with plastic deformation occurring within the craze region. As the crack tip speed increases towards a limiting speed of $0.55 c_R$, the rate of energy dissipated as heat increases slightly but the process zone itself increases in size, yielding a net increase in crack tip temperature. For low-speed crack growth in PMMA, the crack tip process zone consists of a single craze. As the crack tip speed increases and more energy flows into the process zone, the single craze crack tip changes to one consisting of layered, multiple crazes propagating simultaneously.

The question of how much heating in PC can be attributed to plastic work will be addressed in section 5, where results from the experiments presented in this section will be combined with explicit finite-element simulations of a dynamic crack growth event. The opening mode PMMA results will be used in section 6 to build a crack tip thermomechanical constitutive model, or cohesive zone, for high-speed crack propagation in PMMA. The data and insights presented in this section are critical to these endeavors.

4. Shear-Dominated Fracture Experiments

4.1 Introduction

Shear-dominated dynamic crack propagation has been the focus of numerous studies in recent years, on the basis of the realization that shear-dominated crack

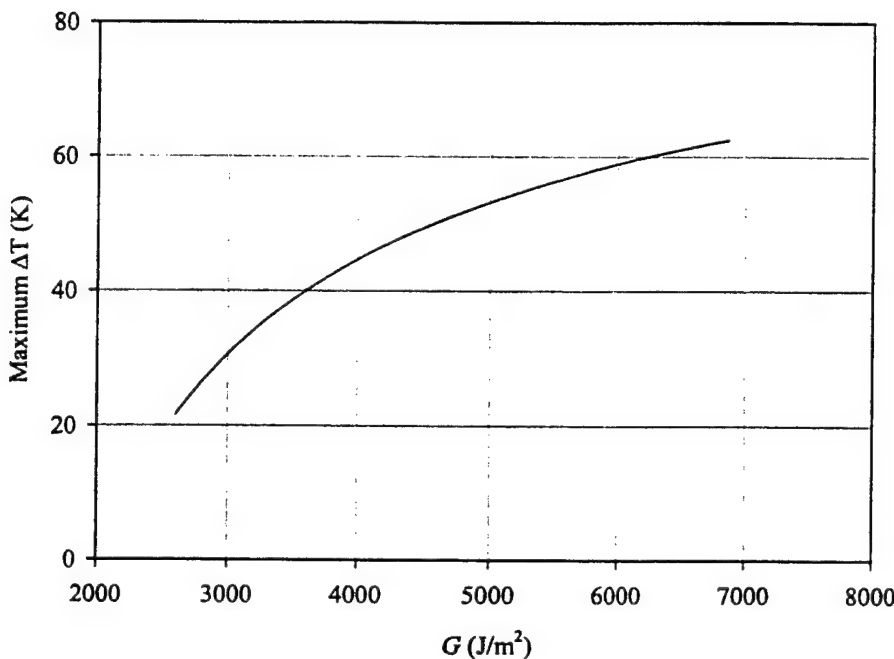


Figure 57. Empirical relationship between maximum crack tip temperature and dynamic energy release rate for opening mode fracture of PMMA.

growth is possible in materials possessing inhomogeneous toughness variation (e.g., interfaces) and/or under large confining pressure (e.g., earthquake events). In a material of homogeneous toughness, mode II loading has been observed to cause a crack to immediately kink and propagate at an angle of $\sim 70^\circ$ relative to the initial crack line. Such crack kinking under dynamic shear conditions can, however, be suppressed.

As discussed in section 1, several approaches have been successfully used to suppress crack kinking, allowing the initiation and growth of dynamic shear cracks in laboratory situations. The method for suppressing crack kinking used in the present study is to introduce a line of weakened material, effectively reducing the shear fracture toughness along that line. This approach has been used successfully by Rosakis et al. (1999) and Ravi-Chandar et al. (2000). Rosakis et al. (1999) were able to generate shear-dominated dynamic fracture of weakly bonded Homalite 100 panels. Bonding was achieved by allowing partial healing of the interface between the two panels. Techniques for interface healing are described by Wool (1995). In contrast, geometric weakening was implemented by Ravi-Chandar et al. (2000), who machined grooves along the sides of edge cracked panels of PMMA, thereby providing a preferred crack propagation path. Asymmetric loading for the Rosakis et al. (1999) and Ravi-Chandar et al. (2000) experiments was achieved using a configuration similar to the Kalthoff and Winkler (1987) configuration discussed in section 1. Crack tip speeds between

the shear and dilatational wave speeds were observed for the experiments of both Rosakis et al. (1999) and Ravi-Chandar et al. (2000). In addition, the fracture surfaces from the PMMA experiments of Ravi-Chandar et al. (2000) showed signs of polymer melting. The shear-dominated fracture experiments of Rosakis et al. (1999) also recorded a peculiar phenomenon occurring at the crack tip: the existence of a finite-contact region immediately behind the advancing crack tip, speculated to be crack face frictional sliding. The limiting speed for mode II crack growth was studied by Andrews (1976) and Burridge et al. (1979) using numerical techniques. Both of these studies modeled the material along the intended crack path with a cohesive traction law that in effect introduced a weakened interface. Andrews (1976) found the crack tip speed to be limited to $\sqrt{2}c_s$. Burridge et al. (1979) found conditions for stable crack growth to exist for $\sqrt{2}c_s < \dot{a} < c_d$, unstable conditions for $\dot{a} < c_R$ and $c_s < \dot{a} < \sqrt{2}c_s$, and a forbidden crack speed regime of $c_R < \dot{a} < c_s$. The experiments of Rosakis et al. (1999) using panels Homalite and Ravi-Chandar et al. (2000) using PMMA resulted in a stable crack speed near $\sqrt{2}c_s$.

Motivated by the observations of surface melting observed by Ravi-Chandar et al. (2000), the work presented in this study provides the first-ever measurement of the thermal dissipation associated with shear-dominated fracture in polymers. It was mentioned in section 1 that thermocouple probes have been used to measure the temperature at a single location during the propagation of an adiabatic shear band in PC (Rittel 2000). The work documented in this section goes well beyond previous studies by providing high resolution real-time multi-point measurements of temperature surrounding the propagating crack tip. These measurements render significant insight of the crack tip process region for shear-dominated fracture.

4.2 Crack Tip Speed Measurements

The experiments of Ravi-Chandar et al. (2000) and Rosakis et al. (1999), along with the computations of Andrews (1976) and Burridge et al. (1979), indicate that intersonic crack tip speeds are possible for a dynamically propagating shear crack. Given this possibility and the desire to quantify the crack tip kinematics associated with crack tip heating, the crack tip speed was determined for the shear-dominated fracture experiments. Crack tip speed was measured in a way similar to the opening mode experiments, except three hand-painted lines were used instead of the 11 or 21 lines applied with a precision template (see Figure 8). This was necessary because of the groove machined into the polymer specimen. One line was painted at the initial notch tip, and the other two were painted 15 and 25 mm from the notch. The region monitored by the infrared detector was half way between these two wires. The impact speed for the shear-dominated experiments was ~ 40 m/s. The signal from the crack propagation

circuit for a typical PMMA experiment is shown in Figure 58. The passage of the crack tip is evident by the abrupt decrease in circuit voltage for each of the three wires. The crack propagation gage data indicated that the disturbance that severed the painted lines was propagating at $\sim 0.6 c_s$ for PC (650 m/s) and varied from $1.1 c_s$ to $\sqrt{2}c_s$ for PMMA (1440 to 1880 m/s). As will be seen in the next section, an adiabatic shear band formed ahead of the shear crack in PC. As such, the speed measured in PC is most likely that of the shear band and not the actual crack tip. The crack tip speed measured for PMMA was at or below the speeds reported by Ravi-Chandar et al. (2000) who used high-speed photography to measure a crack tip speed of $\sqrt{2}c_s$, in nearly the same experimental configuration. The measured speed reported here is reasonably close to that of Ravi-Chandar et al. (2000) given the coarse resolution of the propagation gage for these experiments.

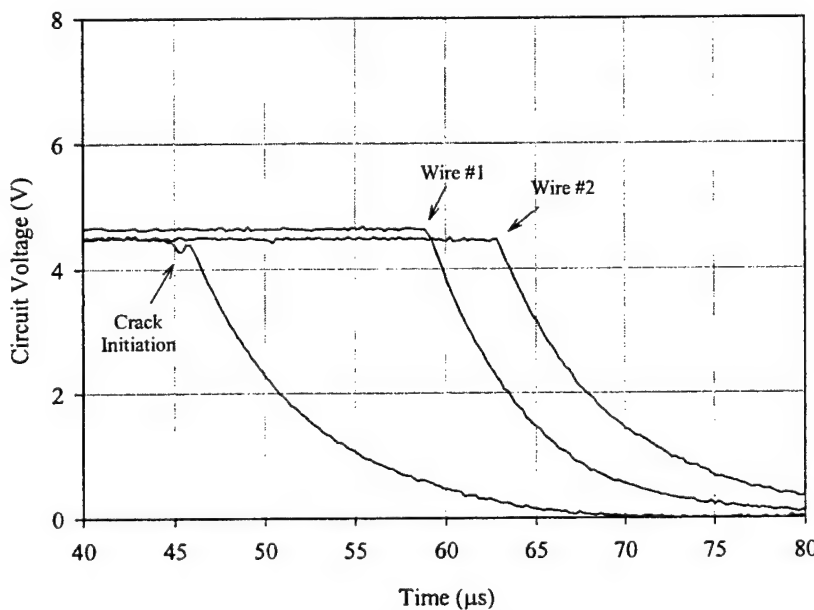


Figure 58. Typical output from the break-wire circuit used to determine the crack tip speed for shear-dominated dynamic fracture of PMMA. Output from the crack initiation and two crack-speed measurement circuits is shown.

4.3 Temperature Field Measurements

Although limited studies exist in the temperature measurement of opening mode dynamic fracture experiments (Fuller et al. 1975; Döll 1976; Rittel 1998; Mason and Rosakis 1992; Zehnder and Rosakis 1991), there have not been any studies of the crack tip heating associated with shear-dominated dynamic fracture for any material. In the present study, the temperature was measured in a manner similar to that used for the opening mode fracture experiments discussed in

section 3. The infrared detector system monitored a location on the polymer panel expected to be within the constant crack tip speed regime based upon crack tip speeds reported by Ravi-Chandar et al. (2000). Figure 8 shows the experimental setup and the location of temperature observation. It should be noted that the initial observation point was not the material point where the measurement was actually made during the experiment because of global specimen motion in front of the stationary detectors. As in the opening mode case, timing from each experiment correlating the time of crack passage, specimen dimensions, and wave speeds of the materials allow for the estimation of the propagating crack tip location with respect to the stationary infrared detector array.

4.3.1 PC Experiment

The infrared detector signals (after calibration and data smoothing, discussed in section 2) for shear-dominated fracture of PC are shown in Figure 59. Each of the 12 curves in Figure 59 is identified by the detector element it corresponds to. Once again, it should be noted that the vertical axis indicates a change of temperature ΔT from ambient. For the representative experiment shown, detector 12 recorded the highest temperature increase, followed by flanking elements with lower temperatures and delayed temperature increases. This suggests that the crack tip passed through the area that detector 12 was monitoring or very close to it. The maximum temperature increase recorded by detector element 12 was 142 K, which is 17 K higher than the glass transition temperature for this material. The nominally ductile (at room temperature) PC polymer is known to produce adiabatic shear bands under shear loading (Ravi-Chandar 1995), thereby introducing an energy dissipation mechanism that decreases the flux of energy to the crack tip, preventing the crack tip from propagating faster than c_s . This dissipation mechanism is evident in the temperature measurements for PC, shown in Figure 59. A slow, gradual 45-K increase in temperature occurs over 180 μ s and is followed by a distinct, large increase in temperature. This large temperature increase, corresponding to the thermal dissipation of a propagating crack, has a magnitude of about 100 K and is of the same magnitude found for the opening mode fracture of PC. It is believed that the second peak in the temperature signal is from frictional heating generated by global relative motion of the two, now fractured, halves. Timing data from the crack propagation gage indicated that the adiabatic shear band was responsible for severing the painted wires (in Figure 59 the second wire was severed at 113 μ s). Thus, the crack propagation gage for the case of PC recorded the propagation speed of the adiabatic shear band.

The initial portion of the temperature curves shown in Figure 59 are qualitatively similar to the temperature curves of propagating adiabatic shear bands in C-300 maraging steel obtained by Zhou et al. (1996a). In light of this, and the fact that

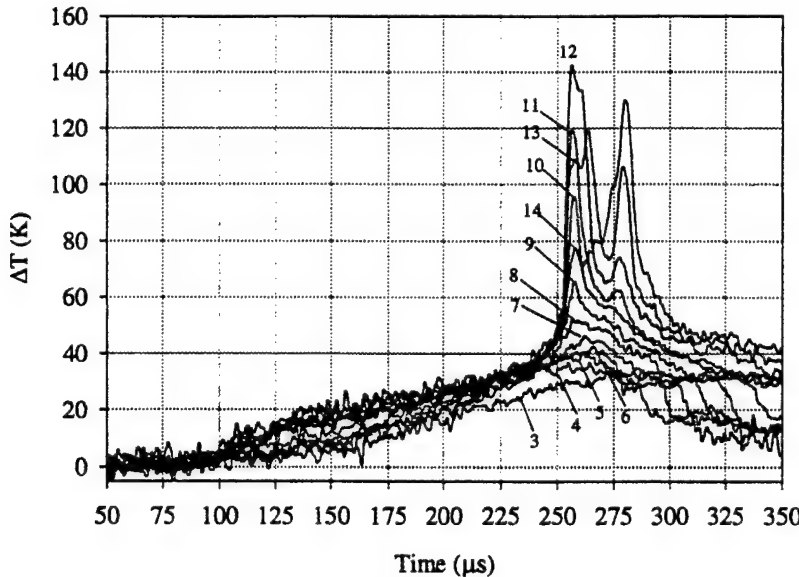


Figure 59. Typical thermal detector output (after calibration) for shear-dominated fracture of PC with side grooves to suppress crack kinking. ΔT denotes temperature change from ambient, and $t = 0$ corresponds to time of impact.

PC can produce adiabatic shear bands (Ravi-Chandar 1995), an experiment to obtain the thermal signature of an adiabatic shear band and arrested crack in PC was performed by impacting a panel of PC with no side grooves at a speed of 45 m/s. This was done to verify that the feature preceding the crack tip in Figure 59 is in fact due to an adiabatic shear band. A slightly different optical configuration with only eight detector elements was used. The detector array monitored a region 5 mm from the starter notch tip (as opposed to ~20 mm for the previously discussed experiment). Upon impact, an adiabatic shear band formed ahead of the starter notch, followed by an arrested crack. The temperature signals from such an experiment are shown in Figure 60. The results are similar to the PC adiabatic shear band temperatures reported by Rittel (2000) using a single thermocouple measurement technique. The same time and temperature scales that were used in Figure 59 are used in Figure 60 to aid in their comparison. The two figures have similar features, especially during the early time portion of the temperature record (first several hundred microseconds). The primary difference is the lower peak temperature in Figure 60 and a shorter time variation. The adiabatic shear band experiment shown produced a peak temperature increase of 118 K, whereas the peak temperature increase for the shear crack experiment was 142 K. An exact comparison should not be made because the adiabatic shear band test specimen did not have side grooves. The similarities do suggest that the PC did generate an adiabatic shear band that was followed by a shear-dominated crack. In the adiabatic shear band experiment shown in Figure 60, however, the crack did not propagate beyond a few millimeters and the specimen was not separated in half.

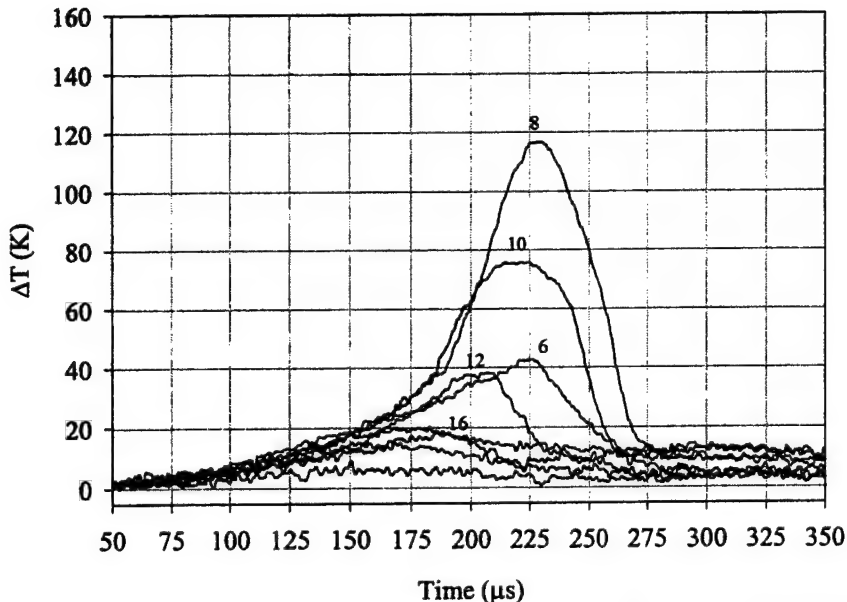


Figure 60. Temperature history of an adiabatic shear band and arrested crack in a PC specimen without side grooves. ΔT denotes temperature change from ambient, and $t = 0$ corresponds to time of impact.

Thus frictional heat generation, either during crack growth or because of subsequent global relative motion, would be nonexistent. This further suggests that the second peak in the experiment of Figure 59 is due to crack face contact and friction.

Assuming steady-state conditions, the temporal evolution in temperature can be converted to a spatial one in the manner described in section 3.4.1. The resulting temperature contour plot for the PC experiment is shown in Figure 61. The peak temperature is indicated by the left side of a horizontal dashed line included in the figures. It should be kept in mind when looking at the contour figure that the vertical distance between adjacent detector element centers is 0.10 mm. Even though in this work only an average value of crack tip speed is measured, the real-time high-speed photography results of Ravi-Chandar et al. (2000) indicate that crack tip speed is approximately constant, at least during part of the crack growth event. A violation of the steady-state crack growth condition assumed in generating Figure 61 would affect only the length of the contours in the propagation direction; the vertical dimensions would not be affected. Only the region near the crack tip is shown in Figure 61, the portion attributable to the adiabatic shear band which would be spatially larger is not shown. The vertical spatial extent of the PC temperature contours is significant, reaching ~ 1 mm near the peak temperature location. This event is similar to what was found for opening mode fracture of PC in section 3. The large lateral dimension of the PC

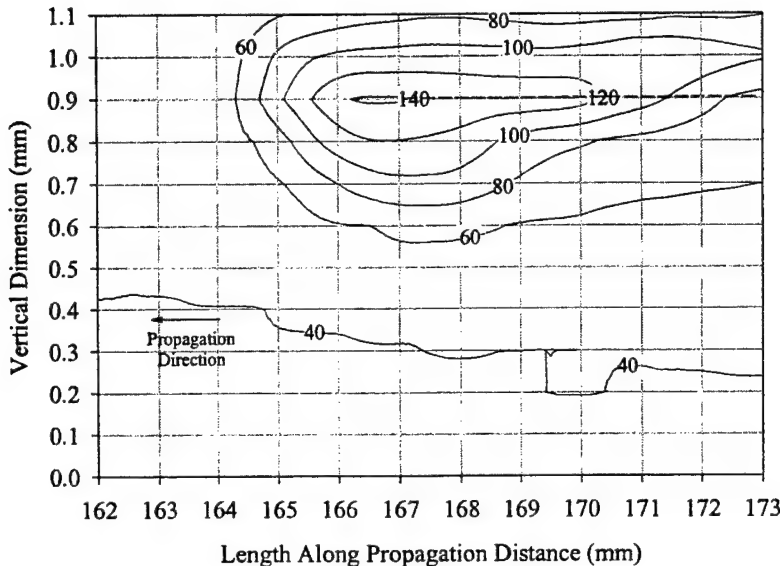


Figure 61. Temperature contours around crack tip region for shear-dominated fracture of PC. Temperature increase from room temperature (K). Steady-state crack growth has been assumed.

temperature field implies that plastic deformation is a significant mechanism for the dissipation of mechanical work during shear-dominated dynamic fracture (aside from the adiabatic shear band that precedes the crack tip).

4.3.2 PMMA Experiments

In the shear-dominated experiments, PMMA exhibited a very different thermal signature than PC. A typical temperature record for PMMA is shown in Figures 62a and 62b. Because PMMA responds in a brittle fashion at room temperature, no early adiabatic shear band dissipation is seen (as in Figure 59 for PC). Instead, the temperature is observed to abruptly increase by ~ 85 K (approximate increase necessary to reach the glass transition temperature) in $7 \mu\text{s}$. Detector element 8 recorded the highest initial temperature increase. The flanking elements detected a significantly smaller temperature increase denoting a highly localized event. After the initial temperature increase, no additional thermal dissipation is evident for approximately $30 \mu\text{s}$. The constant temperature regime is then followed by a slow increase in temperature that goes well above the glass transition temperature of PMMA (see Figure 62a). This temperature profile suggests that the first increase in temperature is due to the thermal dissipation associated with the passage of a shear-dominated crack, and the later high temperature event is frictional heating. Ravi-Chandar et al. (2000) observed in their shear-dominated fracture experiments that the PMMA specimens were cut into two halves very quickly because of the high crack tip speeds. With this in mind, the late time frictional heating observed in this study is likely associated with the global motion of the two specimen halves.

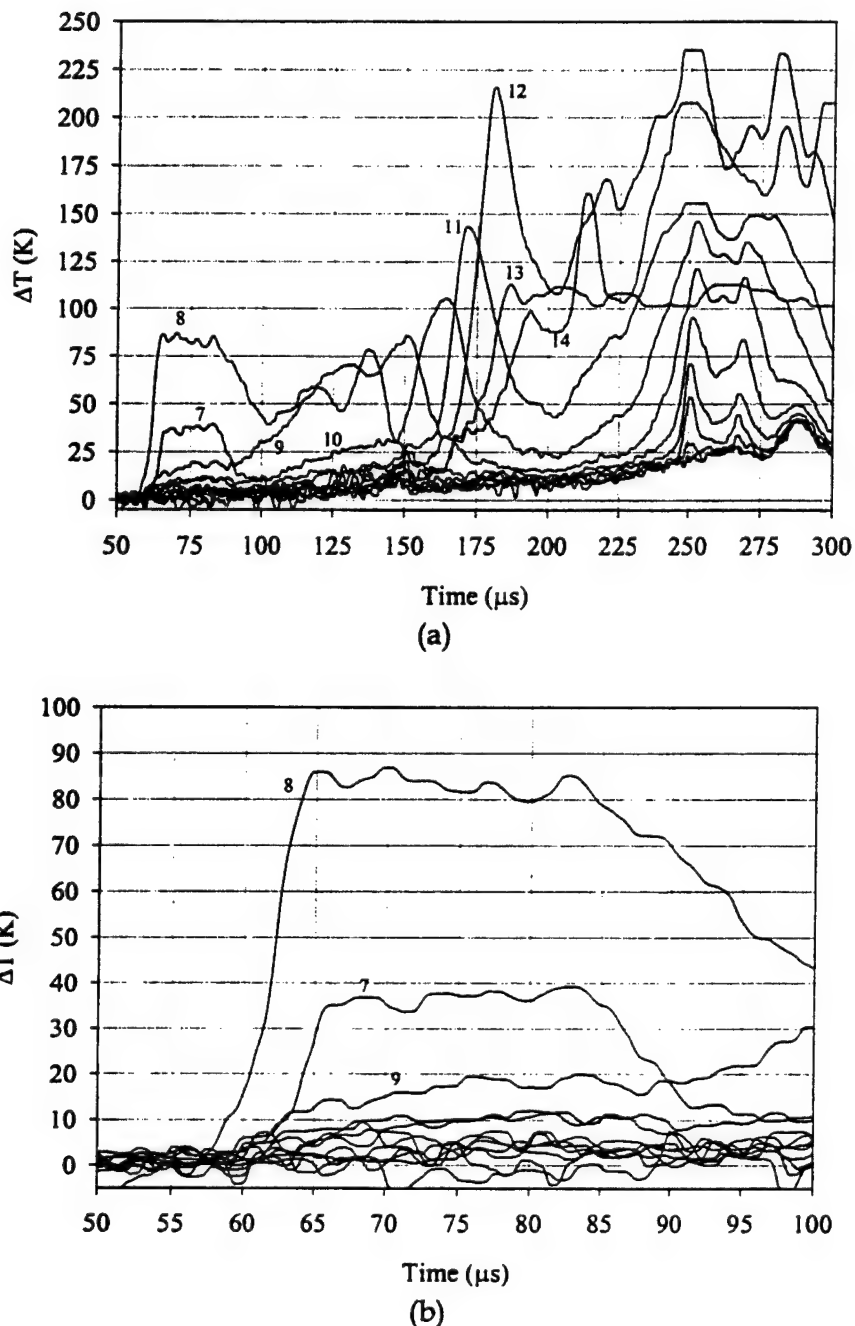


Figure 62. (a) Thermal detector output (after calibration) for shear-dominated fracture of PMMA with side grooves to suppress crack kinking. ΔT denotes temperature change from ambient and $t = 0$ corresponds to time of impact.
 (b) Initial portion of thermal signal from shear-dominated fracture of PMMA with side grooves. Temperature field surrounding crack tip is shown. ΔT denotes temperature change from ambient and $t = 0$ corresponds to time of impact.

To examine the spatial extent of heating, temperature contour plots for PMMA were generated from the infrared detector output in a manner identical to that used in the previous section. Figure 63 shows such a spatial temperature contour plot for PMMA. The temperature contours depict a very narrow zone of thermal dissipation, indicative of a craze-dominant means of dissipation as opposed to plasticity. The lateral span of the heat dissipation region at the location of peak temperature was 140 μm or less. The exact span could not be determined because only one detector element responded at the time of peak temperature. The crack tip speed in PMMA was slightly supersonic relative to the shear wave speed, indicating the possible presence of a shear shock. Both Rosakis et al. (1999) and Ravi-Chandar et al. (2000) observed the presence of stress field discontinuities during their shear-dominated fracture experiments. The temperature contours do not show any discontinuities that would confirm the presence of the shock, but do illustrate the limited extent of temperature increase ahead of the crack tip.

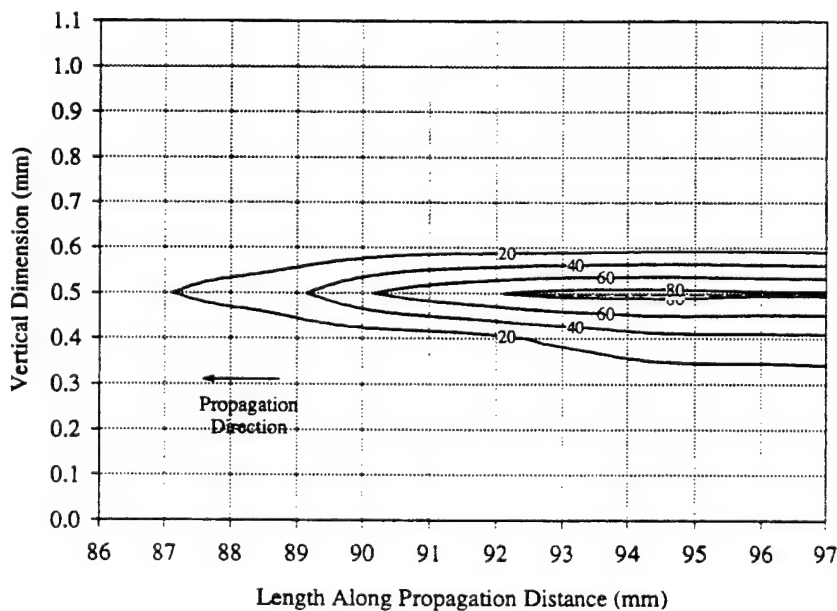


Figure 63. Temperature contours at crack tip region for shear-dominated fracture of PMMA. Temperature increase from room temperature (K). Steady-state crack growth has been assumed.

Recall that the temperature contours for high-speed opening mode fracture of PMMA had a lateral span of $\sim 300 \mu\text{m}$ and significant microcracking was present on the fracture surface for higher crack growth speeds. The contours for shear-dominated fracture of PMMA are much more localized, and as will be seen in section 4.5, microcracking similar to what was observed for the mode I dynamic fracture of PMMA was not present on the fracture surface. The

temperature signals are highly localized, similar to the low-speed PMMA experiments where a single craze was formed. This suggests the possibility that highly localized "shear crazing" is the mechanism responsible for shear-dominated fracture of PMMA.

4.4 Thermal Dissipation of Mechanical Work

As shown in section 1, the heat energy equation for an adiabatic event with negligible thermoelastic cooling reduces to the form

$$\beta \sigma_{ij} \dot{\epsilon}_{ij}^p + \dot{q} = \rho c_p \dot{T}, \quad (36)$$

with the parameters having been defined in section 1.2.2. Contours of plastic work rate ($\sigma_{ij} \dot{\epsilon}_{ij}^p$) and internal heating rate (\dot{q}) were generated from the temperature measurements presented in the previous section using a technique identical to that used for the opening mode experiments discussed in section 3. The large lateral span of the temperature contours for PC (shown in Figure 61) suggest thermal dissipation will be composed primarily of the rate of plastic work term. Figure 64 shows contours of plastic work rate at the crack tip region assuming that this is the only dissipative term in equation (36). A value of $\beta = 0.5$ was assumed. The length and width of the plastic work rate zone is ~ 2 mm and ~ 0.5 mm, respectively. The maximum plastic work rate was $100 \times 10^{12} \text{ J/m}^3 \text{ s}$. These values are similar to those found for opening mode fracture of PC.

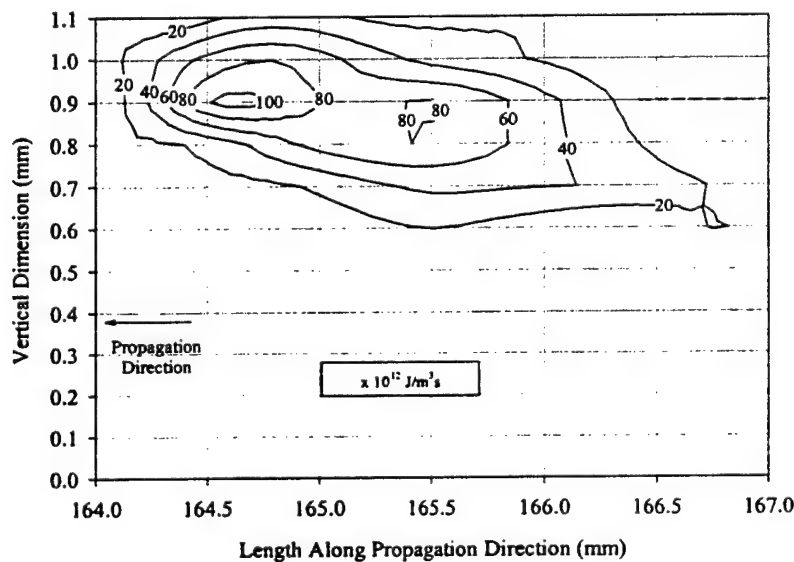


Figure 64. Plastic work rate contours at crack tip region for shear-dominated fracture of PC. $\beta = 0.5$ and steady-state crack growth have been assumed.

Internal heating was assumed to be the sole heat source for PMMA based on the highly localized temperature contours (see section 3.5 for additional discussion). Figure 65 shows contours of internal heat generation rate for PMMA assuming \dot{q} to be the sole coupling term in equation (36). Note that the contours are for a region in the immediate vicinity of the propagating crack tip, the subsequent frictional heating is not included. The length of the heat generation rate region is ~ 3 mm, and the width is less than $200 \mu\text{m}$. The maximum value of dissipation for PMMA is $50 \times 10^{12} \text{ J/m}^3\text{s}$, half the maximum for PC.

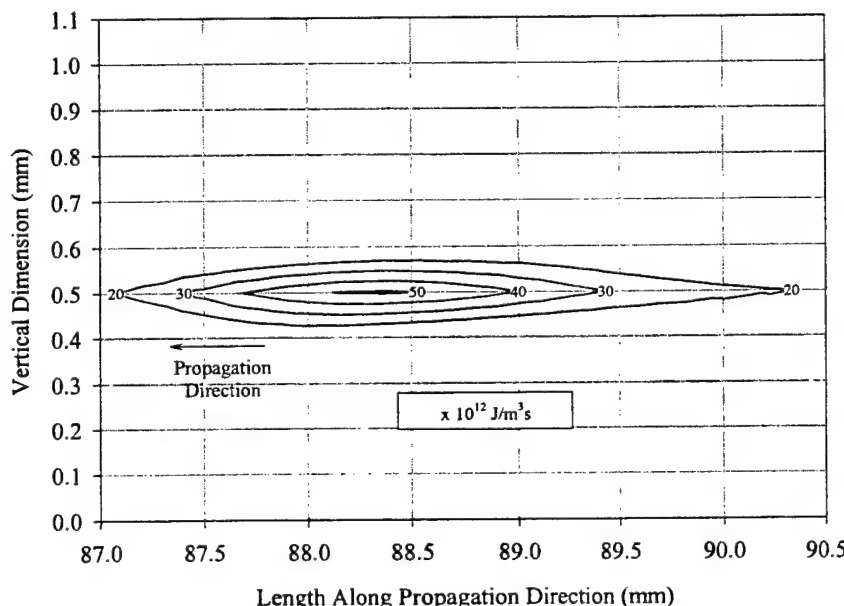


Figure 65. Rate of internal heat generation contours at crack tip region for shear-dominated fracture of PMMA. Negligible plastic work rate and steady-state crack growth have been assumed.

As discussed earlier, low-speed opening mode fracture of PMMA produced a highly localized thermal field. The maximum rate of internal heat generation was $11 \times 10^{12} \text{ J/m}^3\text{s}$ for the low-speed opening mode experiment, considerably less than the maximum for shear-dominated fracture. The thermal dissipative mechanisms for low-speed opening mode and high-speed shear-mode fracture of PMMA are both highly localized. However, the energy dissipation rate for shear fracture is approximately four times larger than low-speed opening-mode fracture. Normalizing the energy dissipation rate by crack-speed yields an energy dissipation per unit crack area. If this is done for the shear- and low-speed opening mode fracture cases, the energy dissipation values become much closer, giving a value of $35 \times 10^9 \text{ J/m}^2$ for shear-dominated fracture and $36 \times 10^9 \text{ J/m}^2$ for low-speed opening mode. This further suggests the possibility of crazing as the dissipation mechanism for shear-dominated fracture.

4.5 Model Friction Experiments

The experiments of Rosakis et al. (1999) showed evidence of crack face contact aft of the advancing crack tip. The infrared detector results for PMMA presented in Figure 62a show two discrete thermal events, one associated with the passage of the crack tip and a subsequent one speculated to be associated with frictional crack face contact. This section discusses a cursory examination aimed at determining if crack face sliding could produce thermal signatures similar to those observed in Figure 62a. The frictional heating study was not a comprehensive effort, it was by design a preliminary study to provide an indication of the magnitude of heating possible from high-speed frictional sliding of PMMA.

Frictional heating of polymers has been the subject of very few studies. The maximum sliding speed for these studies has generally been limited to about 30 m/s (Ettles 1986; Ettles and Shen 1988; Kong and Ashby 1992). Rosakis et al. (1999) found the propagation speed of the trailing crack face contact zone for shear-dominated fracture to be approximately the same as the crack tip, i.e., $\sqrt{2}c_s$. The relative sliding speed between the two crack faces was not determined by Rosakis et al. (1999). However, given that the mechanism that causes shear-dominated fracture originates from an applied material speed mismatch between the top and bottom half of the specimen panel (resulting from projectile impact), it seems reasonable to expect the sliding speed to be on the order of the projectile speed.

Frictional heating of generic materials was first modeled by Blok (1937). For a heat source of intensity \dot{Q} (per unit area) moving over a half space of uniform thermal properties, the surface temperature rise ΔT is

$$\Delta T = 2\dot{Q}\sqrt{\frac{t}{\pi k\rho c_p}}, \quad (37)$$

where t is the time the source had been over the point of interest, and k , ρ , and c_p are thermal properties defined in section 2 (see Table 2). The heat source for frictional contact is given as

$$\dot{Q} = \mu PV, \quad (38)$$

where μ is the coefficient of friction, P is the interface pressure, and V is the sliding speed. The work of Ettles (1986) and Ettles and Shen (1988) determined that the frictional sliding of polymers produced a viscous melt layer between the sliding bodies. The friction coefficient in equation (38) was found to decrease with increasing sliding speed, effectively limiting the maximum temperature increase predicted from equation (37). Kong and Ashby (1992), who studied the speed dependence on the wear behavior of polymers, observed a thin layer of

hot polymeric material deposited on the sliding surfaces. This layer corresponds with the viscous melt layer noted by Ettles (1986) and Ettles and Shen (1988). If the heating observed aft of the shear-dominated crack tip in Figure 62(a) is due to frictional sliding, a thin melt layer would likely be present. The fracture surfaces from the shear-dominated experiments of this study are examined in detail in section 4.6. To help in identifying the features on the fracture surface, melt layers resulting from high-speed friction of PMMA are needed. Additionally, the thermal signature from a high-speed polymer friction event is desired for comparison to the temperature field measurements shown in Figure 62(a). These are the goals of the friction experiments discussed next.

High-speed friction experiments were performed using the configuration illustrated in Figure 66. Pieces of PMMA from the same lot used for the fracture experiments were cut to size and stacked as shown in Figure 66. The middle piece was impacted by a steel projectile, after which it then began to slide relative to the top and bottom pieces. The sliding surfaces were polished prior to the experiments with a 5- μm polishing slurry on a polishing wheel to achieve a glassy, smooth finish. The infrared detector monitored the interface between the top and middle pieces. Normal pressure was applied to the interfaces with four equispaced clamps. The magnitude of the pressure was not measured. The intent of these experiments was not to provide a comprehensive study of polymer frictional heating, but rather to give an indication of the thermal signature associated with high-speed polymer sliding and to obtain sliding surfaces for comparison to the fracture experiments. A much more detailed analysis could form the basis of a future project.

Typical temperature field measurements from the friction experiments are shown in Figure 67. The projectile-impact speed was 40 m/s, identical to the impact speed for the shear-dominated fracture experiments. A peak temperature increase of 43 K was measured by detector element 14, which is about half the temperature increase needed to reach T_g . Flanking elements detected a temperature increase of 15 K and 10 K. The specific variation of temperature with time is likely due to the reflections of the stress waves in the three polymer pieces that produce compressive tractions on the sliding interfaces. The wave reflection pattern will not be similar to the fracture experiments because the overall size of the test specimens differ considerably. The significance of the temperatures shown in Figure 67 is that appreciable temperatures can be generated from dynamic frictional sliding of PMMA. Unique features were found on the sliding surfaces indicating the presence of a friction surface. This will be examined in the next section.

4.6 Fracture Surface Micrography

The fracture surfaces from the shear-dominated fracture experiments were examined to provide additional insight into the dissipation mechanisms in the

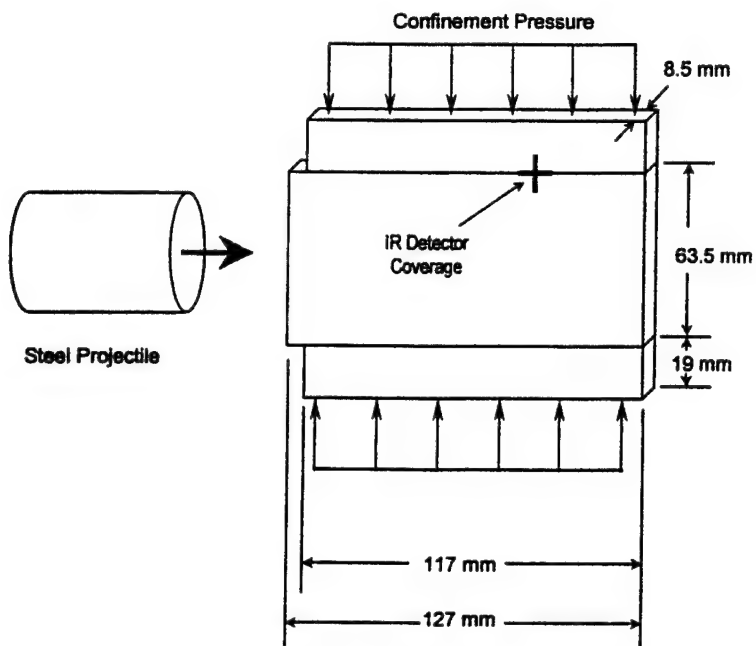


Figure 66. Configuration for high-speed friction experiments. Infrared detector monitored the sliding interface between the top and middle PMMA pieces.

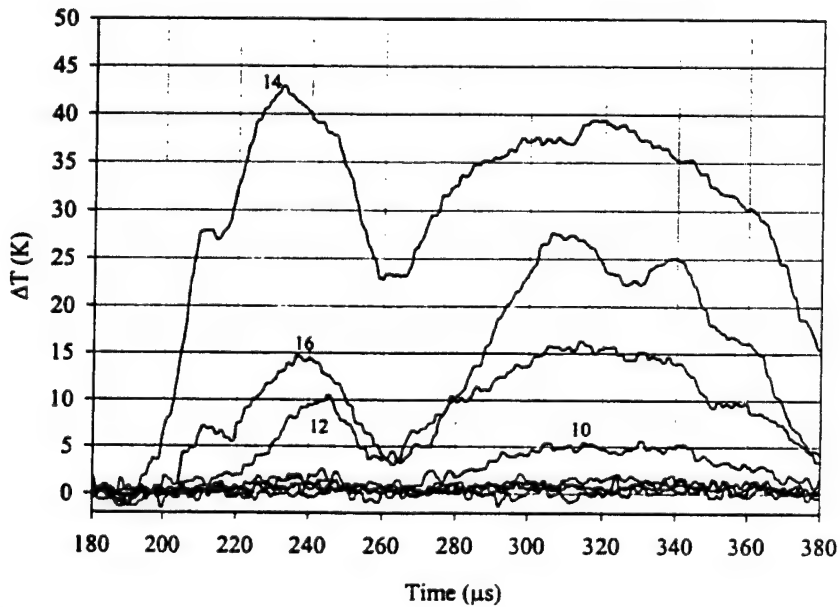


Figure 67. Typical thermal detector output (after calibration) for high-speed friction experiments. ΔT denotes temperature change from ambient and $t = 0$ corresponds to time of impact.

crack tip process zone. Photographs of the PC and PMMA fracture surfaces generated from shear-dominated crack growth are shown in Figures 68 and 69, respectively. The surface for PC has a rippled appearance with the ripples oriented perpendicular to the crack propagation direction. The fracture surface for PMMA has a white-colored coating and small cracks extending below the crack surface.

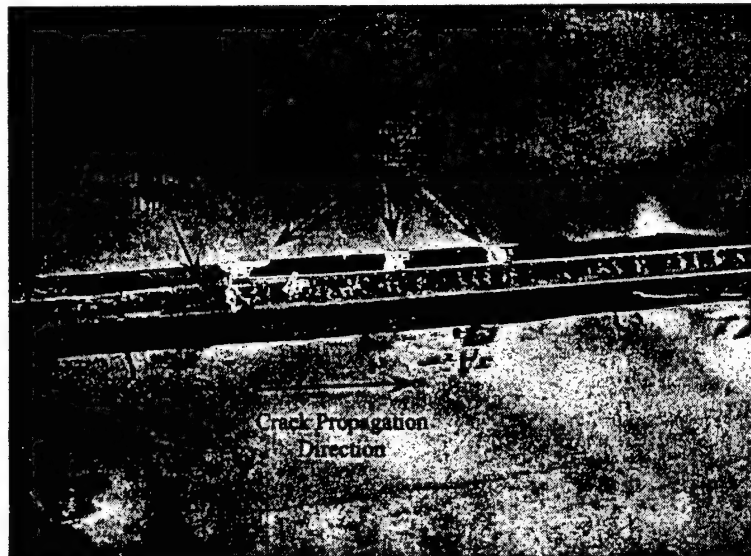


Figure 68. Photograph of fracture surface from shear-dominated dynamic fracture of PC with side grooves to suppress crack kinking. Fracture surface ripples are visible on the crack face.

SEM images of the fracture surfaces were obtained to examine the surface features in greater detail. A fracture surface image for PC is shown in Figure 70 along with a schematic depiction of the location it was taken from. The crack propagated from left to right in the figure. Ripples covering what was once molten material are evident in the figure. Fine strands of material oriented along the crack growth direction are present at a few locations. It is not possible to determine if the features are attributable to the shear band, the shear crack, or late time friction. The features on the fracture surface are considerably different from those observed on the opening mode PC fracture surface, where crazing and ductile tearing was observed (see Figure 53). The formation of ripples observed in Figure 70 is unique to this mode of failure for PC.

The high-temperature increase recorded during the PMMA shear-dominated experiments indicates that evidence of polymer melting should exist on the fracture surfaces. SEM images of the fracture surfaces from this experiment are shown in Figure 71. Two images are shown, one from the specimen interior, and the other from a location near the groove surface. As in the work of

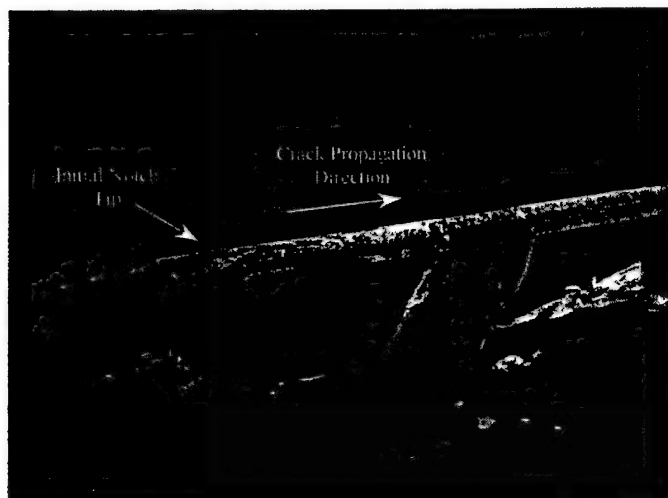


Figure 69. Photograph of fracture surface from shear-dominated dynamic fracture of PMMA with side grooves to suppress crack kinking. White-colored wear layer is visible on the crack face.

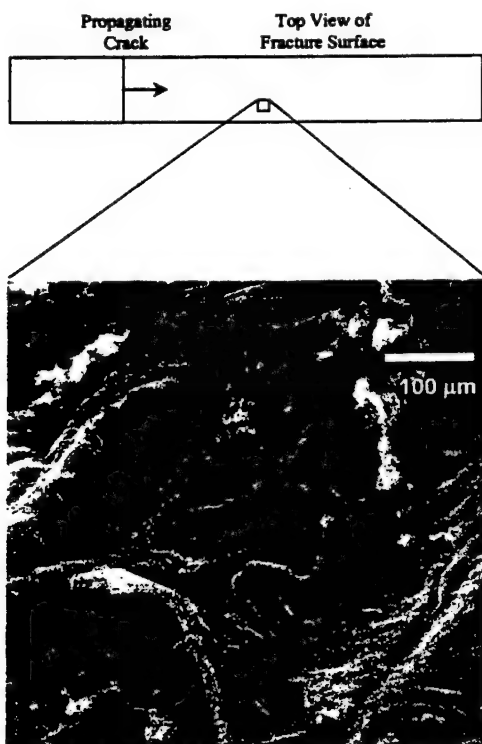


Figure 70. SEM image of fracture surface from shear-dominated dynamic fracture experiment using PC with side grooves. The crack propagated from left to right leaving surface ripples covered with a molten coating.

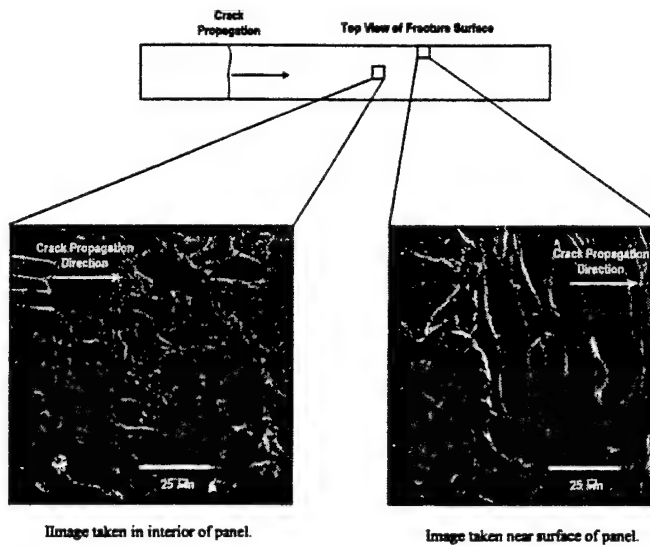


Figure 71. SEM image of fracture surface from shear-dominated dynamic fracture using PMMA with side grooves. Left-side image was taken in the interior of the panel. Right-side image is near location where infrared detector monitored. The crack propagated from left to right.

Ravi-Chandar et al. (2000), the image taken from the interior of the specimen shows signs of considerable polymer melting, suggesting that the shear-dominated fracture event did generate high temperatures. The image taken near the surface of the groove also shows melting, but to a much lesser degree. Figure 71 clearly shows the three-dimensional nature of the thermomechanical phenomenon. Because the infrared detector system collects heat emitted from the specimen surface, the data are expected to be a lower bound of the actual temperature of the propagating crack tip in the interior of the specimen. Variations of the surface features throughout the specimen thickness were not observed for PC. Also evident on the fracture surface is a ripple feature below the melt region. Whether this occurred during the passage of the shear crack or the frictional motion of the two-panel halves remains unknown.

The temperature field measurements for PMMA showed indications that frictional heating of the crack faces occurs aft of the crack tip. An SEM image of the sliding surface from the friction experiment (described in section 4.5) is shown in Figure 72. The friction surface from the experiment is shown on the left and the original surface condition of the surface prior to the experiment is shown on the right. The sliding direction of the mating surface was from left to right. A thin layer of molten material is spread along the surface with thin fibrils of

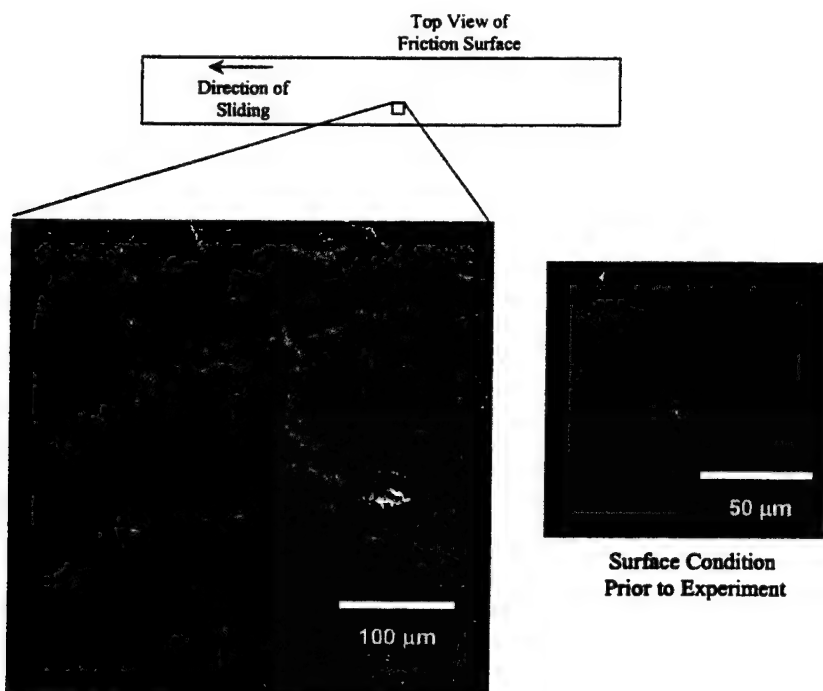


Figure 72. SEM image of PMMA high-speed friction surface. The mating surface slid over the surface shown from left to right. Deposits are visible in the friction surface. The original surface condition prior to the experiment is shown on the right.

material stretched along the sliding direction. However, the temperature increase for the friction experiment was only 45 K, well below the PMMA glass transition temperature. The recorded temperature may be underestimated due to the relative size of the heat source compared to the detector element. This is discussed in section 4.3 and pursued further in section 6. Comparing this image with the PMMA fracture surface in Figure 71 shows some similarity. The fracture surface image shows a thin layer of material that has some resemblance to the resulting surface from the friction experiment. The implication of this is that the melting observed in the SEM image of the PMMA fracture surface may not be entirely due to thermal dissipation from shear-dominated cracking, but may also be the result of subsequent frictional heating that accompanies it.

4.7 Additional Comments on Shear-Dominated Crack Tip Behavior

The interpretation of the infrared emissions during shear-dominated fracture yielded insight into the coupling of mechanical work and thermal dissipation. Substantial heating was observed during shear-dynamic fracture of both PC and PMMA. The temperature signatures from the shear-dominated fracture experiments showed the two polymers to behave very differently to the same loading condition. An adiabatic shear band followed by a fracture event occurred in PC. The maximum temperature increase produced by the

propagating adiabatic shear band was 45 K, similar to that reported by Rittel (2000) who used a single thermocouple. The fracture event, which for the case of PC was subsonic, increased the temperature an additional 100 K. The temperature field of the propagating crack tip indicated the dissipation of mechanical work is primarily through plastic deformation. PMMA, on the other hand, showed an abrupt 85 K increase in temperature resulting from a crack propagating faster than the shear wave speed of the material. Thermal evidence of crack face contact and frictional heating were observed behind the advancing crack tip in PMMA. The frictional heating increased the temperature beyond the glass transition temperature of PMMA. SEM images of fractured PMMA surfaces confirmed that polymer melting did occur during the shear-dominated fracture event.

Comparing the results from the shear-dominated fracture experiments with those of opening mode reveal several similarities and differences. Significant ductile deformation appears to contribute to material heating for PC regardless of fracture mode. The shear loading that causes shear-dominated fracture in PC also induces the formation of a shear band propagating ahead of the crack. The presence of the shear band is believed to decrease the energy flux to the crack tip in PC, resulting in a decrease in terminal crack tip speed. No dissipation mechanisms were found ahead of the shear crack in PMMA, which accounts for the higher terminal crack speed. The highly localized thermal field surrounding the shear-dominated crack-tip was somewhat similar in size and dissipation strength to the single craze dissipation event observed for the low-speed PMMA opening fracture experiments. The fracture surfaces resulting from shear-dominated fracture of both materials contained a ripple feature that was not found on the opening-mode fracture surfaces, as well as on deposits of material that were molten. Given that shear-dominated fracture of these materials consists of multiple distinct events (adiabatic shear band for PC, shear fracture, and frictional sliding), the modeling of the shear-dominated dynamic fracture response of these materials will need to address multiple dissipative events.

The results of the opening-mode and shear-dominated dynamic fracture experiments indicate that material heating is due to either thermoplastic or thermofracture heat sources, depending on the nature of the polymeric material. The next two sections provide a detailed examination of the relative contribution of each of these mechanisms. The next section discusses a computational study that attempts to identify the amount of heating attributable to plastic deformation for opening mode fracture of PC. Section 6 presents a dissipative cohesive zone model derived for dynamic opening-mode fracture of PMMA, where the thermofracture mechanism appears to dominate material heating. This begins the sizeable task of modeling the various dissipative phenomena observed during dynamic fracture of these materials.

5. Effect of Plasticity in Thermomechanical Heating of Ductile Polymers During Opening-Mode Dynamic Fracture

5.1 Introduction

Rapid plastic deformation of a material can produce an increase in temperature. A common example of this is the back-and-forth bending of a thin metal strip. After flexing the metal several times, it will feel warm when touched. This occurs because of the coupling that exists between heat generation and mechanical fields. The coupled heat energy relation was given in section 1 as

$$kT_{,ii} - \alpha(3\lambda + 2\mu)T_0\dot{\varepsilon}_{kk}^e + \beta\sigma_{ij}\dot{\varepsilon}_{ij}^p + \dot{q} = \rho c_p \dot{T}, \quad (39)$$

where the parameters were defined in section 1.2.2. The linear thermoelastic constitutive relation used in deriving the heat energy equation was also given in section 1 as

$$\sigma_{ij} = \lambda\delta_{ij}\varepsilon_{kk} + 2\mu\varepsilon_{ij} - (3\lambda + 2\mu)\delta_{ij}\alpha(T - T_0), \quad (40)$$

where T_0 is the initial temperature of the material. Although the linear thermoelastic constitutive equation is fully coupled, the heat energy equation relation given by equation (39) is not because the dissipative term associated with plastic deformation is not fully coupled. As such, equation (39) can be used to calculate the temperature increase in a material resulting from mechanical fields and internal heating, but the mechanical fields and internal heating are not affected by the temperature increase.

It was shown in sections 2 and 3 that nearly adiabatic conditions exist during dynamic opening mode fracture of PC and PMMA. Additionally, the thermoelastic term was shown in section 3 to be negligible compared to the temperature increases recorded during fracture. Neglecting the conduction and thermoelastic terms reduces equation (39) to the following:

$$\beta\dot{W}^p + \dot{q} = \rho c_p \dot{T}, \quad (41)$$

with \dot{W}^p , the plastic work rate, defined as

$$\dot{W}^p \equiv \sigma_{ij}\dot{\varepsilon}_{ij}^p. \quad (42)$$

The quantity β is the fraction of plastic work rate that is converted to heat. As discussed in section 1, Rittel (1999) found β for PC to vary from 0.4 to 1.0

depending on strain rate, and Li and Lambros (2001) found β for PC to range from 0.5 to 0.6 during high-rate compression.

The thermal fields surrounding propagating crack tips were shown in sections 3 and 4 to produce significant temperature increase. The sources for dissipation were attributed to the work from plastic deformation and internal heating resulting from microstructure breakdown and molecular chain scission. For PMMA, evidence suggested the dissipation source was solely from internal heat generation associated with dynamic fracture. The data for PC, on the other hand, indicated that plastic deformation contributed a significant portion to the overall crack tip temperature.

This chapter examines the contribution of plastic deformation heating to the thermal field measured for PC during opening mode dynamic fracture, presented in section 3 and shown in Figure 73. Finite-element simulations of the dynamic opening mode experiments are performed with an incremental plasticity model that uses a rate-dependent Mises yield surface and isotropic hardening to describe the behavior of PC. The only source of material heating permitted in the simulation is that resulting from plastic deformation. A comparison of temperature increase between experimental and numerical results is made to identify the plasticity contribution to the overall heating of the material. This allows the relative contribution of \dot{W}^p in equation (41) to be determined for PC during opening mode dynamic fracture. The results of this section provide a better understanding of the heating mechanics in ductile polymers during dynamic fracture. This approach has been successfully used in the past in modeling the thermoplastic coupling in ductile metals (Zhou et al. 1996).

5.2 Finite-Element Model

A Lagrangian-based finite-element technique was used in this study for simulating the PC opening-mode fracture experiments presented in section 3. A Lagrangian approach was selected because of the need to accurately track crack tip motion. The finite-element technique was used because it offered a convenient way to propagate the crack tip with time, as discussed later. Of the many Lagrangian finite-element codes available, the ABAQUS/Explicit finite-element code (Hibbit et al. 1998) was chosen primarily because of its ease of use and availability. The ABAQUS finite-element code is available with two different time integration techniques, implicit and explicit. In an implicit time integration scheme, the displacements at any time cannot be obtained without knowledge of the accelerations at the same time. The relationships among velocity, displacement, and acceleration must be combined with the equations of motion and the resulting set of equations, which are then solved simultaneously for each time-step. For problems with large numbers of elements, the

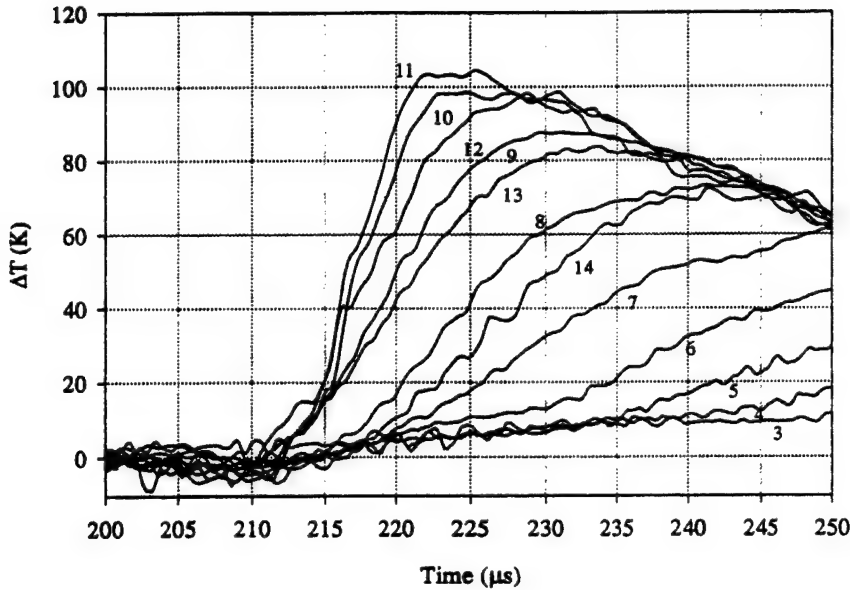


Figure 73. Measured temperature field surrounding a crack tip propagating in PC at 550 m/s under mode I loading.

simultaneous solution of the large set of equations can be a significant computational burden. The explicit time integration scheme does not require the accelerations at a given time to calculate the nodal displacements. An explicit expression for node displacement results from the equation of motion when the node velocities and accelerations are expressed by a central difference relation. Explicit time integration eliminates the need to solve large sets of equations simultaneously. However, explicit integration can cause the computed response to grow without bound (i.e., become computationally unstable) if the time step is too large. Most codes, including the ABAQUS/Explicit finite-element code, that was used in this study, have built-in routines to automatically select stable time-steps during the simulation. User intervention is not required.

The modeling procedure in the ABAQUS finite-element code used is to construct a finite-element mesh of the material in the initial configuration, assign appropriate boundary and initial conditions to the model, supply a description of the material behavior (i.e., a constitutive material model), and then perform the finite-element solution. These various aspects are discussed next.

The finite-element technique was used to simulate dynamic opening mode fracture in PC. The experiment used for comparison with the simulation is described in section 3.4.1, and a typical crack tip temperature field is shown in Figure 73. The projectile-impact speed for this particular experiment was 25 m/s. The finite-element model duplicating the experimental configuration consisted of the polymer fracture specimen and the steel projectile. Because

mode I fracture is symmetric about the crack propagation path, only the top half of the polymer specimen and projectile were modeled, with a plane of symmetry defined along the crack path. Introducing a plane of symmetry enabled a convenient method for advancing the crack tip, and is discussed later. The single edge notched PC specimen was discretized using an expanding mesh of four node-reduced integration quadrilateral elements and three node triangular elements. Quadrilateral elements were used near the region where plastic deformation was expected to occur (i.e., the crack tip region). This is also the location where the temperature fields of the numerical simulation will be compared to those measured during the experiments. Because the infrared detector element size was $80 \mu\text{m}$, the cell size in the plastic deformation zone should also be $\sim 80 \mu\text{m}$ for a valid comparison of temperature results. With such a small cell size in the crack tip region, great flexibility was needed to expand the mesh at locations distant from the crack tip region. This was achieved by transitioning from quadrilateral to triangular elements far from the plastic deformation zone. The triangular elements permitted greater flexibility in expanding the mesh. The steel projectile was also modeled with four node-reduced integration quadrilateral elements. The element size of the projectile was 3 mm. The final mesh used for the dynamic fracture simulation is shown in Figure 74.

Plane stress elements were used throughout. The out-of-plane thickness of the PC plane stress elements was 8.5 mm. An element out-of-plane thickness of 32 mm was used for the projectile to preserve the mass of the projectile. As mentioned earlier, the geometry is symmetric about the crack propagation path so only the top half of the polymer specimen and projectile were modeled. A boundary condition was imposed along the plane of symmetry that prevented nodes along the plane of symmetry from moving in the vertical direction. A mathematically sharp crack in the PC specimen was modeled by excluding from this restriction the nodes along the plane of symmetry that belonged to the crack. The finite-element model had a total of 77,600° of freedom.

Crack growth in the numerical simulation was achieved by manually releasing nodes along the axis of symmetry at a prescribed time to duplicate the experimentally measured crack tip position history obtained from the crack initiation and propagation gages. This manual node release technique has been successfully used in the past (e.g., Lo et al. [1994]). The timing data from the PC experiment used for comparison indicated that crack growth began 165 μs after projectile impact for a 25 m/s impact speed. It is important to determine if there is significant variability in the initiation time because the stress state at the crack tip changes with time as stress waves propagate throughout the polymer specimen. Figure 75 shows the measured crack initiation time for mode I PC dynamic fracture experiments as a function of projectile impact speed. The

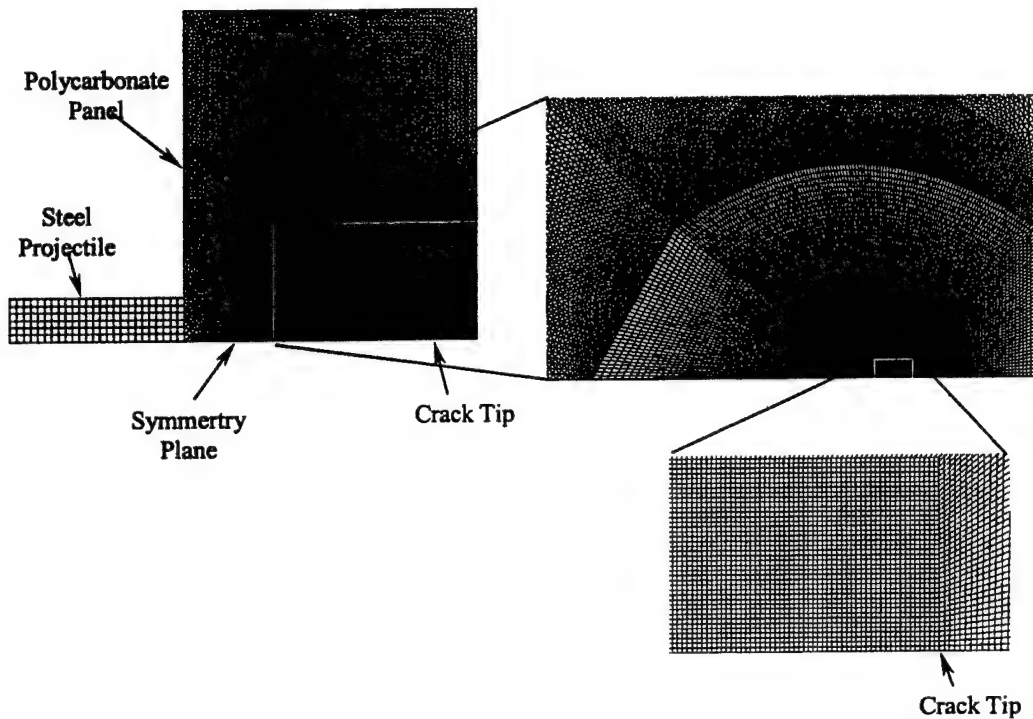


Figure 74. Finite-element mesh used for the numerical simulations. Element size in the crack tip region is $80 \mu\text{m}$. The plane-stress model has $77,600^\circ$ of freedom.

impact speed of interest is 25 m/s. At this speed, there is some data scatter. The initiation time for the experiment corresponding to the temperature field presented in Figure 73 (that will be used for comparison with the numerical simulation) is within the data scatter. As such, the node release scheme used for crack growth was programmed to commence at 165 μs after projectile impact.

Timing data from the crack propagation gage indicated the crack accelerated to terminal speed (550 m/s) within 3 mm of initiation. The position history of the crack tip from the experiment of interest is shown in Figure 76. The position vs. time data shown in Figure 76 was used to indicate the proper time for the sequential release of nodes along the crack path to simulate crack growth. Each node was released individually from its vertical displacement restriction at the appropriate time to cause the crack tip position history in the simulation to conform to Figure 76. Because there were more nodes released during the time interval of interest than there are data points in Figure 76, linear interpolation was used for prescribing the release time for intervals between data points in Figure 76. The manual node release technique has the effect of indirectly applying an empirical fracture toughness vs. crack tip speed criterion and eliminated the need to introduce and calibrate a failure model for elements along the axis of symmetry. Due to computer memory restrictions, only the first 4 mm

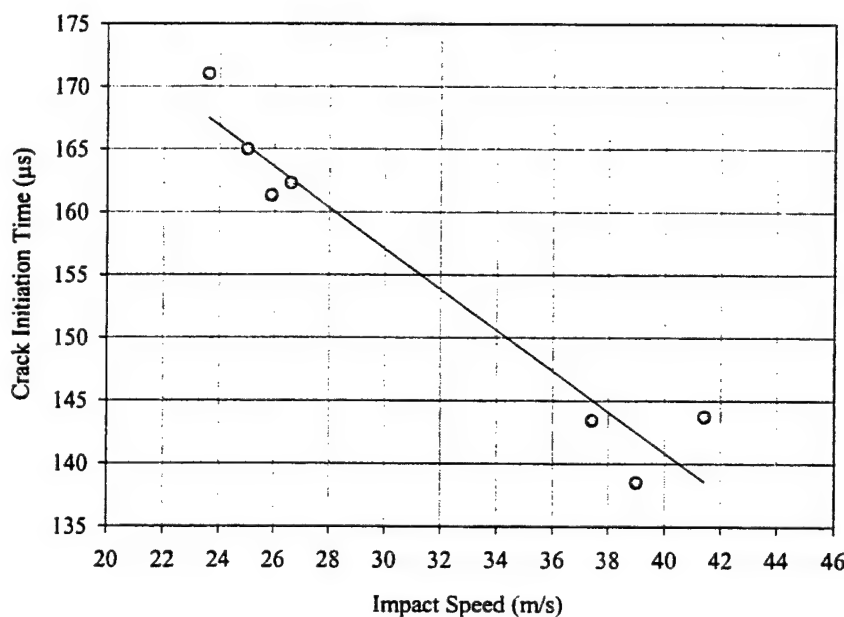


Figure 75. Dynamic crack initiation time measured during the opening-mode fracture experiments using PC for various projectile-impact speed.

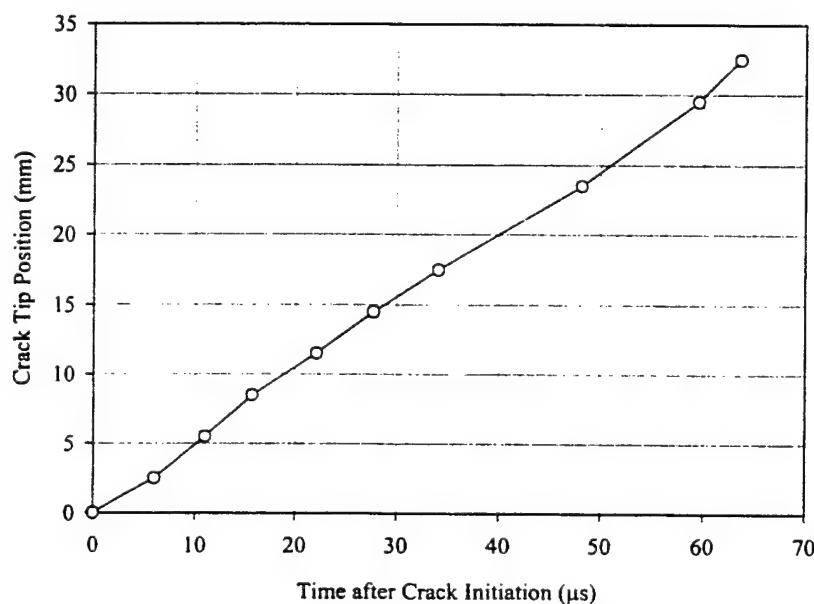


Figure 76. Crack tip position history measured during dynamic opening-mode crack growth in PC. Position history was used for timing the sequential release of nodes along the plane of symmetry to simulate crack tip propagation in the numerical simulation.

of crack propagation were simulated, corresponding to 50 nodes being released. The crack tip speed was 550 m/s for the final 1 mm of crack growth (last 12 nodes released).

The initial conditions specified for the simulation consisted of prescribing an initial horizontal translation speed of 25 m/s for the nodes that comprised the steel projectile. The nodes from the projectile were prevented from penetrating into the PC finite elements at the impact interface by assigning a frictionless contact interface between the projectile and polymer specimen. The contact interface is a standard algorithm available in the ABAQUS/Explicit finite-element code.

A mesh convergence study using square elements near the crack tip with dimensions of 2400, 400, and 80 μm was performed to ensure that the desired element size of 80 μm provided adequate resolution in the plastic deformation region. The material models for PC and steel described in the next section were used for each of the convergence study simulations. The temperatures of elements surrounding the crack tip were compared to evaluate convergence. The temperature fields for the grids with 400- μm and 80- μm cells were identical. The temperature field for the 2400 μm element grid showed essentially no temperature increase, primarily because the element size was about twice as big as the plastic deformation zone. Consistency of the computed temperature fields for the two smaller element size grids indicated that both the 400 and 80 μm element size was adequate. However, the 80- μm size was chosen so that a direct comparison with the infrared detector measurements would be possible.

5.3 Material Model

The heating that occurs during high-rate deformation of ductile materials was shown in section 5.1 to result from plastic deformation through the coupling of plastic strain and temperature given by equations (41) and (42). Because the goal of this section is to establish the relative contribution of ductile deformation heating to the crack tip temperature field measured for PC during dynamic opening-mode fracture, an accurate description of high-rate deformation behavior of PC is needed. It was beyond the scope of this study to develop a rate-sensitive constitutive model for PC. Instead, high-rate behavior from published studies was used. In particular, Li and Lambros (2001) determined the high rate compressive behavior of PC specimens that were taken from the same lot of material used in this study. A split Hopkinson pressure bar technique was used to generate strain rates as high as 2200 s^{-1} . All tests were performed with the polymer material initially at room temperature. The stress-strain data measured by Li and Lambros (2001) for PC at compressive strain rates of 1200, 1700, and 2200 s^{-1} are shown in Figure 77. Note that the data reported by Li and

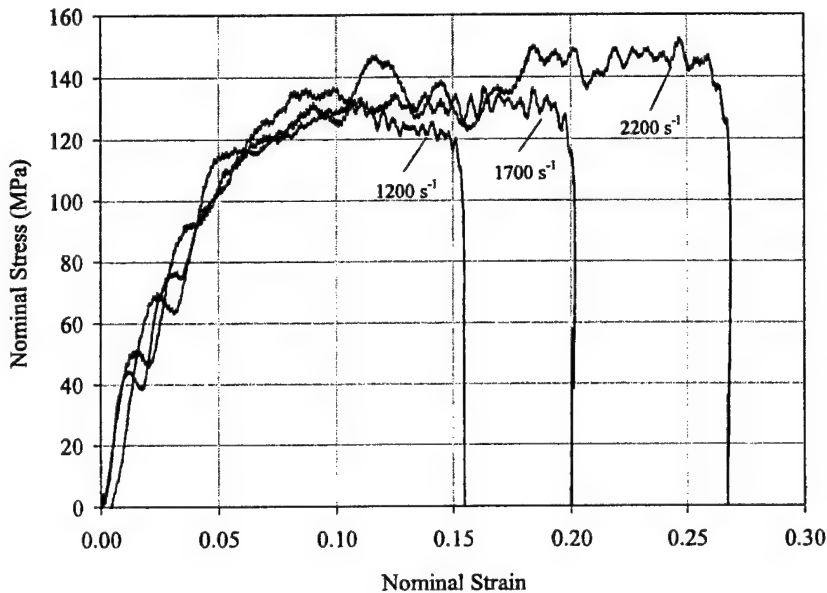


Figure 77. Nominal stress-strain data for dynamic compression of PC reported by Li and Lambros (2001). Results from three different strain rates are shown.

Lambros (2001) and which was shown in Figure 77 is nominal (engineering) stress and strain. The yield stress was observed by Li and Lambros (2001) to be dependent upon strain rate, varying from 45 to 70 MPa for the strain rates shown in Figure 77. The fraction of plastic work rate converted to heat, β , was also measured by Li and Lambros (2001) with the same infrared detector system used in this study. A β value of 0.5 was found for all strain rates examined. Table 3 shows the yield stress and fraction of plastic work converted to heat obtained from the experiments of Li and Lambros (2001). Rittel (1999) observed that β can increase to a value of 1 for strain rates of $\sim 8000\text{ s}^{-1}$.

Table 3. Uniaxial high strain-rate yield stresses and fraction of plastic work converted to heat (β) from Li and Lambros (2001).

Strain Rate (s^{-1})	Yield Stress (MPa)	β
1200	45	0.5
1700	50	0.5
2200	70	0.5

The material model used for PC was a rate-dependent incremental plasticity model that is standard in the ABAQUS/Explicit finite-element code and is commonly used for metals. The model decomposes the strain rate into elastic and plastic components and uses a Mises yield surface with associated plastic flow. Isotropic hardening is permitted. Equivalent compressive and tensile

behavior and the same Young's modulus for all strain rates are assumed in the model. The inputs required by the code user for this material model are the Young's modulus and a table of stress-strain pairs used to define the plastic portion of deformation for each strain rate. The code uses linear interpolation between the discrete number of points for strains not included in the table. To begin this process, the three nominal stress-strain curves shown in Figure 77 were approximated by a number of points connected with straight line segments.

The data points approximating the data of Li and Lambros (2001) are shown in Figures 78-80 for the three strain rates. The actual data input to the material model need to be in the form of Cauchy stress, σ_{Cauchy} , and logarithmic plastic strain, ε_{ln}^p . Assuming plastic deformation of PC to be incompressible (as is found to be the case for most metals), the conversion of nominal stress and strain to Cauchy stress and logarithmic plastic strain is

$$\sigma_{Cauchy} = \sigma_{nom} (1 + \varepsilon_{nom}), \quad (43)$$

$$\varepsilon_{ln}^p = \ln(1 + \varepsilon_{nom}) - \left(\frac{\sigma_{Cauchy}}{E} \right)_{yield point}, \quad (44)$$

where E is Young's modulus and the second term in equation (44) is evaluated at the material yield point. Equations (43) and (44) were used to convert the data points shown in Figures 78-80. The resulting "true" stress-strain data that were used in the code are shown in Figure 81. Note that the logarithmic strain in Figure 81 is plastic strain only. The elastic portion has been removed.

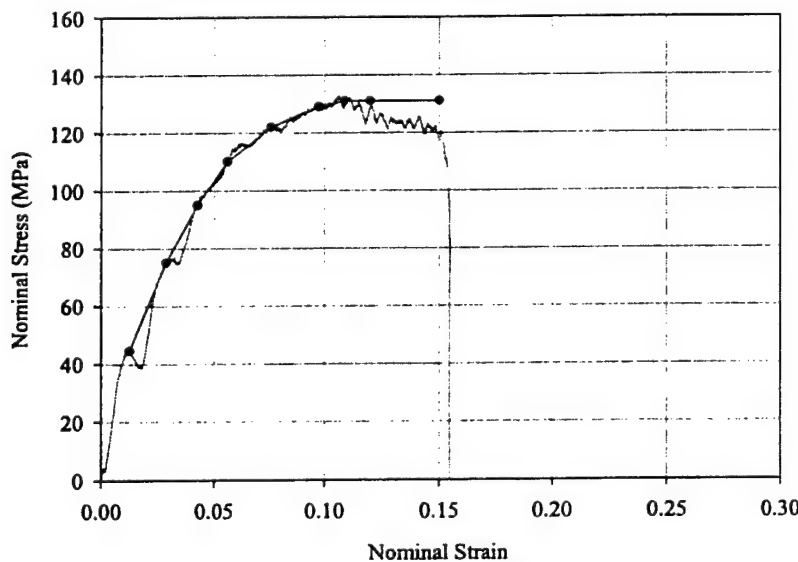


Figure 78. Approximation of the plastic part of the nominal stress-strain curve for PC at a strain rate of 1200 s^{-1} as used in the numerical simulation material model.

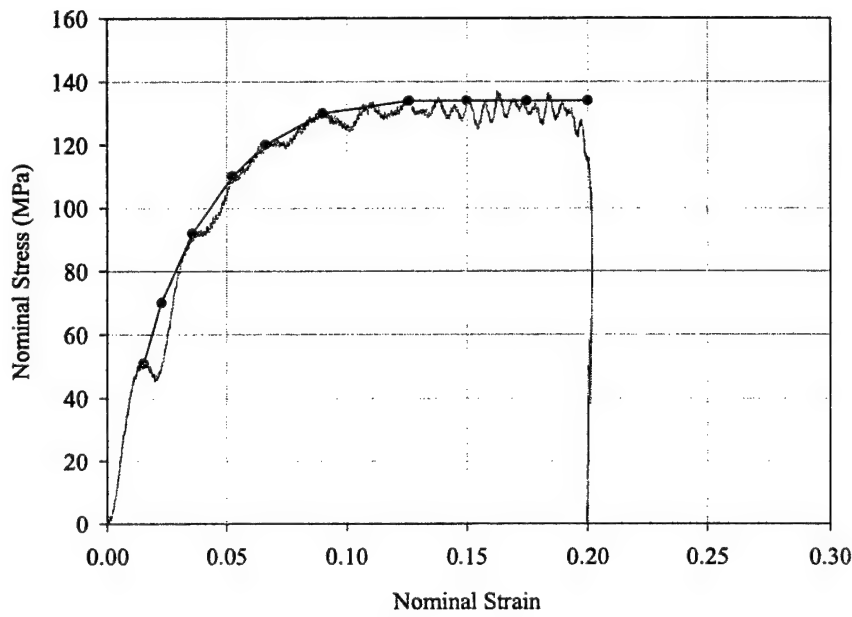


Figure 79. Approximation of the plastic part of the nominal stress-strain curve for PC at a strain rate of 1700 s^{-1} as used in the numerical simulation material model.

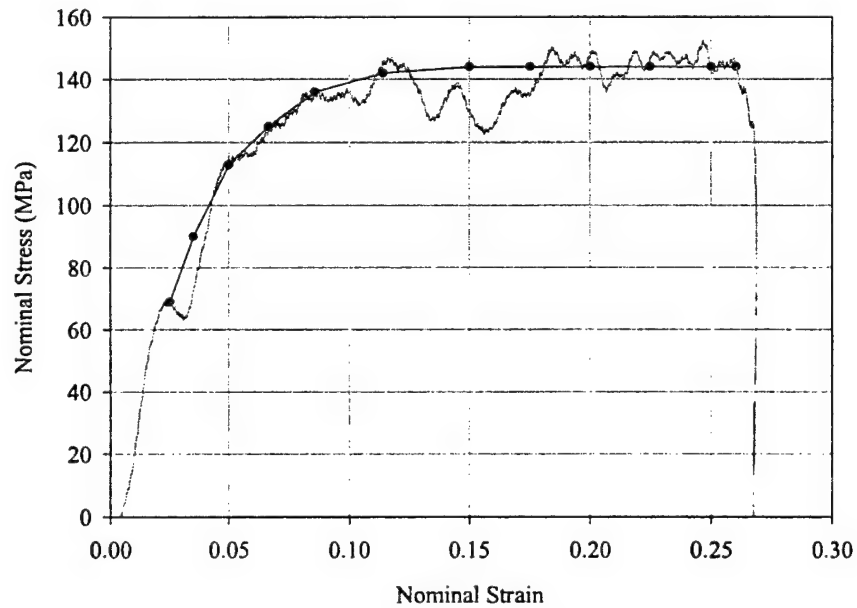


Figure 80. Approximation of the plastic part of the nominal stress-strain curve for PC at a strain rate of 2200 s^{-1} as used in the numerical simulation material model.

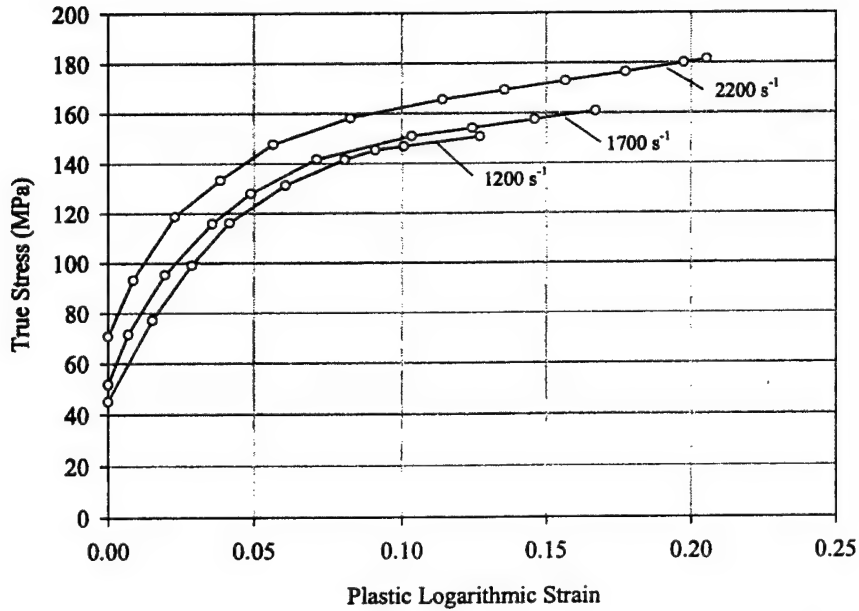


Figure 81. Cauchy (true) stress as a function of plastic logarithmic strain for three different strain rates of dynamic compression for PC.

The density, specific heat capacity, and Young's modulus used for PC were discussed in section 2 and are shown in Tables 1 and 2. It was mentioned in section 2 that Theocaris and Andrianopoulos (1982) found the modulus of PC to be relatively insensitive to strain rate at higher rates. This was also noted by Li and Lambros (2001) and is consistent with the assumptions of the rate-dependent plasticity model that is used here (i.e., constant Young's modulus).

Adiabatic heating of the material was permitted to occur only from plastic deformation (i.e., the internal heat generation term \dot{q} in equation (41) was not included in the thermomechanical coupling). The relationship that the ABAQUS finite-element code uses for thermomechanical heating is thus,

$$\beta \sigma_{ij} \dot{\epsilon}_{ij}^p = \rho c_p \dot{T}. \quad (45)$$

In all cases, β in equation (45) was taken to be 0.5. This was the experimentally obtained value from Li and Lambros (2001). If $\beta = 1$ was used (as suggested by Rittel 1999) the temperature results presented subsequently would scale accordingly. Either way, this does not affect the final conclusion as will be seen in the next section.

5.4 Simulation Results and Discussion

Because of computer memory restrictions, the finite-element simulation was of the first 4 mm of crack growth. After the crack had grown 4 mm according to the

crack tip position history given by Figure 76, the crack tip had reached the terminal speed of 550 m/s, and 50 nodes had been released along the plane of symmetry. The temperature field produced by the plastic deformation surrounding the propagating crack tip is shown in Figure 82. The finite-element grid is also shown in Figure 82. The elements along the plane of symmetry became sufficiently strained so much that the small strain assumptions built into the governing equations of the finite-element code were no longer valid. Hence, the temperatures calculated for these elements are likely not valid. For this reason, the results from the numerical simulation cannot be used to determine the temperature at the tip of a propagating crack, but rather the surrounding field should be used for comparison to the experimental results. In addition, the rigid body motion of the entire specimen in front of the detectors, which affects the experimental results, has not been accounted for in the numerical simulation. The effects of this motion are that the infrared detectors in the experiment view the passage of a crack propagating with an apparent speed slower than actual. Hence, some caution must be exercised when directly comparing the time scale of the numerical and experimental results.

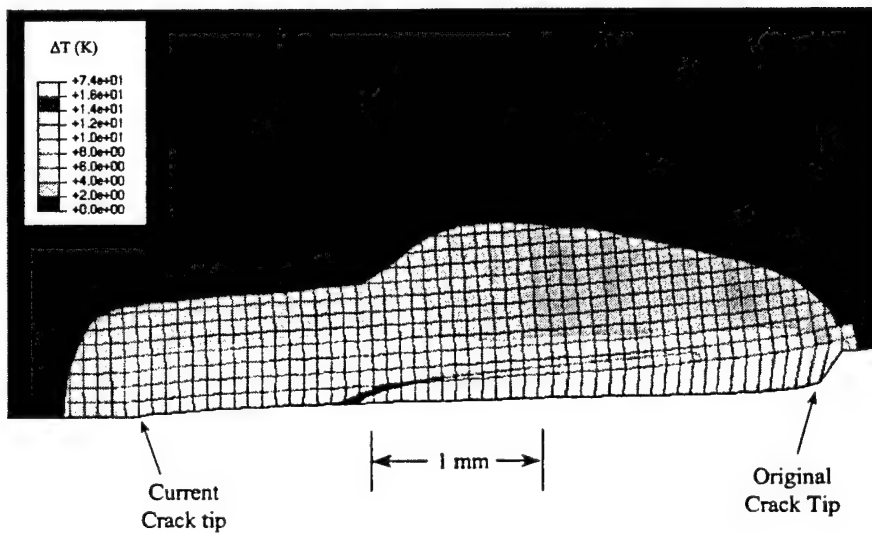


Figure 82. Temperature increase contours at the tip of a crack tip propagating in PC at a speed of 550 m/s predicted from the numerical simulation. Adiabatic heating was due solely to plastic work.

The temperature contours from the numerical simulation show a region of elevated temperature ahead of and lateral to the crack tip. The boundary of this heat affected zone extends ~ 0.5 mm ahead of the crack tip and 0.6 mm transversely. The temperature contours from the experiment, shown in Figure 83, shows the heat affected zone to extend several millimeters ahead of

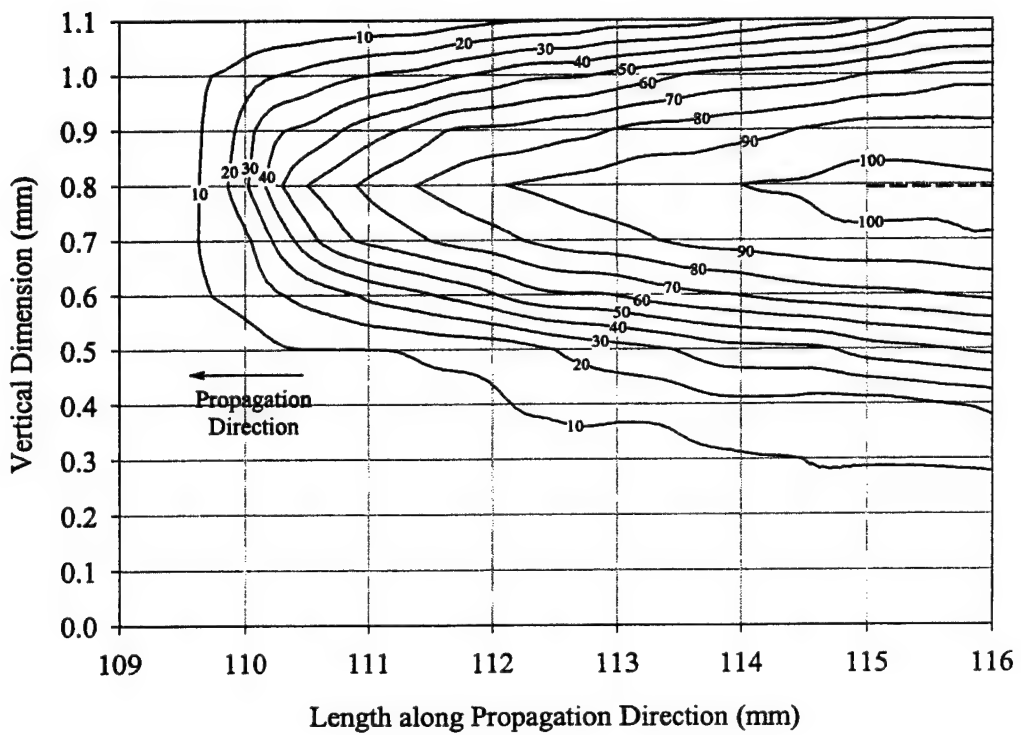


Figure 83. Temperature contours surrounding a crack tip propagating in PC at 550 m/s under mode I loading.

the peak in temperature. This clearly is not consistent with the numerical simulation. However, the lateral span of the measured temperature field is in reasonable agreement with the simulation. The peak temperature increase in the region near the crack tip for the experiment was 105 K. For the simulation, a temperature increase of 8 K was calculated. The simulation produced a maximum temperature increase only 8% of what was measured during the experiment. The simulation contour also shows the temperature to increase aft of the crack tip. This may be artificial because of the overstrained elements discussed earlier.

A column of elements located 3.2 mm (40 nodes) ahead of the initial crack tip was monitored for comparison with the experimental results. The column of nodes was oriented much like the infrared detector elements in the experiments, except the detector array was located 20 mm from the notch, whereas the column of elements in the simulation was 3.2 mm from the notch. The temperature of the first seven vertical elements closest to the crack propagation plane, excluding the element on the symmetry plane, is shown in Figure 84. This figure should be compared to Figure 73, which shows the temperatures measured during the

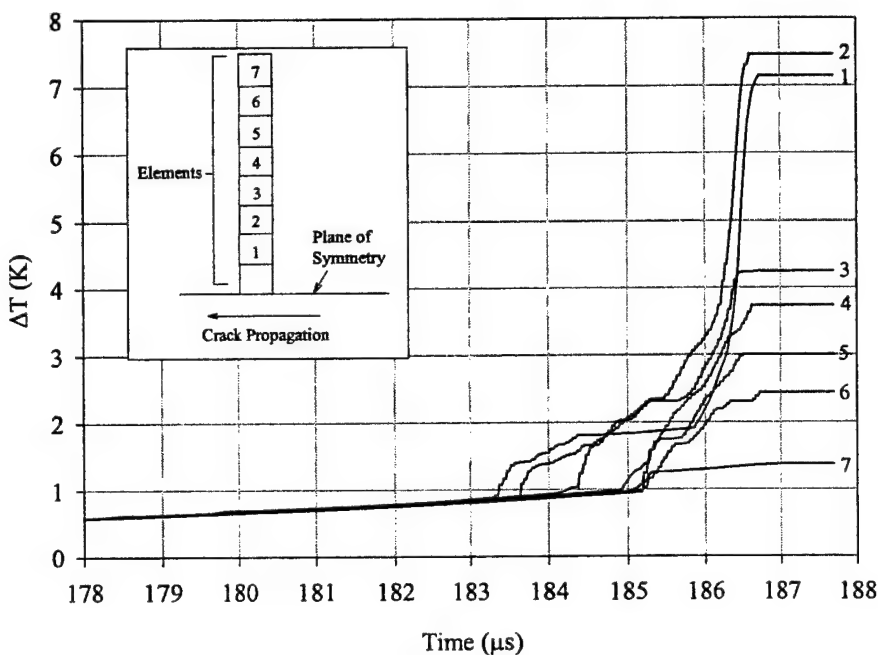


Figure 84. Temperature increase of a vertical array of finite elements located 3.2 mm from the initial notch tip for comparison to infrared detector measurements.

experiment in a similar format. Recall that in the experiments, the detectors are stationary and the crack propagates through their field of view. Thus, the infrared detector array viewed multiple material points passing by the field of view as the polymer specimen fractured and translated. This led to the decrease in recorded thermal signals after crack passage in Figure 73, reasons for which were discussed in section 3. The column of finite elements is tied to the moving specimen, thus the temperature will rise to a maximum and then plateau, as it does in Figure 84. The temperature-time curves for the simulation presented in Figure 84 show the temperature to slowly increase for about 2 μ s, and then abruptly increase to a plateau value during 1 μ s. For the experiment, the temperature rise time was about 8 μ s, considerably longer than for the simulation. There are several possible reasons for the discrepancy in temperature rise time. The node release technique that was used results in an abrupt release of nodes regardless of stress state in the material that it is associated with. In a real material, the failure of the material is likely to be less abrupt, and a gradual transition from fully constrained to fully released may be a more appropriate node release scheme. This could change the stress state in material surrounding the node being released. The recoil of suddenly severed polymer fibrils in the failed craze could potentially introduce a heat source aft of the actual crack tip, increasing the temperature rise time of the experiments. There is also the possibility that the opening of the heated crack faces past the

stationary infrared detector elements could introduce an increased rise time of the temperature signal recorded by the detector system. This is examined in detail in section 6.

The dynamic fracture experiments subjected PC to loading conditions different from those for which the material was characterized, i.e., the compressive split Hopkinson pressure bar experiments of Li and Lambros (2001). The polymer material in the vicinity of the propagating crack tip is predominantly in tension, and the tensile stresses are high enough to cause polymer chain scission and fracture at the tip of the crack. Significant temperature increase was observed during the experiments, and the heat-affected zone was relatively broad. Thus, under the loading conditions of the dynamic fracture experiments, classical metal plasticity behavior might provide an adequate description of PC.

The numerical simulations of the fracture event indicate that classical metal plasticity behavior does not adequately describe PC during opening-mode dynamic fracture. The numerical results, shown in Figures 82 and 84, show the temperature field surrounding the propagating crack to be significantly lower than that recorded during the experiments. There are several possible reasons for the discrepancy in the magnitude of the temperatures surrounding the propagating crack tip. The fracture event in a ductile, amorphous glassy polymer involves triaxial stress states, plastic deformation, and the motion, disentanglement, and scission of long chain molecules (Kambour 1964). The material model that was used to specify the behavior of PC in the finite-element code accounted only for ductile deformation, and the parameters used to describe this deformation were obtained only from uniaxial compression experiments. The mode I fracture surface of PC showed evidence of a highly localized single craze failure at the region where the infrared detector was focused. Given that the temperature contours from the experiments were relatively large in size (compared to those observed in brittle PMMA where a single craze also occurred), it seems likely that an improved ductility model for PC is needed. It stands to reason that adding a significant thermofracture contribution (\dot{q}) to the coupled heat energy equation given by equation (41) will increase the total crack tip temperature, but only in a highly localized manner. The thermofracture contribution to crack tip heating is explored in the next section. Because the thermofracture process is highly complex, crack tip heating in PMMA is considered to avoid introducing plasticity. This will permit a thermofracture model to be developed without needing to include the complexities of coupled plastic deformation.

6. Dissipative Cohesive Zone Model

6.1 Introduction

When a polymer well below the glass transition temperature is subjected to an imposed strain, a competition between classical shear yielding and craze formation occurs. As was discussed in section 1, crazing dominates this competition during opening mode crack growth of brittle polymers. The process of polymer crazing is quite well understood. There are three stages of polymer crazing (Kambour 1973; Kramer 1983), namely craze initiation, widening, and breakdown. These stages are depicted schematically in Figure 85. Using x-ray diffraction techniques, Kawabe et al. (1992) observed polymer chain alignment to occur ahead of the craze in PMMA and PC during quasi-static opening-mode loading. The region of molecular chain alignment is followed by areas of microvoid nucleation. Additional drawing of the material causes the micro-voids to enlarge, leading to the formation of oriented fibrils. The fibrils stretch until they reach a stretch ratio of ~ 4 (Donald and Kramer 1982; Wool 1995). The craze widens by a process of surface drawing (Kramer 1983): new polymer material is drawn into the craze fibrils from the bulk-fibril interface, referred to as the active layer (see Figure 85). The fibrils that do not elongate much beyond a stretch ratio of 4 grow in length by adding more material to their ends from the active layer. Kramer (1983) and Kramer and Berger (1990) assume the material in the active layer to behave as a non-Newtonian fluid. Craze breakdown occurs by the eventual failure of the fibrils. Kramer and Berger (1990) observed fibril failure to occur at the fibril-bulk interface, and not at the center of the craze width, and both noted that the fibril failure event is triggered by impurities in the polymer, which served as failure nucleation sites at the fibril-bulk interface.

The craze breakdown process results in the formation of two new surfaces, adding to the outer surface atoms a greater potential energy than those in the bulk of the material. During the creation of the two new surfaces, energy must be supplied to the material for the elevated potential energy state of the surface atoms. The amount of energy required is 2γ , where γ is the surface energy of the material (a material property). The craze formation event discussed above involves energy consuming processes additional to the surface energy requirements. The energy available for the dissipative crazing mechanisms is $(G-2\gamma)$, where G is the dynamic energy release rate supplied by the far field loading. The relative amount of energy available for additional dissipative processes is evident by comparing the energy needed to fracture a polymer, G , with the surface energy for the polymer. The dynamic energy release rate for

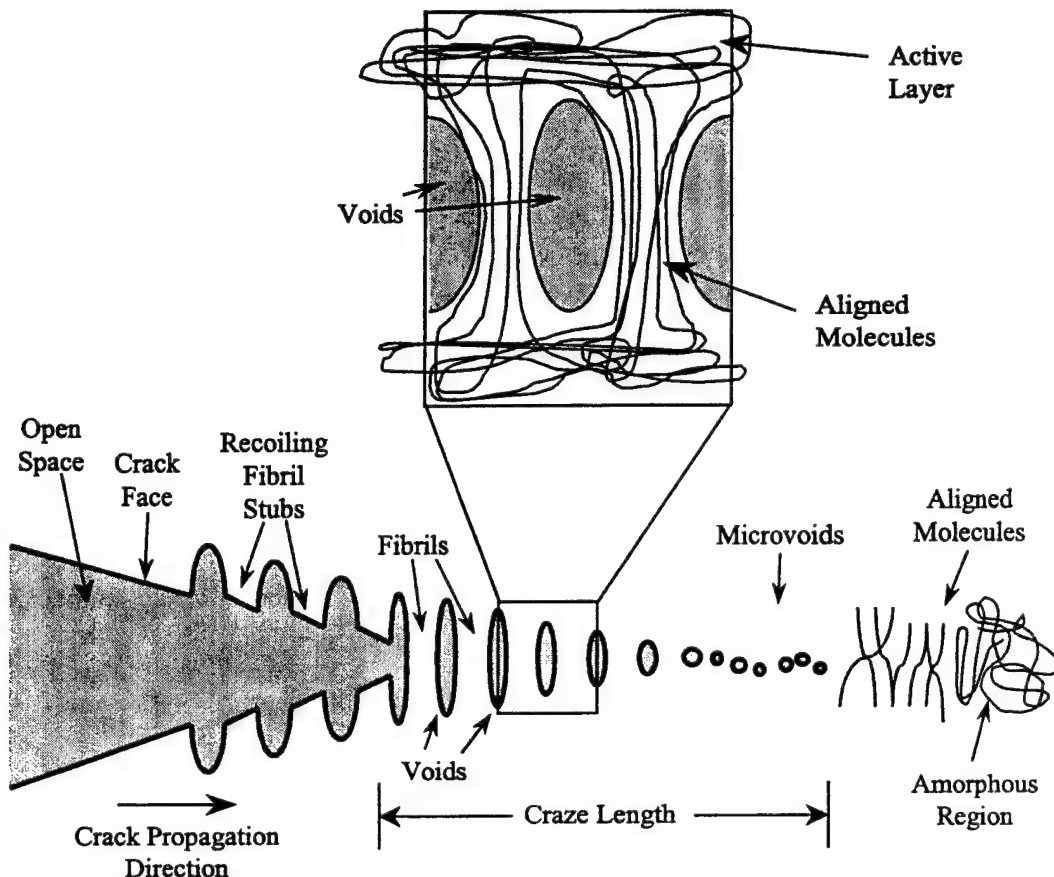


Figure 85. The initiation, widening, and breakdown of a polymer craze during opening-mode fracture. Aligned molecular chains form thick fibrils that resist crack opening.

opening mode fracture in PMMA was found in section 3 to vary from 2800 to 5600 J/m², depending on the crack tip speed measured. These measurements are in line with other previously quoted values (Döll 1976). However, in sharp contrast, the surface energy for polymers has been found to be several orders of magnitude lower than these measured G values. Wool (1995) cites a surface energy of 0.04 J/m² for polystyrene. Berry (1960) estimates the surface energy for PMMA to be ~0.1 J/m². These values for γ are quite small compared to the measured G values solely by added fracture surface area. For example, Sharon et al. (1996) found the amount of fracture surface area to increase six fold during high-speed dynamic fracture of PMMA, as discussed in section 3. Increasing the surface energy requirements by a factor of six still leaves the surface energy requirements for fracture very small compared to measured values of G. As such, approximately all of the energy used for polymer crazing during fracture can be assumed to be dissipated and likely results in the generation of heat. This assumption will be made in the remainder of this section.

The craze formation and breakdown process discussed earlier and shown in Figure 85 includes many mechanisms that likely generate heat. As mentioned earlier, Kawabe et al. (1992) observed molecular chain alignment ahead of a craze in PMMA and PC. Movement of the chains to the oriented configuration (to include sliding and rotation) would lead to heat generation. As craze fibrils form and lengthen, significant molecular chain motion occurs within the active layer (Kramer 1983; Kramer and Berger 1990). The chain motion within the active layer is also a likely source of heat generation. The ultimate failure of the craze fibrils involves molecular chain scission (Kramer and Berger 1990), molecular chain pull-out from surrounding material (Wool 1995), and recoil of the fibril stubs (Kambour 1964; Wool 1995). Each of these events can also occur in a dissipative manner. Although the mechanisms associated with polymer craze formation, growth, and failure have been studied, the amount of heating associated with the mechanisms is unknown.

The anatomy of a craze includes fibrils distributed along the length of the craze that resist craze opening. As mentioned above, this opening resistance occurs in a dissipative manner. The theoretical notion of a cohesive zone, introduced in section 1 and shown in Figure 86, is of similar character. Dugdale (1960) used the cohesive zone concept to account for material inelasticity in the vicinity of the crack tip and to analytically eliminate the stress singularity at the tip of a crack under mode I loading. The cohesive zone consists of a region ahead of the crack tip where the opening of the zone, δ , is resisted by a cohesive stress, σ , distributed along the cohesive zone, L . This is conceptually similar to craze formation ahead of a crack tip in brittle polymers, where the fibrils distributed along the craze length resist craze opening. As a consequence, various studies have successfully modeled the quasi-static crazing process during fracture of polymers with cohesive zones (Brown and Ward 1973; Peterson et al. 1974; Fraser and Ward 1978; Tijssens et al. 2000; Panda and Williams 2000; Allen and Searcy 2001). A critical element of the cohesive zone concept is the cohesive traction law that establishes the cohesion stress as a function of opening, i.e., $\sigma=\sigma(\delta)$.

Tijssens et al. (2000) developed a craze cohesive model with a traction-separation law motivated by micromechanical considerations. Their model includes the initiation, growth, and breakdown of polymer crazes, but unfortunately yields a set of equations that must be solved using a linear incremental analysis within a finite-element framework. Their application was limited to quasi-static loading of a PMMA plate with a central hole. A slow growth crack model for polyethylene using a cohesive zone methodology was developed by Panda and Williams (2000). A traction-separation law was measured using a tensile test

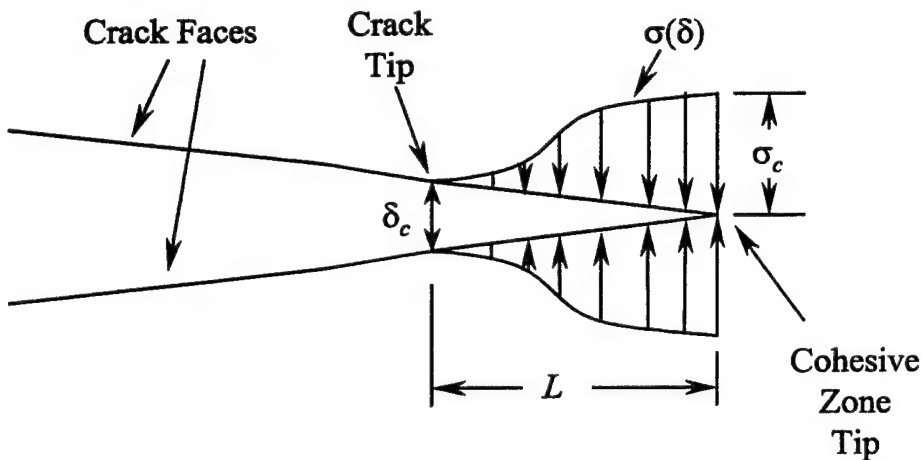


Figure 86. Cohesive zone concept at the tip of a propagating crack. Crack face opening, δ , is resisted by a cohesive traction σ .

specimen with a pre-cut notch to induce a craze. However, in that study the highest displacement rate of the load frame grips was limited to 50 mm/min, far below the rates of interest in this study. Allen and Searcy (2001) presented a viscoelastic cohesive zone model that incorporates dynamic effects. The cohesive traction law for this model was based on micromechanical observations of polymer craze fibril behavior. The model of Allen and Searcy (2001) was presented as an analytical tool and was not evaluated against dynamic fracture experiments. Kubair et al. (2001) derived a rate-dependent cohesive traction law, but it also was not compared to experimental data.

The opening profile of the craze at the tip of a quasi-statically growing crack was measured by Brown and Ward (1973) and Fraser and Ward (1978) for PMMA, and by Morgan and Ward (1977) for PC. Each of these studies concluded that the constant stress cohesive traction law of Dugdale (1960) provided reasonable agreement with the optical measurements of craze opening. However, the studies were limited to quasi-static crack growth. Peterson et al. (1974) used holographic interferometry to deduce the stress distribution along a stationary craze in PC as well as the craze opening profile. In contrast to Morgan and Ward (1977), they concluded that the stress profile was nonlinear, and the peak stress occurred at a position aft of the craze tip. Suzuki et al. (1997) measured the crack face opening profile for cracks propagating at 200 m/s in PMMA. Unfortunately, measurements of crack opening in the vicinity of the craze could not be made in that work. Thus, although some (conflicting) information on the nature of the traction-separation law, $\sigma = \sigma(\delta)$, for quasi-static crack growth in PMMA exists, little is known in the dynamic crack growth case.

This section presents a dissipative cohesive zone model in which the craze energy is assumed to be converted to heat, applicable to brittle polymers prone to single craze failure, such as PMMA impacted at low-speeds. Several cohesive

traction laws are evaluated against experiment, and the model is used to make predictions of crack tip heating for each of the traction laws at various crack tip speeds. The predictions are then directly compared to the temperature measurements presented in section 3 for opening-mode dynamic fracture of PMMA. To the author's knowledge, this effort represents the first attempt to use the cohesive zone concept for modeling thermal dissipation in brittle polymers during high-speed fracture.

6.2 Cohesive Zone Model

The notion of a cohesive zone at the tip of a crack was first introduced by Barenblatt (1959) and Dugdale (1960) to analytically eliminate the stress singularity at the tip of a crack under mode I loading. A cohesive zone is introduced as a line that extends from the crack tip to model the inelastic response of the material ahead of the crack, depicted in Figure 86. In this model, the material opening, δ , ahead of the crack tip is opposed by a cohesive stress, σ , acting along the cohesive zone line of length L . The opening displacement is zero at the front tip of the cohesive zone and reaches a maximum, denoted δ_c , at the rear of the cohesive zone. At the same time the cohesive traction σ , starts from a maximum value of σ_c at the forward tip of the cohesive zone and decreases to zero as the end of the cohesive zone is approached (i.e., at $\delta=\delta_c$). The end of the cohesive zone, which is the first point of separation of the crack faces, can be considered the crack tip. Therefore, the location of maximum opening displacement in the cohesive zone is the location where the physical crack tip begins. Barenblatt (1959) considered the case of pure material cleavage at the tip of a crack. For the crack to advance, atomic bonds must be broken to permit the creation of new surfaces. Barenblatt (1959) assumed a unique relationship between atomic force and the separation between atoms as the basis of a cohesive traction law. Dugdale (1960) considered the cohesive zone for an elastic-perfectly plastic material. The transition from elastic-to-plastic behavior occurred at the leading edge of the cohesive zone. The cohesive traction law used by Dugdale (1960) was of constant stress and will be one of several cohesive laws explored in this chapter.

Freund (1990) extended the cohesive zone idea to the dynamic crack growth case. Because the cohesive zone modeling performed in the present study builds upon the results of Freund (1990), a summary of the Freund (1990) analysis is presented here for completeness. Consider a mode I crack tip propagating with speed a under plane stress conditions. To obtain a relationship between an arbitrary cohesive traction law and the length of the cohesive zone, L , the flux of energy into the crack tip is considered from two different contours surrounding the crack tip, as shown in Figure 87. The contour Γ_{app} is circular in shape with a center at the leading edge of the cohesive zone and has a large radius compared to the length of the cohesive zone. If this contour is located within the region

where the stresses are accurately described by the asymptotic solution given by equation (1), the energy flux F through Γ_{appl} is given by Freund (1990) as

$$F(\Gamma_{appl}) = \frac{\dot{a}A_I}{E} (K_I^d)_{appl}^2, \quad (46)$$

where E is the Young's modulus for the material, A_I is the mode I universal constant defined in section 2 which is a function of \dot{a} , and $(K_I^d)_{appl}$ is the dynamic mode I stress intensity factor resulting from applied far-field tractions.

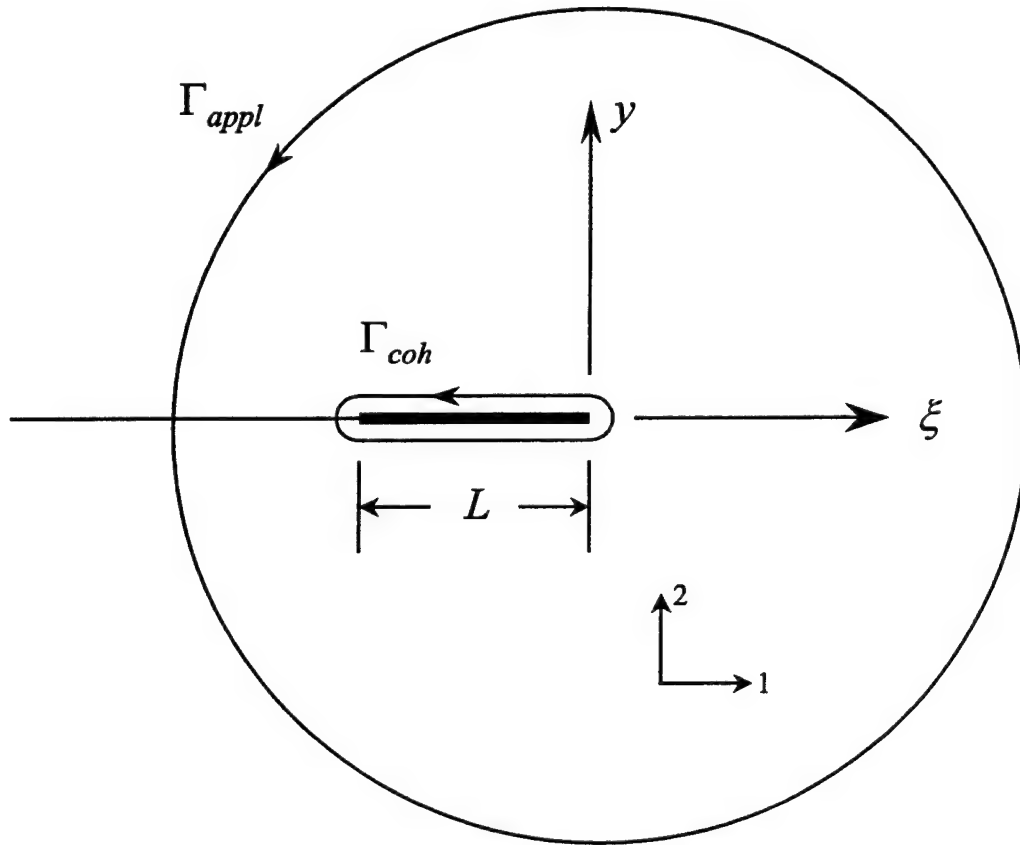


Figure 87. Far field and near tip contours used for calculating energy flux into a crack tip with a cohesive zone of length L (Freund 1990).

A second contour, Γ_{coh} , surrounds the actual cohesive zone itself. The energy flux through this contour (Freund 1990) is

$$F(\Gamma_{coh}) = 2 \int_{-L}^0 \sigma_{2j} \dot{u}_j d\zeta, \quad (47)$$

where u_j is displacement, repeated indices imply summation, and the superposed dot denotes a material time derivative. Within the cohesive zone, $\delta(\xi, t) = 2u_2(\xi, 0, t)$, $\sigma_{12}(\xi, 0, t) = 0$, and $\sigma_{22}(\xi, 0, t) = \sigma[\delta(\xi)]$. Thus, equation (77) reduces to

$$F(\Gamma_{coh}) = \int_{-L}^0 \sigma(\delta) \dot{\delta}(\zeta, t) d\zeta, \quad (48)$$

where the superposed dot again denotes a material time derivative. The material time derivative of $\delta(\xi, t)$ is

$$\dot{\delta}(\xi, t) = \frac{\partial \delta}{\partial t} - \dot{a} \frac{\partial \delta}{\partial \xi}. \quad (49)$$

Using equation (49) in equation (48) gives the following for the energy flux through Γ_{coh} :

$$F(\Gamma_{coh}) = \int_{-L}^0 \sigma(\delta) \frac{\partial \delta}{\partial t} d\zeta + \dot{a} \int_0^{\delta_c} \sigma(\delta) d\delta. \quad (50)$$

Under steady-state crack growth conditions, the first term on the right hand side of equation (50) is zero. Additionally, steady state crack propagation ensures that $F(\Gamma_{coh}) = F(\Gamma_{appl})$, yielding

$$\frac{A_I}{E} (K_I^d)_{appl}^2 = \int_0^{\delta_c} \sigma(\delta) d\delta. \quad (51)$$

The dynamic energy release rate G is introduced using equation (18)

$$G = \frac{A_I}{E} (K_I^d)_{appl}^2, \quad (52)$$

which gives

$$G = \int_0^{\delta_c} \sigma(\delta) d\delta. \quad (53)$$

Equation (53) relates the cohesive traction law to the dynamic energy release rate. It is easy to see from this relation that G is the area under the σ - δ curve. This makes sense physically as well because the cohesive tractions, σ , do exactly this amount of work over the cohesive opening δ , as the crack extends.

The next step in obtaining the relationship between an arbitrary cohesive traction law and the length of the cohesive zone, L , is to obtain an expression for $(K_I^d)_{appl}$ in equation (51). Freund (1990) derived an expression for the stress intensity factor resulting from the cohesive traction, $(K_I)_{coh}$, as

$$(K_I)_{coh} = -\sqrt{\frac{2}{\pi}} \int_0^L \frac{\sigma(l)}{\sqrt{l}} dl, \quad (54)$$

with the negative sign in equation (54) giving a negative stress intensity because the cohesive tractions are resisting crack opening. The total stress intensity factor for the crack is the sum of $(K_I)_{coh}$ and $(K_I^d)_{appl}$. To eliminate the stress singularity at the crack tip (the reason for introducing a cohesive zone in the first place), the total stress intensity factor must equal zero. Thus, $(K_I)_{coh} = -(K_I^d)_{appl}$, giving

$$(K_I^d)_{appl} = \sqrt{\frac{2}{\pi}} \int_0^L \frac{\sigma(l)}{\sqrt{l}} dl. \quad (55)$$

Substituting equation (55) into equation (52) gives the final expression relating the cohesive traction to the length of the cohesive zone (Freund 1990)

$$\int_0^{\delta_c} \sigma(\delta) d\delta = \frac{2A_I}{\pi E} \left[\int_0^L \frac{\sigma(l)}{\sqrt{l}} dl \right]^2. \quad (56)$$

If equation (53) is used, G can be related to the cohesive zone length through the relationship

$$G = \frac{2A_I}{\pi E} \left[\int_0^L \frac{\sigma(l)}{\sqrt{l}} dl \right]^2. \quad (57)$$

To solve for the cohesive zone length, L , a particular form for the cohesive traction law must be assumed. However, as can be seen in equation (56), the cohesive tractions can be expressed either as the cohesive traction law, $\sigma(\delta)$, or as a distribution along the length of the cohesive zone, $\sigma(\xi)$. The $\sigma(\xi)$ relation will be referred to herein as the cohesive zone stress distribution. Freund (1990) provides a relationship between the opening displacement and position along the cohesive zone for an arbitrary cohesive stress distribution as follows:

$$\frac{\partial \delta}{\partial \xi} = \frac{2\lambda_1(1-\lambda_2^2)}{\pi \mu D} \int_0^L \sqrt{\frac{\xi}{\eta}} \frac{\sigma(\eta)}{(\xi-\eta)} d\eta, \quad (58)$$

where λ_1 , λ_2 , and D were defined in section 2, and μ is the material shear modulus. Closed form solution of equation (56), which requires solution of the Cauchy singular integral equation given by equation (58), is then possible only for simple cohesive traction laws, such as the constant stress law used by Dugdale (1960). For more complicated $\sigma(\delta)$ traction laws, an iterative numerical procedure is used to solve equations (56) and (58). An easy

alternative, which has a wider variety of analytical solutions, is to assume a $\sigma(\xi)$ relation. This effectively assumes the spatial variation of stresses ahead of the crack tip. Equation (58) can then be used to analytically solve for a number of $\sigma(\xi)$ relations. Because there is a unique one-to-one relation between $\sigma(\delta)$ relations and resulting $\sigma(\xi)$ relations, it is possible to inversely derive the behavior of various $\sigma(\delta)$ laws. This approach has been used in the present work. Alternatively, a numerical solution of equation (58) for $\sigma(\delta)$ is possible, as discussed in Kubair et al. (2001). This point will be further discussed later.

6.2.1 Thermal Dissipation in a Cohesive Zone

For a specific cohesive stress distribution, equations (56) and (58) give the cohesive zone length and opening profile along the length. The aim of this study is to extend the previous set of equations, derived in Freund (1990), to yield the thermal dissipation within the cohesive zone. For a material that exhibits negligible plastic deformation, the heat energy equation given by equation (8) reduces to

$$\rho c_p \dot{T} = \dot{q}, \quad (59)$$

where \dot{q} is the volumetric internal heating associated with brittle fracture. Integrating equation (59) gives an explicit expression for the temperature increase of the material from an initially traction free state as

$$\Delta T(t) = \frac{1}{\rho c_p} \int_0^t \dot{q}(\tau) d\tau. \quad (60)$$

The primary task in evaluating equation (60) is to relate the internal heating rate, $\dot{q}(t)$, to the cohesive zone.

Sun and Hsu (1996) obtained an analytic expression for \dot{q} of the form $(G - 2\gamma)\dot{a}\delta(x - x_0)\delta(y - y_0)$, under the conditions of stable crack growth, where δ is the Dirac-delta function, x and y are coordinates, and the zero subscript denotes the current crack tip coordinates. Physically the term $(G - 2\gamma)$ represents energy that has flowed through the crack tip region (G), but is in excess of that needed for crack surface formation (2γ), as discussed in the previous section. The analytic expression for \dot{q} by Sun and Hsu (1996) conceptually makes sense, but is dimensionally incorrect. The expression has units of J/m s , whereas the governing equation for which it was derived requires it to have the units of $\text{J/m}^3 \text{s}$. The expression for \dot{q} obtained in this study differs significantly from that of Sun and Hsu (1996) in that the internal heating rate is related to the mechanics of the cohesive zone.

The rate of work \dot{W} done by the cohesive traction at any point inside the cohesive zone is

$$\dot{W}(\xi) = \sigma(\xi)\dot{\delta}(\xi). \quad (61)$$

Equation (61) represents the rate of energy dissipated at a location ξ within the cohesive zone, and is equated to the rate of internal heat generation \dot{q} . However, the work rate given by equation (61) is per unit area, whereas the internal heating rate used in equation (60) is per unit volume. What is needed to remedy this situation is to include in equation (61) the amount of material above and below the fracture surface associated with heat generation. Adding a volumetric aspect to the cohesive zone concept deviates from the development of the cohesive zone model because the cohesive zone is idealized as a line of zero thickness along the crack propagation path. Defining the thickness of material within the cohesive zone associated with material heating as $H(\xi)$, the expression for the internal heating rate is

$$\dot{q}(\xi) = \frac{\sigma(\xi)\dot{\delta}(\xi)}{H(\xi)}. \quad (62)$$

The thickness $H(\xi)$ is not necessarily the same as the cohesive opening displacement $\delta(\xi)$ because, as discussed in section 6.1, polymer material feeds into the fibril from an active layer at the bulk-fibril interface (see Figure 85). The thickness of this active layer is unknown. Substituting equation (62) into equation (60) and noting that under steady-state conditions time and position within the cohesive zone can be interchanged, the expression for the temperature increase within the cohesive zone is

$$\Delta T(t) = \frac{1}{\rho c_p} \int_0^t \frac{\sigma(\tau)\dot{\delta}(\tau)}{H(\tau)} d\tau. \quad (63)$$

Because the temperature predicted by the model derived in this section will be compared to the temperature measurements made by the infrared detector presented in section 3, an expression for the temperature recorded by the infrared detector elements is derived here. As stipulated above, the thickness of material associated with heating is $H(\xi)$. The infrared detector has a dimension of 80 μm and, as discussed in section 3, will provide an output proportional to the radiation incident on the entire detector element area. Figure 88 illustrates the case of H less than the detector size which is most likely the case based on quasi-static results for H . The temperature sensed by the detector element in Figure 88 is

$$\Delta T_{det} = \frac{H}{y_{det}} \Delta T_{actual}, \quad (64)$$

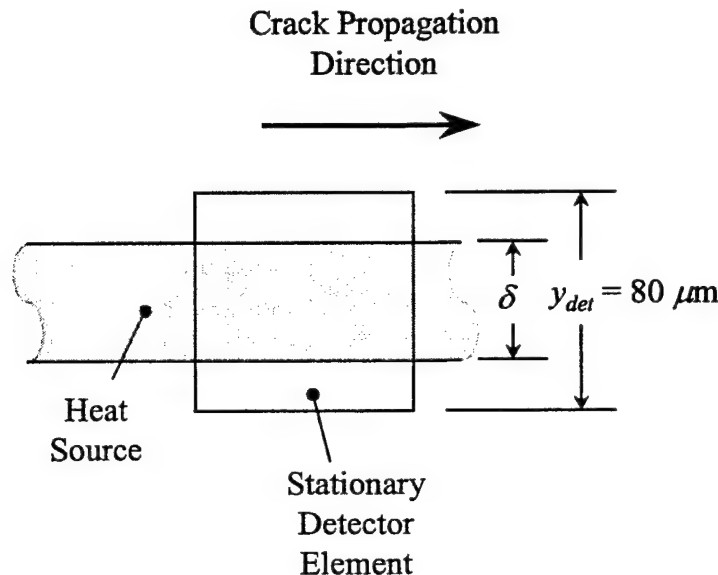


Figure 88. Heat source smaller than the infrared detector element passing over the region monitored by the detector. The element responds to the average radiation incident on the entire area monitored.

where ΔT_{det} is the temperature increase sensed by the detector element, ΔT_{act} is the true temperature of the heat-affected region, and y_{det} is the height of the detector element (80 μm for this study). Substituting equation (64) into equation (63) gives the following as the temperature increase that the infrared detector element would sense from a dissipative cohesive zone,

$$[\Delta T(t)]_{det} = \frac{1}{\rho c_p y_{det}} \int_0^t \sigma(\tau) \dot{\delta}(\tau) d\tau. \quad (65)$$

Calculating the temperature increase for the infrared detector element eliminates the need to determine the actual thickness of the heat affected region. The disadvantage to this is that the true temperature increase cannot be determined unless an additional relationship is introduced to specify the thickness H . For heat sources with a thickness less than the detector element size, the infrared detector system underpredicts the true temperature.

An algorithm based on the previous model development was constructed for predicting the temperature increase at the tip of a dynamically propagating mode I crack in PMMA. The following procedure was used.

- A cohesive stress distribution is specified as $\sigma(\xi)$.
- The dynamic energy release rate G is obtained for a particular crack tip speed.
- The length of the cohesive zone is obtained using equation (57).

- Equation (58) is used to obtain an expression for $\partial\delta/\partial\xi$.
- The temperature increase sensed by the infrared detector element is calculated using equation (65) assuming steady-state crack growth and the result of step 4.

The results prior to step 4 of the algorithm permit the cohesive traction law, $\sigma(\delta)$, to be determined for a given cohesive stress distribution $\sigma(\xi)$, specified in step 1.

It was pointed out in the section 6.1 that the total amount of energy available for dissipation is $(G-2\gamma)$, not simply G as assumed in equation (57). However, it was also discussed that 2γ is several orders of magnitude less than G . In the results that follow, all of the measured G will be assumed available for dissipation within the cohesive zone given the relatively insignificant surface energy requirements.

6.2.2 Cohesive Traction Laws and Stress Distributions

The first step in the algorithm listed above is to select a suitable cohesive zone stress distribution. In doing so, a unique cohesive traction law is implicitly selected given the one-to-one relation between $\sigma(\xi)$ and $\sigma(\delta)$ discussed earlier. Numerous traction laws have been examined in the past, and they generally fall into one of two categories, intrinsic and extrinsic (Kubair and Geubelle 2001). Intrinsic cohesive traction laws, depicted on the left of Figure 89, have a material failure criterion built into the traction law. Material within the cohesive zone strengthens as the zone opens until a critical stress, σ_c , is achieved. Physically, σ_c represents the material strength and must be obtained from experiments, i.e., it is a material property. Further opening of the cohesive zone results in a weakening of the material to eventually zero stress. The area under the $\sigma\text{-}\delta$ curve is equal to the dynamic energy release rate, G . Needleman (1987), Suo et al. (1992), and Xu and Needleman (1994) used an exponential law as an intrinsic cohesive traction. A bilinear intrinsic cohesive traction law was used by Geubelle and Baylor (1998) and Lin et al. (2001), and a trapezoidal-shaped law was used by Tvergaard and Hutchinson (1992). The other category of cohesive traction law is extrinsic, where the strengthening portion of the traction curve is not included, as shown on the right side of Figure 89. Extrinsic laws were used by Barenblatt (1959), Dugdale (1960), Geubelle and Rice (1995), and Camacho and Ortiz (1996). In this study, an extrinsic cohesive traction law will be used; however, as discussed, it is derived from an initial cohesive stress distribution $\sigma(\xi)$. This is done to permit a closed form solution of equation (58). The area under the traction law curve, G , was measured during the experiments discussed in section 3. The material critical stress, σ_c , however, was not directly measured. In fact, it is not very clear how to measure the critical stress of a material. As such, the only parameter that is not known *a priori* is the critical stress, σ_c . However, as will be discussed later,

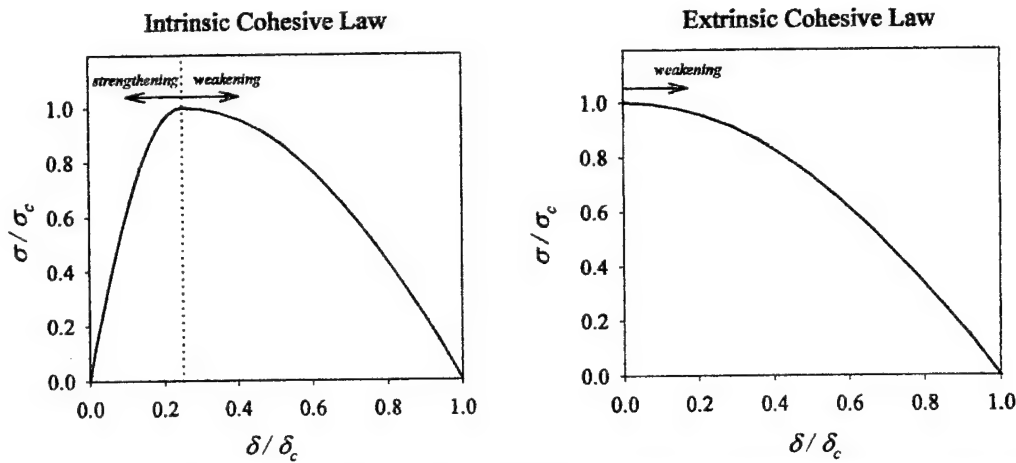


Figure 89. Illustration of intrinsic and extrinsic cohesive traction laws (Kubair and Geubelle 2001).

a reasonable estimate of σ_c can be made from the quasi-static experiments shown in Figure 5. All other parameters needed for the algorithm previously listed are measured quantities.

The two extrinsic rate-independent cohesive stress distributions initially examined are the constant stress distribution and a linear stress decay distribution. These distributions were selected for their simplicity and because an analytic solution of equation (58) could be obtained. The constant stress distribution is considered first. Dugdale (1960) proposed a constant stress cohesive traction law of the form

$$\sigma(\delta) = \sigma_c, \quad (66)$$

where σ_c is a constant, critical stress. Dugdale (1960) assumed the material to deform plastically when stressed beyond σ_c . Because the cohesive stress is constant and independent of the cohesive opening, the cohesive stress distribution $\sigma(\xi)$ is also constant and equal to σ_c , as shown in Figure 90. With this in mind, the length of the cohesive zone, L , is determined from equation (57). Details of the solution procedure are provided in Appendix A. The resulting analytic expression for the cohesive zone length is

$$L = \frac{\pi E G}{8 A_c \sigma_c^2}. \quad (67)$$

With the length of the cohesive zone determined, the rate of change of the cohesive opening displacement, i.e., equation (58), can be obtained. An analytic expression was obtained for equation (58). The solution technique for solving the resulting Cauchy singular integral equation is provided in Appendix B. The final expression is

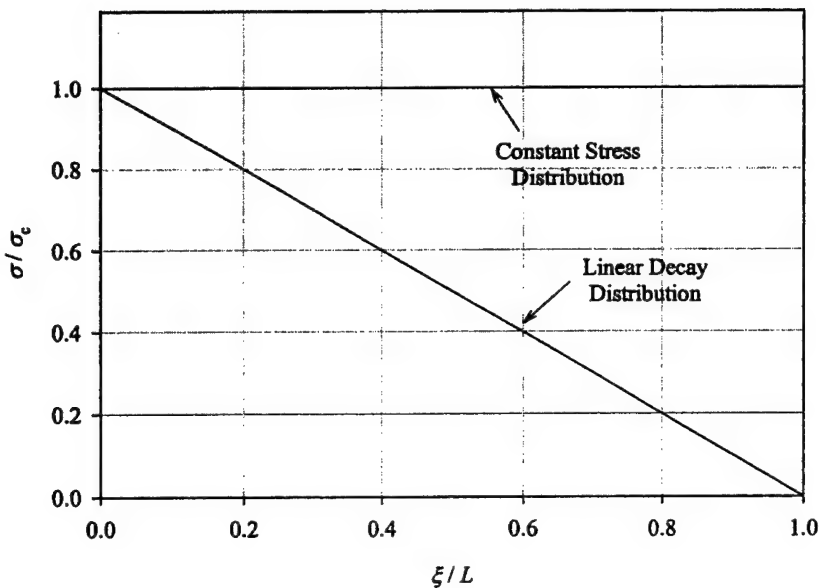


Figure 90. Form of constant and linear decay stress distributions used in the dissipative cohesive zone model.

$$\frac{\partial \delta}{\partial \xi} = -\frac{C\sigma_c}{\pi\mu} \ln\left(\frac{\sqrt{L} - \sqrt{\xi}}{\sqrt{L} + \sqrt{\xi}}\right), \quad (68)$$

where

$$C = \frac{2\lambda_1(1 - \lambda_2^2)}{D}. \quad (69)$$

This completes step (4) from the algorithm outlined above. Calculation of the temperature increase from the widening cohesive zone (solution of equation [65]) requires a change of variables in equation (60) from ξ to t . Assuming steady state crack propagation speed, the change of variables is $\xi = \dot{a}t$. The integration of equation (6.20) to yield ΔT_{det} could not be performed analytically. Instead, numerical integration was performed using a trapezoidal area technique that is standard in SigmaPlot (SPSS Inc. 2000). The high-rate baseline properties for PMMA listed in Tables 1 and 2 were used, along with a G value of 3000 J/m² and a critical stress σ_c of 120 MPa. The value for G corresponds to a crack tip speed of 300 m/s (see Figure 36), which was the low-speed crack growth case in section 3 where a single craze formed along the crack path. It is for this case that the dissipative cohesive model would be expected to have best agreement. The critical stress was estimated based on the tensile stress-strain data presented in section 2 for PMMA, assuming additional rate effects. The critical stress value used is discussed in greater detail in the next section. The predicted temperature

increase (normalized by ambient temperature) for the constant stress cohesive traction law is shown in Figure 91. The normalized temperature increases with normalized time until a final value of 0.062 is reached at the crack tip. A thorough comparison of these results with the dynamic mode I fracture experiments of PMMA will be made in the next section.

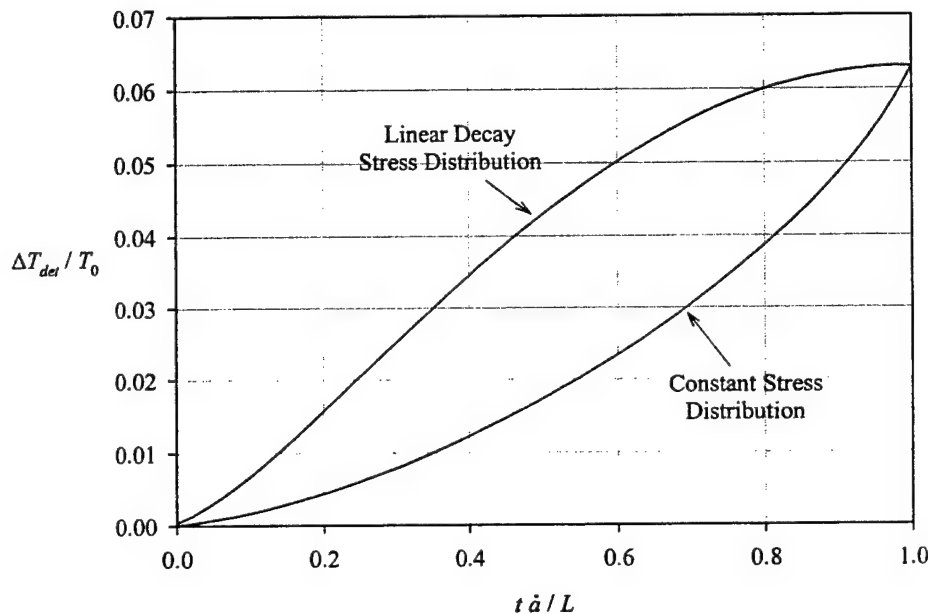


Figure 91. Temperature increase predictions made with the dissipative cohesive zone model using the constant stress and linear decay stress distributions. Baseline material properties for PMMA and a crack propagation speed of 300 m/s were used. Ambient temperature T_0 is 295 K.

The second cohesive stress distribution considered is one where the stress decays linearly. It will be shown that this stress distribution does not result in a linear decay cohesive traction law, $\sigma(\delta)$, as was used by Camacho and Ortiz (1996). The particular form of the stress distribution is shown in Figure 90, and has the following analytic form:

$$\sigma(\xi) = \sigma_c \left(1 - \frac{\xi}{L}\right), \quad (70)$$

where once again σ_c is the critical stress and L is the yet to be determined cohesive zone length. Solution of equation (57) for L using the linear stress distribution results in the following analytic expression:

$$L = \frac{9\pi EG}{32A_I \sigma_c^2}. \quad (71)$$

Details of the solution procedure for obtaining equation (71) are provided in Appendix A. For equivalent crack growth conditions, the cohesive zone length of the linear stress distribution model is 2.25 times greater than that of the constant stress case. The closed form expression of $\partial\delta/\partial\xi$ for the linear decay cohesive stress distribution is derived in Appendix B. The final expression is

$$\frac{\partial\delta}{\partial\xi} = \frac{2C\sigma_c}{\pi\mu} \left[\frac{\sqrt{\xi L}}{L} + \frac{\xi - L}{2L} \ln\left(\frac{\sqrt{L} - \sqrt{\xi}}{\sqrt{L} + \sqrt{\xi}}\right) \right], \quad (72)$$

where C is given by equation (69). The quantity ΔT_{det} from equation (65) was obtained for the linear distribution case in the same manner as was used for the constant stress case. The results are also shown in Figure 91, along with the results from the constant stress case. The temperature increase is approximately the same as was calculated for the constant stress case. However, as will be seen later, the rise time for the temperature increase is considerably longer for the linear case because the cohesive zone length, L is longer (by a factor of 2.25 as previously discussed). A significant difference in the qualitative behavior of the two different stress distributions is that the temperature increase for the constant stress case terminates with a high slope, whereas the linear decay case has a roll-off near the peak temperature. The temperature roll-off will be shown in the next section to be consistent with the general behavior of the temperatures recorded during the fracture experiments presented in section 3.

During the solution procedure previously mentioned, the stress and opening displacement are both calculated as a function of position within the cohesive zone. These two quantities can be cross-plotted to depict the cohesive traction law $\sigma(\delta)$. Figure 92 shows this for the two $\sigma(\xi)$ distributions considered thus far. As should occur, the constant stress distribution is constant in both $\sigma\text{-}\xi$ and $\sigma\text{-}\delta$ space. The linear decay case, however, is not of the same form for the two spaces. Slight deviations from linearity are observed for this traction law. Most of the deviation is for small cohesive zone openings. The remainder of the curve, however, is nearly linear.

Before attempting a comparison with experimental data, a parametric study was performed to examine the sensitivity of the cohesive zone model to parameter variations and thus provide a better understanding of the effects important to the generation of heat within the cohesive zone. The parameters varied were E , G , σ_c , and \dot{a} . The linear decay cohesive stress distribution derived above was used for the parametric study. The cohesive zone algorithm was used to obtain the variations of temperature (ΔT_{det}) and internal heating rate (\dot{q}) with time. A baseline value for each parameter was selected, and one value higher and one value lower than the baseline were investigated in each case. The baseline value for each parameter was based on the nominal value for PMMA and a crack tip

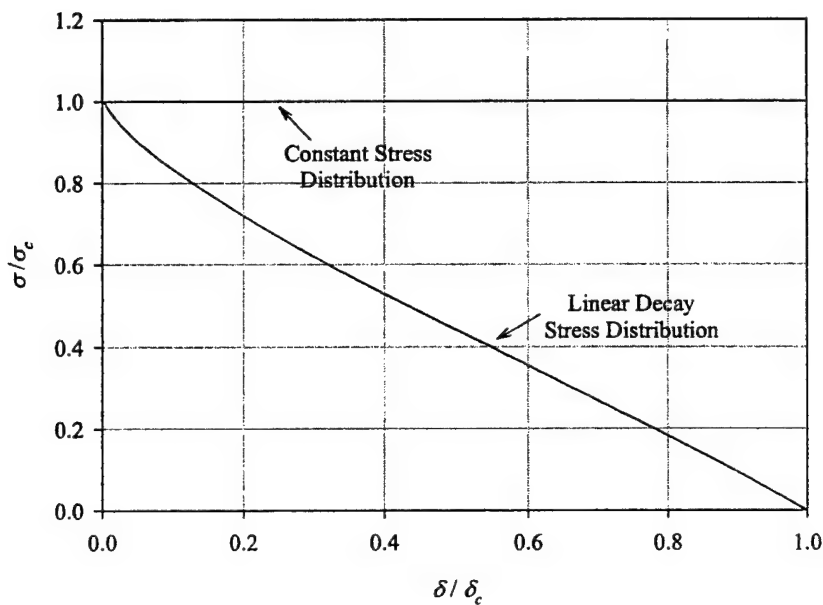


Figure 92. Calculated form of the constant stress and linear decay traction laws obtained from matching cohesive zone stress distributions.

speed of 300 m/s. Table 4 shows the baseline and variation of each parameter examined. Values for the other parameters were taken from Tables 1 and 2. Although the results are not shown here, the remaining parameters used in the model (ν , ρ , and c_p) were systematically varied to determine their influence on calculated temperatures and heating rates. Poisson's ratio, ν , was found to have negligible influence on calculated results for values ranging from 0.3 to 0.4. The other two parameters, ρ and c_p , are present in the algorithm only through equation (65), and have a direct inverse proportionality effect on temperature. The coupling between temperature ρ and c_p for PMMA is discussed in section 6.4.

Table 4. Parameter values used for the parametric study.

Parameter	Parameter Value		
	Low	Baseline	High
E (GPa)	4.5	5.5	6.5
G (J/m ²)	2000	3000	4000
σ_c (MPa)	100	120	140
$\dot{\alpha}$ (m/s)	250	300	350

The results from the parametric study are shown in Figures 93-100. Figures 93 and 94 show Young's modulus influence on predicted temperature ΔT_{det} and internal heat rate \dot{q} , respectively. Increasing E does not change the maximum temperature increase, but it does increase the rise time of the temperature

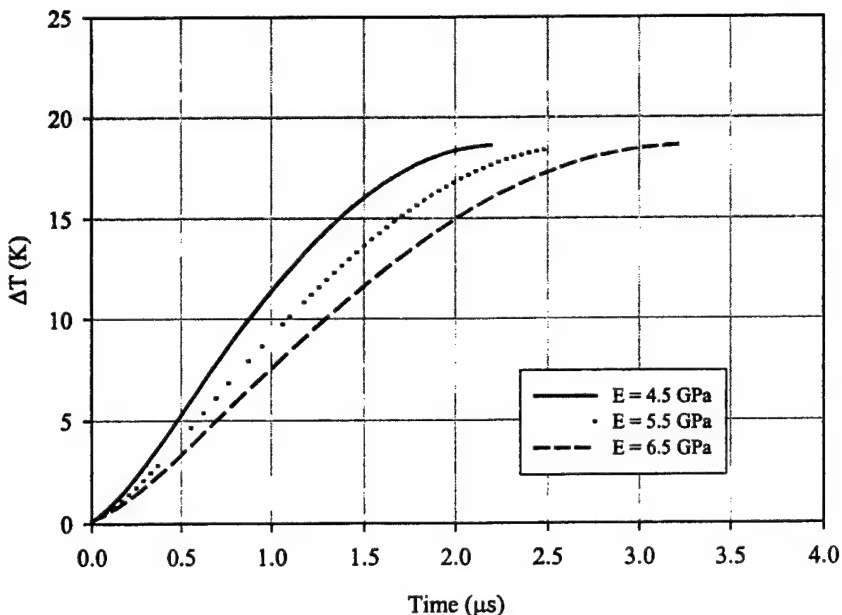


Figure 93. Temperature increase predictions using a linear decay $\sigma(\xi)$ relation from parametric study with E varied.

increase. The magnitude of the internal heat rate (Figure 94) decreases with increasing E and occurs over a longer time duration. In contrast to the effect of E , the dynamic energy release rate, G , is observed to have a significant influence on the maximum temperature increase. Figure 95 shows that doubling G doubles the maximum temperature. This is caused by the increased area under the \dot{q} - t curve, shown in Figure 96. The critical stress, σ_c , in Figure 97 is observed to have a significant influence on the rise time of the temperature increase, but no influence on the peak temperature. Increasing σ_c decreases the rise time of the temperature gain. An increase in σ_c also increases the magnitude of \dot{q} , as shown in Figure 98. But, because G was held constant, the resulting cohesive zone length decreased to keep the area under the \dot{q} - t curve constant for the different critical stress values. Thus, in some sense, the effects of σ_c and G on temperature evolution are complimentary: σ_c increases the rise time and G increases the maximum ΔT_{del} . The crack tip speed is shown in Figures 99 and 100 to have a modest influence on the temperature rise time and magnitude of \dot{q} . Increasing the crack tip speed shortens the temperature rise time and increases \dot{q} .

This parametric study provides a means for bounding the model predictions if there is uncertainty in the experimentally measured parameters. The baseline value of the various parameters correspond to approximately those appropriate for low-speed crack growth in PMMA. There are uncertainties in these values

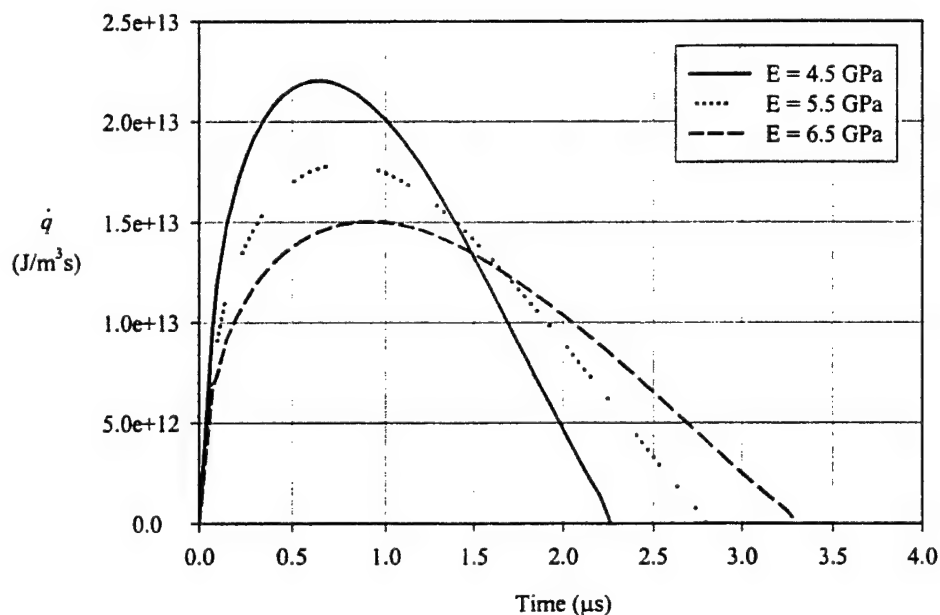


Figure 94. Internal heating rate predictions using a linear decay $\sigma(\xi)$ relation from parametric study with E varied.

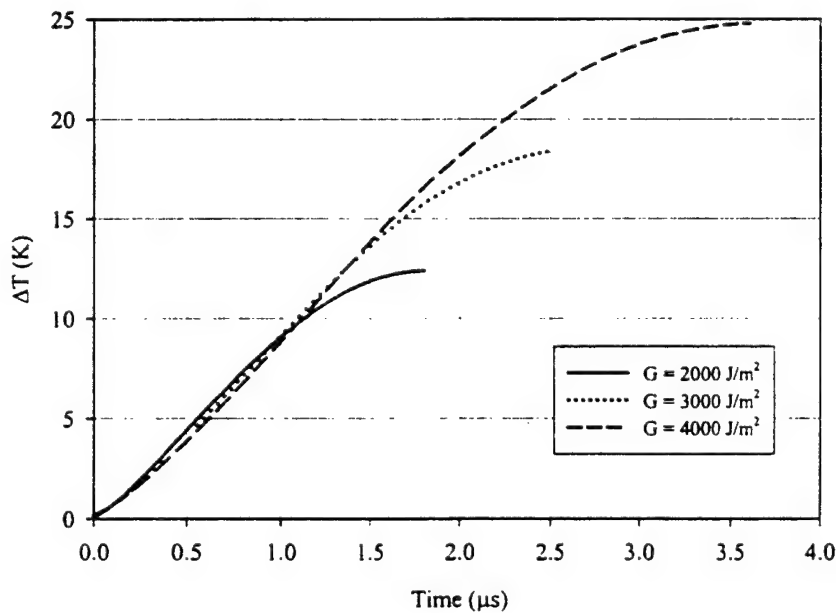


Figure 95. Temperature increase predictions using a linear decay $\sigma(\xi)$ relation from parametric study with G varied.

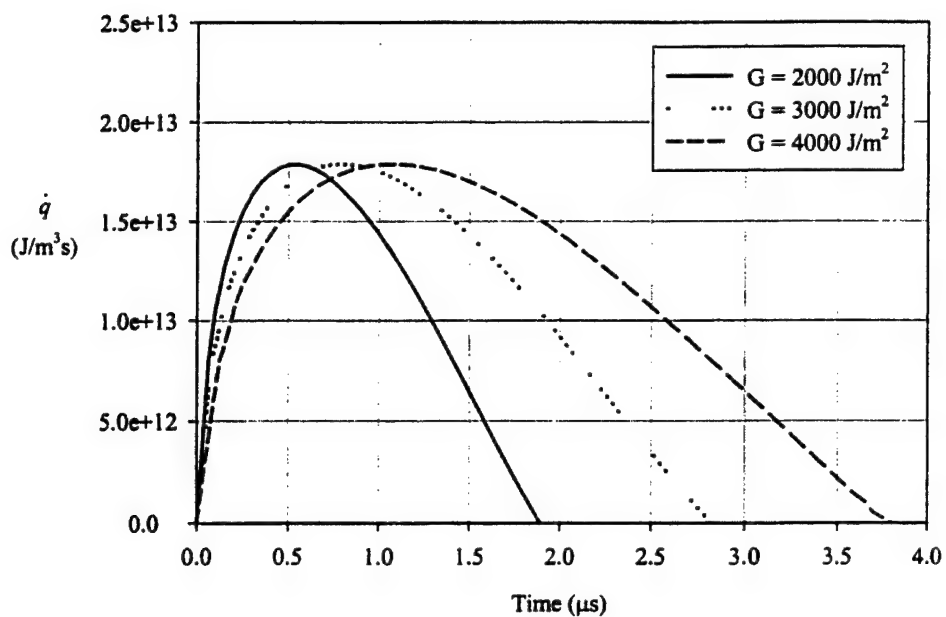


Figure 96. Internal heating rate predictions using a linear decay $\sigma(\xi)$ relation from parametric study with G varied.

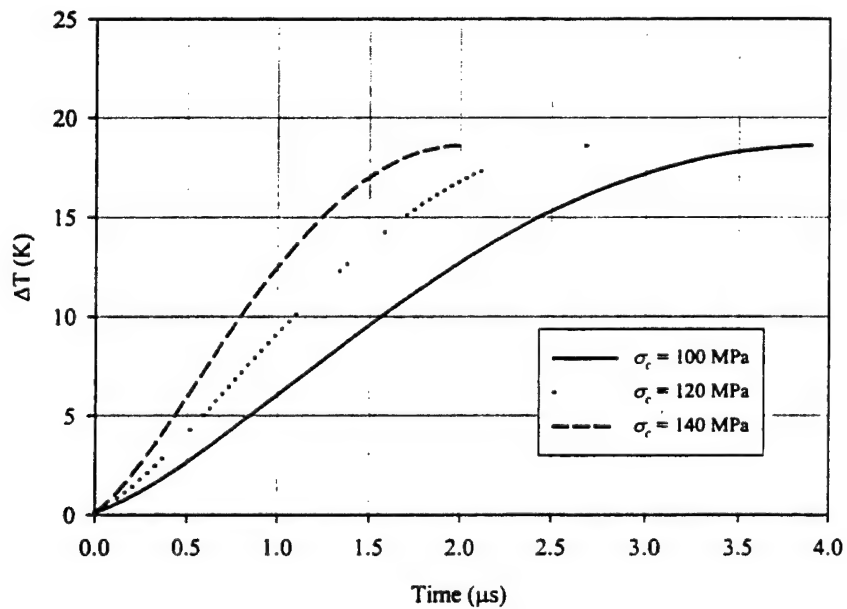


Figure 97. Temperature increase predictions using a linear decay $\sigma(\xi)$ relation from parametric study with σ_c varied.

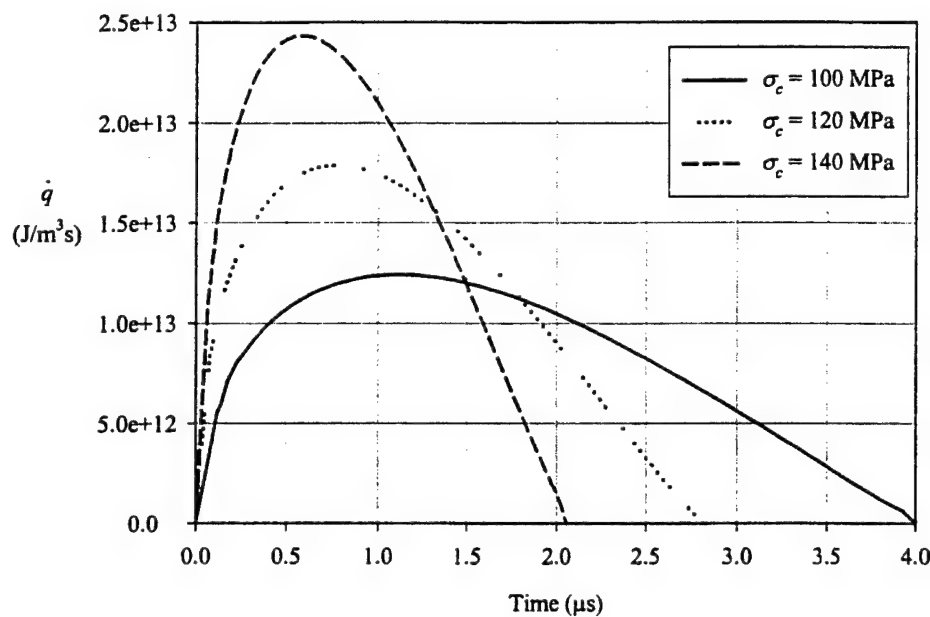


Figure 98. Internal heating rate predictions using a linear decay $\sigma(\xi)$ relation from parametric study with σ_c varied.

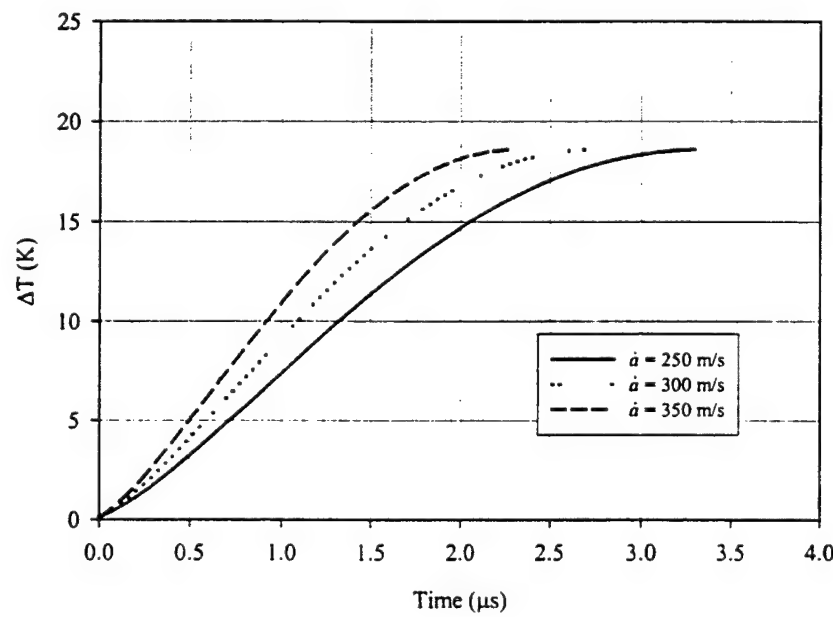


Figure 99. Temperature increase predictions using a linear decay $\sigma(\xi)$ relation from parametric study with \dot{a} varied.

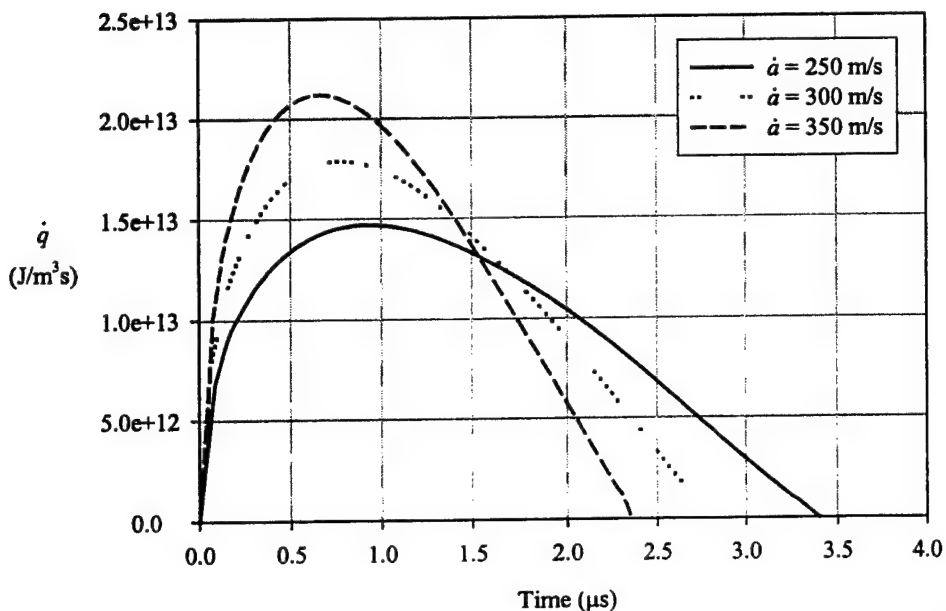


Figure 100. Internal heating rate predictions using a linear decay $\sigma(\xi)$ relation from parametric study with \dot{a} varied.

however. All parameters except σ_c were either measured directly in this study or were obtained from the literature. Uncertainties resulting from measurement technique or even the appropriate load rate locally within the material (for the case of rate sensitive E) prevent the exact values of the parameters from being known. For the parameter σ_c , the exact meaning and the appropriate measurement technique of this parameter is not very clear. With this in mind, the variations of the parameters used in the parametric study are believed to be in excess of the experimental uncertainty.

The parametric study was performed to examine the influence of a single parameter while the other parameters were kept constant. In a real material, it stands to reason that E , G , and σ_c are not independent parameters. Equation (46) shows that the energy flux into the crack tip region is inversely proportional to E . The cohesive model, as formulated in this study, is stress limited, meaning inelastic behavior initiates once a critical stress is exceeded. Increasing only E will result in a decrease in the energy flowing into the crack tip region because the strain energy density in the material resulting from far field tractions will be less. However, the energy flux in equation (46) is simply $(G \dot{a})$, so increasing E will likely decrease G in a real material. Changes in σ_c will also influence G because of strain energy density considerations. Given the possible interdependencies of the various model parameters, a true evaluation of the model will by necessity require comparison with experimental data where many of the needed parameters were measured. In this way, the model can be used

with actual parameter values appropriate for the dynamic fracture event being modeled. This is done in the next section.

6.3 Comparison of Dissipative Cohesive Zone Model With Experiments

6.3.1 Single Craze Failure Mode

The dissipative cohesive zone model derived in section 6.2 was based primarily on first principles. To determine if the model correlates with actual material behavior requires comparison with experimental data. The temperature fields surrounding high-speed opening-mode crack tips in PMMA were presented in section 3. As discussed previously, the lateral span of the temperature fields indicated that there was little, if any, plasticity surrounding the crack tip. Thus, the temperature increase for PMMA was by thermofracture mechanisms rather than thermoplasticity. The dissipative cohesive zone model derived in the previous section is applicable for the thermofracture portion of crack tip heating. The thermoplasticity contribution, present only for ductile materials, was examined in section 5. To examine the validity of the dissipative cohesive zone model for brittle materials, comparisons are made in this section with the temperature measurements of dynamic opening-mode fracture for high MW PMMA. The fracture surfaces from the low-speed PMMA experiments presented in section 3 indicated that a single craze formed along the crack plane (see Figure 55). As discussed earlier, the cohesive zone model is expected to have best agreement with crack growth involving a single craze. Given this, the model is evaluated against the low-speed PMMA dynamic fracture data.

The temperature field measurements of two nonidentical low-speed opening-mode high molecular weight PMMA fracture experiments are shown in Figure 101. The crack tip propagation speed was 300 m/s for both experiments. Recall from section 3 that the thermal signal sensed by the infrared detector system was highly localized for the low-speed case, with only one detector element registering a temperature increase during the early part of the measurement interval. Because of this, the temperature signals from flanking detector elements are not included in Figure 101. The first 4 μ s of the temperature signals are shown, corresponding to the initial temperature increase to peak value. This is the time regime appropriate for model comparison. The inset in Figure 101 shows a longer portion of the temperature signals for perspective. There is little difference between the two temperature signals, indicating good repeatability from test to test.

The cohesive zone model will be compared to one of the low-speed temperature signals shown in Figure 101 to assess the validity of the model, specifically, the signal depicted by the solid line in Figure 101. To further assess model validity,

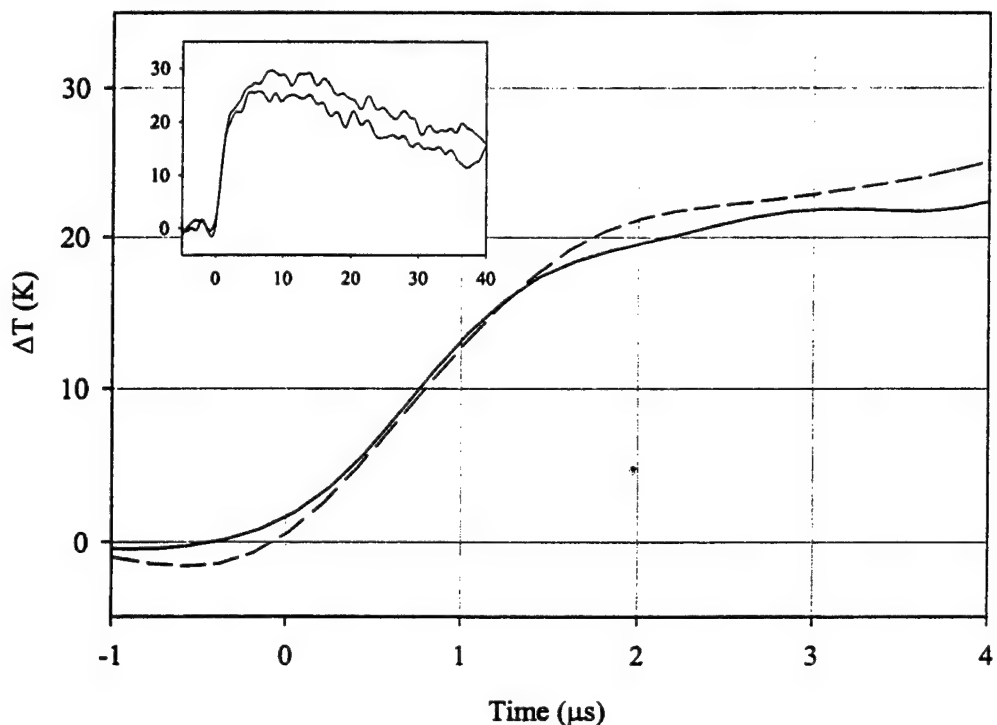


Figure 101. Leading portion of experimentally measured temperature signal from two different PMMA opening-mode fracture experiments with crack tip speeds of 300 m/s. Inset at top left shows a longer time span of the signals.

\dot{q} calculated from the model using equation (62) will be compared to the rate of internal heating obtained from the experimental data using equation (59). This requires the derivative of the experimental temperature signals to be calculated numerically. The procedure used for obtaining the derivative was presented in section 3. The calculated \dot{q} for the low-speed experiments shown in Figure 101 are presented in Figure 102. Again, the two signals are in good agreement. The signal depicted with the solid line in Figure 102 will be used for comparison with the model. Comparing temperature and \dot{q} between the model and experiments is equivalent to comparing an analytic solution and its first derivative to data. This gives a clearer indication of the model's behavior. This is in contrast to earlier cohesive model studies (Tvergaard and Hutchinson 1992; Needleman 1992; Xu and Needleman 1994; Tvergaard and Hutchinson 1996; Camacho and Ortiz 1996) where the traction-separation relation, $\sigma(\delta)$, was based on theoretical arguments or post-mortem fracture surface observations and not on experimental measurements taken during the decohesion process.

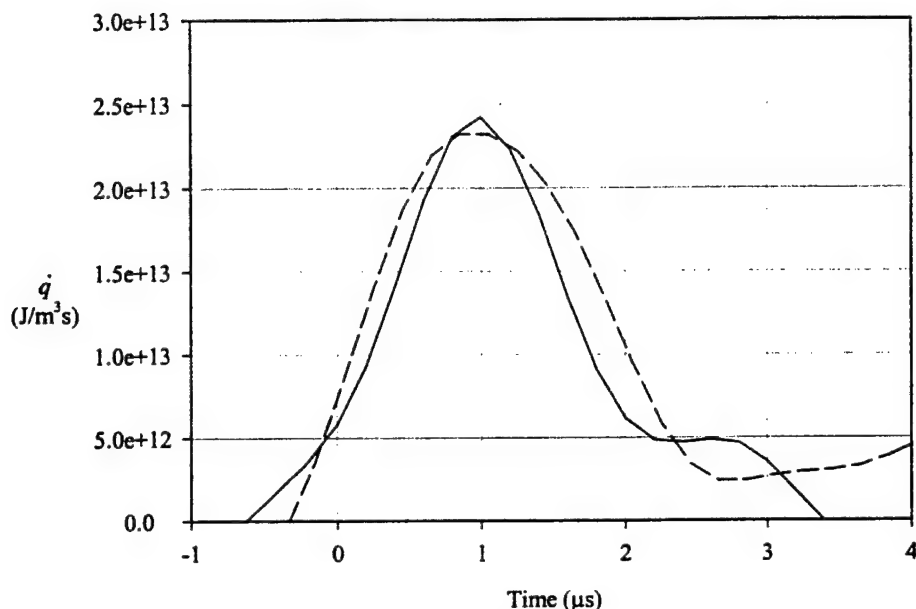


Figure 102. Rate of internal heating derived from dynamic opening-mode fracture of PMMA. The crack tip speeds were 300 m/s, and the experimental signals are from the peak detector.

The dissipative cohesive zone model parameters corresponding to the low-speed experiment in Figure 102 are the baseline values listed in Tables 2 and 4. Recall that G , E , \dot{a} , ρ , c_p , and ν are independently measured. They are not fitted to experimental data. The critical stress, σ_c , is a parameter that was not directly measured. On the basis of the low and moderate rate PMMA tension tests presented in section 2 (see Figure 5), a high-rate estimate of a maximum stress value of 120 MPa was made. This value was used for all of the calculations in this chapter; it was not varied. The constant stress and linear decay stress distributions were used in the dissipative cohesive zone model with the baseline parameter values. The model predictions are compared with the low-speed temperature measurements in Figure 103. Both models predict a peak temperature that is slightly less than the peak temperature measured for the experiment. However, the constant stress distribution has a rise time that is too short, and the linear decay distribution is too slow in reaching peak temperature. With this in mind, a third cohesive stress distribution was used that qualitatively is in between the two distributions previously presented. This stress distribution, referred to as the quad-high stress distribution, is a quadratic function of the form

$$\sigma(\xi) = \sigma_c \left[1 - \left(\frac{\xi}{L} \right)^2 \right]. \quad (73)$$

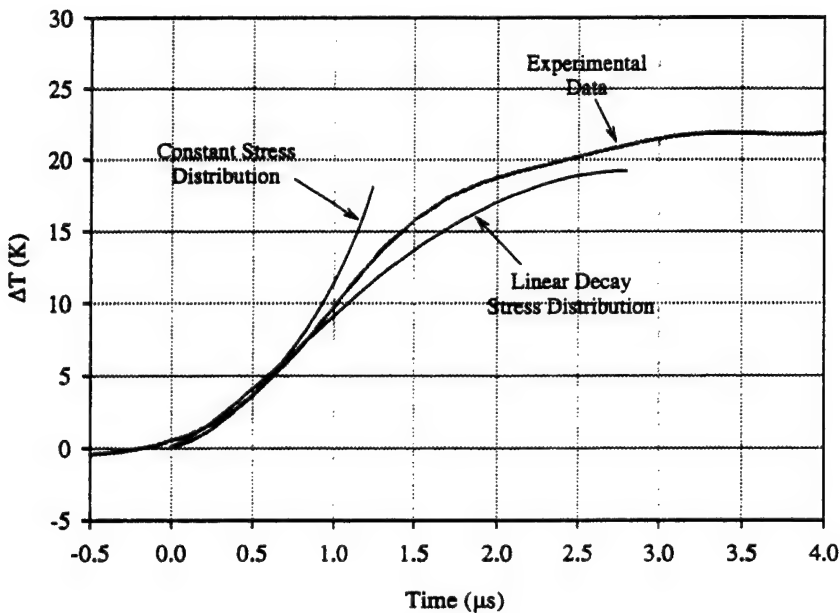


Figure 103. Comparison of the temperature increase predicted by the dissipative cohesive zone model with experimental data for opening-mode fracture of PMMA with a crack speed 300 m/s. Constant stress and linear decay stress distributions were used in the model.

This stress distribution is shown in Figure 104 along with the two previously presented cohesive stress distributions for comparison. This stress distribution was used in the cohesive zone model in the same way as for the other two stress distributions. The solution for the cohesive zone length, L , and $\partial\delta/\partial\xi$ was obtained in a manner similar to that described in Appendices A and B for the linear stress distribution. The resulting expressions are

$$L = \frac{25\pi EG}{128A_t \sigma_c^2}; \quad (74)$$

$$\frac{\partial\delta}{\partial\xi} = \frac{2C\sigma_c}{\pi\mu} \left[\frac{\sqrt{\xi}L}{3L} + \frac{\xi\sqrt{\xi}L}{L^2} + \frac{\xi^2 - L^2}{2L^2} \ln\left(\frac{\sqrt{L} - \sqrt{\xi}}{\sqrt{L} + \sqrt{\xi}}\right) \right]. \quad (75)$$

Although the stress distribution $\sigma(\xi)$ has the desired shape, as shown in Figure 104, the shape of the cohesive traction law $\sigma(\delta)$ is not guaranteed to be the same. The resulting $\sigma(\delta)$ traction law calculated from the cohesive zone algorithm is shown in Figure 105. The baseline values for the various parameters were used. The shape is observed to change slightly from the shape of the stress distribution $\sigma(\xi)$, but it still remains between the two previous traction laws.

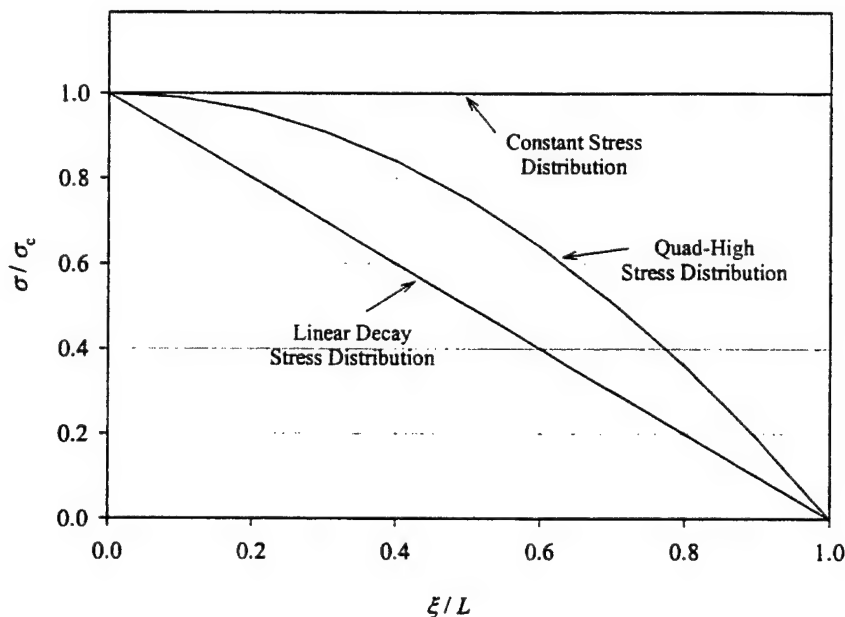


Figure 104. Form of the quad-high stress distribution compared to the constant stress and linear decay stress distribution.

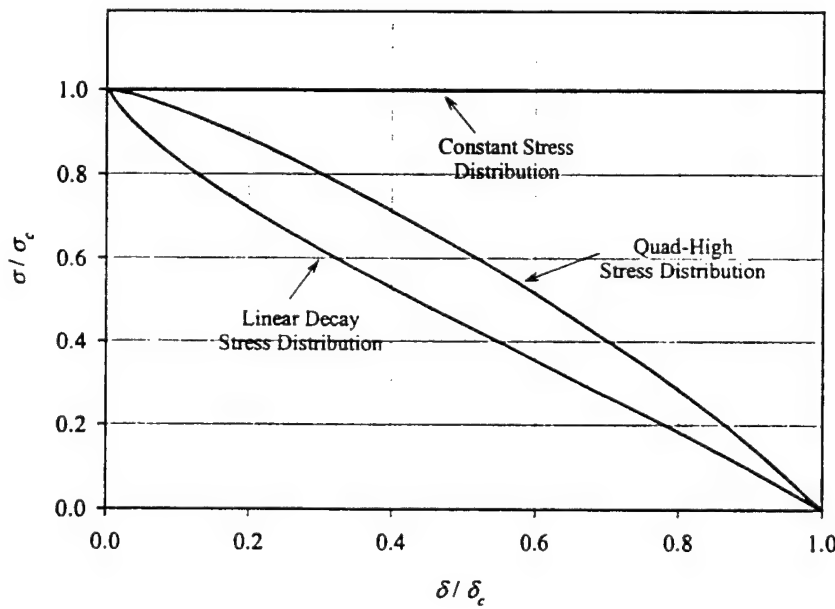


Figure 105. Calculated shape of the quad-high traction law. The constant stress and linear decay traction laws are shown for comparison. The baseline parameters for 300 m/s crack growth in PMMA were used.

The predicted temperature for the quad-high stress distribution is compared to the low-speed PMMA experiment in Figure 106. The maximum temperature increase is about the same as was predicted for the constant and linear decay stress distributions; however, the rise time is in better agreement with the experimental data. To further compare the model with the low-speed PMMA data, the internal heating rate from the experiment was compared with the \dot{q} calculated for the three stress distributions. The comparison is shown in Figure 107. The quad-high distribution closely matches the experimental data, whereas the linear decay distribution underpredicts \dot{q} and the constant stress distribution has a form that deviates significantly from the experimental data. Once again it should be emphasized that the parameter values used in Figures 106 and 107 were not fitted to the experimental data, but rather were independently measured (G , E , \dot{a} , ρ , c_p , ν) or estimated (σ_c). Yet, the agreement for the quad-high stress distribution is remarkably good, both in ΔT_{det} and \dot{q} .

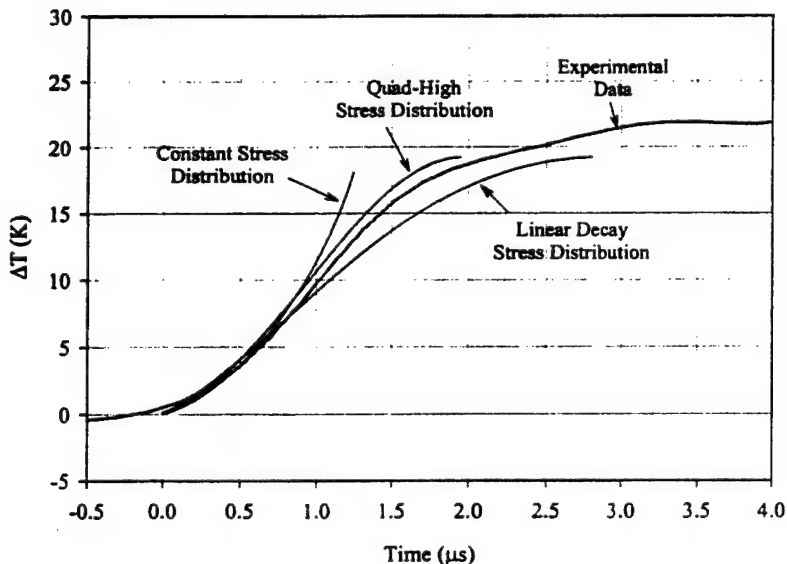


Figure 106. Temperature increase predicted by the dissipative cohesive zone model compared to experimental data for 300 m/s crack growth in PMMA.

6.3.2 Distributed Damage Failure Mode

In addition to the low-speed single craze experiments, the cohesive zone model was used to predict the temperature increase for cracks propagating at higher speeds with the full knowledge that there is considerably more spatial distribution of damage around the crack tip. Higher speed temperature data used for model comparison are shown in Figure 108, along with the results from the low-speed tests. The data are from experiments with cracks propagating at

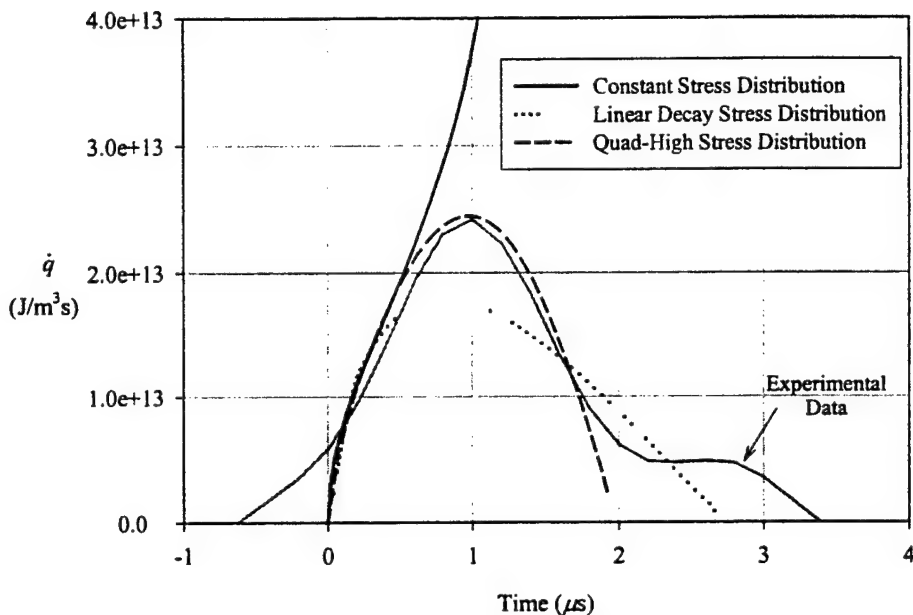


Figure 107. Internal heating predicted by the dissipative cohesive zone model compared to experimental data for 300 m/s crack growth in PMMA.

400 and 600 m/s in high molecular weight PMMA. As before, the temperature signal from the leading detector for each of the two experiments is shown. The inset in the figure shows the temperature data for a longer time duration for perspective. The internal heating rate \dot{q} of the three different speed experiments is shown in Figure 109. The rate of internal heating was calculated in the same way as for the low-speed case. A comparison of predicted \dot{q} with the high-speed data will aid in assessing the model behavior for high-speed crack growth.

The only dissipative cohesive zone model parameters that were changed for the higher speed cases were G and \dot{a} . The G values used were 3550 J/m² for the 400 m/s case and 5600 J/m² for the 600 m/s case. These values were taken from the measured G vs. \dot{a} plot shown in Figure 36. Comparison of the model with the 400 m/s crack speed experimental data is shown in Figure 110. The temperature increases predicted by all three stress distributions were about half the increase measured during the experiment. The three distributions all resulted in a temperature increase of about 22 K, compared to a measured increase during the experiment of 35–45 K. Of the three distributions, the quad-high distribution best matches the data despite the underprediction in temperature. Model comparison for the 600 m/s case is shown in Figure 111. The predicted temperature increases from the three different stress distributions ranged from 31 to 35 K, with the constant stress distribution giving the lowest increase. The experimental data show a temperature increase of ~72 K, roughly twice the model predictions. The quad-high distribution gave the best qualitative agreement.

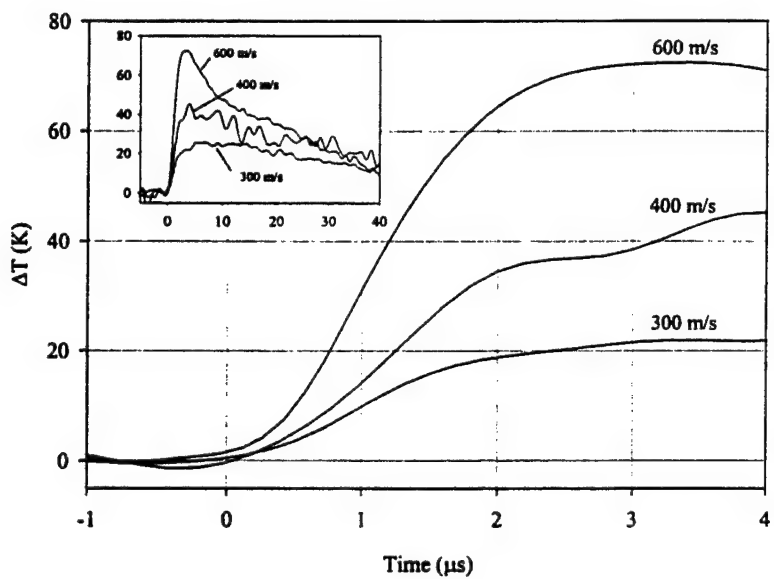


Figure 108. Leading portion of experimentally measured temperature signal from three different PMMA opening mode fracture experiments with crack tip speeds of 300, 400, and 600 m/s. Inset at top left shows a longer time span of the signals. Peak detector only shown for 400 and 600 m/s experiments.

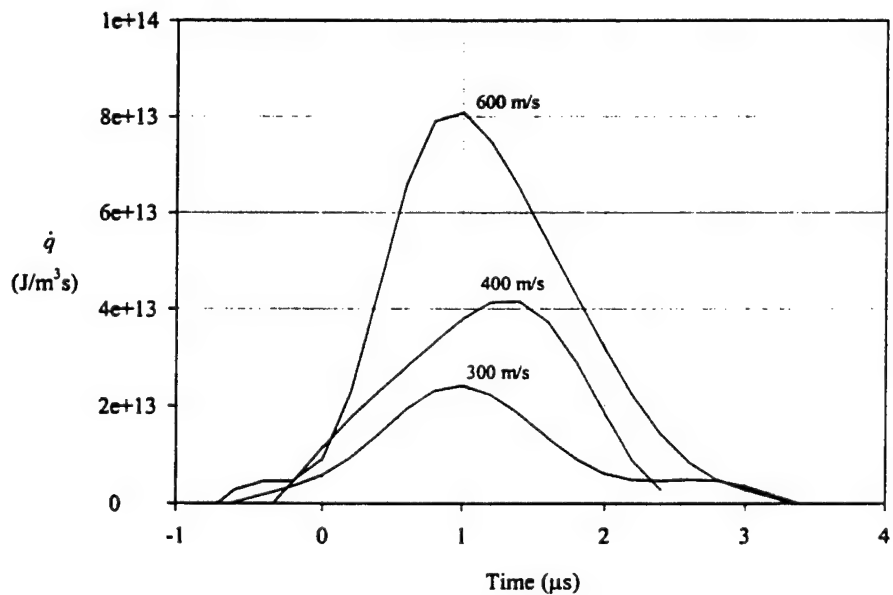


Figure 109. Rate of internal heating derived from dynamic opening mode fracture of PMMA. The crack tip speeds were 300, 400, and 600 m/s, and the experimental signals are from the peak detector.

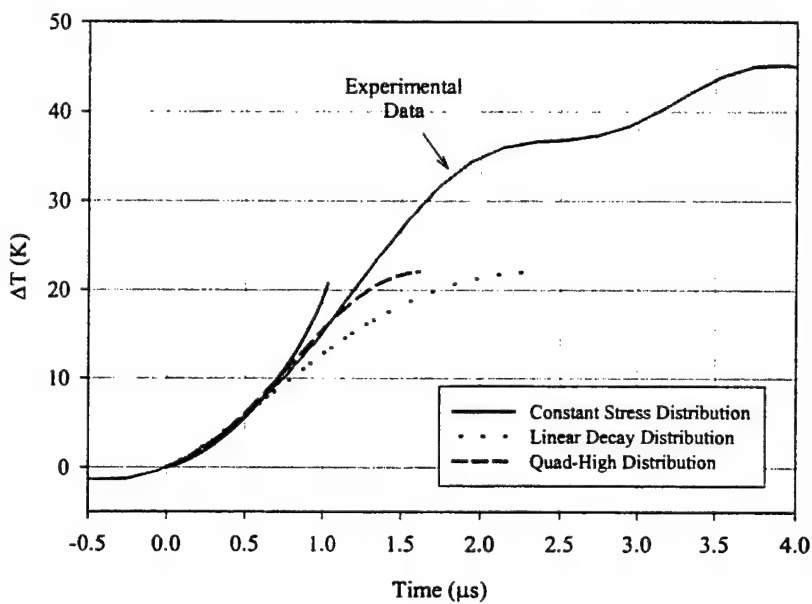


Figure 110. Temperature increase predicted by the dissipative cohesive zone model compared to experimental data for 400 m/s crack growth in PMMA.

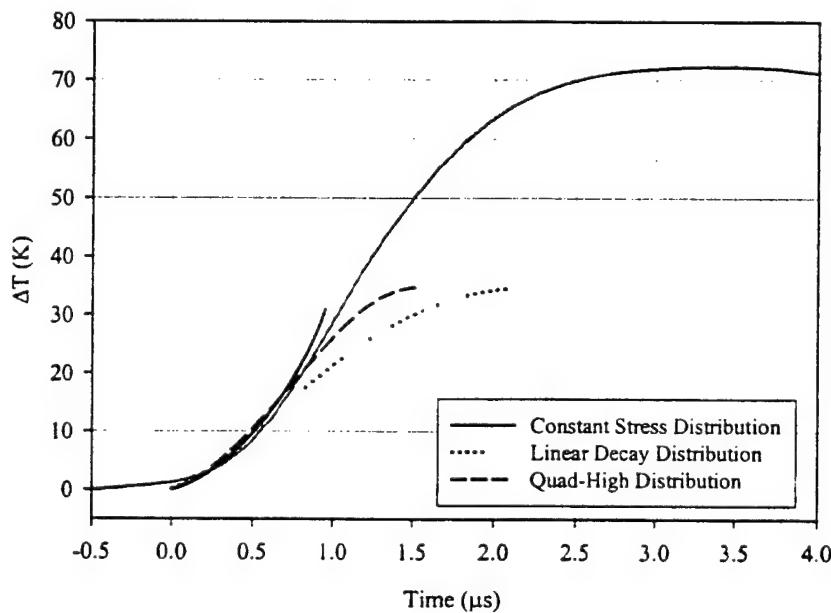


Figure 111. Temperature increase predicted by the dissipative cohesive zone model compared to experimental data for 600 m/s crack growth in PMMA.

To better examine the model behavior relative to the experimental data, the internal heating rates predicted by the quad-high stress distribution for all three crack tip speeds are compared to \dot{q} derived from the experimental data. The comparison is shown in Figure 112. As was shown earlier, good agreement exists for the 300 m/s case. The quad-high model follows the experimental data during most of the active heating phase (i.e., the first 2 to 3 μ s). The lack of agreement between model and experiment for the higher speed temperature data (shown in Figures 110 and 111) is evident in the internal heating comparison. The \dot{q} predicted by the model initially agrees with the experiments. However, \dot{q} from the model reaches a maximum and decreases to zero much earlier than is observed for the experiments, leading to less overall heating and less temperature increase.

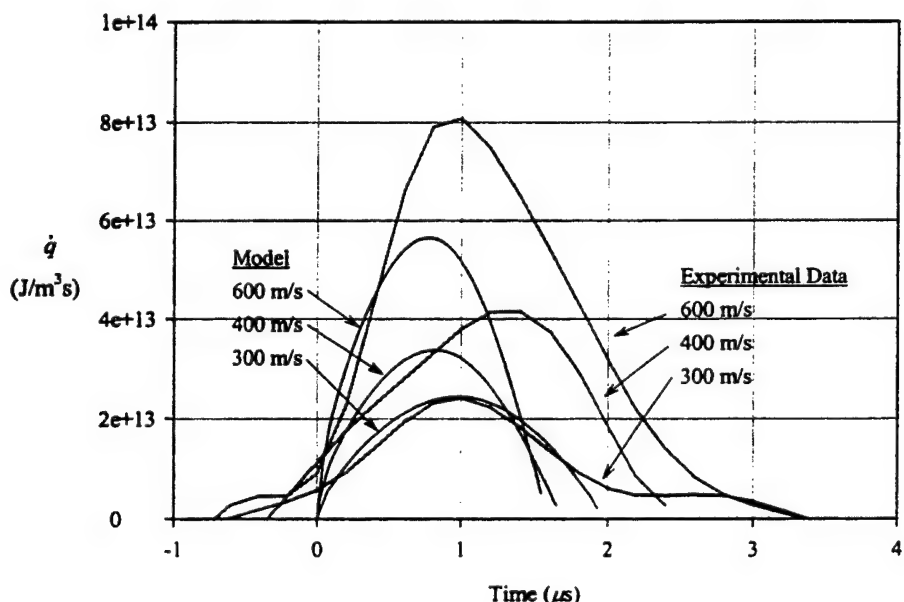


Figure 112. Comparison of the internal heat rate predicted by using the quad-high stress distribution in the dissipative cohesive zone model with experimental data for low, mid, and high crack tip speed fracture of PMMA.

The reason for the discrepancy between model and experiment at the higher crack tip speeds is the microcracking phenomenon discussed in section 3 that occurs during high-speed crack propagation in PMMA. As the crack tip speed increases in PMMA, the fracture surface changes from a smooth "glassy" surface to a rough surface with many microcracks present. The smooth fracture surface is due to the passage of a single polymer craze, and is produced when the crack tip speed is low, typically 300 m/s or lower. For higher crack tip speeds, multiple craze fronts occur above and below the primary fracture plane, resulting in surface roughness (see Figure 54). Thus, whereas a single craze can

be approximated as failure occurring along the fracture plane through a cohesive zone, the multiple, layered crazing that exists during high speed fracture in PMMA is more of a volumetric failure event. The cohesive zone concept assumes failure to occur on a single plane. It was not devised to model distributed damage. Nilsson and Hutchinson (1994) have devised a modified constant stress cohesive law to account for distributed damage; however, it was derived for ductile materials.

To illustrate the volumetric aspect of damage during high-speed fracture of PMMA, the distribution of temperature at a single time was recorded for a representative experiment. The temperature distribution, shown in Figure 113, is the temperature sensed by each detector element at the time of peak temperature. The crack tip speed for the experiment shown was 600 m/s. As observed in Figure 113, three detector elements sensed material heating, implying the thickness of the damage zone was equivalent to the spacing of three elements in the infrared detector array. The finite size of the detector element prevents an exact thickness from being determined, but the damage zone thickness is estimated to be between 110 nm and 190 μm . A more precise measurement would require a detector system with higher spatial resolution. The estimated thickness is consistent with measurements of the surface roughness shown in Figure 54. The damage distribution was fit to a transcendental function of the form

$$\Delta T_{det} = d \cos^2 \left(\frac{2\pi y}{b} \right), \quad (76)$$

where d and b are fitting constants and y corresponds to the vertical position of the elements, i.e., the x axis of the plot. The good agreement suggests a possible empirical damage distribution in the material. Although not shown here, other high-speed experiments showed a similar degree of agreement with equation (76). The modeling of distributed damage is not pursued further in this study and remains a topic of future work.

6.4 Further Analysis of Temperature Field Measurements

The particular stress distribution used in the dissipative cohesive zone model determined the temporal form of the predicted temperature increase. Comparison of the model results with experimental data was used to indicate the validity of the various stress distributions considered. For this comparison to be meaningful, correct interpretation and understanding of the temperature signals from the infrared detector system is crucial. In this section, a detailed analysis of the low-speed experimental data is performed. The aspect of crack tip propagation past a stationary detector array along with crack face opening is further explored. The results of this analysis will place a limit on the precision that can be attributed to the initial portion of the temperature measurements.

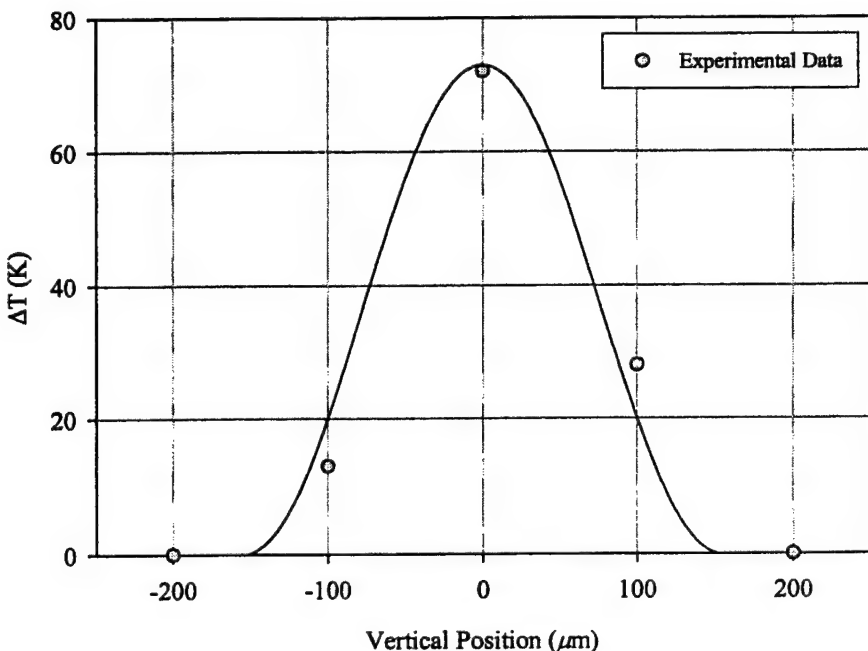


Figure 113. Distribution of temperature among the vertically oriented infrared detector elements at the time of peak temperature.

6.4.1 Flanking Thermal Signal Decay

During the low crack tip speed fracture experiments of PMMA presented in section 3, the stationary infrared detector array monitored the passage of a single craze and the subsequent opening of the newly formed crack faces. The temperature curves from the experiments show a rise in temperature followed by a slower decrease. As was discussed in section 3, Mason and Rosakis (1992) suggest crack opening as the likely reason for the decrease in temperature but do not pursue this further. If the crack is assumed not to open and adiabatic conditions exist (due to the short times involved), the temperature curves would be expected to increase to a peak value and remain constant in the trailing thermal wake. This is precisely what happens during shear-dominated fracture of PMMA, discussed in section 4 (see Figures [62a] and [62b]). If, on the other hand, crack opening occurs, the temperature recorded would decrease as the detector began to view the air gap between separated fracture surfaces as conjectured by Mason and Rosakis (1992). The opening of the crack would move the heated crack faces to adjacent detector elements later in time. A contour plot of the temperature increase measured by the detector system for a crack tip propagating at 300 m/s in PMMA and the trailing thermal wake is shown in Figure 114. The temperature contour plot was constructed in a manner similar to those discussed in section 3, except the time scale was not transformed to length. The displacement of the heated crack surfaces is apparent, consistent with the explanation offered by Mason and Rosakis (1992).

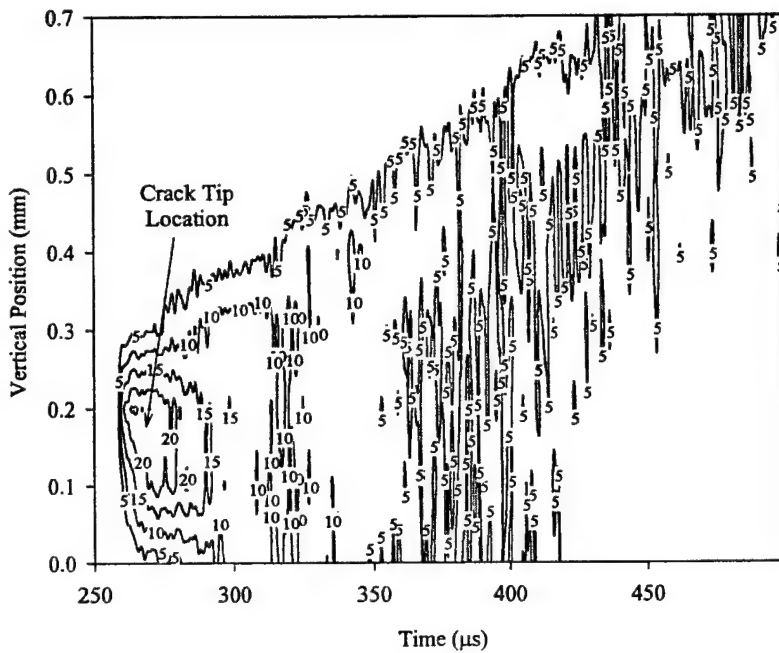


Figure 114. Contours of temperature increase in PMMA for a propagating crack tip and trailing thermal wake. Crack tip propagation speed is ~ 300 m/s. The crack opening displacement is evident by the shape of the trailing wake region.

To better understand the effect of crack face opening on the measured temperature signals, three possible configurations involving the opening of a single craze in the region monitored by the infrared detector elements are considered. Along with each of the configurations considered, the resulting temperature signals from a representative low-speed opening-mode PMMA experiment corresponding to each configuration will be shown. The first configuration, depicted in Figure 115, has the craze passing directly through the region monitored by a single detector element. Experimental temperature signals corresponding to such a situation are shown at the bottom of Figure 115. For a crack tip propagating at 300 m/s, the time required for the tip to move the entire distance of one detector element (80 μm) is 0.26 μs . This is a small fraction of the total rise time actually recorded, indicating that the rise time of the temperature signal is not significantly influenced by crack tip motion in the direction of propagation. However, as the craze widens, more of the area monitored by the detector element is covered, increasing the overall output for that element. Eventually, the craze splits and the heated material moves transversely to the crack propagation direction at the speed of crack face opening. This situation is shown in the middle sketch of Figure 115. Because all the actively heated region is still within the 80- μm detector space, the detector output remains constant until portions of the heated material move outside of

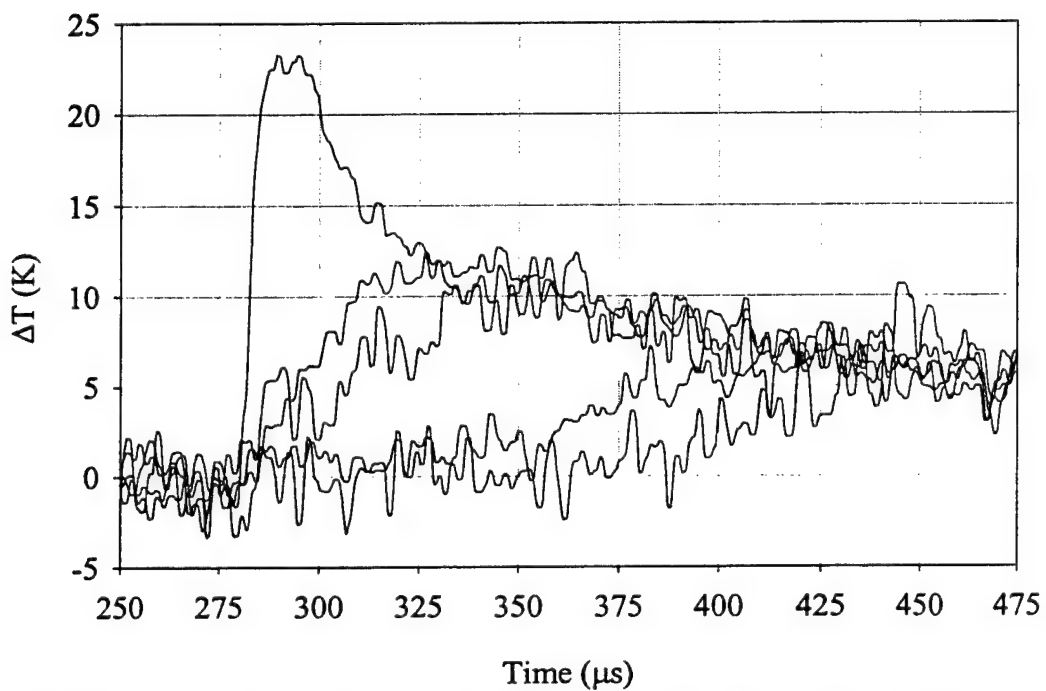
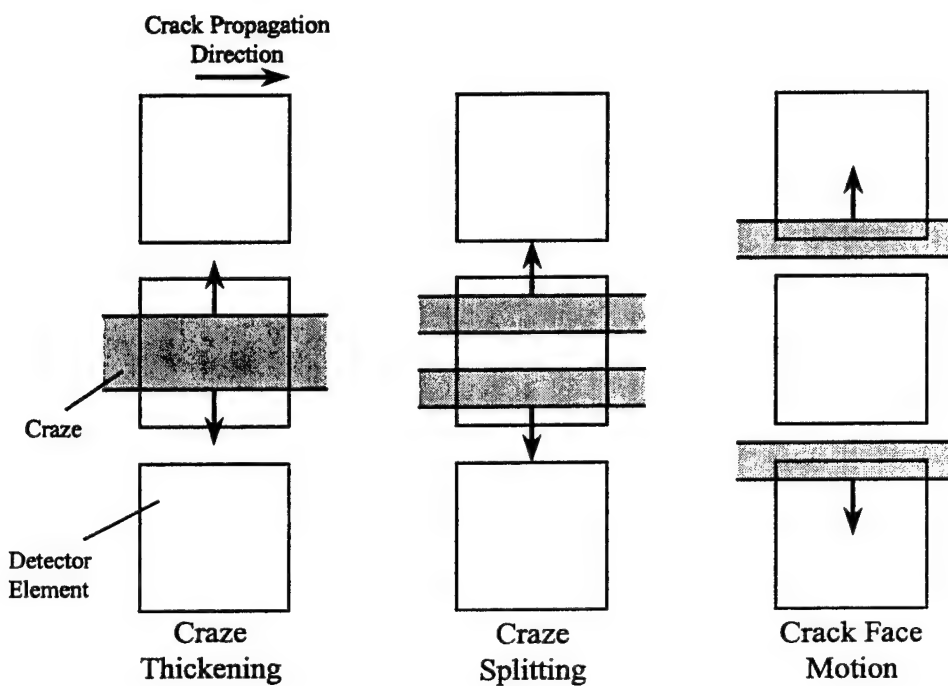


Figure 115. Depiction of craze thickening, splitting, and crack opening relative to the stationary infrared detector elements for a craze passing through the region monitored by an element. Bottom of figure is representative data for the configuration illustrated.

the region viewed by the detector, at which time the output decreases. Eventually the heated material moves to areas monitored by flanking detector elements (right side of Figure 115). The output from these neighboring elements will increase as the heated material moves into the coverage zone, plateau once fully inside the area and then decrease as the heated material exits the coverage zone. However, the thickness of the heated material viewed by neighboring detectors is half the maximum craze thickness, so the detector output should be half that of the center detector. The temperature signals for the flanking detector elements will coincide in time only if the original craze passed exactly through the middle of the central detector element. The signals will not coincide in time if the craze passed slightly high or low through the central detector. This mechanism corresponds to the actual signals recorded during the experiment shown at the bottom of Figure 115.

The second possible configuration of crack opening is shown in Figure 116. For this configuration, the craze passes between two adjacent detector elements, where it splits and separates. This time, both primary detector elements view only half of the original craze thickness. An example of this for low-speed fracture of PMMA is shown at the bottom of Figure 116. The time of crack passage through the detector measurement region cannot be determined solely from the temperature signals for this case.

The third configuration, shown in Figure 117, is for the case where the crack tip passed above or below the entire detector array. The thermal event sensed by the detector elements then corresponds to the vertical propagation of the split craze through the detector field of coverage. A low-speed PMMA experiment illustrating this is shown at the bottom of Figure 117. The crack opening speed can be experimentally determined from an experiment such as the one shown at the bottom of Figure 117, but the crack tip position cannot be ascertained (and hence the position along the crack face corresponding to the transverse speed measurement is unknown).

The temperature signals from the low-speed experiment presented in this section and section 3 show a plateau for each detector, and the elements flanking the peak detector sense a temperature increase half that of the peak. This suggests that configurations similar to Figures 115-117 occurred. In particular, the low-speed PMMA data used for comparison with the dissipative cohesive zone model (Figure 101) show trends that are consistent with the sequence of events depicted in Figure 115. An analytic approximation of the crack face opening speed, \dot{u}_2 , is given by Freund (1990) as

$$\dot{u}_2 \approx \frac{\dot{a} \lambda_1 K_I^d}{\mu D \sqrt{2\pi r}} [(1 + \lambda_2)^2 - 2] \quad (77)$$

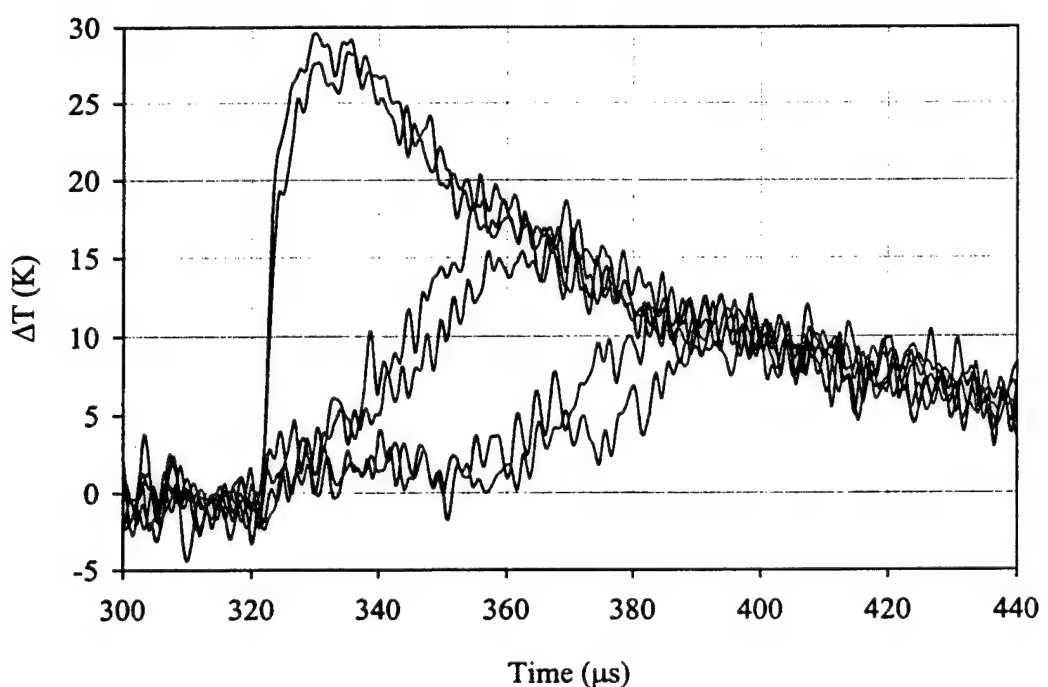
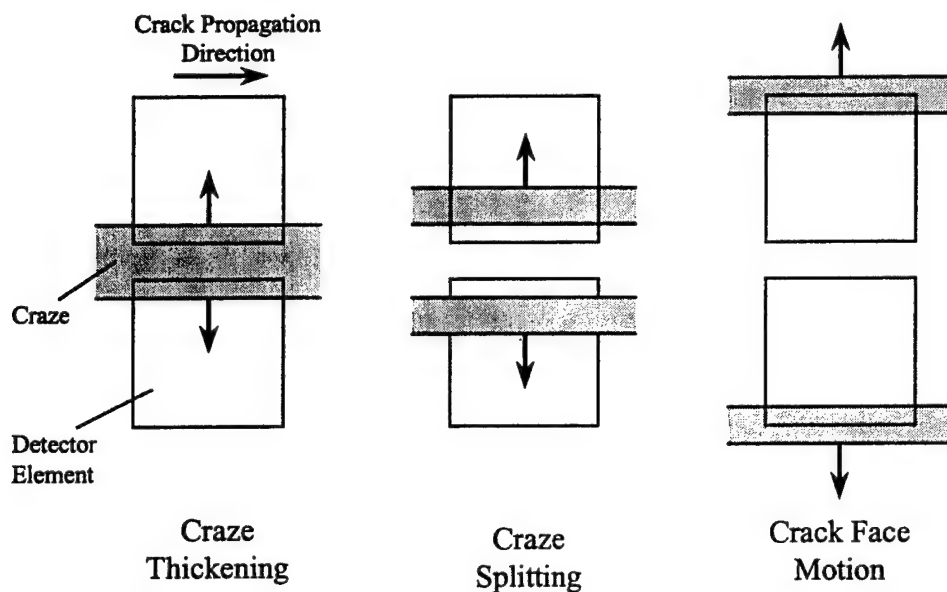


Figure 116. Depiction of craze thickening, splitting, and crack opening relative to the stationary infrared detector elements for a craze passing between two detector elements. Bottom of figure is representative data for the configuration illustrated.

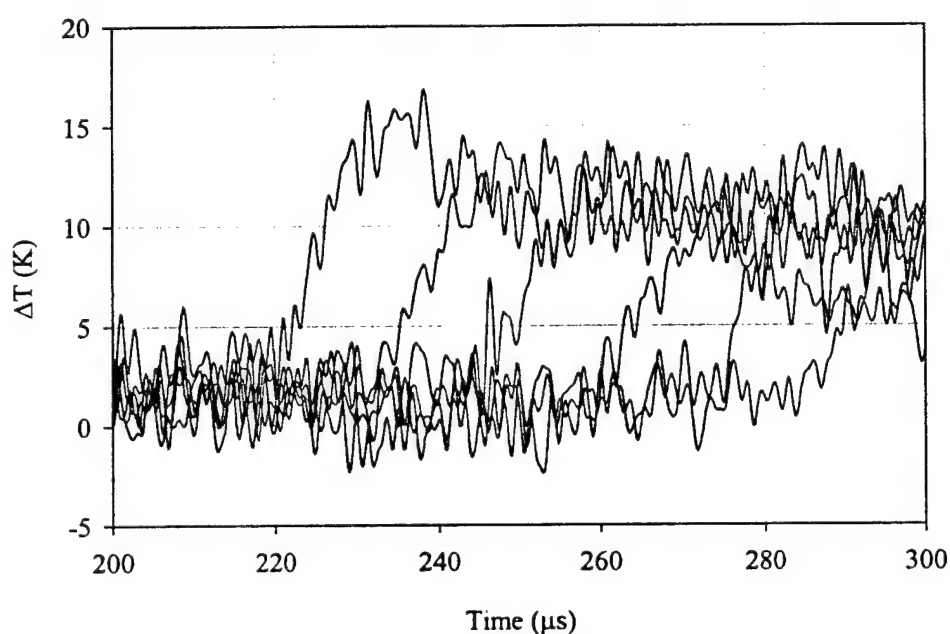
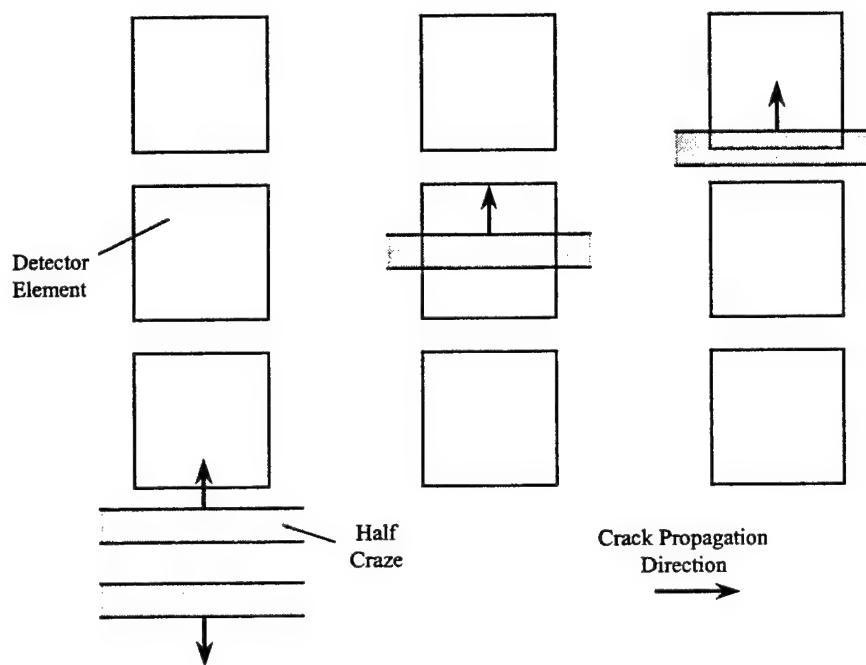


Figure 117. Depiction of crack opening relative to the stationary infrared detector elements for a craze passing below the detector element array. Bottom of figure is representative data for the configuration illustrated.

where r is the distance from the crack tip and the other parameters were defined in section 2. The crack face opening speed predicted using equation (77) for a crack propagating at 300 m/s in PMMA is shown in Figure 118 using K^d , derived from equation (18) and the measured value of G . Also shown in Figure 6.34 are data points obtained from the slow-speed PMMA experiment used for comparison with the cohesive zone model (i.e., the low-speed curve shown in Figure 108). The experimental values of crack face opening speed were obtained by noting the time at which the flanking detector elements in the detector array sensed an increase in temperature. The speed was calculated by dividing the distance between detector elements by the time increment of sensed temperature between adjacent elements. The data are in reasonable agreement with the analytic expression, corroborating the notion of crack face motion as being responsible for the temperature sensed by the detector elements flanking the peak detector.

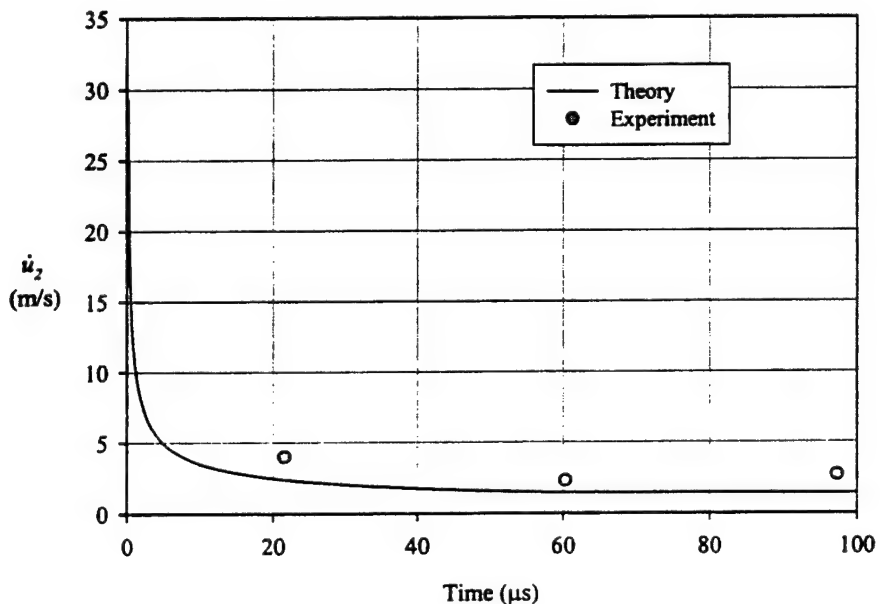


Figure 118. Crack face opening speed for fracture of PMMA with a crack tip speed of 300 m/s. Experimental data derived from temperature measurements are compared to analytical expression from Freund (1990).

Unfortunately, the configuration depicted in Figure 115 indicates that there is some ambiguity in interpreting the initial rise time of the temperature signal. It is possible that the increase in temperature is due to the expanding craze thickness and not an increase in craze temperature. It also suggests that the roll-off in temperature near the peak could be artificial, resulting from the craze halves exiting the detector coverage area. This affects not only the temperature signal, but also the calculated \dot{q} . The quad-high cohesive stress distribution was

identified as best matching the experimental data. If the roll-off portion of the experimental temperature signal is artificial, the constant stress distribution may in fact provide the best match with the data. These issues can only be addressed with a temperature measurement system having a spatial resolution significantly better than the 80 μm resolution used in this study. However, as is, the final resulting difference between the quad-high and linear stress distributions is not large.

6.4.2 Cohesive Zone Length

The length of the cohesive zones predicted by the model for the low-speed case were 375, 585, and 840 μm for the constant, quad-high, and linear stress distributions, respectively. The typical length for a single craze in PMMA grown under quasi-static loading is less than 100 μm (Kambour 1964). Since the cohesive zone concept was introduced in this study to model polymer craze formation and breakdown, the predicted cohesive zone length should compare with typical craze lengths. However, as mentioned above, crazes from quasi-static loading are significantly shorter than the predicted cohesive zone length. If the actual cohesive zone had a length of 100 μm and a speed of 300 m/s, the rise time of temperature for a stationary observer would be $\sim 0.3 \mu\text{s}$. This is on the order of the system response time. Yet, the actual thermal signals are several microseconds long. A more sophisticated rate-dependent traction law (Kubair et al. 2001) could be used to shorten the predicted cohesive zone length, but this does not change the fact that the measured temperature rise lasted microseconds in duration. One possible explanation for this is that the thermally active zone ahead of a crack propagating at high speed in PMMA is considerably longer than the quasi-static craze length. As mentioned in section 6.1, Kawabe et al. (1992) observed polymer chain alignment to occur ahead of the craze in PMMA and PC during opening mode loading. This extended zone of molecular motion would likely result in heat dissipation and could explain the discrepancy between the predicted cohesive zone length and observed craze lengths.

There is an additional phenomenon associated with polymer crazing that may increase the duration of the thermal event sensed by the infrared detector elements. Following rupture of the stretched craze fibrils, molecular chain recoil will occur (Kambour 1964; Wool 1995). During recoil, internal heating of the fibril stubs may be sensed by the detector elements. The heating would occur aft of the crack tip, increasing the length of the thermally active region and thus the duration of the thermal event recorded by the detectors. The internal heating mechanism associated with molecular chain recoil is not pursued in this study, and the magnitude and duration of fibril stub recoil heating is unknown.

6.4.3 Effect of Temperature on μ and c_p

As the material in the vicinity of the crack tip increases in temperature, several material properties may change from their baseline value. A parametric study was performed in section 6.2 to examine the sensitivity of material property variation on the model. Here, the actual variation of two material properties with temperature, namely ρ and c_p , is examined for PMMA (Domininghaus 1988). The temperature dependence noted by Domininghaus (1988) is shown in Figures 119 and 120 for ρ and c_p , respectively. A 70 K increase from room temperature decreases ρ from 1190 to 1168 kg/m³. The same increase in temperature changes c_p from 1470 to 1900 J/kg-K. Note that the variations of ρ and c_p with temperature are inverse to each other. Interpretation of the temperature signals measured during the experiment was done assuming constant values of these parameters (i.e., one-way coupling), despite a measured temperature dependence. However, strictly speaking, the temperature dependence should be taken into account and could potentially form another source of uncertainty in the analysis. These two parameters (ρ and c_p) are used in the cohesive zone algorithm during the final step through equation (65). If the higher temperature values of ρ and c_p are used instead of the nominal room temperature values, the predicted temperature from the dissipative cohesive zone model would be reduced by about 21% for the case of a 75 K temperature increase (the high-speed PMMA case). For the lower speed case where the experiments showed a 25 K temperature increase, the temperature predicted by the model would be lowered by only 7%. Thus, although the model does not include fully coupled material properties, the error in not accounting for the thermal coupling of ρ and c_p is minimal for the low-speed case.

7. Conclusions

7.1 Conclusions

The main goal of this study was to develop a better understanding of the dissipative processes present during opening and shear-dominated dynamic fracture of nominally brittle and ductile amorphous polymers. This was achieved through an experimental, numerical, and analytical investigation of the thermal dissipation of mechanical work in PMMA and PC. The main results of this work are summarized below.

- Opening mode dynamic fracture of ductile PC and brittle PMMA was found to be a highly dissipative event with significant temperature increases observed surrounding the propagating crack tip.

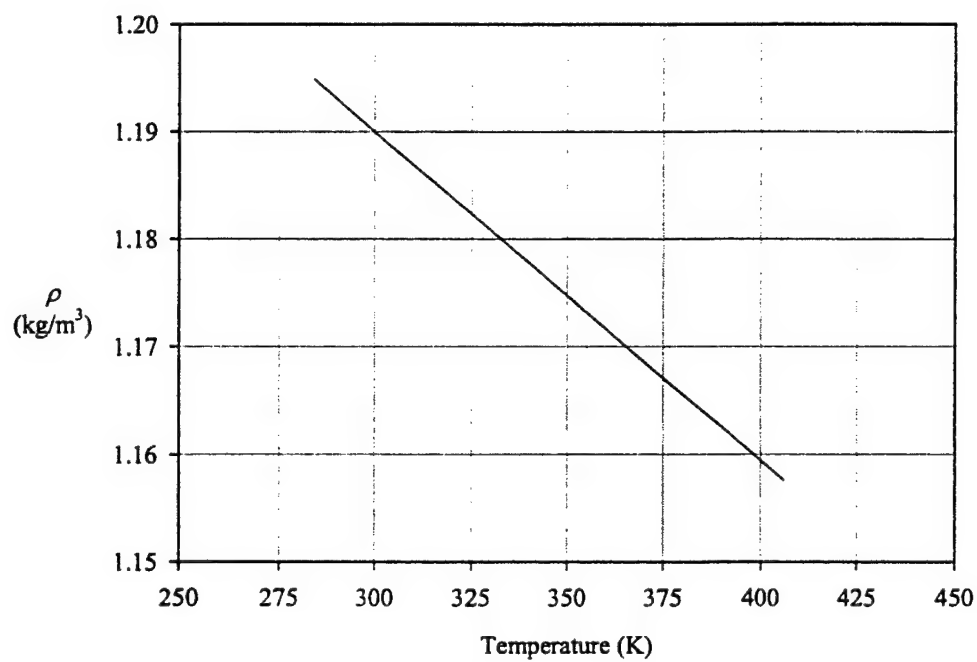


Figure 119. Variation of density with absolute material temperature for PMMA (Domininghaus 1988).

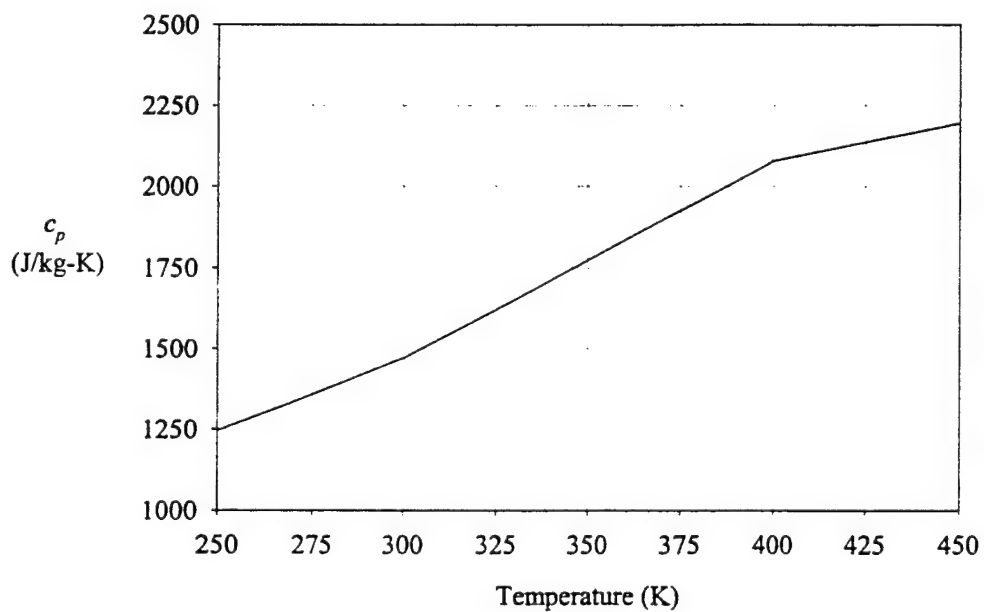


Figure 120. Variation of specific heat with material absolute temperature for PMMA (Domininghaus 1988).

The noncontact method of infrared radiometry was used to measure in high spatial and temporal resolution the temperature fields surrounding the advancing crack tips. This represents the first time dynamic crack tip temperature fields have been measured in polymeric materials. The maximum temperature increase recorded for cracks propagating near the limiting speed of $0.55 c_R$ was 105 K for PC and 72 K for PMMA. Dynamic fracture of PC was found to show dissipation due to plastic deformation as well as polymer craze formation and breakdown. A single craze formed along the surface of the material, where the temperature field was measured. Near the center of the fracture specimen thickness, ductile tearing was found to accompany polymer crazing. The multiple infrared detector thermal signals along with fracture surface microscopy indicated that polymer crazing is the primary energy dissipation mechanism during opening mode dynamic fracture of PMMA (i.e., no plasticity present). For crack speeds in PMMA around $0.24 c_R$, dynamic fracture occurred by the formation of a single craze. As the crack speed increased, multiple layered craze fronts formed along the main fracture surface, leading to increased crack tip heating.

- Shear-dominated dynamic fracture of PC and PMMA was also found to be a highly dissipative event. Such shear-dominated thermal measurements have never before been performed. Interpretation of the temperature signatures from the shear-dominated fracture experiments showed PC and PMMA to behave very differently to the same loading condition. An adiabatic shear band followed by a fracture event occurred in PC. The maximum temperature increase produced by the propagating adiabatic shear band was 45 K. The fracture event, which for the case of PC was subsonic, increased the temperature an additional 100 K. PMMA, on the other hand, showed an abrupt 85 K increase in temperature resulting from a shear crack propagating ~40% faster than the shear wave speed of the material. No dissipation mechanisms were found ahead of the shear crack in PMMA. The highly localized thermal signature indicated the crack tip in PMMA was formed from a shear crazing mechanism. Thermal evidence of crack face contact and frictional heating were observed behind the advancing crack tip in PMMA. The frictional heating increased the temperature beyond the melting point of PMMA. SEM images of fractured PMMA surfaces confirm that polymer melting did occur during the shear-dominated fracture event.
- The dynamic energy release rate was measured for both materials during the opening-mode experiments using a strain gage technique. The fracture energy was measured simultaneously with crack tip speed and temperature for the very first time, offering the ability to directly correlate the crack tip thermal field with crack tip mechanical fields. The measurements indicated that the energy needed to form new surfaces is

relatively insignificant compared to the energy required to propagate the crack dynamically. Thus, nearly all of the energy needed for fracture is dissipated in the form of heat. A numerical simulation of the opening-mode fracture of PC that considered only the energy dissipation from plasticity indicated that less than 10% of crack tip heating was due to plastic deformation of the ductile material. For PMMA, the measured crack tip heating along with the large amount of energy available for dissipation show the material to have a highly dissipative process zone during dynamic fracture. This was somewhat surprising given the nominally brittle nature of PMMA.

- The molecular weight of PMMA was found to influence the crack tip temperature field and the onset of crack branching for opening-mode dynamic fracture. The recorded temperature for the low molecular weight PMMA was only 35% that of the high molecular weight PMMA under similar impact loading conditions. The crack in low molecular weight PMMA was observed to branch much earlier than the high molecular weight PMMA. These measurements and observations suggest the physical mechanisms associated with brittle fracture of PMMA are less dissipative when the molecular weight is reduced. This furthermore suggests that molecular weight may be a significant material parameter for modeling thermal dissipation in brittle polymers.
- A dissipative cohesive zone model was developed by using a dynamic formulation of a cohesive zone and coupling it with an adiabatic form of the heat-energy equation. Several cohesive stress distributions were used to obtain unique cohesive traction laws. Predictions of crack tip heating were made from each of the cohesive stress distributions considered. The predictions were compared to the crack tip temperature field measurements made during opening mode fracture of high molecular weight PMMA. Good agreement was found between experimental data and the model for low crack tip speeds using one of the considered cohesive stress distributions. For high crack tip speeds, the dissipative cohesive zone model predicted only half the temperature increase observed during experiment. The cohesive zone modeling showed remarkable agreement with experiments where dynamic crack growth occurred by the formation of a single polymer craze (i.e., slow-speed crack propagation). For higher speed crack propagation, the single craze is replaced by a region of distributed damage. The dissipative cohesive zone model, as formulated in this study, was unable to account for the high crack tip temperatures observed within the distributed damage zone.

7.2 Future Work

The modeling that was performed for the mode I situation was limited to a rate-independent formulation. The modeling should be expanded to a

rate-dependent cohesive traction law (Kubair et al. 2001), particularly for polymeric materials because they exhibit considerable rate-dependent behavior. Additionally, a means of accounting for the distributed damage observed for high-speed crack propagation in PMMA should be developed within the cohesive zone methodology. Doing so will extend the applicability of the dissipative cohesive zone model to fracture with crack tips propagating near the terminal speed.

The shear-dominated fracture portion of this study included a cursory examination of high-speed frictional heating of PMMA. This is a topic where additional experimental and analytical work is obviously needed. The effort presented in section 4 was not intended to be comprehensive. A more comprehensive study will need to examine the influence of contact pressure, sliding speed, and the non-Newtonian aspect of high-temperature polymer flow. In addition to frictional heating, the entire kinematic behavior of the fracture surfaces aft of the crack tip in shear-dominated fracture of PMMA needs further exploration.

The modeling performed in section 6 was for opening mode fracture of the nominally brittle PMMA. The same techniques used for the dissipative mode I cohesive model should be applied to the shear-dominated case. This will require measurement of the dynamic energy release rate for this loading configuration, which may entail additional theoretical study. However, the cohesive zone approach for the shear-dominated fracture of PMMA will likely be useful because the highly localized thermal signatures of the shear crack suggest a shear-crazing phenomenon.

The ultimate conclusion of this effort will occur when fully coupled thermoplastic and thermofracture relationships are included in numerical algorithms to accurately predict the failure of amorphous polymers. The fully coupled relationships will need the thermal dependence of all material and fracture parameters to be established. The parametric study performed in section 6 to examine the influence of certain parameters on the cohesive zone model showed that material property variation can have a significant impact on resultant heating. However, as was pointed out in section 6, the parameters that were varied are likely not independent of each other. The interdependencies of the material parameters with temperature and each other will need to be established. This is an effort that will likely take many years to complete. Finally, it was shown in the parametric study that the critical stress, σ_c , had significant influence on amount of crack tip heating. The physical meaning of this parameter in the cohesive zone methodology and a means of reliably measuring it will be needed to cast all of the parameters in the dissipative cohesive zone model as material properties.

8. References

Adams, G. W., and R. J. Farris. "Latent Energy of Deformation of Bisphenol A Polycarbonate. *Journal of Polymer Science: Part B: Polymer Physics*, vol. 26, no. 2, pp. 433-445, 1998.

Allen, D. H., and C. R. Searcy. "A Micromechanically-Based Model for Predicting Dynamic Damage Evolution in Ductile Polymers." *Mechanics of Materials*, vol. 33, pp. 177-184, 2001.

American Society for Testing and Materials. "Tensile Properties of Plastics." ASTM D638, West Conshohocken, PA.

Anderson, T. L. *Fracture Mechanics: Fundamentals and Applications*. Vol. 325, Boca Raton: CRC Press, 1995.

Andrews, D. J. "Rupture Velocity of Plane Strain Shear Cracks." *Journal of Geophysical Research*, vol. 81, no. 32, pp. 5679-5687, 1976.

Anthony, S. R., J. P. Chubb, and J. Congleton. "The Crack Branching Velocity." *Philosophical Magazine*, vol. 22, pp. 1201-1206, 1970.

Barenblatt, G. I. "The Formation of Equilibrium Cracks During Brittle Fracture: General Ideas and Hypotheses, Axially Symmetric Cracks." *Applied Mathematics and Mechanics*, vol. 23, pp. 622-636, 1959.

Beahan, P., M. Bevis, and D. Hull. "Electron-Microscopy Studies of Fracture Processes in Amorphous Thermoplastics." *Polymer*, vol. 14, no. 3, pp. 96-102, 1973.

Berger, L. L. "On the Mechanism of Craze Fibril Breakdown in Glassy Polymers." *Macromolecules*, vol. 23, no. 11, pp. 2926-2934, 1990.

Berry, J. P. "Surface Characteristics of Fractured Poly(methyl methacrylate)." *Nature*, vol. 185, no. 4706, pp. 91-92, 1960.

Blok, H. "Theoretical Study of Temperature Rise at Surfaces of Actual Contact Under Oiliness Lubricating Conditions." *Proceedings of the General Discussions on Lubrications and Lubricants*, vol. 2, Institute of Mechanical Engineers, pp. 222-235, 1937.

Boley, B. A., and J. H. Weiner. *Theory of Thermal Stresses*. New York: Dover Publications, pp. 32-37, 1997.

Broberg, K. B. "The Propagation of a Brittle Crack." *Arkiv for Fysik*, vol. 18, pp. 159-192, 1960.

Broberg, K. B. "On Crack Paths." *Engineering Fracture Mechanics*, vol. 28, pp. 663-679, 1987.

Brown, H. R., and I. M. Ward. "Craze Shape and Fracture in Poly(methyl methacrylate)." *Polymer*, vol. 14, pp. 469-475, 1973.

Burridge, R., G. Conn, and L. B. Freund. The Stability of a Rapid Mode II Shear Crack With Finite Cohesive Traction." *Journal of Geophysical Research*, vol. 85, no. B5, pp. 2210-2222, 1979.

Camacho, G. T., and M. Ortiz. "Computational Modeling of Impact Damage in Brittle Materials." *International Journal of Solids and Structures*, vol. 33, no. 20-22, pp. 2899-2938, 1996.

Chona, R. "The Stress Field Surrounding the Tip of a Crack Propagating in a Finite Body." Ph.D. dissertation, University of Maryland, College Park, MD, 1987.

Cotterell, B. "Velocity Effects in Fracture Propagation." *Applied Materials Research*, vol. 4, pp. 227-232, 1965.

Döll, W. "Application of an Energy Balance and an Energy Method to Dynamic Crack Propagation." *International Journal of Fracture*, vol. 12, no. 4, pp. 595-605, 1976.

Döll, W. "Fractography and Failure Mechanisms of Amorphous Thermoplastics." *Fractography and Failure Mechanisms of Polymers and Composites*. New York: Elsevier Science, pp. 387-436, 1989.

Domininghaus, H. *Plastics for Engineers - Materials, Properties, Applications*. New York: Hanser Publishers, pp. 268-269, 428-429, 1988.

Donald, A. M., and E. J. Kramer. "Craze Initiation and Growth in High-Impact Polystyrene." *Journal of Polymer Science*, vol. 27, no. 10, pp. 3729-3741, 1982.

Duffy, J. "Temperature Measurements During the Formation of Shear Bands in a Structural Steel." *Mechanics of Material Behavior*, edited by G. J. Dvorak and R. T. Shield, Amsterdam: Elsevier Science Publishers B. V., pp. 75-86, 1984.

Dugdale, D. S. "Yielding of Steel Sheets Containing Slits." *Journal of the Mechanics and Physics of Solids*, vol. 8, no. 2, pp. 100-104, 1960.

Dulaney, E. N., and W. F. Brace. "Velocity Behavior of a Growing Crack." *Journal of Applied Physics*, vol. 31, pp. 2233-2236, 1960.

Erdogan, F., and G. C. Sih. "On the Crack Extension in Plates Under Plane Loading and Transverse Shear." *Journal of Basic Engineering*, vol. 85, no. 1, pp. 519-527, 1963.

Ettles, C. C. M. "The Thermal Control of Friction at High Sliding Speeds." *Journal of Tribology – Transactions of the ASME*, vol. 108, no. 1, pp. 98-104, 1986.

Ettles, C. C. M., and J. H. Shen. "The Influence of Frictional Heating on the Sliding Friction of Elastomers and Polymers." *Rubber Chemistry and Technology*, vol. 61, no. 1, pp. 119-136, 1988.

Farren, W. S., and G. I. Taylor. "The Heat Developed During Plastic Extension of Metals." *Proceedings of the Royal Society of London, Series A*, vol. 107, pp. 422-451, 1925.

Fineberg, J., S. P. Gross, M. Marder, and H. L. Swinney. "Instability in Dynamic Fracture." *Physical Review Letters*, vol. 67, p. 457, 1992.

Fraser, R. A. W., and I. M. Ward. "Temperature Dependence of Craze Shape and Fracture in Polycarbonate." *Polymer*, vol. 19, pp. 220-224, 1978.

Freund, L. B. *Dynamic Fracture Mechanics*. New York: Cambridge University Press, 1990.

Fuller, K. N. G., P. G. Fox, and J. E. Field. "The Temperature Rise at the Tip of fast Moving Cracks in Glassy Polymers." *Proceedings of the Royal Society of London, Series A*, vol. 341, no. 1627, pp. 537-557, 1975.

Geubelle, P. H., and J. Baylor. "Impact-Induced Delamination of Laminated Composites: A 2-D Simulation." *Composites B*, vol. 29, pp. 589-602, 1998.

Geubelle, P. H., and J. R. Rice. "A Spectral Method for 3-D Elastodynamic Fracture Problems." *Journal of the Mechanics and Physics of Solids*, vol. 43, pp. 1791-1824, 1995.

Henkee, C. S., and E. J. Kramer. "Crazing and Shear Deformation in Crosslinked Polystyrene." *Journal of Polymer Science Part B: Polymer Physics*, vol. 22, no. 4, pp. 721-737, 1984.

Hibbitt, Karlsson, and Sorensen. *ABAQUS/Explicit User's Manual*. HKS Incorporated, Providence, RI, 1998.

Hodowany, J., Ravichandran, G., Rosakis, A. J., and Rosakis, P. "Partition of Plastic Work Into Heat and Stored Energy in Metals." *Experimental Mechanics* vol. 40, no. 2, pp. 113-123, 2000.

Incropera, F. P., and D. F. DeWitt. *Fundamentals of Heat Transfer*. New York: John Wiley & Sons, pp. 582-589, 1980.

Irwin, G. R., 1980. Series Representation of the Stress Field Around Constant Speed Cracks. University of Maryland Lecture Notes, College Park, MD, unpublished data.

Jandel Scientific. *TableCurve 2D User's Manual*. Jandel Scientific, San Rafael, CA, 1994.

Kallivayalil, J. A., and A. T. Zehnder. "Measurement of the Temperature Field Induced by Dynamic Crack Growth in Beta-C Titanium." *International Journal of Fracture*, vol. 66, no. 2, pp. 99-120, 1994.

Kalthoff, J. F., and S. Winkler. "Failure Mode Transition at High Rates of Shear Loading." *Impact Loading and Dynamic Behaviour of Materials*, edited by C. Y. Kunze, H. D. Chiem, and L. W. Meyer, Berlin: Springer Verlag, 1987.

Kambour, R. P. "Direct Observation of the Craze Ahead of the Propagating Crack in PMMA and Polystyrene." *Journal of Polymer Science: Part A-2*, vol. 4, pp. 349-358, 1964.

Kambour, R. P. "Mechanism of Fracture in Glassy Polymers: I. Fracture Surfaces in Polymethyl Methacrylate." *Journal of Polymer Science: Part A*, vol. 3, pp. 1713-1724, 1965.

Kambour, R. P. "Mechanism of Fracture in Glassy Polymers: II. Survey of Crazing Response During Crack Propagation in Several Polymers." *Journal of Polymer Science: Part A-2*, vol. 4, pp. 17-24, 1966a.

Kambour, R. P. "Mechanism of Fracture in Glassy Polymers. III. Direct Observation of the Craze Ahead of the Propagating Crack in Poly(methyl methacrylate) and Polystyrene." *Journal of Polymer Science: Part A-2*, vol. 4, pp. 349-358, 1966b.

Kambour, R. P. "A Review of Crazing and Fracture in Thermoplastics." *Journal of Polymer Science Part D: Macromolecular Reviews*, vol. 7, pp. 1-154, 1973.

Kambour, R. P., A. S. Holik, and S. Miller. "Plane-Strain Fracture Energy Instability and Mixed Mode Crack Propagation in Polycarbonate at Room Temperature." *Journal of Polymer Science Part B: Polymer Physics Edition*, vol. 16, pp. 91-104, 1978.

Kapoor, R., and S. Nemat-Nasser. "Determination of Temperature Rise During High Strain Rate Deformation." *Mechanics of Materials*, vol. 27, no. 1, pp. 1-12, 1998.

Kawabe, H., Y. Natsume, Y. Higo, and S. Nunomura. "Micromechanism of a Deformation Process Before Crazing in a Polymer During Tensile Testing." *Journal of Material Science*, vol. 27, no. 20, pp. 5547-5552, 1992.

Khanna, S. K., and A. Shukla. "On the Use of Strain Gages in Dynamic Fracture Mechanics." *Engineering Fracture Mechanics*, vol. 51, no. 6, pp. 933-948, 1995.

Kong, H., and M. F. Ashby. "Wear Mechanisms in Brittle Solids." *Acta Metallurgica et Materialia*, vol. 40, no. 11, pp. 2907-2920, 1992.

Kramer, E. J. "Microscopic and Molecular Fundamentals of Crazing." *Journal of Advanced Polymer Science*, vol. 52-53, pp. 1-56, 1983.

Kramer, E. J. "Craze Fibril Formation and Breakdown." *Journal of Polymer Engineering Science*, vol. 24, no. 10, pp. 761-769, 1984.

Kramer, E. J., and L. L. Berger. "Fundamental Processes of Craze Growth and Fracture." *Journal of Advanced Polymer Science*, vol. 91/92, pp. 1-68, 1990.

Krishnaswamy, S., A. J. Rosakis, and G. Ravichandran. "On the Extent of Dominance of Asymptotic Elastodynamic Crack-Tip Fields: Pt. 2—Numerical Investigation of Three-Dimensional and Transient Effects." *Journal of Applied Mechanics*, vol. 58, no. 1, pp. 95-103, 1991.

Kubair, D. V., and P. H. Geubelle. "Comparative Analysis of Extrinsic and Intrinsic Cohesive Models of Dynamic Fracture." *International Journal of Solids and Structures*, 2001.

Kubair, D. V., P. H. Geubelle, and Y. Y. Huang. "Analysis of a Rate-dependent Cohesive Model for Dynamic Crack Propagation." *Engineering Fracture Mechanics*, 2001.

Lambros, J., and A. J. Rosakis. "Development of a Dynamic Decohesion Criterion for Subsonic Fracture of the Interface Between Two Dissimilar Materials." *Proceedings of the Royal Society of London, Series A*, vol. 451, pp. 711-736, 1995.

Li, Z., and J. Lambros. "Strain Rate Effects on the Thermomechanical Behavior of Polymers." *International Journal of Solids and Structures*, vol. 38, no. 20, pp. 3549-3562, 2001.

Lin, G., P. H. Geubelle, and N. R. Sotos. "Simulation of Fiber Debonding with Friction in a Model Composite Pushout Test." *International Journal of Solids and Structures*, vol. 38, no. 46-47, pp. 8547-8562, 2001.

Lo, C. Y., T. A. Nakamura, and A. Kushner. "Computational Analysis of Dynamic Crack Propagation Along a Bimaterial Interface." *International Journal of Solids and Structures*, vol. 31, no. 2, pp. 145-168, 1994.

Mason, J. J., and A. J. Rosakis. "On the Dependence of the Dynamic Crack Tip Temperature Fields in Metals Upon Crack Tip Velocity and Material Parameters." *Mechanics of Materials*, vol. 16, no. 4, pp. 337-350, 1992.

Mason, J. J., A. J. Rosakis, and G. Ravichandran. "On the Strain and Strain Rate Dependence of the Fraction of Plastic Work Converted to Heat: An Experimental Study Using High-Speed Infrared Detectors and the Kolsky Bar." *Mechanics of Materials*, vol. 17, no. 2, pp. 135-145, 1994.

Measurements Group Inc. "Errors Due to Wheatstone Bridge Nonlinearity." Measurements Group Tech Note TN-507, Raleigh, NC, 1982.

Morgan, G. P., and I. M. Ward. "Temperature Dependence of Craze Shape and Fracture in Poly(methyl methacrylate)." *Polymer*, vol. 18, pp. 87-91, 1977.

Murray, J., and D. Hull. "Dependence on Strain Rate of Nucleation of Cracks in Polystyrene at 293 Degrees K." *Journal of Polymer Science: Part A-2*, vol. 8, no. 9, pp. 1521-1540, 1970.

Needleman, A. "A Continuum Model for Void Nucleation by Inclusion Debonding." *Journal of Applied Mechanics*, vol. 54, no. 3, pp. 525-531, 1987.

Needleman, A. "Micromechanical Modeling of Interfacial Decohesion." *Ultramicroscopy*, vol. 40, no. 3, pp. 203-214, 1992.

Nilsson, K. F., and J. W. Hutchinson. "Interaction Between a Major Crack and Small Crack Damage in Aircraft Sheet Material." *International Journal of Solids and Structures*, vol. 31, no. 17, pp. 2331-2346, 1994.

O'Shea, D. C. *Elements of Modern Optical Design*. New York: John Wiley & Sons, 1985.

Panda, K. C., and J. G. Williams. "Cohesive Zone Modeling of Crack Growth in Polymers. Part 1—Experimental Measurement of Cohesive Law." *Plastics, Rubber and Composites*, vol. 29, no. 9, pp. 439-446, 2000.

Paxson, S. L., and R. A. Lucas. "An Investigation of the Velocity Characteristics of a Fixed Boundary Fracture Model." *Dynamic Crack Propagation*, edited by G. C. Sih, Leyden: Noordhoff International Publishing, pp. 415-426, 1973.

Peterson, T. L., D. G. Ast, and E. J. Kramer. "Holographic Interferometry of Crazes in Polycarbonate." *Journal of Applied Physics*, vol. 45, no. 10, pp. 4220-4228, 1974.

Planck, M. *The Theory of Heat Radiation*. New York: Dover Publications, 1959.

Poulikakos, D. *Conduction Heat Transfer*. New Jersey: Prentice Hall, pp. 146-150, 1994.

Ravi-Chandar, K. "On the Failure Mode Transitions in Polycarbonate Under Dynamic Mixed Mode Loading." *International Journal of Solids and Structures*, vol. 32, no. 6, pp. 925-938, 1995.

Ravi-Chandar, K., J. Lu, B. Yang, and Z. Zhu. "Failure Mode Transitions in Polymers Under High Strain Rate Loading." *International Journal of Fracture*, vol. 101, no. 1-2, pp. 33-72, 2000.

Rittel, D. "Experimental Investigation of Transient Thermoelastic Effects in Dynamic Fracture." *International Journal of Solids and Structures*, vol. 35, no. 22, pp. 2959-2973, 1998.

Rittel, D. "On the Conversion of Plastic Work to Heat During High Strain Rate Deformation of Glassy Polymers." *Mechanics of Materials*, vol. 31, no. 2, pp. 131-139, 1999.

Rittel, D. "Experimental Investigation of Transient Thermoplastic Effects in Dynamic Fracture." *International Journal of Solids and Structures*, vol. 37, no. 21, pp. 2901-2913, 2000.

Rosakis, A. J. "Application of Coherent Gradient Sensing (CGS) to the Investigation of Dynamic Fracture Problems." *Optics and Lasers in Engineering*, vol. 19, no. 1-3, pp. 3-41, 1993.

Rosakis, A. J., O. Samudrala, and D. Coker. "Cracks Faster Than the Shear Wave Speed." *Science*, vol. 284, no. 5418, pp. 1337-1340, 1999.

Sanford, R. J., and J. W. Dally. "Strain-Gage Methods for Measuring the Opening-Mode Stress-Intensity Factor." *Experimental Mechanics*, vol. 27, pp. 381-388, 1987.

Sanford, R. J., J. W. Dally, and J. R. Berger. "An Improved Strain Gage Method for Measuring K_{ID} for a Propagating Crack." *Journal of Strain Analysis*, vol. 25, no. 3, pp. 177-183, 1990.

Sharon, E., S. P. Gross, and J. Fineberg. "Energy Dissipation in Dynamic Fracture." *Physical Review Letters*, vol. 76, no. 12, pp. 2117-2120, 1996.

Singh, R. P., J. Lambros, A. Shukla, and A. Rosakis. "Investigation of the Mechanics of Intersonic Crack Propagation Along a Bimaterial Interface Using Coherent Gradient Sensing and Photoelasticity." *Proceedings of the Royal Society of London, Series A*, vol. 453, pp. 2649-2667, 1997.

SPSS Inc. SigmaPlot 2000 Programming Guide. Chicago, IL, 2000.

Stalder, B., P. Beguelin, and H. H. Kausch. "A Simple Velocity Gauge for Measuring Crack Growth." *International Journal of Fracture*, vol. 22, R47-R54, 1983.

Sun, N. S., and T. R. Hsu. "Thermomechanical Coupling Effects on Fractured Solids." *International Journal of Fracture*, vol. 78, no. 1, pp. 67-87, 1996.

Suo, Z., M. Ortiz, and A. Needleman. "Stability of Solids With Interfaces." *Journal of the Mechanics and Physics of Solids*, vol. 40, pp. 613-640, 1992.

Suzuki, S., Y. Nozaki, and H. Kimura. "High-Speed Holographic Microscopy for Fast-Propagating Cracks in Transparent Materials." *Applied Optics*, vol. 36, no. 28, pp. 7224-7233, 1997.

Taylor, G. I., and H. Quinney. "The Latent Energy Remaining in a Metal After Cold Working." *Proceedings of the Royal Society, Series A*, vol. 143, pp. 307-326, 1934.

Theocaris, P. S., and N. P. Andrianopoulos. "Strain Rate Effects on the Mechanical Properties of Polymers." *Proceedings of the VIIth SESA International Conference*, edited by A. Bester, Haifa, Israel, pp. 473-482, 1982.

Tijssens, M. G. A., E. van der Giessen, and L. J. Sluys. "Modeling of Crazing Using a Cohesive Surface Methodology." *Mechanics of Materials*, vol. 32, no. 1, pp. 19-35, 2000.

Tvergaard, V., and J. W. Hutchinson. "The Relation Between Crack Growth Resistance and Fracture Process Parameters in Elastic-Plastic Solids." *Journal of the Mechanics and Physics of Solids*, vol. 40, no. 6, pp. 1377-1397, 1992.

Tvergaard, V., and J. W. Hutchinson. "Effect of Strain-Dependent Cohesive Zone Model on Predictions of Crack Growth Resistance." *International Journal of Solids and Structures*, vol. 33, no. 20-22, pp. 3297-3308, 1996.

Wool, R. P. *Polymer Interfaces: Structure and Strength*. New York: Hanser Publishers, 1995.

Xu, X. P., and A. Needleman. "Numerical Simulations of Fast Crack Growth in Brittle Solids." *Journal of the Mechanics and Physics of Solids*, vol. 42, no. 9, pp. 1397-1434, 1994.

Yang, A. C., E. J. Kramer, C. C. Kuo, and S. L. Phoenix. "Craze Fibril Stability and Breakdown in Polystyrene." *Macromolecules*, vol. 19, no. 7, pp. 2010-2019, 1986.

Yoffe, E. H. "The Moving Griffith Crack." *Philosophical Magazine*, vol. 42, no. 330, pp. 739-750, 1951.

Zehnder, A. T., and A. J. Rosakis. "Dynamic Fracture Initiation and Propagation in 4340 Steel Under Impact Loading." *International Journal of Fracture*, vol. 43, no. 4, pp. 271-285, 1990.

Zehnder, A. T., and A. J. Rosakis. "On the Temperature Distribution at the Vicinity of Dynamically Propagating Cracks in 4340 Steel: Experimental Measurements Using High-Speed Infrared Detectors." *Journal of the Mechanics and Physics of Solids*, vol. 39, no. 3, pp. 385-417, 1991.

Zehnder, A. T., and A. J. Rosakis. "Temperature Rise at the Tip of Dynamically Propagating Cracks: Measurements Using High-Speed Infrared Detectors." *Experimental Techniques in Fracture III*, Society for Experimental Mechanics, Bethel, CT, pp. 125-169, 1993.

Zehnder, A. T., P. R. Guduru, A. J. Rosakis, and G. Ravichandran. "Million Frames per Second Infrared Imaging System." *Review of Scientific Instruments*, vol. 71, no. 10, pp. 3762-3768, 2000.

Zhou, M., A. J. Rosakis, and G. Ravichandran. "Dynamically Propagating Shear Bands in Impact-Loaded Prenotched Plates—I. Experimental Investigations of Temperature Signatures and Propagation Speed." *Journal of the Mechanics and Physics of Solids*, vol. 44, no. 6, pp. 981–1006, 1996a.

Zhou, M., G. Ravichandran, and A. J. Rosakis. "Dynamically Propagating Shear Bands in Impact-Loaded Prenotched Plates—II. Numerical Simulations." *Journal of the Mechanics and Physics of Solids*, vol. 44, no. 6, pp. 1007–1032, 1996b.

INTENTIONALLY LEFT BLANK.

Appendix A. Closed Form Solution of Cohesive Zone Length

The analytical expression for the cohesive zone length, L , was given in section 6 as (Freund 1990),

$$G = \frac{2A_I}{\pi E} \left[\int_0^L \frac{\sigma(l)}{\sqrt{l}} dl \right]^2, \quad (A-1)$$

where the parameters were defined in section 6. An explicit analytic solution of equation (A-1) for L is provided here for two cohesive stress distributions, namely the constant stress and linear decay distributions discussed in section 6.

The constant stress cohesive distribution has the form

$$\sigma(\xi) = \sigma_c, \quad (A-2)$$

where σ_c is a constant and ξ is the length along the cohesive zone as shown in Figure 87. Substituting equation (A-2) into (A-1) gives

$$G = \frac{2A_I \sigma_c^2}{\pi E} \left[\int_0^L \frac{1}{\sqrt{l}} dl \right]^2. \quad (A-3)$$

The integral is solved by using the substitution $\eta = \sqrt{l}$, which gives

$$G = \frac{2A_I \sigma_c^2}{\pi E} \left[\int_0^{\sqrt{L}} 2d\eta \right]^2. \quad (A-4)$$

Solution of the integral in equation (A-4) yields

$$G = \frac{2A_I \sigma_c^2}{\pi E} [2\sqrt{L}]^2. \quad (A-5)$$

Solving equation (A-5) for L gives the length of the cohesive zone for the constant stress case,

$$L = \frac{\pi E G}{8A_I \sigma_c^2}. \quad (A-6)$$

The analytical expression for the linear decay cohesive stress distribution was given in section 6 as

$$\sigma(\xi) = \sigma_c \left(1 - \frac{\xi}{L} \right). \quad (A-7)$$

Substituting the linear decay distribution into equation (A-1) gives the following:

$$G = \frac{2A_I\sigma_c^2}{\pi E L^2} \left[\int_0^L \frac{(L-l)}{\sqrt{l}} dl \right]^2. \quad (\text{A-8})$$

Using the same substitution as was used for the constant stress case (i.e., $\eta = \sqrt{l}$) in equation (A-8) yields

$$G = \frac{2A_I\sigma_c^2}{\pi E L^2} \left[\int_0^{\sqrt{L}} 2(L-\eta^2) d\eta \right]^2. \quad (\text{A-9})$$

Solution of the integral in equation (A-9) results in the following expression:

$$G = \frac{8A_I\sigma_c^2}{\pi E L^2} \left[\frac{2}{3} L \sqrt{L} \right]^2. \quad (\text{A-10})$$

The solution of the cohesive zone length for the linear decay distribution thus becomes

$$L = \frac{9\pi E G}{32A_I\sigma_c^2}. \quad (\text{A-11})$$

Appendix B. Closed Form Solution of Cohesive Zone Opening Rate

Closed form expressions for the rate of cohesive zone opening, $\partial\delta/\partial\xi$, are next derived in this Appendix for the constant stress and linear decay cohesive stress distributions. The Cauchy singular integral equation for $\partial\delta/\partial\xi$ was given in section 6 as (Freund 1990):

$$\frac{\partial\delta}{\partial\xi} = \frac{C}{\pi\mu} \int_0^L \sqrt{\frac{\xi}{\eta}} \frac{\sigma(\eta)}{(\xi-\eta)} d\eta, \quad (B-1)$$

where

$$C = \frac{2\lambda_1(1-\lambda_2^2)}{D}, \quad (B-2)$$

and the parameters were defined in section 6. The constant stress cohesive distribution has the form

$$\sigma(\xi) = \sigma_c, \quad (B-3)$$

where σ_c is a constant and ξ is the length along the cohesive zone as shown in Figure 87. Substituting the constant stress distribution given by equation (B-3) into equation (B-1) yields

$$\frac{\partial\delta}{\partial\xi} = \frac{C\sigma_c}{\pi\mu} \int_0^L \sqrt{\frac{\xi}{\eta}} \frac{1}{(\xi-\eta)} d\eta. \quad (B-4)$$

Performing the substitution $l = \sqrt{\eta}$ in equation (B-4) gives

$$\frac{\partial\delta}{\partial\xi} = \frac{-2C\sigma_c\sqrt{\xi}}{\pi\mu} \int_0^{\sqrt{L}} \frac{1}{(l^2 - \xi)} dl. \quad (B-5)$$

Using partial fractions, the integrand can be simplified to the following equivalent expression:

$$\frac{\partial\delta}{\partial\xi} = \frac{-C\sigma_c}{\pi\mu} \int_0^{\sqrt{L}} \left(\frac{1}{l - \sqrt{\xi}} - \frac{1}{l + \sqrt{\xi}} \right) dl. \quad (B-6)$$

The integral in equation (B-6) contains two terms, which are solved individually. Starting with the second term, the substitution $u = l + \sqrt{\xi}$ gives

$$\int_0^{\sqrt{L}} -\frac{1}{l+\sqrt{\xi}} dl = - \int_{\sqrt{\xi}}^{\sqrt{L}+\sqrt{\xi}} \frac{1}{u} du. \quad (B-7)$$

Evaluating the integral on the right hand side of equation (B-7) yields

$$\int_0^{\sqrt{L}} -\frac{1}{l+\sqrt{\xi}} dl = \ln \frac{\sqrt{\xi}}{\sqrt{L}+\sqrt{\xi}}. \quad (B-8)$$

The first term in the integral of equation (A-6) is now evaluated. The path of integration is from zero to \sqrt{L} ; however, the expression has a singularity along the integration path at $\sqrt{\xi}$. Because the integrand is not analytic at the singularity, the integral cannot be evaluated by simply "passing through" the singular point. Instead, the integral will be evaluated along the interval $\sqrt{\xi} - \varepsilon$ to $\sqrt{\xi} + \varepsilon$, where ε is a very small number, and then along the remaining interval $\sqrt{\xi} + \varepsilon$ to \sqrt{L} . The resulting expression is then evaluated in the limiting case of $\varepsilon \rightarrow 0$. Proceeding in this manner:

$$\int_0^{\sqrt{L}} \frac{1}{l-\sqrt{\xi}} dl = \lim_{\varepsilon \rightarrow 0} \left[\int_{\sqrt{\xi}-\varepsilon}^{\sqrt{\xi}+\varepsilon} \frac{dl}{l-\sqrt{\xi}} + \int_{\sqrt{\xi}+\varepsilon}^{\sqrt{L}} \frac{dl}{l-\sqrt{\xi}} \right]. \quad (B-9)$$

The integrals are evaluated to give

$$\int_0^{\sqrt{L}} \frac{1}{l-\sqrt{\xi}} dl = \lim_{\varepsilon \rightarrow 0} \left\{ \left[\ln(-\varepsilon) - \ln(\varepsilon - \sqrt{\xi}) \right] + \left[\ln(\sqrt{L} - \sqrt{\xi}) - \ln(\varepsilon) \right] \right\}. \quad (B-10)$$

This simplifies to

$$\int_0^{\sqrt{L}} \frac{1}{l-\sqrt{\xi}} dl = \lim_{\varepsilon \rightarrow 0} \left[\ln \left(\frac{-\varepsilon}{\varepsilon - \sqrt{\xi}} \right) + \ln \left(\frac{\sqrt{L} - \sqrt{\xi}}{\varepsilon} \right) \right]. \quad (B-11)$$

Noting the following:

$$\ln \left(\frac{-\varepsilon}{\varepsilon - \sqrt{\xi}} \right) = \ln \left(\frac{\varepsilon}{\sqrt{\xi} - \varepsilon} \right), \quad (B-12)$$

equation (B-11) becomes

$$\int_0^{\sqrt{L}} \frac{1}{l-\sqrt{\xi}} dl = \lim_{\varepsilon \rightarrow 0} \left[\ln \left(\frac{\varepsilon}{\sqrt{\xi} - \varepsilon} \right) + \ln \left(\frac{\sqrt{L} - \sqrt{\xi}}{\varepsilon} \right) \right]. \quad (B-13)$$

Equation (B-13) simplifies to

$$\int_0^{\sqrt{L}} \frac{1}{l - \sqrt{\xi}} dl = \lim_{\varepsilon \rightarrow 0} \left[\ln \left(\frac{\sqrt{L} - \sqrt{\xi}}{\sqrt{\xi} - \varepsilon} \right) \right], \quad (B-14)$$

which, in the limit, becomes:

$$\int_0^{\sqrt{L}} \frac{1}{l - \sqrt{\xi}} dl = \ln \left(\frac{\sqrt{L} - \sqrt{\xi}}{\sqrt{\xi}} \right). \quad (B-15)$$

Equation (B-15) provides the expression for the integral of the first term in the integrand of equation (B-6). With the integral of equation (B-15) now completely solved, the expression for $\partial\delta/\partial\xi$ is

$$\frac{\partial\delta}{\partial\xi} = -\frac{C\sigma_c}{\pi\mu} \left[\ln \left(\frac{\sqrt{L} - \sqrt{\xi}}{\sqrt{\xi}} \right) + \ln \left(\frac{\sqrt{\xi}}{\sqrt{L} + \sqrt{\xi}} \right) \right], \quad (B-16)$$

which simplifies to the expression presented in section 6 for the constant stress distribution case,

$$\frac{\partial\delta}{\partial\xi} = -\frac{C\sigma_c}{\pi\mu} \ln \left(\frac{\sqrt{L} - \sqrt{\xi}}{\sqrt{L} + \sqrt{\xi}} \right). \quad (B-17)$$

A similar procedure is used to derive an expression of $\partial\delta/\partial\xi$ for the linear decay cohesive stress distribution. The analytical expression for the linear decay stress distribution was given in section 6 as

$$\sigma(\xi) = \sigma_c \left(1 - \frac{\xi}{L} \right). \quad (B-18)$$

Substituting equation (B-18) into the Cauchy singular equation (B-1) gives

$$\frac{\partial\delta}{\partial\xi} = -\frac{C\sigma_c}{\pi\mu} \int_0^L \sqrt{\frac{\xi}{\eta}} \frac{(1 - \eta/L)}{(\eta - \xi)} d\eta. \quad (B-19)$$

As before, the substitution $l = \sqrt{\eta}$ is used in the integrand. The resulting expression is

$$\frac{\partial\delta}{\partial\xi} = \frac{2C\sigma_c\sqrt{\xi}}{\pi\mu L} \int_0^{\sqrt{L}} \frac{l^2 - L}{l^2 - \xi} dl. \quad (B-20)$$

The integrand can be expressed in a more tractable form for integration by performing polynomial division on the integrand and then simplifying with partial fractions to give

$$\frac{\partial \delta}{\partial \xi} = \frac{2C\sigma_c \sqrt{\xi}}{\pi \mu L} \int_0^{\sqrt{L}} \left[1 + \left(\frac{\xi - L}{2\sqrt{\xi}} \right) \left(\frac{1}{l - \sqrt{\xi}} \right) - \left(\frac{\xi - L}{2\sqrt{\xi}} \right) \left(\frac{1}{l + \sqrt{\xi}} \right) \right] dl. \quad (B-21)$$

The second and third terms in the integrand have a form similar to the integrand in equation (B-6) that was obtained during the derivation for the constant stress distribution. Using the same procedure to evaluate these two terms as was used before, i.e., equations (B-7) through (B-15), and integrating the first term in the integrand results in the following expression:

$$\frac{\partial \delta}{\partial \xi} = \frac{2C\sigma_c \sqrt{\xi}}{\pi \mu L} \left[\sqrt{L} + \frac{\xi - L}{2\sqrt{\xi}} \ln \left(\frac{\sqrt{L} - \sqrt{\xi}}{\sqrt{L} + \sqrt{\xi}} \right) \right]. \quad (B-22)$$

This expression simplifies to

$$\frac{\partial \delta}{\partial \xi} = \frac{2C\sigma_c}{\pi \mu} \left[\frac{\sqrt{\xi L}}{L} + \frac{\xi - L}{2L} \ln \left(\frac{\sqrt{L} - \sqrt{\xi}}{\sqrt{L} + \sqrt{\xi}} \right) \right], \quad (B-23)$$

which is identical to equation (111) given in section 6.

REPORT DOCUMENTATION PAGE			Form Approved OMB No. 0704-0188
<p>Public reporting burden for this collection of information is estimated to average 1 hour per response, including the time for reviewing instructions, searching existing data sources, gathering and maintaining the data needed, and completing and reviewing the collection of information. Send comments regarding this burden estimate or any other aspect of this collection of information, including suggestions for reducing this burden, to Washington Headquarters Services, Directorate for Information Operations and Reports, 1215 Jefferson Davis Highway, Suite 1204, Arlington, VA 22202-4302, and to the Office of Management and Budget, Paperwork Reduction Project (0704-0188), Washington, DC 20503.</p>			
1. AGENCY USE ONLY (Leave blank)	2. REPORT DATE	3. REPORT TYPE AND DATES COVERED	
	August 2002	Final, October 1997–December 2001	
4. TITLE AND SUBTITLE		6. FUNDING NUMBERS	
Thermomechanical Behavior of Amorphous Polymers During High-Speed Crack Propagation		IL1601102AH42	
6. AUTHOR(S)		8. PERFORMING ORGANIZATION REPORT NUMBER	
Todd W. Bjerke		ARL-TR-2793	
7. PERFORMING ORGANIZATION NAME(S) AND ADDRESS(ES)		10. SPONSORING/MONITORING AGENCY REPORT NUMBER	
U.S. Army Research Laboratory ATTN: AMSRL-WM-TC Aberdeen Proving Ground, MD 21005-5066			
9. SPONSORING/MONITORING AGENCY NAMES(S) AND ADDRESS(ES)			
Department of the Army 4201 Wilson Blvd. Arlington, VA 22230			
11. SUPPLEMENTARY NOTES			
12a. DISTRIBUTION/AVAILABILITY STATEMENT		12b. DISTRIBUTION CODE	
Approved for public release; distribution is unlimited.			
13. ABSTRACT (Maximum 200 words)			
<p>The dissipative processes that occur during opening and shear-dominated dynamic fracture of amorphous polymers were examined in a combined experimental, computational, and analytical investigation. Experiments were performed using two materials, nominally brittle polymethyl methacrylate and nominally ductile polycarbonate to quantify crack tip heating and identify dominant dissipative mechanisms. Shear-dominated dynamic fracture of polymethyl methacrylate was found to exhibit heating from craze formation and frictional sliding of the fracture surfaces aft of the propagating crack tip. Heating in polycarbonate during shear-dominated dynamic fracture was from two dissipative processes, the formation of an adiabatic shear band and plastic deformation surrounding the propagating crack. Plastic deformation heating was noted for opening mode fracture of polycarbonate. Finite-element simulations of dynamic crack growth in polycarbonate were performed to isolate the heating from thermoplasticity. The simulations indicated that although thermoplastic heating does occur, thermofracture heating may be significant. Heating from craze formation was observed during opening mode fracture of polymethyl methacrylate. A dissipative cohesive zone model was developed to predict heating from thermofracture mechanisms associated with polymer crazing. The model predictions were consistent with measurements of single craze heating during opening mode fracture of polymethyl methacrylate.</p>			
14. SUBJECT TERMS		15. NUMBER OF PAGES	
dynamic fracture, polymer fracture, craze, thermomechanical heating		192	
		16. PRICE CODE	
17. SECURITY CLASSIFICATION OF REPORT	18. SECURITY CLASSIFICATION OF THIS PAGE	19. SECURITY CLASSIFICATION OF ABSTRACT	20. LIMITATION OF ABSTRACT
UNCLASSIFIED	UNCLASSIFIED	UNCLASSIFIED	UL

INTENTIONALLY LEFT BLANK.